

**Characterizing the Effect of Increasing Albedo on Urban Meteorology and
Air Quality in Cold Climates, a Case Study for Montreal**

Ali Gholizadeh Touchaei

A Thesis
in
the Department
of
Building, Civil and Environmental Engineering

Presented in Partial Fulfillment of the Requirements
For the Degree of Doctor of Philosophy at
Concordia University
Montreal, Quebec, Canada

March 2015

© Ali Gholizadeh Touchaei, 2015

CONCORDIA UNIVERSITY
SCHOOL OF GRADUATE STUDIES

By: Ali Gholizadeh Touchaei

Entitled: Characterizing the Effect of Increasing Albedo on Urban Meteorology and Air Quality in Cold Climates, a Case Study for Montreal

and submitted in partial fulfillment of the requirements for the degree of

DOCTOR OF PHILOSOPHY (Building Engineering)

complies with the regulations of the University and meets the accepted standards with respect to originality and quality.

Signed by the final examining committee:

Dr. M. Z. Kabir	Chair
Dr. D. Sailor	External Examiner
Dr. D. H. Matthews	External to Program
Dr. F. Haghigat	Examiner
Dr. L. Wang	Examiner
Dr. H. Akbari	Thesis Supervisor

Approved by

Dr. F. Haghigat	Graduate Program Director
Dr. A. Asif	Dean of Faculty

March 30, 2015

Abstract

Characterizing the Effect of Increasing Albedo on Urban Meteorology and Air Quality in Cold Climates, a case study for Montreal

Ali Gholizadeh Touchaei, Ph.D.

Concordia University, 2015

The higher temperature of urban areas compared to their surrounding rural areas is called urban heat island (UHI). UHI during summer may harm inhabitants and aggravate cooling energy demand. Increasing urban albedo is proposed to counter the undesirable impacts of UHI. To analyze the effect of albedo enhancement on urban climate, land-atmosphere interactions and various physical processes in the atmosphere and on the land should be modeled. Weather Research and Forecasting (WRF) model, urban canopy model (UCM), building energy model (BEM), and chemical transport model (CHEM) are coupled, to accurately investigate the effect of an increase in the urban albedo. To select appropriate models sensitivity of near surface air temperature and near surface wind velocity to the choice of parameterization is evaluated. Montreal and Toronto, as the two most populated Canadian cities, are selected for evaluation of UCMs and an increase in the urban albedo.

Seasonal performance of the increase in albedo of roofs, walls, and road by 0.45, 0.4, and 0.25, respectively, results in an average decrease of 0.25 °C during summer and a negligible effect during winter (<0.1 °C). The daily building energy savings of HVAC systems in summertime is about 18 Wh/100m², while, the winter heating penalty is about 2 Wh/100m². Considering the effect of aerosols and other pollutants, in summertime, the simulated maximum air temperature decreased by about 1 °C, near surface 8-hour average ozone concentration decreased by 0.1 ppbv, and 24-hour average PM_{2.5} concentration decreased by 2 µg/m³. Simulations show that increasing the urban albedo results in a reduction in summertime air temperature, leading to a lower cooling energy use and an improved outdoor air quality.

Preface

The results of this thesis are presented in conferences, published in a journal, submitted to a journal, and under preparation for submission to different journals, as listed.

Published journal papers:

Ali G. Touchaei, and Hashem Akbari, "The climate effects of increasing the albedo of roofs in a cold region", *Advances in Building Energy Research*, Vol. 7 (2), pp. 186-191, 2013.

Ali G. Touchaei, and Yupeng Wang. "Urban Morphology of Montreal (Canada) for Characterizing Urban Heat Island", *Sustainable Cities and Society*, 2015.

Conference presentations:

Ali G. Touchaei, and Hashem Akbari, "The climate effects of increasing the albedo of roofs in a cold region", 34th AIVC conference, Athens, Greece, 25-26 September 2013.

Ali G. Touchaei, and Hashem Akbari, "The Seasonal Effect of Increasing Urban Albedo in Cold Climates", International Conference on Countermeasures to Urban Heat Islands 13-15 October 2014, Venice, Italy.

Journal papers under review:

Ali G. Touchaei, Hashem Akbari, and Dev Millstein, "Characterization of Urban Heat Island and the Effect of Increasing Roof Albedo in Two Canadian Cities Using Urban Canopy Models in WRF", submitted to a journal.

Ali G. Touchaei, and Hashem Akbari, "Sensitivity Analysis of Physical Parameterizations in WRF over Montreal (Canada)", in preparation for submission to a journal.

Ali G. Touchaei, and Hashem Akbari, "The Seasonal Effect of Increasing Urban Albedo in Cold Climates", submitted to a journal.

Ali G. Touchaei, Hashem Akbari, and Mirata Hosseini, "Energy Saving Potentials of Commercial Buildings by Urban Heat Island Reduction Strategies in Montreal (Canada)", in preparation for submission to a journal.

Ali G. Touchaei, Hashem Akbari, Chris Tessum, and Julian Marshall, "Effect of Increasing the Urban Albedo on Urban Meteorology and Air Quality of Montreal (Canada)", in preparation for submission to a journal.

Contribution of other authors:

Dr. Dev Millstein at LBNL directed me in using the WRF model and guided me on analyzing outputs. Dr. Yupeng Wang (Concordia University) provided some of data (calculated sky view factor) presented in Chapter Six. Mr. Mirata Hosseini shared the building energy model (DOE2) input files that he used for his thesis at Concordia University with me for comparisons in Chapter Eight. Dr. Chris Tessum, and Dr. Julian Marshall trained me on preprocessing anthropogenic emission data for WRF-CHEM at University of Minnesota.

Acknowledgment

I would like to express my deepest appreciation to my mentor and supervisor Professor Hashem Akbari who has taught me how to think about sophisticated issues. I learnt how to perform an applied research, to train engineers through teaching courses, to lead a research group, and to communicate in the scientific environment. Influence of Professor Akbari on my scholarly life is undoubtable and my gratitude and respect for him extends beyond words.

I am grateful of the supervisory committee, Professor David Sailor (Portland State University, Mechanical and Materials Engineering), Professor Fariborz Haghighat (Concordia University, BCEE), Dr. Damon Mathews (Concordia University, Geography), and Dr. Leon Wang (Concordia University, BCEE), for their advices to keep me on the right track. I thank Professor Haghighat in particular for his inspiring suggestion through my studies. I am sincerely thankful of Dr. Matthews for building the foundation of my research through the Environmental Modeling course.

Funding for this research was provided by the Natural Science and Engineering Research Council of Canada to Professor Akbari under the discovery program. CalculQuebec and ComputeCanada provided the computational facilities for this research. I would like to thank Mr. Daniel Stubb for his help and guidance for parallel computing of software .

Getting Ph.D. was the biggest challenge of my life and I could not imagine accomplishing the work without the support of my family and friends. Special thanks to my lovely mother, my wonderful wife, and magnificent brother.

And now,

“It is better to leave all the science

It is better to hang my heart to tress of my love

Before the faith takes my blood

It is better to pour the blood of grapes into the bowl”

Kayyam Neishaboori

Ali Gholizadeh Touchaei

March 2015

To Shabnam and Reza

Table of Contents

List of Figures	xiii
List of Tables	xviii
List of Symbols	xxi
Chapter One: Introduction to urban climate	1
1.1. Background	1
1.2. Urban fabric	2
1.3. UHI in cold climates	2
1.4. Energy consumption	3
1.5. Air pollution.....	3
1.6. Health impact.....	3
1.7. Mitigation.....	4
1.8. Research objectives.....	4
1.9. Thesis structure	5
Chapter Two: Literature review	7
2.1. Atmospheric response to global and regional increase of the urban albedo.....	9
2.2. The role of urban canopy models in urban climate simulations	12
2.3. The role of building energy models in energy consumption estimation.....	15
2.4. Quantification of effects of increasing albedo on urban climate and air quality	17
2.4.1. The role of urban morphology and building characteristics	22
2.5. Summary of the literature review	23
2.6. Concluding remarks	24
Chapter Three: Methodology	26
3.1. Simulation tool.....	26
3.1.1. Parameterizations	28
3.1.1.1. Microphysics.....	28
3.1.1.2. Cumulus.....	29
3.1.1.3. Planetary boundary layer (PBL)	29
3.1.1.4. Radiation	29
3.1.1.5. Land-Surface.....	30

3.2. Urban Canopy Models	30
3.2.1. Slab Model	30
3.2.2. Single layer UCM	31
3.2.3. Multi-layer UCM	31
3.2.3.1. Building Energy Model.....	31
3.3. Simulations and analysis of outputs.....	32
3.3.1. Selection of the urban canopy model.....	33
3.3.2. Sensitivity experiment on physical parameterizations.....	33
3.3.3. Modifications to UCM,.....	33
3.3.4. Seasonal assessment of albedo enhancement	34
3.3.5. Detailed building energy evaluation	34
3.3.6. Air quality modeling.....	34
Chapter Four: The choice of urban canopy model for climate modeling	35
4.1. Methodology of selecting an UCM and characterizing climatic effect of an increase in roof albedo	35
4.1.1. Simulation.....	35
4.1.2. Input data	37
4.1.3. Evaluation method	38
4.2. Results of simulations for Montreal and Toronto.....	39
4.2.1. Air temperature	39
4.2.2. Wind velocity.....	43
4.2.3. Temporal UHI.....	44
4.2.4. Spatial UHI	45
4.2.5. Effect of increasing the roof albedo.....	47
4.2.6. Spatial distribution of temperature difference from the albedo increase.....	49
4.2.7. Clear day of Toronto.....	51
4.3. Discussion.....	53
4.3.1. Characterization of UHI.....	53
4.3.2. Effect of increasing the roof albedo.....	55
4.3.3. Limitations	56
4.3.3.1. Microphysics and PBL parameterizations	56

4.3.3.2. Urban morphology and building characteristics	56
4.3.3.3. Selecting the weather stations	57
4.4. Conclusion on the choice of UCM and the effect of an increase in roof albedo	58
Chapter Five: Sensitivity Analysis of Physical Parameterizations in WRF	60
5.1. Methodology of sensitivity analysis of model ensembles within WRF	61
5.2. Results and discussions on air temperature, wind speed, relative humidity, and precipitation in Montreal	63
5.2.1. Air temperature	63
5.2.2. Wind speed.....	66
5.2.3. Relative humidity.....	69
5.2.4. Precipitation	72
5.3. Conclusion on the appropriate model ensemble	75
Chapter Six: Characterization of Urban Morphology of Montreal.....	77
6.1. Methodology of simulations	77
6.1.1. Selected parameterizations.....	80
6.2. Urban characteristics.....	80
6.2.1. Urban morphology	81
6.2.2. Efficiency/performance of energy systems in buildings.....	84
6.3. Urban heat island and urban cool island in summer	85
6.4. Methods of calculating sky view factor for a canopy	88
6.5. UHI simulation with modified data	90
6.6. Conclusion	92
Chapter Seven: Effect of Increasing Albedo on Urban Climate and Energy Consumption of Buildings in Montreal.....	93
7.1. Methodology of evaluating seasonal performance of an increase in urban albedo ...	93
7.1.1. Monthly Typical Meteorological Days	93
7.1.2. Episodes and domains of simulations	95
7.1.3. Urban parameters	96
7.1.4. Scenarios	96
7.1.5. Analysis.....	96
7.2. Simulation results.....	97

7.2.1. Urban heat island mitigation	98
7.2.2. Energy consumption of buildings	103
7.3. Discussion on the predicted air temperature and energy consumption of HVAC systems	104
7.3.1. Air temperature	105
7.3.2. Energy consumption of buildings	106
7.3.3. Limitations	107
7.4. Conclusion of the seasonal evaluation of an increase in the urban albedo	110
Chapter Eight: Energy Saving Potentials of Commercial Buildings by Urban Heat Island Reduction Strategies in Montreal	111
8.1. Methodology of the detailed energy calculation in buildings	111
8.1.1. Simulation tool and its structure	111
8.1.2. Roof modeling in DOE-2	112
8.1.3. Description of the buildings	112
8.1.3.1. Small office	113
8.1.3.2. Medium office	113
8.1.3.3. Large office	114
8.1.3.4. Retail store	114
8.1.4. Snow properties	116
8.1.5. Weather file for DOE-2	117
8.1.6. Scenarios	119
8.2. Simulations results and discussions	120
8.2.1. Small Office	120
8.2.2. Medium Office	121
8.2.3. Large Office	123
8.2.4. Retail store	124
8.3. Conclusion on the energy consumption of commercial buildings	125
Chapter Nine: Effect of Increasing the Urban Albedo on Air Quality of Montreal	126
9.1. Methodology of meteorological and air quality modeling	126
9.1.1. Simulation domain and the summer episode	126

9.1.2. Meteorological setup.....	127
9.1.3. Chemistry setup	127
9.1.4. Input data	130
9.1.4.1. Meteorological input.....	130
9.1.4.2. Anthropogenic emissions.....	131
9.1.4.3. Biogenic emissions	135
9.1.4.4. Other data.....	135
9.2. Results of the simulations with WRF-CHEM, and discussions	136
9.2.1. Air temperature	136
9.2.2. Skin temperature	138
9.2.3. Shortwave radiation	140
9.2.4. Sensible heat flux	140
9.2.5. PBL height	141
9.2.6. Mixing ratio	142
9.2.7. Moisture flux.....	142
9.2.8. Wind speed.....	143
9.2.9. Ozone concentration	143
9.2.10. PM 2.5 concentration	146
9.2.11. Energy consumption	149
9.3. Conclusion on the characterization of the effect of an increase in the urban albedo on the air quality of Montreal.....	150
Chapter Ten: Summary and Conclusion.....	151
10.1. Summary	152
10.2. Conclusion	154
10.2.1. Urban climate modeling.....	154
10.2.2. The albedo enhancement strategy	155
10.3. Contributions.....	155
10.4. Future works	156
10.5. Policy recommendations.....	157
References.....	158
Appendix A: Description of WRF solver and physical models	180

Appendix B: Can urban ozone generation be modeled correctly based on major gaseous atmospheric reactions?	199
--	------------

List of Figures

Figure 1-1. Typical variation of air temperature along a city and occurrence of the UHI	2
Figure 2-1. Diurnal average extraterrestrial global horizontal solar irradiance in four cities	9
Figure 3-1. Flowchart of WRF modeling system for urban climate simulation	28
Figure 4-1. Simulation domain of (a) the Greater Montreal and (b) the Greater Toronto.....	36
Figure 4-2. Land Use Land Cover (LULC) of (a) the Greater Montreal and (b) the Greater Toronto extracted from USGS dataset.....	38
Figure 4-3. Location of weather stations in (a) Greater Montreal and (b) Greater Toronto.....	40
Figure 4-4. Hourly observed and simulated 2-m air temperature (°C) [left] and the difference between modeled and observed temperatures [right] in the urban areas of Montreal [top] and Toronto [bottom] in 12-July-2005 observed data and results of simulations using the three UCMs.....	42
Figure 4-5. Temporal variation of 2-m air temperature (°C) difference between urban area and rural area of Greater Montreal [left] and Greater Toronto [right] in 12-July-2005 using three UCMs..	45
Figure 4-6. 24- hour (a), daytime (b), and nighttime (c) averaged 2-m air temperature (°C) of Greater Montreal and Toronto in 12-July-2005 [CTRL case] using Multi-Layer UCM.....	46
Figure 4-7. 24-hour (a), daytime (b), and nighttime (c) averaged skin temperature (°C) of Greater Montreal and Toronto in 12-July-2005 [CTRL case] using Multi-Layer UCM.....	47
Figure 4-8. Hourly variation of (a) 2-m air temperature difference and (b) skin temperature difference between CTRL case and ALBEDO case in Montreal using different UCMs	48
Figure 4-9. Hourly variation of (a) 2-m air temperature difference and (b) skin temperature difference between CTRL and ALBEDO in Toronto using different UCMs	49

Figure 4-10. Mean daily 2-m air temperature (°C) and mean skin temperature (°C) difference between CTRL and ALBEDO of Greater Montreal on 12-July-2005.....	50
Figure 4-11. Mean daily 2-m air temperature (°C) and mean skin temperature (°C) difference between CTRL and ALBEDO of Greater Toronto on 12-July-2005. (a) Multi-layer UCM, (b) Single-layer UCM, and (c) slab model.....	51
Figure 4-12. Hourly variation of (a) 2-m air temperature difference and (b) skin temperature difference between urban area and rural area on 15-July-2005 in Toronto using different UCMs.	52
Figure 4-13. Hourly variation of (a) 2-m air temperature difference and (b) skin temperature difference between CTRL and ALBEDO on 15-July-2005 in Toronto using different UCMs.....	52
Figure 4-14. 2-m air temperature and skin temperature difference (°C) between (a) Multi-layer UCM and Single-layer UCM, and (b) Multi-layer UCM and slab model of Greater Montreal in 12-July-2005.....	53
Figure 4-15. 2-m air temperature difference (°C) between (a) Multi-layer UCM and Single-layer UCM, and (b) Multi-layer UCM and slab model of Greater Toronto in 12-July-2005	54
Figure 4-16. 24-hour averaged heat flux difference (W/m ²) between (a) ML-UCM and slab model (ML-slab), and (b) ML-UCM and SL-UCM (ML-SL) of Greater Montreal in 12-July-2005	54
Figure 6-1. Map of Montreal and selected neighborhoods (www.maps.google.com).....	82
Figure 6-2. Number of buildings sorted by the height on the left axis and the probability distribution of building heights on the right axis	83
Figure 6-3. 2-m air temperature (°C) in different hours of July 14th, 2005	87
Figure 6-4. Schematic of the arrays of buildings considered as the urban morphology, (a) 2D model randomly distributed height of building rows, (b) 2D model with constant height of buildings, (c) 3D model, and (d) 2D model with randomly distributed height of buildings.....	88
Figure 6-5. 2-m temperature observed at McTavish weather station and reproduced by considering different cases.....	91

Figure 6-6. Urban heat island intensity from observed data (the difference between air temperature measured at urban area [McTavish], and rural area [Mirabel Airport]) and simulated cases	91
Figure 7-1. Three domains of simulations (Domain 1: grid size of 10×10 km, Domain 2: grid size of 3.3×3.3 km, and Domain 3: grid size of 0.6×0.6 km).....	95
Figure 7-2. The 2-m air temperature difference (°C) in ALBEDO and CTRL on MTMD of all months of a year at 9 a.m.	100
Figure 7-3. The 2-m air temperature difference (°C) in ALBEDO and CTRL on MTMD of all months of a year at 3 p.m.	101
Figure 7-4. The 2-m air temperature difference (°C) in ALBEDO and CTRL on MTMD of all months of a year at 9 p.m.	102
Figure 7-5. The daily-total energy consumption difference (W/m ² -h) in ALBEDO and CTRL on MTMD of summer months of 2005.....	103
Figure 7-6. Difference of the daily averaged 2-m air temperature (°C) in ALBEDO and CTRL cases on 21st day of all months of a year.....	108
Figure 7-7. Difference of the daily average energy consumption of buildings for air conditioning (W/m ²) in ALBEDO and CTRL cases on 21st day of all months of a year.....	109
Figure 8-1. Snow depth and characterization of snow type in Montreal, 2005.	117
Figure 9-1. Schematic of the size distribution of aerosols considered the MADE/SORGAM.....	129
Figure 9-2. NO _x emission (mole/km ² /hr) in different hours of a weekday in Domain 3 (the dashed line is the urban border and dark blue color represents rivers) ...	133
Figure 9-3. PM _{2.5} emission (mole/km ² /hr) in different hours of a weekday in Domain 3 (the dashed line is the urban border and dark blue color represents rivers) ...	134
Figure 9-4. Temporal variation of the spatially averaged PM _{2.5} and NO _x emission in the urban area.....	134
Figure 9-5. SO ₂ emission (mole/km ² /hr) in different hours of a weekday in Domain 3 (the dashed line is the urban border and dark blue color represents rivers) ...	135
Figure 9-6. Average isoprene emission (mole/km ² /hr) in Domain 3 for biogenic calculations in MEGAN.....	136

Figure 9-7. 2-m air temperature of urban and rural areas in the three-day heatwave period and the difference between CTRL and ALBEDO.....	137
Figure 9-8. 2-m air temperature difference (°C) between CTRL and ALBEDO on July 11 th , 2005	138
Figure 9-9. 2-m air temperature difference (°C) between CTRL and ALBEDO on July 12 th , 2005	139
Figure 9-10. Surface temperature of urban and rural areas in the three-day heatwave period and the difference between CTRL and ALBEDO.....	139
Figure 9-11. Shortwave radiation on the ground in urban and rural areas in the three-day heatwave period and the difference between CTRL and ALBEDO	140
Figure 9-12. Sensible heat flux of urban and rural areas in the three-day heatwave period and the difference between CTRL and ALBEDO.....	141
Figure 9-13. PBL height above urban and rural areas in the three-day heatwave period and the difference between CTRL and ALBEDO.....	141
Figure 9-14. 2-m mixing ratio of urban and rural areas in the three-day heatwave period and the difference between CTRL and ALBEDO.....	142
Figure 9-15. Moisture flux of urban and rural areas in the three-day heatwave period and the difference between CTRL and ALBEDO.....	143
Figure 9-16. 10-m wind speed (advection) in urban and rural areas in the three-day heatwave period and the difference between CTRL and ALBEDO.....	143
Figure 9-17. Ozone concentration at the first vertical level (~5m from the ground) in urban and rural areas in the three-day heatwave period and the difference between CTRL and ALBEDO.....	144
Figure 9-18. Ozone concentration difference (ppbv) between CTRL and ALBEDO on July 11 th , 2005.....	145
Figure 9-19. Ozone concentration difference (ppbv) between CTRL and ALBEDO on July 12 th , 2005.....	146
Figure 9-20. PM2.5 concentration at the first vertical level (~5m from the ground) in urban and rural areas in the three-day heatwave period and the difference between CTRL and ALB	147
Figure 9-21. PM2.5 concentration difference ($\mu\text{g}/\text{m}^3$) between CTRL and ALBEDO on July 11 th , 2005.....	148

Figure 9-22. PM2.5 concentration difference ($\mu\text{g}/\text{m}^3$) between CTRL and ALBEDO on July 12 th , 2005	149
Figure 9-23. Energy consumption of HVAC systems of buildings in the three-day heatwave period and the difference between CTRL and ALBEDO (DIFF). .	150
Figure A-1. Information transfer flowchart of WRF model	182
Figure B-1. Schematic of stock and flows for a pollutant in STELLA software.....	205
Figure B-2. Anthropogenic emissions of NO ₂ , NO and CO ($\frac{\text{molecule}}{\text{cm}^3}$) as a function of time (hour)	206
Figure B-3. a)Wind velocity (m/s), b)Temperature (K), c)Zenith angle (degree), and d)Relative humidity (%) of Los Angeles in specified period of time (National Solar Radiation Data Base, 2011).....	207
Figure B-4. Time series CO, NO ₂ and NO concentration ($\frac{\text{molecule}}{\text{cm}^3}$) variation	208
Figure B-5. Cyclic changes of photochemical reaction rates.....	208
Figure B-6. Time series Ozone ($\frac{\text{molecule}}{\text{cm}^3}$) and Temperature (K) variation.....	209
Figure B-7. Sensitivity of ozone to the temperature ($T = 0.9T_0$, $T = T_0$ and $T = 1.1T_0$)	210

List of Tables

Table 2-1. Qualitative comparison of concentration of gaseous pollutants in different seasons	18
Table 4-1. Correlation (R^2) of 2-m air temperature, MBE, MAE, and RMSE of observed and modeled 2-m air temperature in Montreal	41
Table 4-2. Correlation (R^2) of 2-m air temperature, MBE, MAE, and RMSE of observed and modeled 2-m air temperature in Toronto.....	41
Table 4-3. MBE, MAE, and RMSE of observed and modeled 10-m wind speed in Montreal.....	43
Table 4-4. MBE, MAE, and RMSE of observed and modeled 10-m wind speed in Toronto.....	44
Table 4-5. 24-hour averaged, daytime averaged, and night-time averaged 2-m air temperature and skin temperature calculated for Montreal and Toronto by coupling ML-UCM, SL-UCM, and slab model to the mesoscale model	49
Table 5-1. Simulation set-ups with different options on parameterizations of microphysics, cumulus, PBL, and radiation	62
Table 5-2. MBE in predicted temperature ($^{\circ}\text{C}$) with different WRF settings	64
Table 5-3. MAE in predicted temperature ($^{\circ}\text{C}$) with different WRF settings.....	65
Table 5-4. RMSE in predicted temperature ($^{\circ}\text{C}$) with different WRF settings.....	66
Table 5-5. MBE in predicted wind speed (m/s) with different WRF settings	67
Table 5-6. MAE in predicted wind speed (m/s) with different WRF settings	68
Table 5-7. RMSE in predicted wind speed (m/s) with different WRF settings	69
Table 5-8. MBE in predicted relative humidity (%) at 2-m height with different WRF settings	70
Table 5-9. MAE in predicted relative humidity (%) at 2-m height with different WRF settings	71
Table 5-10. RMSE in predicted relative humidity (%) at 2-m height with different WRF settings.....	72
Table 5-11. MBE in predicted precipitation (mm) with different WRF settings.....	73
Table 5-12. MAE in predicted precipitation (mm) with different WRF settings.....	74

Table 5-13. RMSE in predicted precipitation (mm) with different WRF settings.....	75
Table 6-1. The characteristics of selected urban areas and the regions in Montreal	83
Table 6-2. Energy use for space cooling and heating in Quebec by equipment type and their stock efficiency in 2005.....	85
Table 6-3. View factors of the selected cities and region in Montreal using different urban morphology.....	90
Table 7-1. Daily-spatially-averaged 2-m air temperature (°C), energy consumption for air conditioning (Wh/m ²), sensible heat flux from the ground (W/m ²), downward shortwave radiation on the ground (W/m ²), and PBL height (m) in CTRL and (CTRL –ALBEDO) for Montreal (Canada) on the MTMD of each month in 2005.....	98
Table 7-2. 24-hour, diurnal, nocturnal, and peak UHI intensity and the performance of albedo enhancement to mitigate the UHI in the MTMD of each months.....	99
Table 7-3. Annual, winter, and summer energy consumption and expenditure of buildings in CTRL, energy savings/penalty and money savings/penalty in ALBEDO.	104
Table 7-4. Average, maximum, and minimum of the difference of daily averaged 2-m air temperature (°C), Energy consumption for air conditioning (W/m ²), Sensible heat flux from the ground (W/m ²), Downward shortwave radiation on the ground (W/m ²), Cloud fraction (%), and PBL height (m) in ALBEDO case and CTRL case for Montreal (Canada) on 21st of each month in 2005.	105
Table 8-1. General characteristics of prototype buildings and HVAC systems.....	115
Table 8-2. Specific characteristics for office building and retail building prototypes.....	116
Table 8-3. Summary of the weather statistics in CTRL.....	118
Table 8-4. Summary of the weather statistics in ALB	119
Table 8-5. Summary of the energy consumption and energy expenditure of a small office with different HVAC systems and building characteristics using dark roof, white roof with weather data in CTRL, and white roof with weather data in ALBEDO in Montreal, 2005.....	121
Table 8-6. Summary of the energy consumption and energy expenditure of a medium office with different HVAC systems and building characteristics using dark	

roof, white roof with weather data in CTRL, and white roof with weather data in ALBEDO in Montreal, 2005.....	122
Table 8-7. Summary of the energy consumption and energy expenditure of a large office with different HVAC systems and building characteristics using dark roof, white roof with weather data in CTRL, and white roof with weather data in ALBEDO in Montreal, 2005.....	123
Table 8-8. Summary of the energy consumption and energy expenditure of a retail store with different HVAC systems and building characteristics using dark roof, white roof with weather data in CTRL, and white roof with weather data in ALBEDO in Montreal, 2005.....	124
Table A-1. Physical models interaction with the ARW solver, i indicates the input to the model and o represents the output of the model	193
Table B-1. rate of photolysis reaction of 15 degrees zenith angle and zenith sun at 0.5 km altitude	201

List of Symbols

English Symbols

A	Area
C_g	Convection heat transfer coefficient from the ground to the canopy
C_w	Convection heat transfer coefficient from walls to the canopy
c_p	Specific heat capacity
d	Displacement height
E	Latent heat
e	Energy
E_C	Energy consumption of HVAC systems
E_g	Total radiation on the ground
E_w	Total radiation on the wall
e'	Fluctuation of energy
F_a^H	Horizontal forcing of the prognostic variables
F_a^V	Vertical forcing of the prognostic variables
f_{urb}	Urban fraction
$F_{g \rightarrow w}$	View factor of wall to ground
$F_{w \rightarrow g}$	View factor of ground to wall
$F_{w \rightarrow w}$	View factor of wall to wall
g	Gravity
GFX	Ground heat flux
H	Sensible heat
h	Convection heat transfer coefficient
\tilde{h}	Height of the wall
H_a	Sensible heat from the canopy
H_g	Sensible heat from the ground
H_w	Sensible heat from the wall
h_m	Mean height of buildings
HFX	Sensible heat flux

k	Von Karman constant
k_{cond}	Conductivity
K_h	Heat exchange coefficient
K_m	Momentum exchange coefficient
L	Monin-Obukhov length scale
l	Length scale
l_v	Specific latent heat of evaporation
LH	Latent heat flux
p	Pressure
P_{occup}	Peak number of occupants
Q_c	Heat emission from buildings to the canopy
q_{equip}	Sensible heat gain from equipment
q_m	Mixing ratio of water
q_{occup}	Heat generated by occupants
Rad	Net radiation on the surface
R_{air}	Gas constant of the air
R_g	Reflectance of the ground
R_{lw}	Longwave radiation
R_{sw}	Shortwave radiation
R_w	Reflectance of the wall
S_{q_m}	Source and sink of water
S_θ	Source and sink of energy
S_{χ_m}	Source and sink of pollutants
T	Temperature
U	Advection
u	A component horizontal velocity
U_a	Synoptic wind speed
U_r	Wind speed at roof level
U_s	Wind speed in the canopy
u_*	Friction velocity

u'	Fluctuation of a component horizontal velocity
V	Wind velocity
v	A component horizontal velocity
V_{ach}	Air change volume
v'	Fluctuation of a component horizontal velocity
V^A	The volume of the air in the grid
V^R	The volume of the room
w'	Fluctuation of vertical velocity
z_0	Momentum roughness length
z_{0T}	Thermal roughness length
w	Vertical velocity
w_{road}	Width of street

Greek Symbols

α	Thermal diffusivity
β	Characteristic vertical mixing length
δ	Width of the wall
ε	Molecular dissipation
ϵ	emissivity
θ	Potential temperature
τ	Shear stress
λ	Thermal efficiency of the heat exchanger
λ_f	Frontal area density
λ_p	Plan area density
μ	Viscosity
ϑ	Specific viscosity
ρ	Density
σ	Stefan-Boltzman constant
ϕ_p	Ratio of hourly occupants
χ_m	Concentration of pollutants

Ψ_h	Stability correction functions for heat
Ψ_m	Stability correction functions for momentum
Ω_j	Angular velocity of the earth

Abbreviations

BEM	Building Energy Model
CFD	computational fluid dynamics
COP	Coefficient of performance
EER	Energy Efficiency Ratio
HDD	heating degree days
HVAC	Heating, Ventilating, and Air Conditioning
IAIV	Increase Albedo Increase Vegetation
LSM	Land-Surface Model
LULC	Land Use Land Cover
MADE	Modal Aerosol Dynamics Model for Europe
MAE	Mean Absolute Error
MBE	Mean Bias Error
ML-UCM	Multi-Layer Urban Canopy Model
MTMD	Monthly Typical Meteorological Day
NDVI	Normalized Difference Vegetation Index
NVI	Normal Vegetation Index
NWP	Numerical Weather Prediction
PBL	Planetary Boundary Layer
RADM2	Regional Acid Deposition Model version 2
RMSE	Root Mean Square Error
SEER	Seasonal Energy Efficiency Ratio
SL-UCM	Single Layer Urban Canopy Model
SORGAM	Secondary Organic Aerosol Model
SVF	Sky View Factor
TKE	Turbulent Kinetic Energy
TMY	Typical Meteorological Year

UCM	Urban Canopy Model
UHI	Urban Heat Island
VOC	Volatile Organic Compound
WRF	Weather Research and Forecasting

Dimensionless Numbers

C_h or St	Stanton number
C_l	Dalton number
Nu	Nusselt number
Pr	Prandtl number
Re	Reynolds number
Ri	Richardson number

Chapter One: Introduction to urban climate

This dissertation contributes to the understanding of climatology, air quality, and the energy use of buildings in urban areas in cold climates. Climate simulation is a computationally expensive approach in the comprehensive assessment of human-related issues in urban areas. These simulations deal with complex interactions between the meteorological parameters (e.g., temperature, wind, moisture, etc.), urban morphology, heat emission from buildings to canopy, and aerosols in the atmosphere. Results would be used by decision-makers to make policies to improve lives of urban dwellers. The fine-resolution meteorological simulation is an appreciated technique to acquire detailed information on the scale of the neighborhood for further analysis. In particular, the focus of this work is to investigate the effect of increasing the albedo of urban surfaces on air temperature, air quality and energy consumption of buildings.

This chapter provides the background of the urban climatology and the effect of urban structure (e.g., buildings) on air temperature and wind field. Additionally, the potential impacts of changing surface characteristics on energy consumption of buildings and pollution generation are introduced.

1.1. Background

Earlier observations of air pollution episodes in England drew the attention of scientists to urban climatology, and the difference between urban and non-urban climates. Howard (1833) and Unwin (1980) compared the measured temperature of urban areas and their surroundings and they observed a distinct elevation of air temperature in metropolitan areas. Scientists concluded that areas with higher human population (i.e., urban areas) are usually warmer than their surroundings; this phenomenon is called urban heat island (UHI). UHI has a considerable nocturnal effect and the temperature difference can be as high as 12 °C (Oke, 1987; Roth et al., 1989). Figure 1-1 illustrates the typical spatial distribution of air temperature around a city.

UHI causes more energy consumption for cooling (Akbari and Konopacki, 2005), and more air pollution generation (Akbari et al., 2001). Impacts of UHI on human life include an increase in mortality (Kosatsky et al., 2005) and a change on the urban ecosystem (Kayleigh et al., 2013).

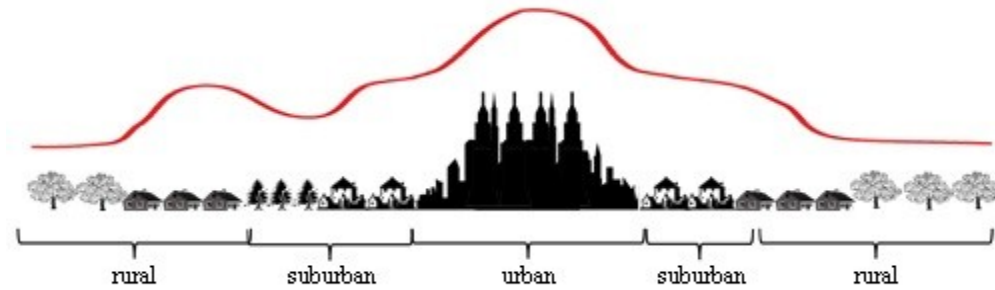


Figure 1-1. Typical variation of air temperature along a city and occurrence of the UHI

1.2. Urban fabric

The urban fabric comprises buildings, roadways, sidewalks, parking lots, vegetation, and bare soils in urban areas. However, by definition, the ideal urban area is structured by canopies with four components; roofs, walls, pavements, and natural surfaces. UHI is a result of heat release from the urban canopy. Roofs and pavements cover about 60% of an urban area and absorb more than 80% of incoming solar energy. Furthermore, changing land surface properties from permeable and moist (e.g., soil and vegetated lands) to dry and impermeable (e.g., roads, buildings) reduces evaporation and latent heat flux (Wong, 2008). Human activities in urban areas, such as air conditioning, transportation and manufacturing, also increase the heat emission rate.

1.3. UHI in cold climates

UHI in tropical and moderate climates counts as common knowledge; however, UHI is a serious issue in many urban areas located in cold climates. The number of heating degree days (HDD) in low-temperature regions located in high latitudes (less sun energy) or high altitude (low pressure), is high. ASHRAE defines regions with $7200 < \text{HDD} < 9000$ as cold (zone 6) and $9000 < \text{HDD} < 12600$ as very cold (zone 7) climates (ASHRAE, 2007a). Based on this criterion, many cities in Canada, the US, Russia, and Europe are considered as cold climate regions.

One of the characteristics of the weather in Canada is the counter-clockwise rotation of the wind (i.e., anticyclone) (Korolevych and Richardson, 2012). An anticyclone causes high pressure and a stable climate condition that increases the urban temperature and UHI intensity (Unwin, 1980;

Beranova and Huth, 2005; Morris and Simmonds, 2000; Szegedi and Kircsi, 2003). Mostly, UHI is significant during the stable synoptic weather condition (Arnfield, 2003).

1.4. Energy consumption

A well-documented effect of UHI is a decrease in summer thermal comfort. For air conditioned buildings, UHI causes an increase in cooling energy demand. In summer, urban areas absorb more solar energy that increases the surface temperature compared to their surroundings. Hence, the cooling energy demand increases. This process has a small effect on the temperature in winter because: (1) the urban surfaces are covered with snow for a long period of time, (2) the zenith angle that reduces solar energy on the ground is large, and (3) the sky is mostly cloudy. UHI increases both mean cooling load and peak cooling load of buildings, in summer.

1.5. Air pollution

Different emission sources contribute to the air pollution in urban areas. Among them, industries and vehicles are the most important sources of pollution. Moreover, buildings and other anthropogenic activities release heat and moisture that can increase the rate of reaction of pollutants. An increase in energy consumption may lead to more pollution generation as well (Rosenfeld et al., 1998). Furthermore, higher ozone generation, as a secondary product of the reaction of nitrogen oxides (NO_x) and volatile organic compounds (VOCs), is a consequence of temperature increase in urban areas.

1.6. Health impact

The UHI impacts urban inhabitants' health in two ways: (1) increasing the risk of premature deaths due to heatwaves, and (2) causing respiratory system diseases and cancer due to the air pollution. The number of deaths related to weather conditions has become greater than that from any other natural disasters. In Canada, also, the number of premature deaths is correlated to the heatwaves (Kosatsky et al., 2005). On the other hand, the cumulative number of Canadian deaths from the impact of air pollution (both short-term and long-term exposures) was estimated to be 21,000 people in 2008 (Geduld, 2008). This number is predicted to increase to 39,000 people in 2031, with Quebec and Ontario sharing the largest proportion. In another study, the annual rate

of excess deaths due to air pollution was estimated to be about 18% of the total number of deaths (Judek et al., 2004).

1.7. Mitigation

Due to growing concerns about UHI threats, scientists have proposed many techniques to mitigate UHI. Three main strategies to mitigate the UHI are: (1) implementing reflective surfaces, (2) vegetating urban surfaces, and (3) reducing anthropogenic heat emissions. The focus of my research is on studying the effect of cool surfaces on urban climate, energy consumption, and air quality.

1.8. Research objectives

Policy and decision makers need to have clear guidelines for urban development and urban planning in Canadian cities. They need to have a quantified effect of UHI mitigation strategies on urban climate, air quality, and energy consumption of buildings. The importance of characteristics of the urban fabric is woven into the purpose of this study. In this research, albedo, moisture content, and vegetation cover of urban areas are important in terms of energetics. Additionally, urban morphology is the essence of climate modeling using fine-resolution grid cells.

The effect of increasing urban albedo in moderate and tropical climates is studied by researchers around the globe. Here, the objective is to perform detailed simulations and analyze results of the effect of increasing the albedo of urban areas in cold regions, especially in Canadian cities. To accomplish this objective, four consecutive stages are defined.

1. Selecting the appropriate models for urban climate simulation

Mesoscale models are comprised of many parameterizations (cumulus, microphysics, planetary boundary layer, radiation, and land-surface) that have been used for predicting the weather condition. Urban areas are considered as a part of the land-surface parameterization to predict the heat and moisture fluxes from land to atmosphere. Urban canopy models (UCMs) are used to represent the urban areas for more accurate estimation of desired parameters. Building energy models (BEMs) can also be coupled to UCMs to calculate the heat emission from buildings into the canopy.

Measured meteorological parameters (e.g., temperature and wind speed) from weather stations around selected cities are compared to the simulated parameters. The time-efficient parameterizations with the least errors are selected for further modeling. The selected parameterizations are applicable for simulating an urban area in cold climates using a fine-resolution approach.

2. *Modifying current models*

The current UCMs and BEMs are simple and they do not consider many complexities of urban areas. Some aspects of those models are modified to improve them for urban climate simulations. In UCM, the effect of multi-reflection between urban surfaces is modified. In BEM, the coefficient of performance (COP) is modified.

3. *Selecting simulation episodes and collecting urban morphological data*

A methodology to select the weather data for episodic urban climate simulation is proposed using the typical meteorological year (TMY) approach (Hall et al., 1978). Analyzing the urban morphology is also a complicated procedure; hence, I propose a method to simplify the process without missing essential information.

4. *Evaluation of the effect of increasing the urban albedo*

The current weather condition for the selected cities is modeled with the platform provided in the earlier stages of the research and by adding the chemistry model (CHEM). Thereafter, the albedo of urban surfaces is increased under different scenarios. The effect of increasing the albedo on UHI, air quality, and energy consumption of buildings is investigated. The feasibility of applying this mitigation strategy for the case studies is discussed.

1.9. Thesis structure

In Chapter Two, the current state of knowledge is reviewed and the shortcomings are cataloged. A short description of the simulation tool and an introduction to the methodology of selecting the model ensemble, evaluating it, and performing simulations in this dissertation is presented in Chapter Three. In the next two chapters, the selection of appropriate parameterizations for mesoscale modeling and the choice of urban canopy models are discussed. Chapter Six is devoted to urban morphology and buildings' properties, in terms of their importance in predicting the urban heat island intensity. In Chapter Seven, the mesoscale-UCM-BEM ensemble

is used to investigate the seasonal effect of increasing the albedo of urban surfaces on the air temperature and building energy consumption of Montreal. Chapter Eight is dedicated to detailed analysis of the change in building energy consumption from the albedo enhancement by considering the dynamics of the HVAC systems. The air quality modeling of Montreal using the mesoscale-UCM-BEM-CHEM ensemble is discussed in Chapter Nine. The last chapter provides a summary, conclusion of this research, and possible future work.

Chapter Two: Literature Review

There is a distinct difference between strategies to fight climate change (global warming) and to fight heatwaves in urban areas. The contribution of the air temperature in urban areas on climate change is believed to be negligible (Parker, 2004; Peterson, 2003), whereas, the anthropogenic activities in urban areas are the main emitter of greenhouse gases (Kalnay and Cai, 2003). On the other hand, climate change has a significant effect on urban climate and extreme events (IPCC, 2014; Oyeyinka et al., 2011). Strategies to reduce the impact of climate change are mostly focused on reducing anthropogenic emissions. Instead, UHI mitigation strategies are applied to reduce the air temperature in urban areas, where more than 65% of the world's population is predicted to live in cities by 2050 (United Nations, 2014), and which are vulnerable to heatwaves (Patz et al., 2005; WHO, 2002). Mitigation strategies such as urban greenery and increasing the urban albedo are proposed to fight UHI. Increasing the urban albedo is an interesting UHI mitigation strategy for policymakers. Implementing reflective roofs and reflective pavement increases the albedo of the whole city and backscatters the incoming solar radiation into the sky. However, the magnitude of the effect of implementing the mitigation strategy depends on the specific factors associated with a selected city, such as synoptic weather condition, urban morphology, and topology.

To investigate the performance of albedo enhancement on urban climate, many complications and physical interactions in urban areas should be taken into account. Physical assumptions applied to urban climate simulation in mesoscale modeling (e.g., the building environment parameterization) are different from the physical assumptions on regional or global scales. For urban climate simulations more details of urban heterogeneity, such as the size of buildings and roads, should be considered. Mesoscale meteorological models provide the basis for solving conservation equations for the atmosphere above urban areas. The capability of nesting in the recent state-of-science mesoscale models enables researchers to efficiently model urban climate by accounting for the synoptic climate condition. For these models, land is considered as a bottom boundary condition where required parameters are determined by different parameterizations. Among different parameterizations, the urban canopy model (UCM) and building energy model (BEM) are essential for urban climate simulations. These models can

estimate the heat and momentum flux on the surface (using the land-surface model) which interacts with the above atmosphere, as well as the collateral effect of buildings and the canopy on surface fluxes.

There are some concerns about the benefits and penalties of reflective materials. A very first criticism is to address the penalty of using reflective materials in winter; in response, it has to be mentioned that (1) in winter the solar radiation striking the ground is much less than in summertime because of the greater zenith angle and thicker cloud cover in winter; (2) cooling energy is more costly than heating energy. A second caveat points to the risk of reflecting UV light which might harm human health; so far, almost all reflective materials absorb the UV light and they are only capable of reflecting the Visible and NIR part of the sunlight (Berdahl et al., 2008; Berdahl and Bretz, 1997; Synnefa et al., 2007; Prado and Ferreira, 2005; Levinson et al., 2005) which does no harm to human health. Finally, the main motive for increasing the urban albedo is to confront undesirable impacts of heatwaves in summer, which have become more frequent due to climate change.

The diurnal average of extraterrestrial global horizontal solar irradiance in four cities with different latitudes is shown in Figure 2-1. The average extraterrestrial global horizontal solar irradiance in summer in Montreal, with higher latitude (cold climate), is close to that of other cities. However, Montreal has substantially lower solar radiation (even without considering the effect of clouds), in winter. In principle, lower sunlight in winter decreases the penalty of using reflective surfaces.

Many articles and review papers have addressed different aspects of urban climate modeling and mitigation strategies (Santamouris, 2013; Gago et al., 2013; Rizwan et al., 2008; Ming et al., 2014). Mirzaei and Haghighat (2010) summarized approaches and limitations in studying the urban climate in different scales. Many of the limitations are overcome by recent advancements in single and multi-layer urban canopy models (SL-UCM and ML-UCM). The coupled modeling (UCM-mesoscale model) systems are also well developed by researchers. Arnfield (2003) provided a detailed review of three major effective mechanisms in urban climate (turbulence, energy exchange, and water balance). He explained the development of mesoscale models by revealing new experiments for heterogeneous surfaces. Recent models treat the momentum exchange and heat fluxes more accurately by considering well-estimated anthropogenic heat

emission and net radiation on the urban surface. In a report for DOE (Navigant Consulting, 2009), all research related to the Urban Heat Island (UHI), to that date, has been summarized.

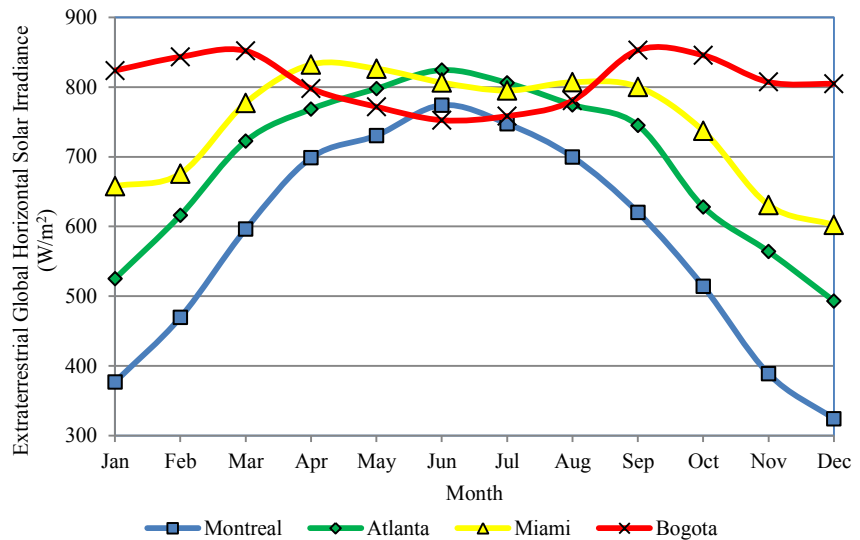


Figure 2-1. Diurnal average extraterrestrial global horizontal solar irradiance in four cities; Montreal (CA), Atlanta (US), Miami (US), Bogota (CO). [<http://www.nrel.gov/midc/solpos/solpos.html>]

I cataloged the literature into four categories:

- Atmospheric response to global and regional increase of the urban albedo
- The role of urban canopy models in urban climate simulations
- The role of building energy models in energy consumption estimation
- Quantification of effects of increasing albedo on urban climate and air quality

2.1. Atmospheric response to global and regional increase of the urban albedo

Increasing or decreasing surface albedo can affect regional and global climate. Akbari et al. (2009) determined the global cooling effect of increasing the albedo by considering a simple radiative forcing model. The global negative radiative forcing of 0.044 W/m^2 that offsets the emission of 44 Gt of CO_2 by a 0.1 increase in the urban albedo was estimated. In another study, effects of global increase of albedo on long-term temperature variation and its CO_2 offset were investigated (Akbari and Matthews, 2012; Akbari et al., 2012). The global temperature was decreased by about $2 \text{ }^\circ\text{C}$ and $1 \text{ }^\circ\text{C}$ by increasing the albedo of the land areas between $\pm 45^\circ$ and

$\pm 20^\circ$ latitude by 0.1, respectively. The intermediate complexity model (University of Victoria Earth System Climate Model) predicted 0.01 °C to 0.07 °C decrease in the global temperature from an increase only in the urban albedo.

In another study, Menon et al. (2010) found the global radiative forcing of the earth can be reduced by 0.5 W/m² and the global temperature can be decreased by about 0.008 °C in response to a 0.1 increase in urban albedo (a 0.003 increase in global surface albedo). Similarly, in the continental US the outgoing radiation was increased by 2.3 W/m² (the average summer increase was about 18.2 W/m²) and the temperature was decreased by 0.03 °C for the average surface albedo increase of 0.01. Results were calculated by the Catchment Land Surface Model (Koster et al., 2000) using incoming global shortwave radiation, downward longwave radiation, 2-m air temperature, 2-m specific humidity, rainfall, snowfall, wind, and surface pressure as inputs.

Using satellite observations with radiation models is a new approach to evaluate the effect of albedo enhancement in urban areas. Salamanca et al. (2012a) calculated the reflected shortwave radiation from two pairs of roofs in two Indian cities that were half painted in cool colors. In their model the atmospheric transmittance was considered, which accounts for the multi-reflection of radiation inside the atmosphere. A radiative transfer model showed a difference of about 50 W/m² (of the roof area) in outgoing shortwave radiation on top of the atmosphere for a 0.1 increase in roof albedo. Building on the method presented in Salamanca (2012a), the annual effect of an urban-wide increase in the roof albedo in six Indian cities was assessed (Millstein and Fischer, 2014). The magnitude of effect of aerosols on the radiative performance of reflective roofs was estimated. The annual average benefit of a 0.5 increase in roof albedo was about 1 kWh/m² per day (~40 W/m²; normalized by the area of the roof).

Oleson et al. (2010) investigated the global effect of implementing white surfaces on urban climate by coupling an urban canopy model to a global climate circulation model. Roofs were chosen as the main urban covering surface for global increase of albedo. The urban canopy model was able to consider HVAC systems of buildings. Simulations showed that by implementing strategies using white roofs, it is possible to mitigate the urban heat island effect by 33% and reduce maximum temperature of urban areas by about 0.5 °C. On the other hand, the strategy was less effective at high latitudes in terms of energy savings.

Jacobson and Hoesung (2012) used a model called “GATOR_GCMM,” which is designed to address global-scale phenomena. The model is claimed to consider almost all conventional processes and chemical species in the atmosphere. Land use data was extracted from MODIS¹ satellite remotely sensed data and analyzed for the grid domain. Based on their calculation, 0.128% of land with non-permanent ice is urban areas. Vegetation occupies half of urban areas, and the roofs-to-roads ratio was 1.5. A white-roof scenario was implemented by changing overall albedo of urban areas from 0.15 to 0.65. Simulations were performed for different scenarios of a 20-year period, in addition to six perturbation simulations for sensitivity analysis of results. The air temperature of urban areas was increased by 0.11 °C and the earth warmed up about 0.07 °C. This change resulted from two main factors: 1) the carbon dioxide dome over urban areas, which absorbed reflected solar radiation from white surfaces, and 2) reduction in evapotranspiration from urban surface as a result of cooler surface which decreases cloud optical depth. Decrease in cloud optical depth is inversely proportional to the amount of sunlight striking urban surfaces.

Coupling land-surface and atmospheric circulation models and using land feedbacks provide more reliable results for assessing global effects of changing the albedo. Millstein and Menon (2011), in one scenario, implemented cool materials for roofs and pavements of urban areas in North America. In another scenario, they assessed using PV panels in two sites (increasing absorptivity). They used Weather Research and Forecasting (WRF) for modeling. Results of the first scenario indicated that the net reflected solar energy increased, while the urban air temperature decreased in most parts of the continent. In some regions the surface temperature did not change, and some regions experienced an increase in the surface temperature due to the change in wind pattern. The temperature decrease in urban areas was less than previous researches showed, due to the effect of atmospheric circulation. Implementation of PV panels in a large area (Mojave Desert of California) caused the local afternoon air temperature to increase about 0.4 °C.

Levinson and Akbari (2010) estimated the annual energy saving and pollution reduction from bulk implementation of cool roofs for offices and retail stores in US. They calculated the energy cost saving by defining a cost function as the heating cost subtracted from the cooling cost. Air

¹ Moderate-Resolution Imaging Spectroradiometer.

pollutants' emission is described by summation of greenhouse gases and air pollutants emitted from natural gas furnaces and power plants. They divided offices and retail stores into two categories of old (built before 1980) and new (built after 1980). For the modeling, they calculated the cooling energy saving and the heating penalty per unit conditioned roof area and the cost saving of prototype buildings, with respect to regional energy prices. Simulation of office buildings in 236 U.S. cities showed calculations varying mostly due to energy prices and climate of target region. Energy cost saving in Alaska (cold climate with low density population) was the lowest, and in the southern part of the US was the highest. Retrofitting 80% of the commercial buildings' conditioned roof area in the US would yield an annual cooling energy saving of 10.4 TWh; and an annual energy cost saving of \$735 million.

In another study (Georgescu and Moustauoui, 2012), expansion of the Sun Corridor metropolitan area in Arizona State was simulated with WRF to find out the effect of different surface modification strategies on its air temperature and water content. Moreover, the extended effects of the urban expansion on the statewide climate were investigated. The surface modification was defined by changing albedo of roofs to its maximum value of 0.88 and decreasing the permeability of the urban surfaces. Urban expansion (i.e., applying impermeable area) increased the average and maximum air temperatures up to about 1 °C and 4 °C, respectively. Implementing cool roofs resulted in less temperature increase, due to urban expansion, with a difference of 0.27 °C in summertime. Expansion of the land use resulted in reduction of evapotranspiration and precipitation for all scenarios; lower precipitation was the consequence of reducing potential water storage within the soil.

2.2. The role of urban canopy models in urban climate simulations

The coupled UCM-mesoscale model gives a more accurate prediction of the climate parameters compared to models that do not consider the urban morphology. There are different types of UCMs available that can calculate the effect of canopy on the atmosphere with different levels of complexity. In this section, I investigate the related research associated with UCMs coupled with mesoscale models. In general, UCMs are divided into three groups; (1), slab, (2) single-layer, and (3) multi-layer.

Bulk (slab) urban canopy models are the simplest form of urban canopy models. They are one-dimensional models based on the energy budget of urban surfaces. Solving the energy balance equation can give the air temperature near the surface (Moriyama and Takebayashi, 1999; Moriyama and Matsumoto, 1988). Chen and Dudhia (2001), and Liu et al. (2006) developed a Land Surface Model (LSM) that can predict the length of urban boundary layer based on local Richardson Number.² Lower albedo, higher soil thermal conductivity, and higher heat capacity are expected for urban areas. Liu et al. (2006) modified surface roughness and background albedo of urban areas in the model to be 0.8 m and 0.15, respectively. The modified model was implemented in a mesoscale model (i.e., MM5³) for further validation comparing the measured data of Oklahoma City (OK, USA). An improvement in estimating the wind speed and its direction, temperature, specific humidity, and boundary layer height was observed compared to results of the earlier version of the model by Chen et al (2001).

To study the effect of vegetation on air temperature, Moriyama et al. (1999) built a single-layer soil slab model. They calculated the heat transfer coefficients using Monin-Obukhov similarity theory (Monin and Obukhov, 1954). In their model, reflectivity, evaporation efficiency, thermal conductivity, and heat capacity were a function of Normal Vegetation Index (NVI). Anthropogenic heat emission and surface roughness of their area of study (Kobe, Japan) was based on measured data. They concluded there was a linear correlation between NVI and the minimum air temperature.

Arnfield and Grimmond (1998) used a new heat storage parameterization to find the energy budget of urban canopies. Storage heat flux was estimated based on a linear function of net radiation and rate of radiation. The coefficients of the linear function were determined statistically. They used observed data to consider the effect of wind in a canopy and of radiation trapping in their model. The model was validated against observed data and showed a good agreement. Some of these simple slab models have been used to find the effect of roofing materials on the sensible flux of the roofs (Takebayashi and Moriyama, 2007). Results showed that using reflective materials (which absorb less energy) can reduce the sensible heat flux. Likewise, green roofs reduce the sensible heat flux by increasing latent heat flux. Takebayashi

² Richardson Number is a measure of the stability of the atmosphere (explained in Appendix A).

³ Mesoscale Model Version 5

and Moriyama (2012) used their slab model to calculate the radiant environment of urban areas. The energy absorbing portion of urban surfaces was determined and their effect on the surface energy balance quantified. They modified the thermal properties of urban canopy. South–north and east–west streets’ orientations were considered in their UCM, with variable building heights.

Kusaka et al. (2001, 2004) developed a single-layer urban canopy model and compared it with slab and multi-layer models. The concept of the proposed model was based on a simple energy balance of sensible heat fluxes from the surface, and heat flux into the surface. This model needs wind speed, air temperature, solar position, and solar radiation flux as inputs of iterations from a mesoscale model. The outputs are heat and momentum fluxes, in addition to the temperature on different urban surfaces (i.e., roofs, walls, and roads). Solar flux absorbed by the surfaces was calculated based on a two-dimensional geometry of urban canopy by considering shadow and reflection effects. The same approach was used for longwave solar radiation fluxes. Wind speed in the canopy was estimated with roof level wind speed, which is a function of synoptic wind and logarithmic distribution in the canopy. Sensible heat exchange between canopy and the overlaying atmosphere was calculated based on the Monin-Obukhov similarity theory (Monin and Obukhov, 1954). Surface temperatures were estimated based on their energy balance (Fourier law for thermal diffusion). The model was compared with different observed data and against other models, and results showed a good agreement in predicting surface temperatures and a fairly good estimation of heat fluxes. Finally, three basic urban canopy models were compared, and single-layer model results were in a very good agreement with the multi-layer canopy model.

The multi-layer model can consider indoor-outdoor heat exchange and the canopy boundary layer effect (Chen et al., 2009). Martilli (2002) introduced a multi-layer UCM that can address interactions between urban surfaces and synoptic airflow. In their model, geometry of an urban area is defined by a constant width of streets and buildings with the same length as the grid. Height of buildings is approximated by a probability function that defines the building distribution. The model solves conservation equations explicitly except for the Poisson equation of pressure. It uses k-l closure of Bougeault and Lacarrere (1989) for the turbulent kinetic energy equation. This model also modifies the radiation (shortwave radiation: Schayes and Grossi, 1997; and longwave radiation: Sasamori, 1968) trapped within the urban canopy. They have validated a

simple mesoscale model coupled to the UCM with measured data. The comparison of their model with previous research showed a significant improvement in thermal properties of the canopy. Additionally, they concluded that the model can predict Reynolds stress components and turbulent intensity more accurately based on observations. No anthropogenic heat emission is considered in ML-UCM but it can be improved by coupling a building energy model. The model uncertainty was evaluated against different urban canopy parameters. Simulations by using urban/WRF software showed that the model can well estimate diurnal variation of temperature and wind distribution, atmospheric circulation, and lower boundary layer properties.

There are numbers of coupled UCM-mesoscale models that have been further developed to overcome their limitations in estimating the momentum and heat exchange on urban surfaces (Bornstein and Lin, 2000; Ohashi and Kida, 2002). Best (2005) modified the fluxes of urban areas in the Met Office operational mesoscale model and the modifications resulted in a better prediction of urban air temperature. Dupont et al. (2004) modified the impact of urban components (buildings, vegetation, and pavement) in an MM5 mesoscale model using a single-layer UCM based on Masson (2000). Masson (2000) considered roofs, pavements, and walls (each of them comprising three layers) as urban surfaces. Her model, combining UCM and LSM, accounts for the water content and temperature of deep ground soil. The model calculates the temperature and water content of all surfaces by considering the effect of anthropogenic and industrial heat emission in the urban canopy. The total heat and momentum flux from the canopy is estimated by averaging the fluxes calculated for all canopy orientations. Otte et al. (2004) developed a multi-layer urban canopy model by improving drag-force properties of urban surfaces. They used the thermodynamics approach of Dupont et al. (2004) in their model and validated the model by using observations in Philadelphia (PA, USA).

2.3. The role of building energy models in energy consumption estimation

The beneficial effect of using reflective coatings for roofs and pavements in urban areas on energy consumption of buildings is discussed in several reports (Akbari and Konopacki, 2005, 2004; Scherba, 2011). Taha et al. (1988) coupled a simple one-dimensional PBL model (URBMET) with a comprehensive BEM (DOE2). The PBL model considers heat and moisture fluxes of the urban surfaces. BEM uses the weather data for the outdoor conditions to find the energy consumption of buildings. The coupling of these models was done offline and, after

updating the weather data by PBL model output, BEM calculated the energy saving of increasing the albedo.

Akbari et al. (2001) studied the effect of increasing albedo on the energy saving in buildings. They used a mesoscale model (i.e., CSUMM⁴) coupled with a photochemical model (i.e., UAM⁵) to update the weather data and study the energy consumption change of buildings. They increased the albedo of roof and pavements, and the vegetation fraction of Los Angeles. They coupled a mesoscale model to a BEM (i.e., DOE2) for updating the weather data. The coupling between the BEM and mesoscale model was done offline and the resolution of the square grids was about 5 km. Results showed a decrease of 20 ppb in peak ozone concentration and 20% reduction in cooling energy consumption.

Reviewing numbers of papers that coupled BEM and urban climate models showed that air temperature decreased up to 2 °C by increasing the albedo (Taha, 1997a). Anthropogenic heat emission has a small effect on UHI in most parts of the US except for cold regions in winter.

UCMs are also coupled with computational fluid dynamics (CFD) models to calculate interactions of building energy and urban environment. Ashie et al. (1999) used this approach for Tokyo where the urban surface modification decreased the air temperature by 0.4-1.3 °C and cooling energy by 3–25%, based on their model. Bruse et al. (1998) developed a simple CFD model that uses input of meteorological parameters to build initial and boundary conditions. The model considers interactions between urban surfaces, urban vegetation, and atmosphere. The model provides the surface and air temperature as well as moisture content in different parts of the domain. However, the model is not validated based on the observational data and it does not have the capability of online coupling to mesoscale models.

One of the widely used BEM models is based on the research performed by Salamanca et al. (2010a, 2010b) and validated with previous BEMs. Their model is a modified version of the BEM developed by Kikegawa (2003). The BEM gets air temperature, humidity, and the amount of radiation from a mesoscale model. Outputs of BEM to the mesoscale model are temperature of urban surfaces and heat flux from buildings to the canopy. In this model, temporal variation of

⁴ Colorado State University Mesoscale Model.

⁵ Urban Airshed Model.

indoor air temperature is solved based on the sensible heat load difference between indoors and outdoors. Indoor air humidity is also solved following the same approach, based on the difference between the indoor and outdoor latent heat load. Indoor sensible heat load is calculated by the convective heat transfer between room surfaces, air exchange of ventilation, anthropogenic heat of occupants, and other internal loads. Outdoor loads are related to the heating and cooling loads of each floor. Surface temperatures of walls, floor, and ceiling are estimated using Fourier law of 1D conduction. Windows are assumed to be non-absorbent and temperature is constant along its thickness. Roos (1997) and Karlsson et al.'s (2000) approach is used to find the transmission of radiation through windows. The BEM can consider the comfort temperature (with its range) and maximum heating and cooling capacity of the HVAC system. The model was validated against other BEMs and good agreement was found. Sensitivity of thermal load to the effect of windows, ventilation system, and convection heat transfer coefficient was explored. The coupled BEM-BEP model (Martilli et al., 2002) was also validated using the experimental data of the BUBBLE project of Basel, Switzerland. Offline simulation with the coupled model was performed in one dimension for the neighborhood of measurement-tower. However, it was shown that the BEM cannot predict the building energy consumption accurately (Bueno et al., 2011).

It should be noted that only the contribution of urban climate to energy consumption of buildings and the indoor thermal comfort is significant, as discussed in the literature. The effect of climate change on the indoor thermal comfort is negligible (Sailor, 2014).

2.4. Quantification of effects of increasing albedo on urban climate and air quality

Urban air pollution is one of the most complicated issues that science is facing (Seinfeld, 1989). There are six different air pollutants of main concern for the United States Environmental Protection Agency (EPA): carbon monoxide (CO), lead (Pb), nitrogen dioxide (NO₂), ozone (O₃), particulate matter (PM) and sulfur dioxide (SO₂) [<http://www.epa.gov/air/criteria.html>]. Among these pollutants, ozone is of more interest due to its generation dependence on temperature. Unlike the other pollutants, temperature has a direct and substantial effect on ozone generation by chemical reactions. While most pollutants are emitted directly, some are secondary products of reactions between primary pollutants such as NO_x and Hydroperoxyl. Furthermore, those reactions that produce the secondary pollutants strongly depend on the ambient condition.

Hence, different pollutants may be observed in different times of the year or during the day. Unlike other gaseous pollutants, ozone, as a secondary product pollutant, has higher concentration in summertime (Table 2-1). Ozone is also expected to have a high concentration in the afternoon (Zeldin and Meisel, 1978) due to the secondary reactions.

Table 2-1. Qualitative comparison of concentration of gaseous pollutants in different seasons (Zeldin and Meisel, 1978)

Pollutant	Spring	Summer	Fall	Winter
SO _x	Medium	Low	Medium	High
NO _x	Medium	Low	Medium	High
CO	Medium	Low	Medium	High
O ₃	Medium	High	Medium	Low

Ozone concentration quantity, in different regions around the world, is reported in the literature based on simulations and experimental data (see Baldwin et al., 1977; Dickerson et al., 1997; Carter et al., 1979; and the references therein) that investigated the relationship of the temperature increase in summertime to ozone generation. Walcek et al. (1994) improved the simulation methodology to study effects of the temperature increase on the ozone concentration. They considered reactions of both organic and inorganic compounds to explore their sensitivity to different meteorological parameters. Finally, they concluded that the increase in temperature results in more ozone pollution. In a project in Greece, researchers evaluated the ozone concentration and the temperature quantity using experimental data recorded in different locations of Athens (Stathopoulou et al., 2008). They concluded that there was a linear correlation between the ozone concentration and the temperature. Moreover, a smooth change in the ozone concentration compared to the temperature variation was observed. Other researchers studied the relationship experimentally, based on ozone-related reactions in a bench-scale reactor with different gaseous baths (see Hippler et al., 1990; Atkinson et al., 2004, 2006, 2007, 2008, 2010, 2013; and the references therein). Accordingly, different advanced models have been developed to simulate chemical reactions in the atmosphere. Some coupled chemistry-meteorological models are able to consider meteorological variables as the inputs to determine feedbacks of the system (Jacobson, 2001a, 2001b; Wu et al., 2007; Eyring et al., 2006). Many of these models are used to find the ozone concentration, considering all effective variables. However, these models are too complex to provide sensitivity analysis of the response of the ozone generation to temperature, anthropogenic emission, and trace gases. Hess et al. (1992)

reported the effect of the temperature and initial compositions on four reaction mechanisms. Touchaei et al. (2013) showed that to have a valid chemical transport model, emission of Volatile Organic Compounds (VOCs) should be considered.

There is a distinct relation between urban climate and air quality (e.g., air pollution dispersion). Temperature rise in summer can increase the concentration of pollutants (e.g., ozone) by increasing the reaction rate. For example, Akbari et al. (2001) reported an increase of ozone concentration in Los Angeles with temperature rise in summertime. However, a longer urban boundary layer would disperse the pollution vertically; hence, the ozone concentration might have no significant change. Changing the urban temperature affects the precipitation and cloud cover (their correlation is still under investigation). Precipitation would cause wet deposition of pollutants. Consequently, predicting the effect of mitigation strategies on precipitation of urban areas is essential for studying the air quality. Coupling a meteorological model with a chemistry model is acknowledged by researchers to simulate the air quality of a region.

Taha et al. (1997b) used the coupled CSUMM (mesoscale meteorological simulation) and UAM photochemical model (chemical transport simulation) to investigate the air quality of the South Coast Air Basin. Simulations were performed for 0.07 and 0.13 average increase in albedo of possible grids for moderate and extreme scenarios, respectively. Vegetation cover was increased by the average amount of 0.06 and 0.12 for moderate and extreme scenarios, respectively. Increasing the urban albedo had a positive effect on almost all parts of the region by decreasing the summertime temperature and ozone formation. Nevertheless, increasing vegetation cover of the region is only effective (non-uniformly) for extreme conditions; in both moderate and extreme scenarios it was assumed that trees with low biogenic hydrocarbon emission were planted.

Climate and air quality of three U.S. cities (Salt Lake City, Baton Rouge and Sacramento) were modeled to evaluate the heat island mitigation and ozone reduction by increasing urban albedo and vegetation (Taha et al., 2000). Meteorological modeling performed for current condition and output of this model was used as a direct input to the photochemical model and indirect input to the emission processor. Parameters needed by these models include (but are not limited to): density, specific heat, albedo, Normalized Difference Vegetation Index (NDVI), thermal inertia, anthropogenic heat flux, thermal diffusivity, moisture content, and roughness length. Chaotic

topography of a region like Salt Lake City imposes a large gradient in outputs that do not grant generalization. Results indicated that all three cities had benefits from IAIV⁶ strategies. All of the cities experienced reduction in temperature but the city with a greater portion of urban area had greater reduction of ozone generation compared to other cities.

Civerolo et al. (2007) coupled MM5 and CMAQ⁷ to study the effects of changing the land use land cover in New York City. They used a two-way nested approach to prepare the boundary condition for 4-km grids. Expansion of urban land use increased the air temperature by about 0.6 °C. Furthermore, maximum 8h-averaged O₃ levels increased more than 6 ppb across the region. Taha (2005) studied urban surface modification in central and southern California as a potential ozone air quality improvement strategy. The main purpose of the study was to ensure the positive effect of increasing surface albedo and vegetation on air quality as well as air temperature. He predicted 2.5 °C and 3.5 °C air temperature decrease for central and southern California, respectively. The peak ozone concentration of 2h-averaged and 3h-averaged O₃ levels decreased by up to 3 and 12 ppb, respectively. He used the MM5-CMAQ coupled model with a grid size of 5 km for the simulations. A very important outcome of the simulations was a smaller improvement of air quality by further surface modification after a threshold (Taha, 2008a). Sarrat et al. (2006) coupled mesoscale and chemical transport models with an urban canopy model to investigate the air pollution concentration over Paris. The simulation was done for a stable synoptic weather condition with a grid size of 3 km. The simulation well captured the dispersion and generation of pollutants and their variation during nighttime and daytime.

Since about 2008, researchers have started to develop fine-resolution models to see a more precise variation of concentration of pollutants. Urban climate and air quality of Houston (TX, USA) was simulated using Urbanized MM5 to find the sensitivity of the ozone concentration and air temperature to albedo and vegetation cover (Taha, 2008b). The model was the modified version of multi-layer UCM of Dupont et al. (2004). Modifications increased the accuracy of urban parameterization in constructing on mass, momentum, Turbulent Kinetic Energy (TKE), and energy equations. Simulations were performed using detailed information of the domain for a grid size of 1 km. Results indicated that the effect of increasing vegetation on the air

⁶ Increase Albedo Increase Vegetation.

⁷ Community Multi-scale Air Quality model

temperature in dense regions is greater than that of increasing albedo. The air temperature decreased between 1 and 3 °C for different parts of the city. The same model has been used for Sacramento (CA, USA) where the maximum air temperature change was reported to be the same (Taha, 2008c). The peak ozone concentration (8h-averaged) was decreased 4% to 13%, while the short time interval ozone decrease was about 16–26 ppb. However, presence of upwind had a negative effect on ozone concentration of some regions (an increase of 9–11 ppb). Taha (2009a, 2009b) used the same approach to characterize the potential air quality improvement strategy of urban surface modification in different cities of California.

Atkinson (2003) used a single-layer UCM based on the previous research (Kusaka et al., 2001; Masson, 2000) coupled with a mesoscale model to investigate the effect of albedo, anthropogenic heat emission, sky view factor, and emissivity. The simulation domain was an idealized realistic urban area that represents London, UK, with a grid size of about 1 km. By sensitivity analysis, he found that the daytime effect of those factors on air temperature near the urban surface was 0.2 °C – 0.8 °C. Nighttime effect of the factors ranged between 0.3 and 0.75 °C, except for anthropogenic heat emission, which had a much larger effect, up to 2 °C.

The effect of a fractional increase in the roof albedo and in implemented green roofs in the urban scale through the Washington–Baltimore area using coupled WRF-PUCM was investigated (Li et al., 2014a). The temperature reduction in urban areas was prominent during the day, with a small nocturnal effect. Increasing the albedo of 30% of conventional roofs (albedo = 0.3) to the value of 0.7 decreased the surface temperature by 1 °C; while, to reduce the 2-m air temperature by 0.5 °C required change in 95% of the roof area. Reduction of UHI intensity was proportional to the change in the roof albedo. In another case, the albedo of 50% of the roof area was increased to 0.5 (0.2 lower than the default case 0.7, to consider the effect of dirt on the roof) and 0.9 (0.2 higher than the default case 0.7, to consider the highest extreme). For the default case (albedo = 0.7), the surface UHI and 2-m UHI was decreased by 1.7 °C and 0.23 °C at peak, respectively, which were 0.82 °C and 0.18 °C higher than the lower albedo case (0.5), respectively, and 0.8 °C and 0.14 °C lower than higher albedo case (0.9), respectively.

In the Princeton UCM some of the shortcomings with the current UCM models, including the moisture balance and fractional reflectance within WRF, have been resolved. Alternatively, the surface temperature of the grid is replaced by the surface temperature of the urban area to modify

the calculation of 2-m air temperature. The model is capable of considering heterogeneous surfaces such as a combination of a conventional roof and a green roof (Li and Bou-Zeid, 2014b).

2.4.1. The role of urban morphology and building characteristics

Urban areas are complex surfaces that current urban canopy models (UCMs) are not able to consider in all their details. Therefore, in numerical weather prediction, a practical method of assuming uniform distribution of buildings in the urban grids is applied (Martilli, 2009, and references therein). In general, 2D UCMs assume rows of buildings with equal width, and constant or randomly distributed height. Whereas, for the sake of simplicity, 3D models only consider buildings with constant height. The effect of assuming 2D and 3D streets on the sky view factor (SVF) in urban canopy models was tested for five cities in Europe and Northern America (Martilli, 2009). Accurate estimation of SVF is a crucial part of energy calculation in urban areas. Analytical approaches are sophisticated and need simplification of urban geometry (Johnson and Watson, 1984). One of the well-accepted methods to determine the SVF is image processing of fish-eye photography (Steyn, 2010; Hämmerle et al., 2011) or aerial images (Brown et al., 2001; Ratti et al., 2005). However, the empirical method is costly. The last option to calculate the SVF is to use numerical methods that are cost-efficient and accurate in the scale of urban areas (Unger, 2009; Kastendeuch, 2013).

Urban geometry is described by three main factors: mean building height (h_m), plan area density (λ_p), and frontal area density (λ_f). Considering a 2D street where the building size (b) and street width (w) are known, plan area density and frontal area density are as follows:

$$\lambda_p = \frac{b}{b+w} \quad (2-1)$$

$$\lambda_f = \frac{h_m}{b+w} \quad (2-2)$$

Similarly, for a 3D street with identical buildings following equations should be used.

$$\lambda_p = \frac{b^2}{(b+w)^2} \quad (2-3)$$

$$\lambda_f = \frac{bh_m}{(b+w)^2} \quad (2-4)$$

The mean building height, plan area density, and frontal area density of selected cities were empirically estimated by Ratti et al. (2002). The sky view factor for 2D and 3D streets was calculated based on proposed models of Martilli et al. (2002) and Kanda et al. (2005), respectively. Based on results, the 2D street model estimates the sky view factor of the canopy better than the one using 3D streets. The error of the 3D street model is an order of magnitude larger than that of the 2D street model.

2.5. Summary of the literature review

A majority of the research related to urban climate modeling and methodologies to evaluate the effect of surface modification strategies are reviewed. Increasing the urban albedo is believed to reduce the air temperature in global and regional scales. Mesoscale meteorological models coupled to urban canopy models (UCMs) provide a pertinent framework to investigate the effect of increasing the urban albedo on air temperature and air quality. Different types of UCMs (urban parameterization) are studied to design an algorithm for choosing the most appropriate one.

Current UCMs have some shortcomings, such as considering a single reflection from urban surfaces that underestimates the absorbed energy in the canopy. Moreover, sensitivity of the air temperature in the canopy to different choices of UCM is not investigated for cold climate regions. Accurate simulation of urban climate in the scale of the neighborhood using UCMs needs a fine-resolution grid size. Owing to computational limitations, the fine-resolution approach has only recently been used, and it needs to be investigated thoroughly to understand the limitations and proper practical assumptions.

The effect of mitigation strategies on building energy consumption is evaluated by adding the building energy model (BEM) to meteorological models. Recently, the feedback of heat emission from buildings to the canopy has also been considered. However, BEMs coupled with mesoscale models are simple and they do not consider complex HVAC systems with their part-load performance. Coupling mesoscale, BEM, UCM, and chemical transport models is also essential to characterize the urban air quality, and this has not been performed yet. Online coupling of the chemical transport model to the mesoscale model improves the results by considering the instant effect of meteorological parameters on pollution dispersion.

The literature review is followed by reviewing the reports on urban climate and the improvement of air quality modeling techniques in recent years. It is important to mention that studying the effect of large surface modification on urban climate is a site-specific process. None of the performed research characterized the effect of increasing albedo in cold climate regions.

2.6. Concluding remarks

Here, I explain the research objectives in more detail based on the reviewed studies. These objectives try to resolve some of the remaining shortcomings in urban climate simulation to find an answer to the scientific question of this thesis of evaluating the albedo enhancement strategy in cold climates.

1. *Selecting appropriate model ensemble*

The model ensemble for urban climate simulation includes parameterizations for microphysics, cumulus, planetary boundary layer, radiation, land surface, and urban canopy. Analyzing the sensitivity of meteorological parameters (e.g., air temperature and wind speed) to a different set of parameterizations (i.e., model ensemble) enables me to select the most accurate model ensemble for urban climate simulation in cold regions. The fine-resolution grid spacing provides more detailed information on the spatial variation of the air temperature; hence, the selected model ensemble should be compatible with the selected technique. The sensitivity analysis is based on the comparison between a predicted variable and the observed value in the weather stations. Since my goal is to study the effect of albedo enhancement on urban heat island, I mostly concentrated on air temperature, wind speed, relative humidity, and precipitation through the simulation domain.

2. *Characterizing the urban morphology and building properties*

The urban canopy model (UCM) requires detailed information of urban areas, including: building height distribution, width of buildings, width of roads, orientation of streets, and urban fraction. Additionally, the UCM (multi-layer UCM, ML-UCM, which can be coupled to the building energy model, BEM) uses building environment characteristics as inputs, including: performance of HVAC systems, roof albedo, walls albedo, road albedo, thermal capacity of roof, thermal capacity of walls, thermal capacity of road, and so on. Collecting all those data for Montreal (the city selected as the case study) is not feasible. Hence, an algorithm is proposed to

use urban characteristics of a few neighborhoods to calculate the required parameters for the UCM. Building characteristics are specified analyzing the reported energy consumption of the region and using different simplifying assumptions. Meanwhile, the UCM is modified to consider the effect of multi-reflection between urban surfaces (similar to Sailor and Fan, 2002) and a new type of ideal urban canopy is proposed. The modifications are meant to increase the accuracy of the model in calculating the energy balance on the surface. The BEM is also modified by correcting some of the assumptions on the performance of HVAC systems to improve the calculation of heat emission from buildings to the canopy. The modified version of the model is tested and compared with the default settings of WRF.

3. Evaluating the seasonal effect of an increase in the urban albedo

An algorithm is proposed to select a day of each month to represent the whole month for climate simulations, since running the simulation for the whole year is not computationally feasible. Evaluating the seasonal performance of an increase in the urban albedo would grant the net annual benefit of implementing cool materials over their potential penalties. In particular, I determine the energy consumption of HVAC systems in the selected days and compare them for different months.

4. Annual energy consumption of buildings

The BEM coupled to WRF and ML-UCM is a simple model that does not consider the dynamics of the HVAC systems. Therefore, I use a BEM with a higher degree of complexity (named DOE2.1E) with updated air temperature, humidity, wind speed, solar radiation, and cloud cover to calculate the annual energy consumption of buildings.

5. Characterizing the effect of an increase in the urban albedo on urban climate and air quality

There is a gap in previous studies in that the effect of heat emission from buildings has not been considered. I use the coupling of BEM-UCM to WRF-CHEM for evaluating an increase in the reflectivity of urban surfaces. The online coupling of WRF-CHEM would result in a realistic interaction between the chemistry part of WRF and meteorological simulations. By performing simulations, I would be able to quantify the magnitude of the effect of the albedo enhancement in cold climates.

Chapter Three: Methodology

The methods and algorithms of accomplishing each research step are discussed separately in this chapter, which provides details of the urban climate simulation basics and an introduction to modifications of models discussed in following chapters. In Section 3.1, the mesoscale model, its governing equations, and parameterizations are introduced. The urban canopy model as the major contributor to my research is discussed in Section 3.2. A summary of the methodology of urban climate and air quality modeling based on my simulation framework is presented in Section 3.3.

3.1. Simulation tool

Various advanced models have been developed for climate and air quality modeling of urban areas (Skamarock et al., 2008; Met Office, 2011). Some of the worldwide accepted models and restrictions in utilizing them for urban climate and air quality simulations were reviewed by Ching (2013). The quality of handling some critical shortcomings in previous generation models (e.g., MM5, CSUMM) was my main concern in selecting the appropriate tool. Fine-grid resolution of a domain and detailed input data for urban canopy is the main issue in urban climate simulations (Ching, 2013; Wyngaard, 2004). Moreover, capability of online coupling between the meteorological model and chemical transport model has been my serious concern to achieve the research objectives. Availability of a variety of physical parameterizations within the mesoscale model is another desired feature. Flexibility of selecting different physical models would provide a possibility of proposing a more accurate approach for urban climate simulation in cold regions. Finally, I am interested in a mesoscale model that can provide all three types of urban canopy models. Based on these criteria *I selected the Weather Research and Forecasting (WRF) model to characterize increasing albedo in urban areas.*

The ARW⁸ solver of WRF includes different physical models, which makes it more complicated than the NMM⁹ solver (Mass et al., 2006). ARW's nesting capability makes it even more

⁸ Advanced Research WRF.

⁹ Non-hydrostatic Mesoscale Model.

attractive for researchers who are studying urban climate. Simultaneously, it is applicable to different research topics (e.g., regional climate research, coupled models, etc.) and for domain ranges from meters to thousands of kilometers. WRF is written in FORTRAN and the interfaces are in C programming language; its efficient parallel computing ability is state-of-the-art. There are some challenges in using WRF which come from the complexity of climate simulation problems. For instance, the software design is unintuitive for physics scientists, and it produces huge input/output files (mainly in netCDF format). On the other hand, though it can take hours to perform a simulation, recompiling is not normally needed.

The WRF modeling system needs appropriate inputs to define the boundary conditions (BCs) and initial condition (IC). Then, it uses WRF Preprocessing System to digest these data and prepare them for the initialization program (i.e., Real). The Real program, as a part of the WRF model, sets the BCs and IC for the simulation period. The ARW solver includes different parameterizations to numerically solve the problem. Finally, a post-processing program (e.g., NCL¹⁰) is used to visualize the results. Figure 2-1 illustrates the complete procedure that I use in my simulations. A complete description of the WRF model and its components can be found in the ARW user guide (2012).

Version 3.x of WRF consists of the Noah Land Surface Model, which can be coupled with some Planetary Boundary Layer (PBL) schemes, to characterize surface properties (Chen and Dudhia, 2001). Detailed surface properties can provide sensible and latent heat fluxes in urban areas. WRF can simulate the effect of urban areas based on the slab urban canopy model by using the Noah LSM option. For a more detailed estimation of the heat fluxes and skin temperature of urban surfaces a single-layer UCM option can be coupled with WRF. And the most sophisticated option combines Building Environment Parameterization and the building energy model (BEP+BEM), which is available by enabling multi-layer UCM. In order to use these options downscaling of the meteorological parameters should be performed. There are some challenges in using urbanized WRF, such as initialization (data is not available in the scale of a city) and parameter specification. Appendix A provides more details of the WRF solver.

¹⁰ NCAR Command Language.

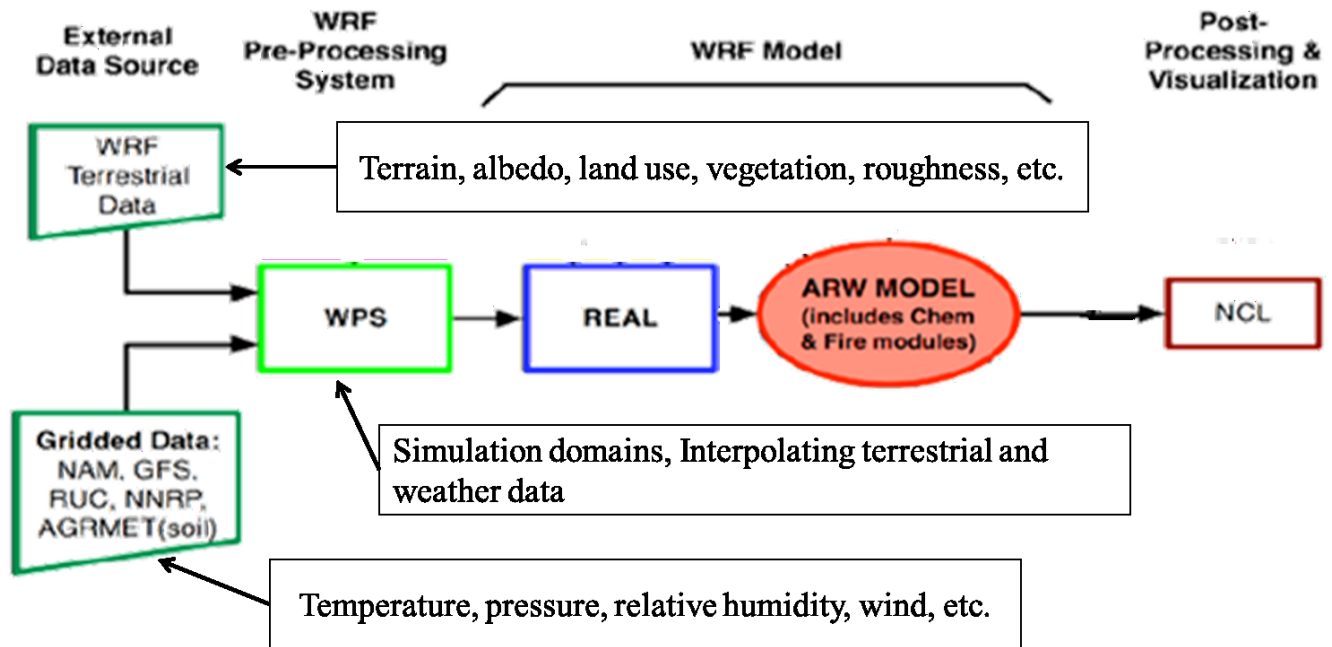


Figure 3-1. Flowchart of WRF modeling system for urban climate simulation (modified from (ARW user guide, 2012)

3.1.1. Parameterizations

Parameterization is a simple way of representing physical processes such as cloud formation and precipitation. Here, the parameterizations used in ARW-WRF (microphysics, cumulus, planetary boundary layer, radiation, land-surface, UCM) are described. Many sub-routines are implemented within the ARW solver, which provides different physical model options. These models define the source and sink values of RHS in governing equations and hold tendencies fixed during Runge-Kutta steps of time marching. Physical models are separated from the dynamic solver; some of them are calculated before the dynamic solver, and the rest of them after that. In this case velocities are also de-staggered and exerted into proper physical models (See Appendix A on parameterizations of WRF).

3.1.1.1. Microphysics

Microphysics models determine the process of transforming water from one form (rain, snow, graupel, vapor, etc.) to another form. In general, water vapor creates cloud water and cloud ice to shape snow, rain and other types of precipitation. The main equations governing the processes are conservation of momentum, energy, and mass of water (eq. 3-2) in the cloud, rain, snow, and other precipitation. Terminal velocity of precipitation particles can be calculated from the

governing equations. The main challenge of the microphysics model is predicting the different conversion process of water in cold clouds.

3.1.1.2. Cumulus

Cumulus parameterizations consider the effect of convective air movement outside clouds on updrafting and downdrafting of clouds. Inclusion of the cumulus model affects the vertical heat and moisture fluxes in a column of air above individual grids. In addition, some models are able to predict the cloud and precipitation tendencies. All WRF options estimate the convective component of surface rainfall. In general, the models have three parts; 1) trigger function to identify the convection, 2) flux equations for mass and/or momentum and/or energy, 3) the closure assumptions.

3.1.1.3. Planetary boundary layer (PBL)

Planetary boundary layer (PBL) is responsible for vertical flux exchange in the whole column of air in a grid cell. PBL quantifies the influence of momentum, heat and moisture fluxes in the vertical sub-grid terms. In mesoscale models, PBL is divided into three sub-layers. The viscous layer goes from the ground to the height of surface roughness where fluxes of heat, moisture, and other constituents are experimentally estimated based on the von Karman constant and friction velocity. The surface layer and transition layer are the two other parts of PBL and they can be estimated as a function of height (Pielke, 2002). Urban surfaces are heterogeneous surfaces and the parameterization is based on more complex methods.

3.1.1.4. Radiation

Radiation parameterization determines the energy balance of the domain. The surface of the domain (e.g., urban surface) can receive shortwave energy from the sun or longwave energy from the sky. Urban surfaces absorb part of the energy and reflect the rest, while emitting longwave radiation. The amount of energy that strikes the surface is a function of sky condition and zenith angle. The energy exchange on the surface is well discussed by Liou (1980), and a different algorithm with a different level of complexity has been developed to quantify it (ASHRAE, 2007b; Duffie and Beckman, 2006; Iqbal, 1983). Incoming solar radiation and emitted longwave radiation from the ground varies through different mechanisms in the atmosphere. In a clear sky, part of the sunlight energy on top of the atmosphere is absorbed by different tracer gases (e.g., ozone, water vapor, etc.) and the rest reaches the ground. However,

cloudy and polluted sky increases the absorption by increasing the normal optical thickness of the air layer (Liou, 1980). The part of the radiation reflected from the ground goes through the same process. Longwave radiation from the surface of the earth and gases are absorbed by the atmosphere or transmitted.

3.1.1.5. Land-Surface

A Land-Surface Model (LSM) provides information of momentum, heat and moisture fluxes on land points and sea ice by using atmospheric feedback of other schemes in a simulation (it can be considered as a boundary condition for the model). All options in the ARW solver are multi-level models that provide the lower boundary for PBL. LSM updates surface variables (e.g., the ground temperature, soil temperature profile, soil moisture profile, snow cover, and canopy properties) in each iteration step as independent variables.

Using Urban Canopy Models (UCMs) is essential for the urban climate simulation and, consequently, Unified Noah LSM should be used as the main LSM due to WRF limitations. Noah LSM is a developed version of Oregon State University LSM, described by Chen and Dudhia (2001), to which further modifications were applied (Liu et al., 2006; Tewari et al., 2004). Section A.4.4 describes the land surface model in detail.

To calculate the skin temperature UCMs, WRF simplifies the heterogeneity of urban surfaces into a single class of an impervious surface and use eq. 3-1.

$$T_{s,grid} = f_{urb}T_{s,urban} + (1 - f_{urb})T_{s,rural} \quad (3-1)$$

WRF assumes the thermal roughness length of the grassland over impervious surfaces.

3.2. Urban Canopy Models

Urban Canopy Models (UCMs) can provide more accurate feedback of urban areas for surface layer and PBL schemes. There are three types of UCMs within WRF: slab (bulk), single-layer, and multi-layer. Here, a general formulation for the UCMs and my modifications are presented; a complete set of equations for single-layer and multi-layer UCMs are discussed in Section A.6).

3.2.1. Slab Model

Slab models are one-dimensional UCMs that consider buildings as an increased roughness in urban areas. These models are simple and they do not need the detailed information of the

desired regions. Consequently, simulating the urban climate with a coupled mesoscale-slab model is fast. In the slab model coupled to WRF, Monin-Obukhov length scale (Monin and Obukhov, 1954) represents the mixing length and calculations are performed within LSM (Chen and Dudhia, 2001). In this model, background albedo of the surface is constant during the day with a slight modification for radiation trapping. Additionally, thermal capacity and conductivity of the soil is greater than that of urban areas.

3.2.2. Single-Layer UCM

Single-layer UCM calculates the multi-reflection effect (radiation trapping) according to the urban geometry (Kusaka et al., 2001). It also provides a more accurate estimation for sensible heat by assuming a wind distribution in the canopy. In most cases, the horizontal wind is vertically distributed as a combination of logarithmic and exponential function. The model considers two-dimensional approximation for streets (very long streets) with a single orientation. The surface properties could be averaged for different orientations of streets.

3.2.3. Multi-Layer UCM

More accurate urban parameterization, than with the slab and SL-UCM models, is needed to better understand the effect of a complex surface like urban areas with their vertical mixing. The multi-layer UCM developed by Martilli et al. (2002) has been integrated in WRF (Chen et al., 2011) and validated for different cities (Hamdi and Schayes, 2007). ML-UCM divides the urban canopy into separate units and calculates the urban surface parameters (wall and roof temperature, heat fluxes, etc.) related to each unit. This type of model usually predicts the vertical exchange of momentum, heat, and moisture more accurately (the other two models do not include the conservation equation for Turbulence Kinetic Energy, TKE). Building heights in the model are not constant and their shading is estimated by the model (for a constant building width and road width). Based on my estimation, this model increases the time of simulation up to 35% compared to the slab model.

3.2.3.1. Building Energy Model

A further step to provide feedback from the urban structure to its climate is to study the effect of the heat emission from buildings on heat flux from the canopy. Using heating and cooling systems in buildings can increase the outdoor air temperature while regulating the indoor comfort. Modeling the energy consumption of buildings is a complicated process that uses

different weather parameters (e.g., solar radiation, wind speed, etc.). The Building Energy Model (BEM) can be coupled with Building Environment Parameterization (BEP; or the ML-UCM) to predict the energy consumption of buildings. Results can determine the effect of heat generation of buildings on urban climate.

The BEM that can be coupled to WRF was developed by Salamanca et al. (2010a, 2010b). BEM treats buildings as boxes and calculates sensible and latent heats separately. The BEM calculates the cooling and heating energy demand for the air conditioning system of buildings as well as heat emission to the canopy. The inputs to BEM are air temperature, wind velocity, humidity, and the shortwave and longwave radiations from the mesoscale model. An algorithm is designed for energy consumption of the air conditioning system that can consider the comfort temperature (with its range) as well as heating and cooling capacity of the HVAC system. The energy consumption of HVAC systems and heat emission of buildings are calculated from eqs. 3-2 and 3-3, respectively.

$$\left\{ \begin{array}{ll} E_C = \frac{H_{out} + E_{out}}{COP} & \text{for cooling} \\ E_C = \frac{H_{out} + E_{out}}{\eta} & \text{for heating} \end{array} \right. \quad (3-2)$$

$$\left\{ \begin{array}{ll} Q_C = E_C(COP_{cooling} + 1) & \text{for cooling} \\ Q_C = \eta \cdot E_C & \text{for heating} \end{array} \right. \quad (3-3)$$

3.3. Simulations and analysis of outputs

Different versions of WRF with the same governing equations but added capabilities are introduced. I utilized computational developments of WRF throughout my research—for example, solving online coupled BEM-UCM with cluster computing become available in version 3.5 since 2012. Step-by-step development of the model to characterize the effect of increasing urban albedo started with selection of UCMs. Meanwhile, the first estimation of the effectiveness of albedo enhancement is tested by increasing the roof albedo and observing the change in the air temperature. Thereafter, a complete set of model ensembles based on the available options in version 4 of WRF is tested to evaluate different parameterizations of physical processes. Building on the model and to increase accuracy, detailed information of the greater Montreal area (the case study) is analyzed and appropriate parameters are gathered. In addition, an

algorithm is proposed for further modification of the UCM. Though the increase in albedo is potentially beneficial in summertime, the seasonal effect should be quantified. Hence, an algorithm is developed to assess the change in the air temperature throughout a year. In spite of corrections applied to the simple BEM, resulting energy consumption of HVAC systems is not accurate. A detailed BEM that considers the dynamics of the HVAC system is used to calculate savings and penalties in the net energy consumption of commercial buildings. Finally, the developed platform is coupled to the chemical transport part of WRF to study the effect of increasing urban albedo on the air quality.

3.3.1. Selection of the urban canopy model

As discussed in Section 3.2, WRF has three UCM options and they result in different air temperature distributions in urban areas. Six sets of simulations are established; three for the case without any change in the urban albedo (hereafter CTRL) and three for the case with an increase in the roof albedo (hereafter ALBEDO). The air temperature and wind speed in CTRL is compared to measure data from weather stations to evaluate UCMs, accordingly. In the second set of simulations, the roof albedo is increased to calculate the change in air temperature and skin (or surface) temperature. Other physical models are not altered and they have been selected based on previous studies. Detailed methodology and results are presented in Chapter Four.

3.3.2. Sensitivity experiment on physical parameterizations

In Chapter Five, the total of 20 simulations is performed with different model ensembles (combination of different physical parameterizations) for a summer period. Air temperature, wind speed, moisture content of the air, and precipitation are selected to measure their sensitivity to parameterizations. Simulated values for the parameters are compared to measured data from weather stations through the domain. Then, a model ensemble with the least mean average error (MAE) in predicting the selected parameters and with timely manner computation is chosen for further investigations.

3.3.3. Modifications to UCM

The detailed information of the urban morphology of Montreal is gathered and its effect on determining the UHI is tested. The ML-UCM coupled to the BEM is activated in WRF to consider the heat emission from buildings. Modifications to the UCM are applied, and change in

the intensity of UHI and the air temperature is evaluated. Detailed discussion on the methodology is provided in Chapter Six.

3.3.4. Seasonal assessment of albedo enhancement

Since urban climate modeling for a long period (e.g., a year) with a high-resolution grid size (i.e., blocks of buildings) is not computationally feasible, an algorithm is proposed to select a day representing a month. In addition, some corrections are applied to the BEM regarding the calculation for energy consumption of HVAC systems. The total of 24 simulations (CTRL and ALBEDO for 12 months) is performed and the difference of air temperature and energy consumption of HVAC systems between CTRL and ALBEDO is calculated. Details of the algorithm and the correction to the BEM are discussed in Chapter Seven.

3.3.5. Detailed building energy evaluation

Building energy calculations deal with sophisticated dynamics of HVAC systems that cannot be reported by a simple BEM designed for the scale of blocks of buildings (a few hundred meters). Even adding to the sophistication of the BEM may not increase the accuracy of calculations because of the variability in type of systems in a grid cell of mesoscale meteorological models. Hence, a comprehensive BEM that has been widely used by the scientific community and has been tested with a variety of experimental data is employed for quantification of direct (less heat absorption by the building) and indirect (change in the ambient condition; air temperature, relative humidity, etc.) effects. Results are presented in Chapter Eight.

3.3.6. Air quality modeling

Chapter Nine is dedicated to the coupling of the chemical model to WRF with an active UCM-BEM option. Using WRF-CHEM imposes additional limitations on choices of parameterizations (e.g., only two microphysics options are available for chemical modeling). Moreover, available anthropogenic emission data and tools within WRF are other factors to restrict the choice of chemical mechanism and aerosol scheme. Besides, the same procedure is used for CTRL and ALBEDO, and the differences of pollutants' concentration and of meteorological parameters are calculated.

Chapter Four: The choice of urban canopy model for climate modeling

The Weather Research and Forecasting model (WRF) is coupled to UCMs for urban climate simulation. The slab model implemented within WRF is based on Chen et al. (2001) and some of its urban properties are modified with respect to Liu et al. (2006). SL-UCM of WRF was developed and validated by Kusaka et al. (2001, 2004). The widely used ML-UCM coupled to WRF is based on research by Martilli et al. (2002). WRF is evaluated for the continental United States in different studies (Zhang et al., 2009; Millstein et al., 2011).

4.1. Methodology of selecting an UCM and characterizing climatic effect of an increase in roof albedo

The Greater Montreal and Toronto areas are selected for this study. They are the most populated cities in Canada, with more than 9 million inhabitants (about 30% of the population of the country; Statistics Canada, 2007). The heatwaves in the cities can have viral impacts on vulnerable groups of people (e.g., seniors). The cities have distinct climate characteristics (Environment Canada, 2013) due to their geographical locations. Montreal has a lower temperature than Toronto because of the higher latitude. Meanwhile, the wind speed and precipitation in Montreal is higher. However, both cities experiences UHI during summer. Since proposing a mitigation strategy (i.e., the albedo enhancement) can affect lives of a large number of people, it should be intensively evaluated by numerical weather prediction models. We evaluate different UCMs for simulating a summer period in the selected cities as the base case. Then, the air temperature change by an urban-scale increase in roof albedo is compared to the base case to determine the performance of the selected mitigation strategy on reducing the UHI intensity. As a result, the UHI intensity and effect of the albedo enhancement under various assumptions for the physical processes in urban areas is quantified.

4.1.1. Simulation

Weather Research and Forecasting (WRF) version 3.4 (next-generation non-hydrostatic model) is used for the urban climate simulation (ARW user guide, 2012; Skamarock et al., 2008). The Greater Montreal modeling domain is 100×100 km centered at ~45.5° N and ~73.6° W with 333×333 m grid cells [Figure 4-1 shows the areas of interest]. The Greater Toronto domain is

also 100×100 km (grid size 333×333 m) and the domain is centered at ~43.7° N and ~79.3° W. For both cities 51 ETA vertical levels are telescopically defined. The simulation period starts from 11-July-2005 1200 UTC [11-July-2005 0800 LST] to 13-July-2005 1200 UTC [13-July-2005 0800 LST]. The first 16 hours is disregarded as a spin-up time and outputs of the next 24 hours of simulations are analyzed [12 July LST]. The sky condition on the selected day was clear in Montreal and cloudy in Toronto. I am aware of the deficiency of numerical weather prediction models in forecasting the cloud formation but the selected day happened to be a hot and humid day, which increased the chance of heat island occurrence in Toronto. Additionally, it was one of a few summer days with clear sky in Montreal. It should be mentioned that clouds are unevenly distributed above the regions and the cloud cover changes during the day. As a result, a clear day does not necessarily mean there is no cloud at all or a cloudy day does not mean that there is no clear sky during the day.



Figure 4-1. Simulation domain of (a) the Greater Montreal and (b) the Greater Toronto (<http://maps.google.ca>).

The Noah (NCEP, Oregon State University, Air Force, and NWS Office of Hydro.) land-surface model (Chen et al., 2001) is coupled with the three UCMs to provide heat and moisture fluxes for the lower boundary. Noah-LSM calculates the ground temperature, soil temperature profile, soil moisture profile, snow cover, and other surface variables in each iteration step. Interaction between the LSM and planetary boundary layer (PBL) is managed by the surface-layer model. Here, ETA similarity theory (Janjic, 2002) connects feedback of the LSM to PBL. The vertical flux of heat and moisture in the whole column of air above a grid is determined by the Mellor-Yamada-Janjic scheme (Janjic, 1990, 1994) as the PBL scheme. The Grell-Devenyi ensemble cumulus model (Grell et al., 2002) estimates the effect of cloud convection in a grid.

WRF calculates shortwave radiation and longwave radiation with separate models. A new rapid radiative transfer model (named “RRTMG”) by Clough et al. (2005) is selected to simulate the longwave radiation. Additionally, the Goddard scheme (Chou et al., 1994), which considers the effect of ozone and cloud, is selected as the shortwave radiation model. Different forms of water and the transformation in the atmosphere is estimated by microphysics models. The Lin scheme (Lin et al., 1983), comprising six classes of hydrometeors (rain, snow, graupel, vapor, vapor. cloud, and ice cloud), is used for the simulations.

The slab model considers the albedo of 0.15 for urban areas in the control case (“CTRL”). SL-UCM and ML-UCM assume 0.2 reflectivity for all urban surfaces in CTRL (considering multi-reflection between urban surfaces drops the total albedo of the urban area to a number close to 0.15 that changes by the solar position from 0.14 through 0.16). In another scenario (“ALBEDO”) albedo of roofs is increased to 0.8. In the latter case, when using SL-UCM or ML-UCM, calculations are based on the reflectivity of 0.8 (an increase of 0.6) for roofs. In the slab model, albedo of urban areas increased by 0.2 ($0.35 \times 0.6 \approx 0.2$); where, roofs are considered to cover 35% of the urban area.¹¹ In SL-UCM and ML-UCM, the albedo of roofs is considered as an independent parameter. Simulations were performed for all three UCMs to compare their performance in characterizing the modification of the urban surface. In SL-UCM, both selected cities are assumed to have the same anthropogenic heat emission distribution during the summer episode. In slab and ML-UCM, the anthropogenic heat emission is not considered.

4.1.2. Input data

Standard 24-category USGS implemented within WRF categorized the Land Use Land Cover properties of the regions (Figure 4-2). Initial and boundary conditions for weather data are extracted from 3-hourly, high resolution 32 km, North America Regional Reanalysis (NARR) data (Mesinger et al., 2006). Background albedo of the domains is based on the Advanced Very High Resolution Radiometer (AVHRR) measurements on a polar orbiting satellite (Csiszar et al., 1999). A uniform urban class is considered with the default characteristics of WRF, except for the street orientation. The street orientation in Toronto is 0° and 90° from the north and in Montreal is 45° and 135° from the north.

¹¹ This value is good for high-density residential areas; for combination of low-density and high-density residential areas, 25% might be a better estimation of roof cover.

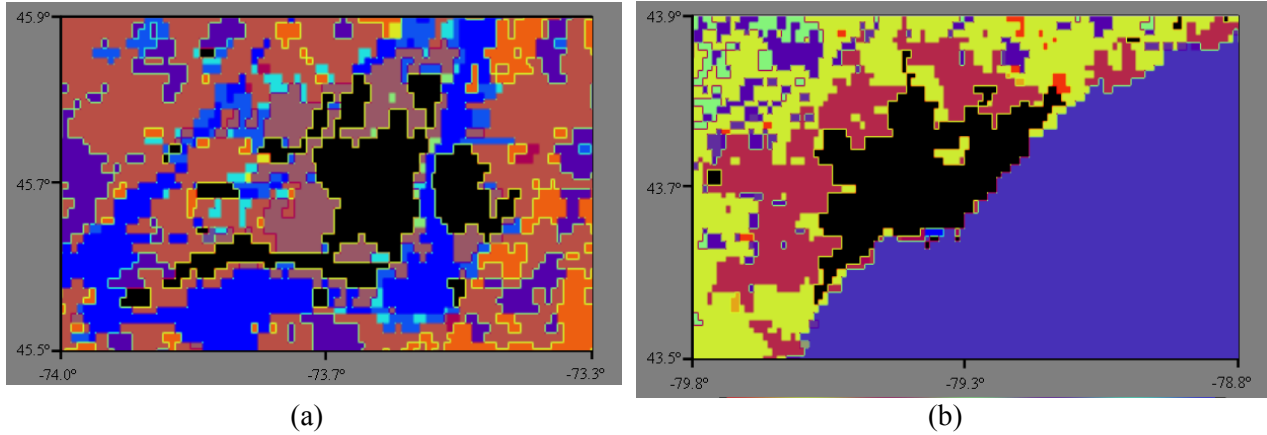


Figure 4-2. Land Use Land Cover (LULC) of (a) the Greater Montreal and (b) the Greater Toronto extracted from USGS dataset. (Black regions are urban areas)

4.1.3. Evaluation method

Measured 2-m air temperature and 10-m wind speed from all weather stations located in the selected domains are compared to the modeled values of related grids. A limited number of the stations reported weather data on hourly basis. The Greater Montreal area has 12 weather stations that record both air temperature and wind speed and one of them is in the urban area (Figure 4-3). Four weather stations located in the Greater Toronto area, as shown in Figure 4-3, recorded the air temperature and three of them provided the wind speed data (the urban station did not have wind data). Both urban stations are located in residential area and buildings around the weather stations affect measurements. Measurement instruments are placed in parks above grass. The weather stations are categorized as urban or rural based on the USGS data that has been used in simulations (Figure 4-2).

For statistical analysis of the UCMs the first criterion for comparison is mean absolute error (MAE), which is calculated using eq. 4-1.

$$MAE = \frac{\sum_{i=1}^{24} |error_i|}{24} \quad (4-1)$$

Individual errors are the difference between observed and modeled 2-m air temperature of the weather stations. Two other measures to evaluate the UCMs are root mean square error (RMSE) and mean bias error (MBE). RMSE and MBE are reported using eqs. 4-2 and 4-3, respectively.

$$RMSE = \left(\frac{\sum_{i=1}^{24} |error_i|^2}{24} \right)^{1/2} \quad (4-2)$$

$$MBE = \frac{\sum_{i=1}^{24} error_i}{24} \quad (4-3)$$

Although these two measures are not as clear and natural as MAE (Willmott et al., 2005), they have been used in the literature. The correlation between the observed and the modeled air temperatures is also calculated.

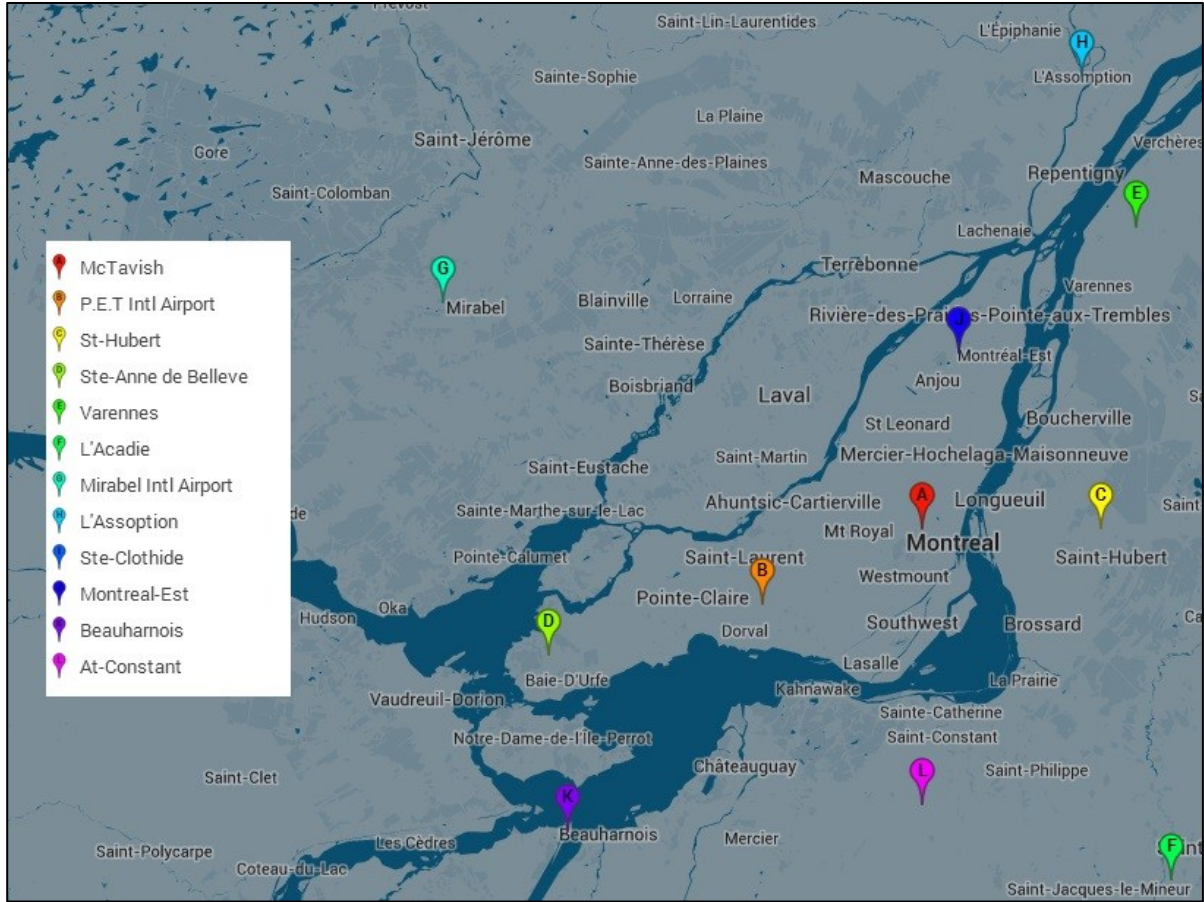
4.2. Results of simulations for Montreal and Toronto

The method described in Section 4.1 is used to select the appropriate urban canopy model (UCM) in Weather Research and Forecasting (WRF) software. The 2-m air temperature and 10-m wind speed of simulations using the three UCMs is compared to the observational data. MBE, MAE, and RMSE are calculated for each weather station for the whole simulation period. The correlation between the observational air temperature and simulated air temperature is calculated. The three UCMs are used to investigate temporal distribution and spatial pattern of UHI in selected cities. Then, temporal and spatial distribution of the difference of 2-m air temperature (ΔT_a) and skin temperature (ΔT_s) in ALBEDO and CTRL are analyzed to quantify the performance of increasing the albedo in the selected cities.

4.2.1. Air temperature

In the Greater Montreal the simulated 2-m air temperatures with all UCMs are well correlated with the observational data ($R^2 \approx 0.97$). As shown in Table 4-1, the MBE, MAE and RMSE of the UCMs are the same, equal to 0.2 °C, 1 °C, and 1.3 °C, respectively. In the urban area, the correlation of 2-m air temperature is the same (a negligible increase of about 0.01). Additionally, other statistical criteria (MBE, MAE and RMSE) are improved by 0.2 °C when using ML-UCM, in the urban area. The UCMs have a tendency to overestimate the air temperature in the simulation domain and the overestimation is magnified in the urban areas.

a)



b)

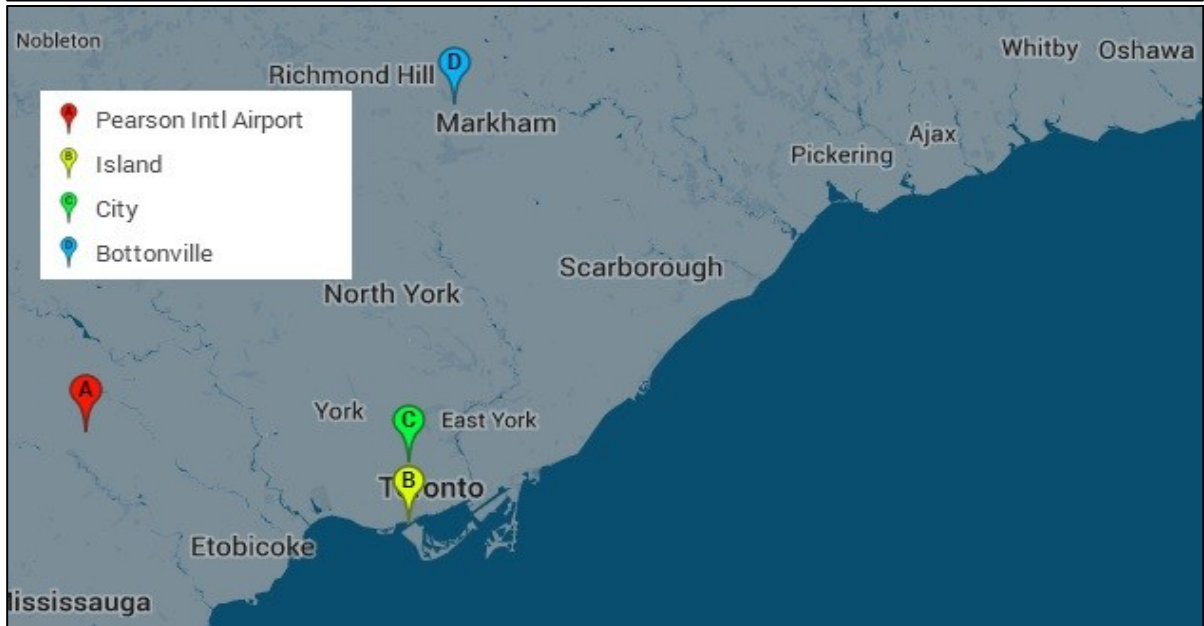


Figure 4-3. Location of weather stations in (a) Greater Montreal and (b) Greater Toronto (<http://maps.google.ca>)

Table 4-1. Correlation (R^2) of 2-m air temperature, MBE, MAE, and RMSE of observed and modeled 2-m air temperature in Montreal

Montreal Station name	R^2			MBE (°C)			MAE (°C)			RMSE (°C)		
	ML	SL	Slab	ML	SL	Slab	ML	SL	Slab	ML	SL	Slab
McTavish*	0.98	0.97	0.98	1.1	1.3	1.3	1.1	1.3	1.3	1.3	1.5	1.5
P. E. T. INTL Airport	0.98	0.99	0.99	-0.9	-0.7	-0.8	0.9	0.7	0.7	1.2	0.9	1.0
St-Hubert	0.98	0.97	0.97	0.5	0.5	0.5	0.8	0.8	0.8	1.2	1.2	1.2
Ste Anne De Bellevue	0.96	0.96	0.96	0.8	0.7	0.8	0.9	0.9	1.0	1.4	1.3	1.4
Varennes	0.98	0.98	0.98	1.0	0.9	0.9	1.1	1.1	1.0	1.5	1.5	1.4
L'Acadie	0.96	0.96	0.97	-0.4	-0.4	-0.5	1.2	1.1	1.0	1.5	1.4	1.2
Mirabel INTL Airport	0.98	0.98	0.98	-0.8	-1.1	-1.1	1.1	1.1	1.1	1.2	1.3	1.3
L'Assomption	0.97	0.97	0.97	-0.5	-0.6	-0.6	1.2	1.1	1.1	1.3	1.3	1.3
STE-CLOTHIDE	0.93	0.95	0.95	1.1	0.6	1.0	1.5	1.5	1.4	2.2	1.8	2.0
Montreal-Est	0.96	0.97	0.97	-0.4	-0.4	-0.4	0.7	0.7	0.7	1.1	1.0	1.1
Beauharnois	0.95	0.93	0.93	0.2	0.2	0.1	0.9	1.0	1.0	1.0	1.1	1.1
St-Constant	0.94	0.95	0.95	1.2	1.1	1.1	1.2	1.2	1.1	1.7	1.5	1.5
Average	0.96	0.97	0.97	0.2	0.2	0.2	1.0	1.0	1.0	1.4	1.3	1.3

*The weather station in the urban area

In Toronto, the correlation (R^2) between simulated and observed 2-m air temperatures is about 0.93 for all UCMs (Table 4-2). The MAE of using ML-UCM, SL_UCM, and slab model are 0.9 °C, 1.7 °C, and 1.5 °C, respectively. Similarly, RMSE of the ML-UCM (1.5 °C) is lower than that of other UCMs. In the urban area SL-UCM estimates the air temperature more accurately, with a MAE of about 1 °C.

Table 4-2. Correlation (R^2) of 2-m air temperature, MBE, MAE, and RMSE of observed and modeled 2-m air temperature in Toronto

Toronto Station name	R^2			MBE (°C)			MAE (°C)			RMSE (°C)		
	ML	SL	Slab	ML	SL	Slab	ML	SL	Slab	ML	SL	Slab
City*	0.93	0.93	0.93	-1.4	-0.6	-0.7	1.7	1.0	1.1	2.0	1.3	1.4
Pearson INTL Airport	0.94	0.92	0.93	-2.5	-2.6	-2.6	2.6	2.6	2.6	3.2	3.2	3.2
Island	0.97	0.94	0.96	-0.5	0.5	-0.0	1.4	0.9	1.0	1.7	1.1	1.3
Buttonville	0.97	0.92	0.95	-1.1	-1.1	-0.1	0.1	1.2	1.5	1.2	1.6	1.7
Average	0.95	0.93	0.94	-1.4	-1.4	-0.7	0.9	1.7	1.5	1.5	2.1	1.8

*The weather station in the urban area

Figure 4-4 illustrates the 2-m air temperature variation in the weather station located in the urban area and the simulated 2-m air temperature using three UCMs. In Montreal, the maximum difference occurred at the sunrise and sunset. The difference between the simulated and measured air temperatures is positive during the day. In Toronto, except for a few hours in the evening, the UCMs have a tendency to underestimate the air temperature. There are two peaks between the difference of observed and simulated air temperature (5 °C and 3 °C) by using ML-UCM in early morning and late night. The large differences occur when there is a sharp change in the observed hourly temperature. The 2-m temperature of SL-UCM and slab model has almost the same pattern.

The anthropogenic heat emission added to the SL-UCM resulted in a better estimation of the 2-m air temperature. However, as Salamanca et al. (2011, 2012) stated, adding other sophisticated models such as the building energy model will potentially improve the predicted UHI intensity by ML-UCM.

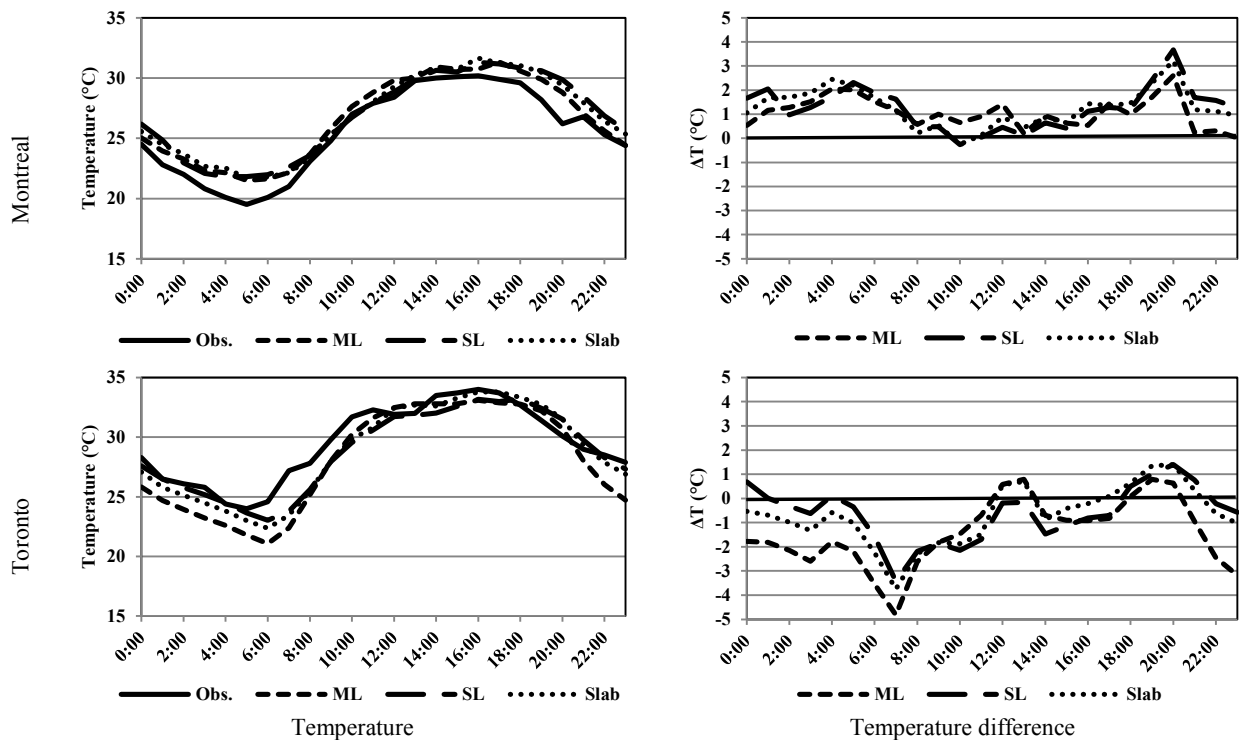


Figure 4-4. Hourly observed and simulated 2-m air temperature (°C) [left] and the difference between modeled and observed temperatures [right] in the urban areas of Montreal [top] and Toronto [bottom] in 12-July-2005 observed data and results of simulations using the three UCMs. Obs., ML, SL, and slab denote observation, ML-UCM, SL-UCM, and the slab model, respectively.

4.2.2. Wind speed

All UCMs underestimate the 10-m wind speed (averaged in the entire domain) in the Greater Montreal area (Table 4-3). In the urban area (areas colored black in Figure 4-2) ML-UCM underestimates and other UCMs overestimate the wind velocity. ML-UCM has the largest MAE and RMSE in the domain and the smallest MAE and RMSE in the urban area, respectively. The average MAE and RMSE of UCMs in the domain is almost the same but these criteria are significantly improved in urban areas by using ML-UCM. The correlation between wind speed of different UCMs and measured data was poor.

Table 4-3. MBE, MAE, and RMSE of observed and modeled 10-m wind speed in Montreal

Montreal Station name	MBE (m/s)			MAE (m/s)			RMSE (m/s)		
	ML	SL	Slab	ML	SL	Slab	ML	SL	Slab
McTavish*	-1.5	1.8	2.2	2.4	3.8	4.6	3.4	4.3	5.1
P. E. T. INTL Airport	-4.5	-3.3	-3.6	5.9	5.2	5.2	6.8	6.0	6.0
St-Hubert	-1.1	-0.7	-0.8	3.6	3.3	3.6	4.6	4.1	4.2
Ste Anne De Bellevue	-2.6	-0.5	-0.7	4.1	2.8	2.9	4.8	3.3	3.4
Varennes	0.2	0.9	0.5	3.7	3.9	4.3	4.7	4.6	5.0
L'Acadie	-0.2	0.1	0.1	3.4	2.7	2.9	4.2	3.1	3.4
Mirabel INTL Airport	-1.4	0.0	-0.7	4.6	4.2	4.0	5.8	5.4	5.5
L'Assomption	-1.5	-0.8	-0.6	4.4	3.7	3.6	4.8	4.2	3.9
STE-CLOTHIDE	0.4	1.5	1.0	3.7	3.6	3.3	4.1	4.3	4.0
Montreal-Est	-0.1	-0.7	-0.2	3.3	3.3	2.7	4.1	3.9	3.0
Beauharnois	-3.5	-3.6	-3.3	4.1	4.5	4.3	5.1	5.3	5.1
St-Constant	-0.9	0.0	-0.2	3.5	3.3	3.0	4.3	4.1	3.8
Average	-1.4	-0.4	-0.5	3.9	3.7	3.7	4.7	4.4	4.4

*The weather station in the urban area

In Toronto, the wind speed in the urban area was not recorded, so, I cannot comment on the performance of UCMs in reproducing the wind field on the selected cloudy day. Table 4-4 shows the result of simulations for other stations in the region where the three UCMs overestimate the wind velocity. ML-UCM improved the accuracy of the model by reducing the MAE and RMSE of the summer day.

Table 4-4. MBE, MAE, and RMSE of observed and modeled 10-m wind speed in Toronto

Toronto		MBE (m/s)			MAE (m/s)			RMSE (m/s)		
Station name		ML	SL	Slab	ML	SL	Slab	ML	SL	Slab
Pearson INTL Airport		3.8	4.2	4.0	4.7	4.7	4.4	5.6	5.5	5.2
Island		-1.6	2.4	3.0	3.2	3.9	4.4	3.7	4.8	5.3
Buttonville		-1.0	4.5	4.8	3.0	5.6	5.8	3.5	6.7	7.3
Average		0.4	3.7	3.9	3.6	4.7	4.9	4.2	5.7	5.9

*The weather station in the urban area

4.2.3. Temporal UHI

The difference between 2-m air temperatures in an urban area and its surroundings is considered as UHI intensity. Figure 4-5 illustrates the 2-m air temperature in the urban and rural areas of both cities during the simulation day. The observational data are from weather stations in urban areas (McTavish [Montreal] and City [Toronto]) and selected weather stations in rural areas (St-Hubert [Montreal] and Pearson Intl. Airport [Toronto]). In Montreal, observation shows that the nocturnal UHI is intensive, starting in the evening. Slab and SL-UCM have a better estimation of UHI intensity compared to the ML-UCM, which underestimates the UHI intensity. However, in Toronto, the ML-UCM gives a more accurate prediction of UHI, while other UCMs overestimate it during the nighttime.

The UHI intensity of Toronto in cloudy weather (solar irradiance is smaller than a clear day in some hours) is well predicted by the ML-UCM without considering the anthropogenic heat emission. On the other hand, in Montreal where the sky is clear on the simulated day, ML-UCM underestimates the UHI intensity during the night. Adding heat emission from buildings increases the air temperature of the urban areas (as investigated by Salamanca et al., 2011) mainly during the night (anthropogenic heat emission is much smaller than the solar radiation during the day), resulting in a better estimation of nocturnal UHI intensity in Montreal.

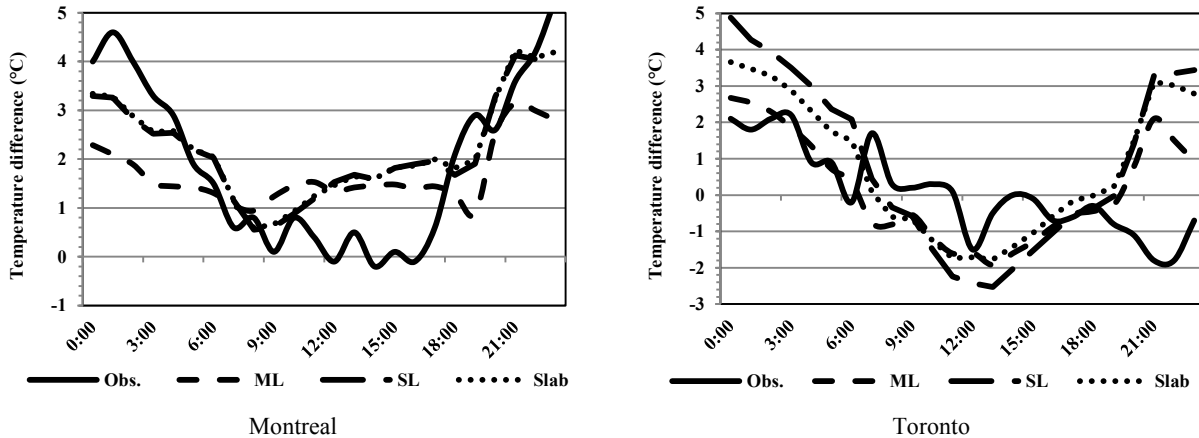


Figure 4-5. Temporal variation of 2-m air temperature (°C) difference between urban area and rural area of Greater Montreal [left] and Greater Toronto [right] in 12-July-2005 using three UCMs. Obs., ML, SL, and slab denote observation, ML-UCM, SL-UCM, and the slab model, respectively.

4.2.4. Spatial UHI

Historically, atmospheric UHI intensity is defined as the difference between the air temperature of urban areas and their surroundings. In some research an index based on skin temperature is considered as the indicator of UHI intensity (Jin, 2012; Gupta, 2012). In WRF, the air temperature is a function of skin temperature and sensible heat flux, calculated in land-surface model. In principle, the air temperature varies due to the change in skin temperature while it considers the effect of convection. On the other hand, the skin temperature is strongly depended only on the urban fabric.

Here, to show the spatial distribution of the skin and air temperatures, 24-hour, daytime, and nighttime averages are calculated. Figure 4-6 shows the air temperature averages (Montreal in the left column and Toronto in the right column). Peak air temperature occurred at the center of the urban area of Montreal in all time periods. There are also some hot spots in the southern and western parts of the domain caused by the type of land use there (forest) that can store latent heat. Lake Ontario has a significant effect on regulating the temperature of Toronto during the cloudy day, especially during the daytime. As shown in Figure 4-6, near the water body, even in the daytime, the temperature is lower than in the other regions. For both cities atmospheric UHI is magnified during the night.

Skin temperature of the cities well represented the urban boundaries (Figure 4-7). It can be concluded that skin temperature is mostly related to the urban fabric. Skin UHI is captured well in both cities, and again, in Toronto skin temperature near the lake is lower. In Montreal, the center of the urban area has the maximum skin temperature during all time periods.

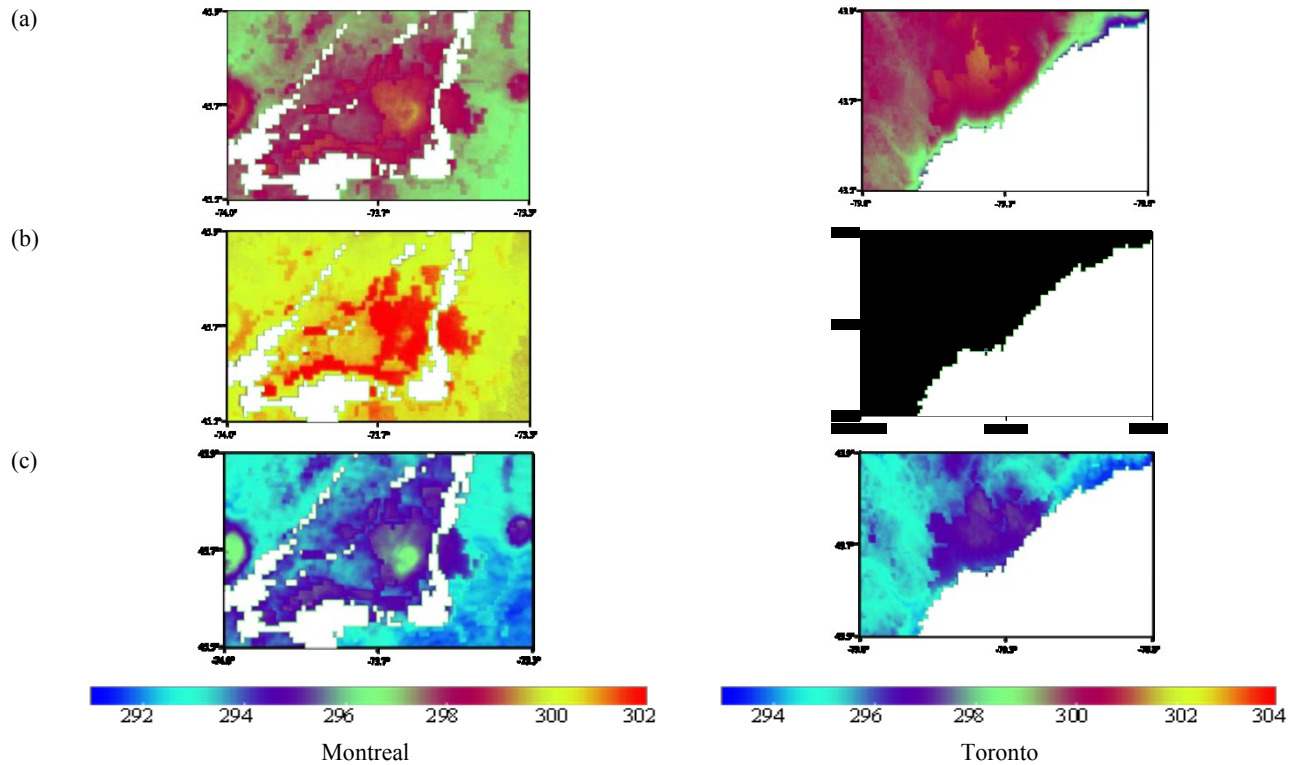


Figure 4-6. 24- hour (a), daytime (b), and nighttime (c) averaged 2-m air temperature (°C) of Greater Montreal and Toronto in 12-July-2005 [CTRL case] using Multi-Layer UCM [similar to (Touchaei et al., 2013)]

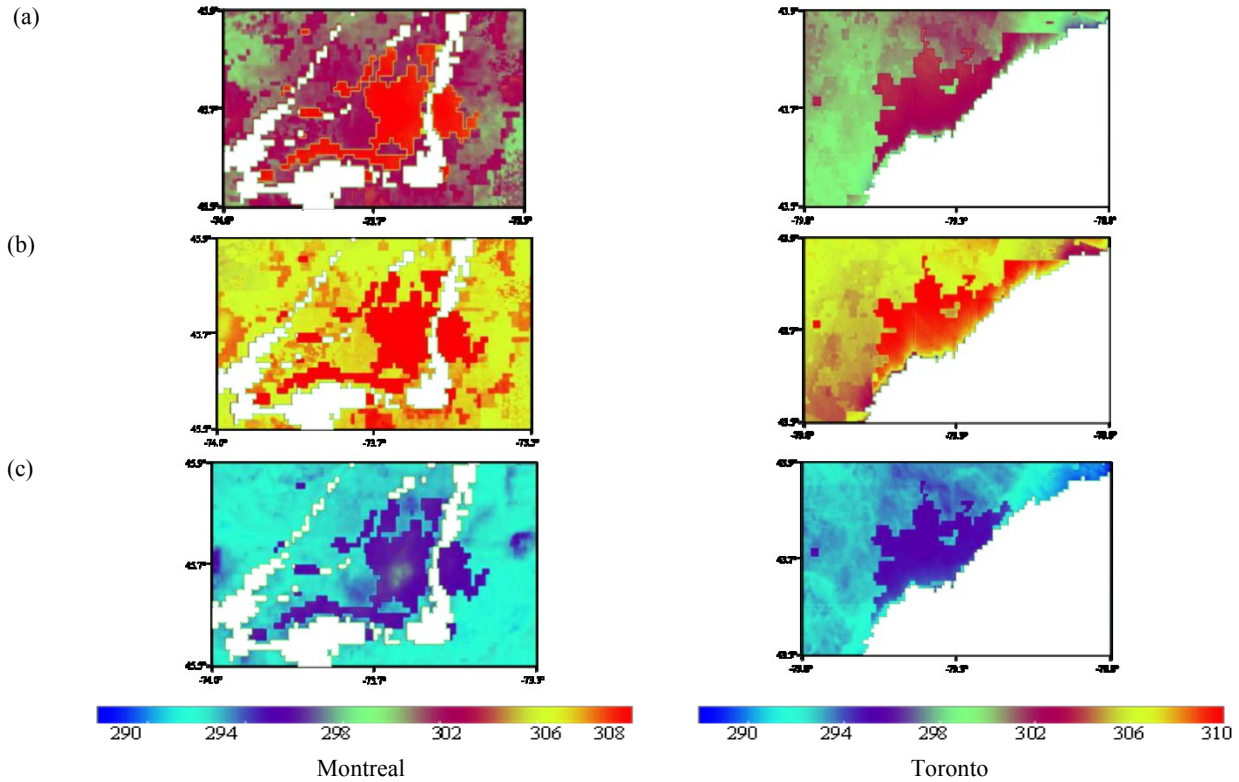


Figure 4-7. 24- hour (a), daytime (b), and nighttime (c) averaged skin temperature ($^{\circ}\text{C}$) of Greater Montreal and Toronto in 12-July-2005 [CTRL case] using Multi-Layer UCM [similar to (Touchaei et al., 2013)]

4.2.5. Effect of increasing the roof albedo

To determine the heat island reduction of urban areas the air temperature difference (ΔT_a) and skin temperature difference (ΔT_s) are calculated. Spatial average of air temperature difference (CTRL-ALBEDO) and skin temperature difference (CTRL-ALBEDO) of Montreal and Toronto on 12-July-2005 LST are shown in Figure 4-8 and Figure 4-9, respectively. Comparison of observed and simulated temperatures in sections 4.2.1 and 4.2.3 indicate that ML-UCM has the smallest MAE; hence, the temporal distribution of temperature from the slab model and SL-UCM is compared to results by using ML-UCM. In both cities, the daytime ΔT_a is well predicted by the slab model compared to ML-UCM. The air temperature difference of SL-UCM is close to the air temperature difference of ML-UCM during the nighttime.

In Montreal, the air temperature difference (ΔT_a) is negligible at the beginning of the day (Figure 4-8). ΔT_a is increased to 1°C (maximum difference) in the morning at 0800 LST. At sunset ΔT_a of CTRL and ALBEDO is about 0°C and after that the air temperature difference

risers about 0.2 °C. The skin temperature difference (ΔT_s) between the two considered scenarios is also negligible after the midnight and it starts to increase at about 0400 LST. The maximum value of ΔT_s is about 5 °C from 0700 LST to 1100 LST, where, ΔT_s gradually starts decreasing. The slab model has a good estimation of ΔT_a during the daytime, and SL-UCM is appropriate for capturing the nocturnal effect of increasing albedo. During the whole day SL-UCM predicts ΔT_s better than the slab model.

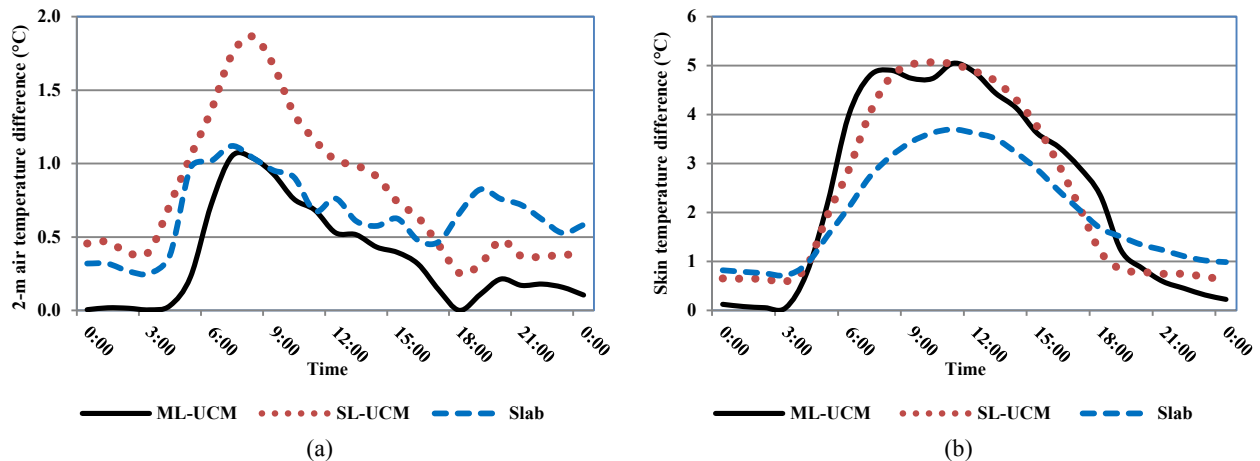


Figure 4-8. Hourly variation of (a) 2-m air temperature difference and (b) skin temperature difference between CTRL case and ALBEDO case in Montreal using different UCMs

The variation of air and skin temperature differences in Toronto during 12 July 2005 (Figure 4-9) is qualitatively similar to the case of Montreal. Nocturnal ΔT_a is small and the maximum ΔT_a is about 1 °C in the morning. Skin temperature difference starts from sunrise and the maximum ΔT_s is 5 °C.

The 24-hour, daytime, and nighttime averaged values of ΔT_a and ΔT_s for Montreal and Toronto using different UCMs are summarized in Table 4-5. Increasing the roof albedo in Montreal and Toronto decreases the air temperature by a daily averaged value of about 0.4 °C and 0.5 °C, respectively. In Montreal and Toronto, ΔT_s is about 2.4 °C and 2.2 °C, respectively. During the day, results of the slab model are close to the variation of ΔT_a predicted by ML-UCM, for both cities. Although ΔT_a is not well estimated by SL-UCM and the slab model during the night, the averaged values of SL-UCM is closer to the results of ML-UCM.

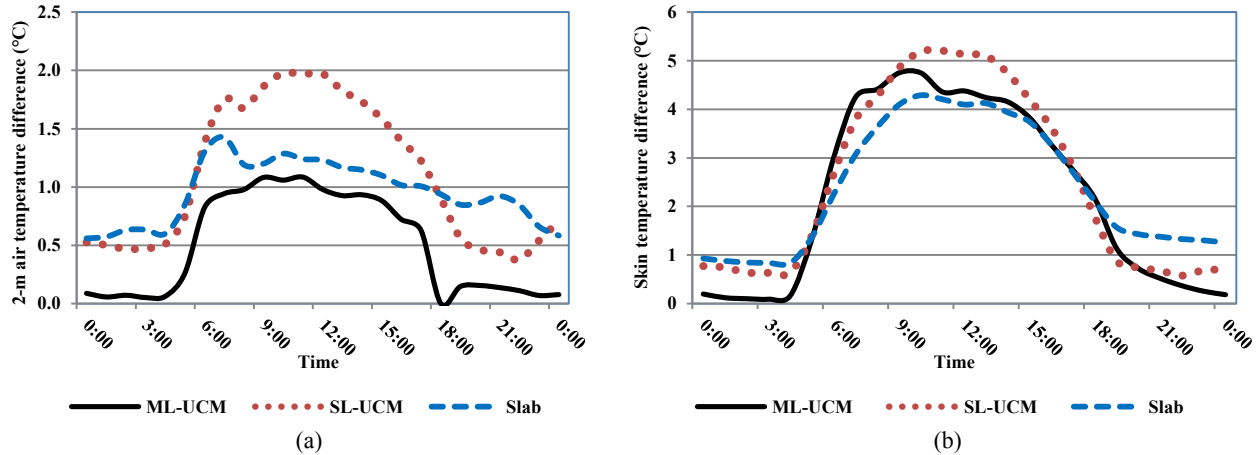


Figure 4-9. Hourly variation of (a) 2-m air temperature difference and (b) skin temperature difference between CTRL and ALBEDO in Toronto using different UCMs

In Toronto the maximum mitigation of UHI occurred at midday (the peak incoming shortwave radiation reaching the ground). However, in Montreal, ΔT_a had its maximum value during the morning and the difference decreased during the simulation day. The main reason for closer air temperature in CTRL and ALBEDO in Montreal is an increase in wind speed and cloud cover. The incoming solar irradiance is inversely proportional to the cloud cover, and as discussed in (Krayenhoff et al., 2010), the effect of convection on the air temperature is notable.

Table 4-5. 24-hour averaged, daytime averaged, and night-time averaged 2-m air temperature and skin temperature calculated for Montreal and Toronto by coupling ML-UCM, SL-UCM, and slab model to the mesoscale model

	Montreal						Toronto					
	2-m air temperature (°C)			skin temperature (°C)			2-m air temperature (°C)			skin temperature (°C)		
	ML-UCM	SL-UCM	slab	ML-UCM	SL-UCM	slab	ML-UCM	SL-UCM	slab	ML-UCM	SL-UCM	slab
24- hour averaged	0.4	0.8	0.7	2.4	2.4	2.0	0.5	1.1	1.0	2.2	2.5	2.4
Daytime averaged	0.5	1.0	0.8	3.8	3.6	2.8	0.8	1.5	1.1	3.5	3.7	3.2
Night-time averaged	0.1	0.5	0.5	0.4	0.7	1.0	0.1	0.5	0.7	0.3	0.7	1.1

4.2.6. Spatial distribution of temperature difference from the albedo increase

Mean daily temperature (2-m air temperature and skin temperature) differences between the CTRL case and the ALBEDO case for Montreal and Toronto are illustrated in Figure 4-10 and Figure 4-11, respectively. Increasing the roof albedo by 0.6 decreases air and skin temperatures of both cities using all different types of UCM. In both cities, the minimum air temperature difference is predicted by ML-UCM and the maximum air temperature difference is estimated by

SL-UCM. The decrease in 2-m air temperature (ΔT_a) of the urban areas results in a decrease in ΔT_a of their surroundings due to advection. The skin temperature difference is directly correlated to the urban fabric. The variation of skin temperature (ΔT_s) according to the increase of albedo is more than that of the air temperature. In Montreal, ΔT_s of the urban area is similar when using SL-UCM and ML-UCM, whereas the slab model results in a lower ΔT_s . The maximum daily averaged ΔT_a in the domain is as high as 0.5 °C, 1.2 °C, and 0.9 °C using ML-UCM, SL-UCM, and slab model, respectively.

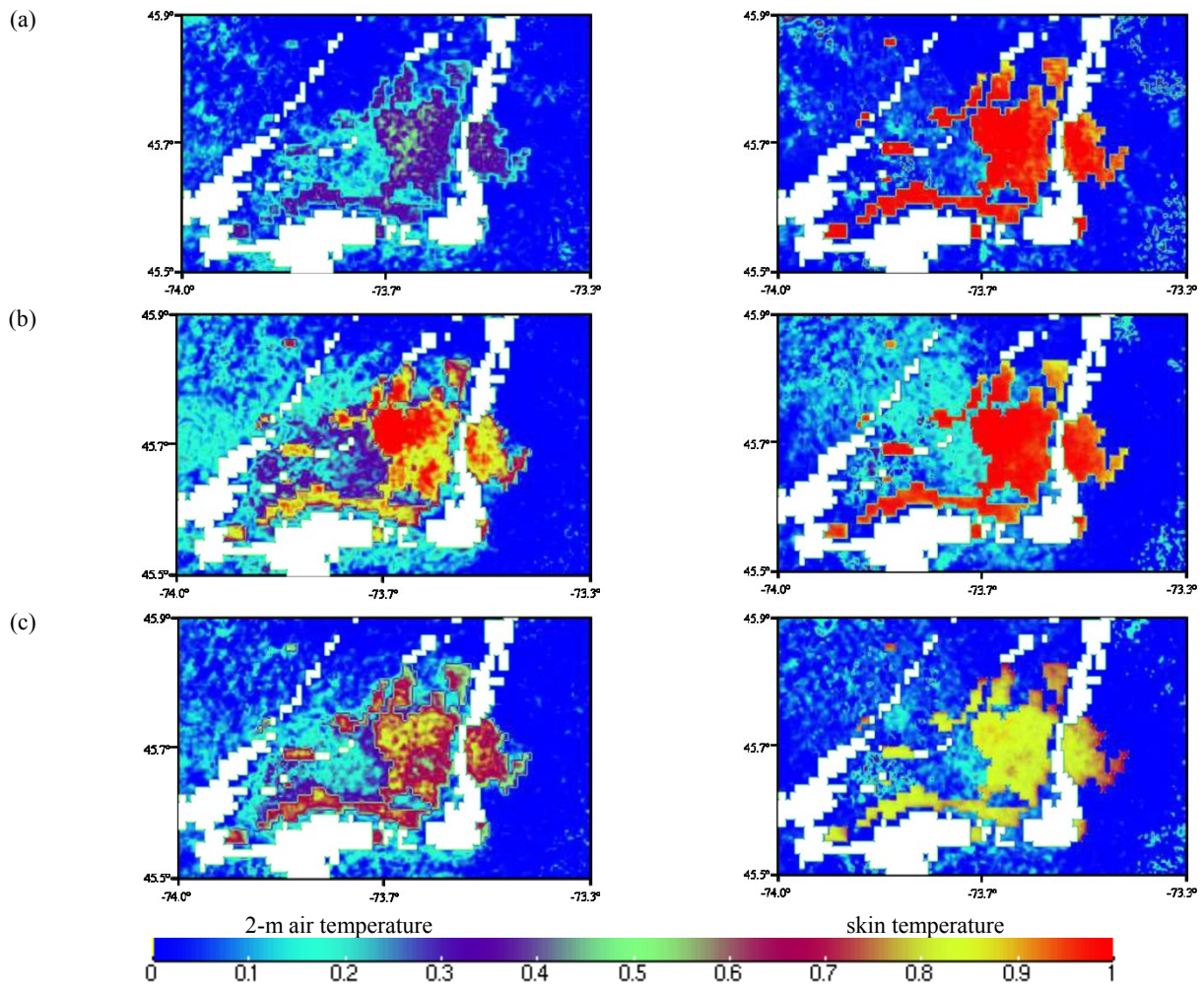


Figure 4-10. Mean daily 2-m air temperature (°C) and mean skin temperature (°C) difference between CTRL and ALBEDO of Greater Montreal on 12-July-2005. (a) Multi-layer UCM, (b) Single-layer UCM, and (c) slab model.

(White regions are water bodies)

In Toronto, ΔT_s of the urban area is the lowest when using ML-UCM, whereas the SL-UCM resulted in the highest ΔT_s . ML-UCM, SL-UCM, and the slab model predicted the mean daily ΔT_a with the highest value of 0.7, 1.4, and 1.2 °C, respectively.

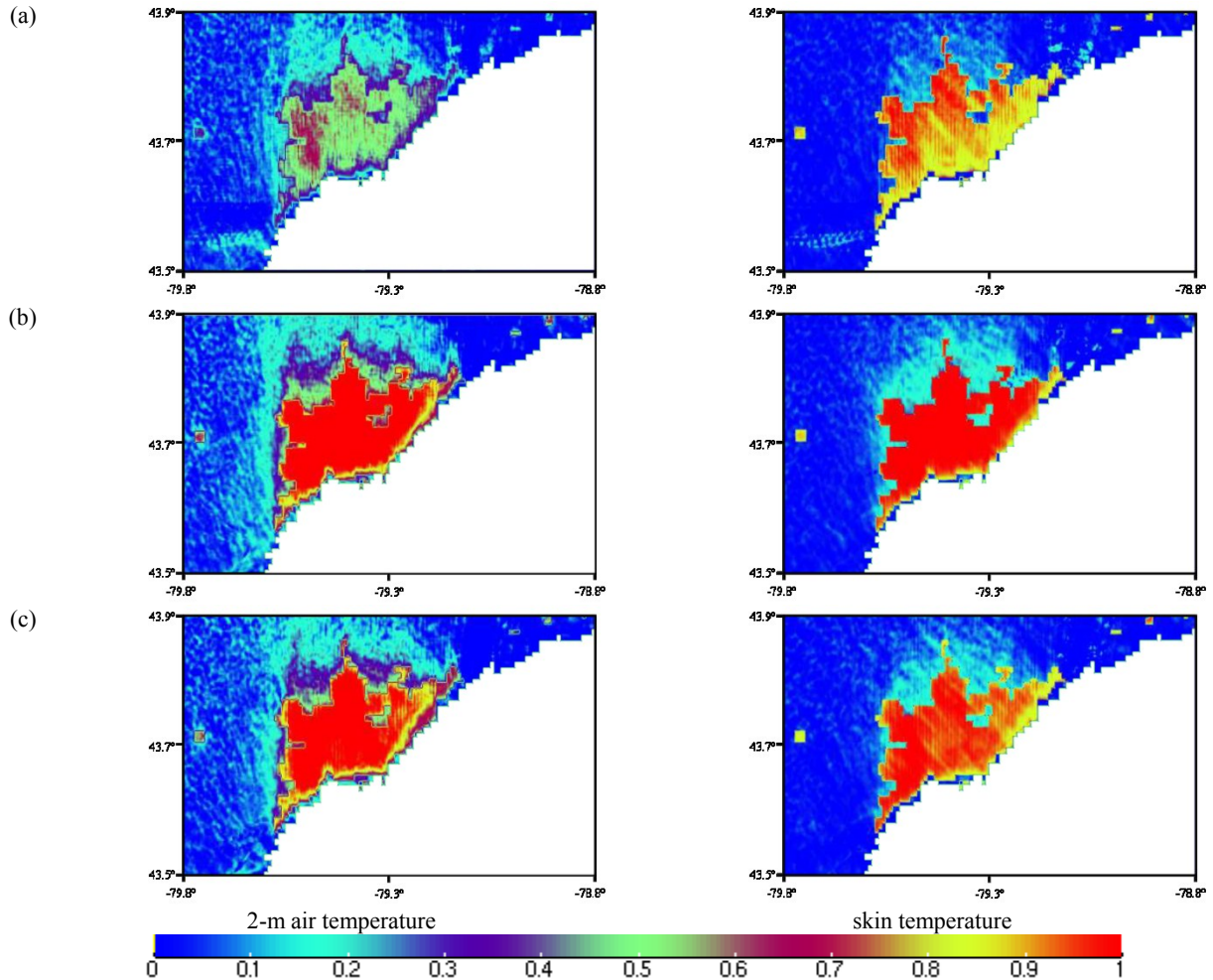


Figure 4-11. Mean daily 2-m air temperature (°C) and mean skin temperature (°C) difference between CTRL and ALBEDO of Greater Toronto on 12-July-2005. (a) Multi-layer UCM, (b) Single-layer UCM, and (c) slab model.

(White regions are water bodies)

4.2.7. Clear day of Toronto

The selected day was a cloudy day in Toronto and the effect of albedo enhancement on air temperature might be different in a clear day. Therefore, we simulate 15 July, which had a clear sky but with a maximum temperature 5 °C less than on 12 July. In addition, the average wind speed during 15 July was greater than on 12 July, which potentially decreases the temperature difference between CTRL and ALBEDO. The 2-m air temperature difference between the urban and rural areas is as high as 2.8 °C, 2.2 °C, and 1.2 °C using slab, SL-UCM, and ML-UCM at 3

p.m., respectively (Figure 4-12). Increasing the roof albedo from 0.2 to 0.8 decreases the 2-m air temperature by a maximum of 0.8 °C, 1.0 °C, and 0.4 °C using slab, SL-UCM, and ML-UCM. (Figure 4-13). ML-UCM well estimated the nocturnal effect of albedo enhancement on air temperature and skin temperature, in agreement with Li et al. (2014). On the other hand, slab and SL-UCM overestimated the air and skin temperature differences during the night.

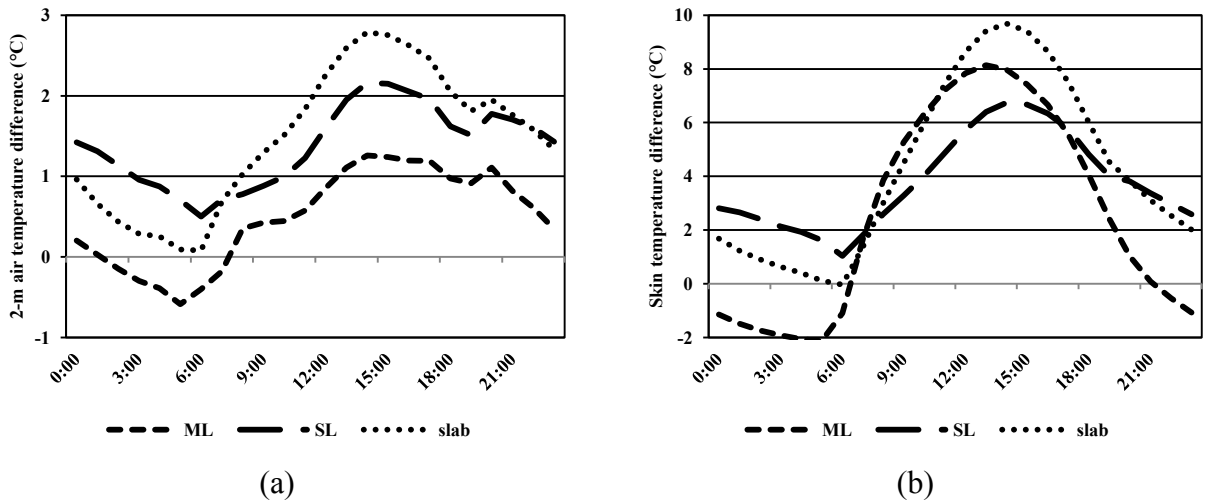


Figure 4-12. hourly variation of (a) 2-m air temperature difference and (b) skin temperature difference between urban area and rural area on 15-July-2005 in Toronto using different UCMs. ML, SL, and slab denote ML-UCM, SL-UCM, and the slab model, respectively.

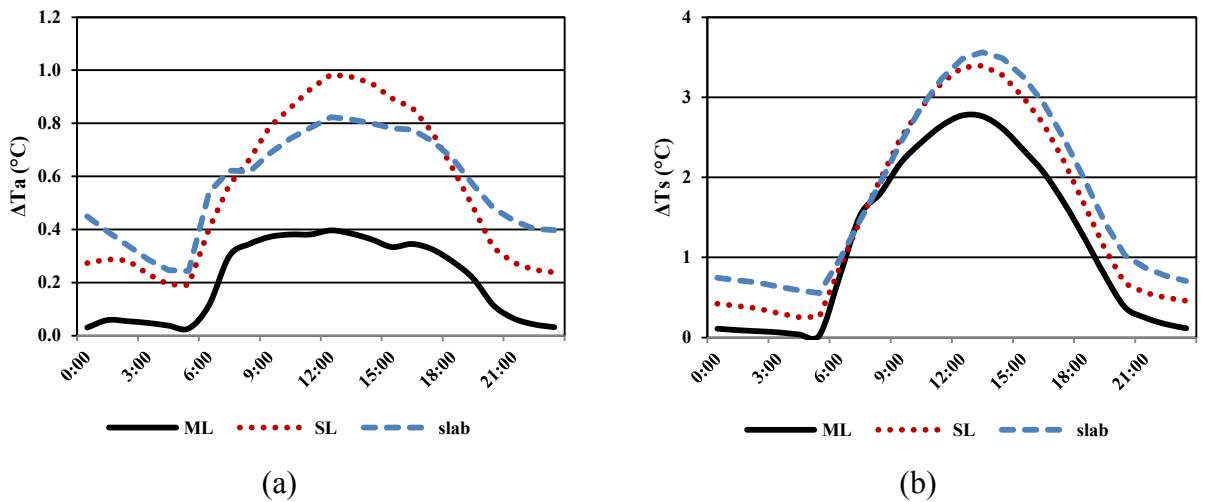


Figure 4-13. hourly variation of (a) 2-m air temperature difference and (b) skin temperature difference between CTRL and ALBEDO on 15-July-2005 in Toronto using different UCMs. ML, SL, and slab denote, ML-UCM, SL-UCM, and the slab model, respectively.

4.3. Discussion

4.3.1. Characterization of UHI

The daily averaged difference between the skin temperature calculated by ML-UCM and SL-UCM (or the slab model) is less than 1 °C (Figure 4-14). Moreover, the 2-m air temperature, which is estimated based on the skin temperature and the heat flux from the urban areas, is changed within the range of the change in the skin temperature (less than 1 °C). The air and skin temperatures of the Greater Toronto area predicted by ML-UCM are lower than SL-UCM and the slab model with a maximum of about 1 °C (Figure 4-15). Since the difference between ML-UCM and the other UCMs falls into the order of their accuracy (based on MAE presented in Table 4-1 and Table 4-2), either of the models can be used for urban climate simulation of the domain. However, based on the results presented in Section 4.2, ML-UCM can increase the accuracy of calculating air temperature and UHI intensity. Consequently, an evaluation of surface modification strategies requires more sophisticated models (i.e., ML-UCM) to consider the effect of turbulence on vertical flux of momentum, heat, and moisture.

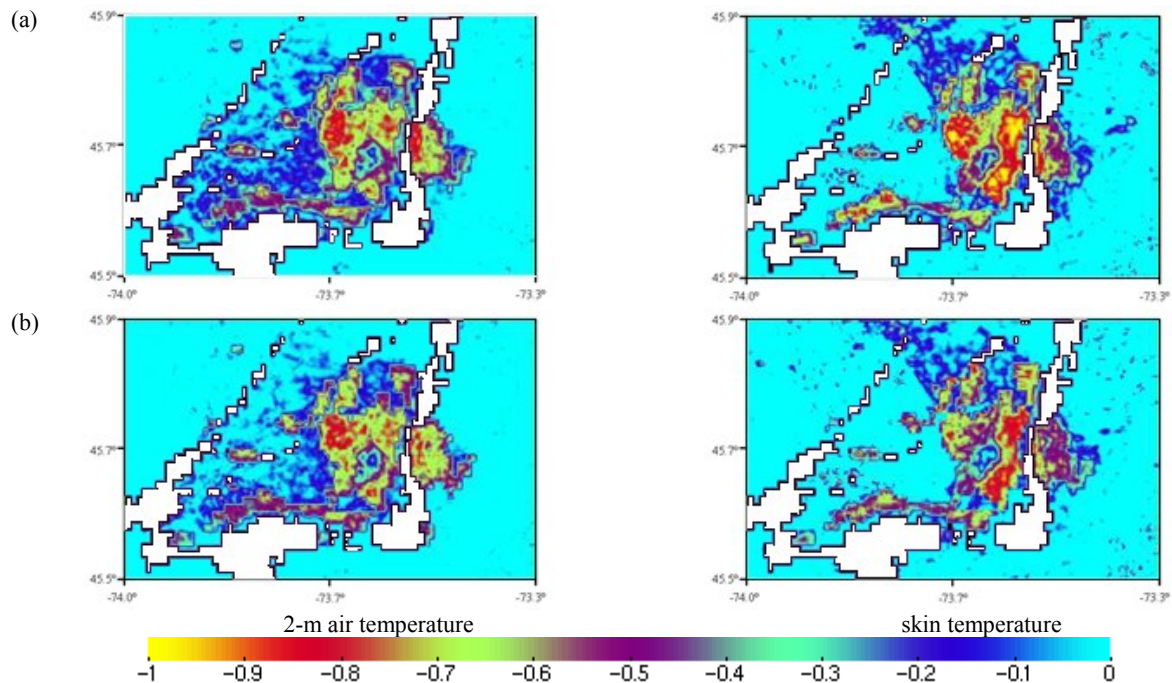


Figure 4-14. 2-m air temperature and skin temperature difference (°C) between (a) Multi-layer UCM and Single-layer UCM, and (b) Multi-layer UCM and slab model of Greater Montreal in 12-July-2005. White color represents water bodies.

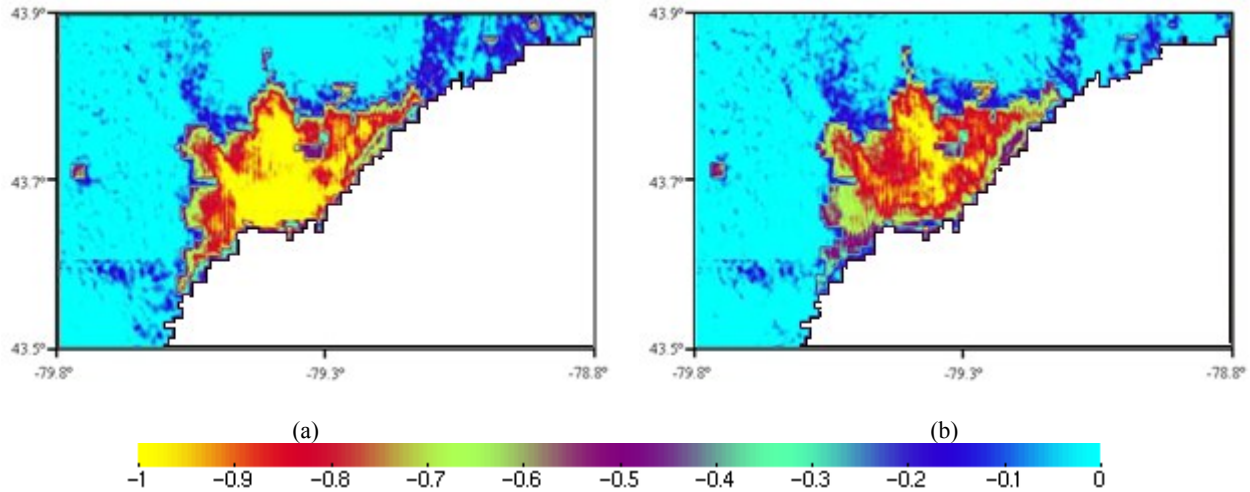


Figure 4-15. 2-m air temperature difference (°C) between (a) Multi-layer UCM and Single-layer UCM, and (b) Multi-layer UCM and slab model of Greater Toronto in 12-July-2005. White color represents water bodies

The difference between ML-UCM and other UCMs is calculated from the predicted skin temperature and the predicted sensible heat flux from urban areas. Both the slab model and SL-UCM underestimate the heat flux from the urban area (Figure 4-16). Hence, in some parts of Montreal (e.g., the western part) the difference between air temperature in ML-UCM and the slab model is more than the difference in the skin temperature. The slab model and SL-UCM are not as capable as ML-UCM of accurately accounting for the heat flux of the canopy during the day, as they do not consider the turbulence.

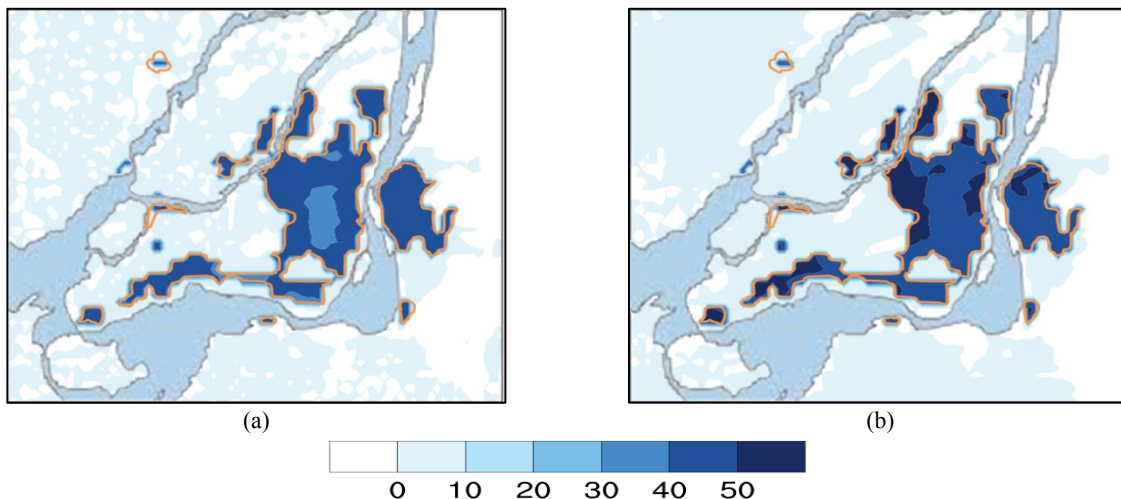


Figure 4-16. 24-hour averaged heat flux difference (W/m²) between (a) ML-UCM and slab model (ML-slab), and (b) ML-UCM and SL-UCM (ML-SL) of Greater Montreal in 12-July-2005. Light blue color represents water bodies.

Running the model for selected cities with ML-UCM increases the computation time 30–40% compared to the time needed for the slab model and SL-UCM. Therefore, if the climate prediction is the only purpose of the modelling, the slab model will have acceptable results in a shorter time for numerical calculations.

4.3.2. Effect of increasing the roof albedo

The ML-UCM predicts the lowest decrease in the air temperature because it considers the turbulence within the canopy. Therefore, the heat exchange from the canopy to the planetary boundary layer increases (Figure 4-16). Meanwhile, SL-UCM considers the sensible heat flux from the urban canopy only as a function of the horizontal wind. So, SL-UCM underestimates the vertical heat flux from urban areas, and consequently overestimates the temperature difference from increasing the albedo. The slab model and SL-UCM result in more temperature difference between CTRL and ALBEDO, since the vertical momentum and heat fluxes from the canopy are not considered.

Simulations are performed for a clear day of summer in Montreal with a low wind speed (~6 km/h at McTavish weather station) to investigate the ultimate performance of the reflective roofs in the region. In Toronto, during the cloudy (solar radiation is more diffused) and stable weather (wind speed of about 5 km/h at Island weather station), the albedo enhancement is not as effective as on a clear day in Montreal. The clear day in Toronto had a high wind speed (~22 km/h at Island weather station), which also reduced the expected change in the 2-m air temperature. Both Montreal and Toronto are located in cold climates and the magnitude of the effect of an increase in the urban albedo is deemed to be negligible (Oleson et al., 2010; Taha H., 1997). Current results confirm that the episodic effect of an increase in the roof albedo of cold urban areas during summer can be as significant as in other climates.

The UHI is an indication of the possible difference in the urban air temperature because of the change in the land use. However, the main intention of increasing the albedo is to decrease the air temperature only in urban areas, and mostly during the daytime. The albedo enhancement is an effective strategy when the solar radiation is available and the air temperature has a greater value (despite the chance of lower UHII). Additionally, the mitigation strategy is less effective during hours with lower air temperatures (despite having higher UHII).

4.3.3. Limitations

There are some limitations in simulating urban climate and investigating heat island using a fine-resolution approach. The main issue is to intensively analyze aerial images to characterize the urban morphology and also collect appropriate data to identify properties of building envelopes. In addition, the PBL options in WRF are not able to resolve sub-km processes (i.e., small eddy generation) by using fine-resolution grids that affect calculation of the UHI intensity. Additionally, comparison of single point data measured at weather station with the area-averaged output of simulations is another source of inaccuracy (Tartaglione et al., 2005).

4.3.3.1. *Microphysics and PBL parameterizations*

The cloud formation process has been a critical issue for scientists to effectively utilize numerical weather prediction (NWP) models (Brooks et al., 1991; Rajeevan et al., 2010; Zhang et al., 2013). The calculated solar radiation striking the surface is highly dependent on the predicted cloud cover, which is highly affected by the deficiency of current microphysics schemes (Cullather et al., 1997). The temperature of the surface and heat transferred to the air from the surface is directly related to the solar radiation striking the ground. Therefore, prediction of temperature fluctuations (temporal and spatial) is coherent with the treatment of hydrometeors (Liu et al., 2003). In addition, PBL parameterizations can profoundly affect cloud formation processes considered in microphysics models (Xie et al., 2012). A comparison of different PBL and microphysics parameterizations in WRF with field measurements and satellite observations revealed large uncertainties of current NWP models (Cintineo et al., 2014). As a result, poor treatment of hydrometeors and PBL is an influential factor in simulations. The fine-resolution approach was chosen to evaluate the preliminary result of coupling UCMs and WRF. Using a fine-resolution approach without the nesting option of WRF has some negative effects on cumulus modeling. Cumulus models need a large horizontal grid size to predict the convection of clouds; introducing errors for the grid size selected in this study on the order of the neighborhood (333×333 m).

4.3.3.2. *Urban morphology and building characteristics*

Fine-resolution grid size in NWP models helps the policymakers to give priority to different neighborhoods for implementing mitigation strategies. However, the fine-resolution approach is challenging because of some shortcomings in controlling factors (Arnold et al., 2012). Among

them, (1) the deficiency of PBL parameterization to resolve horizontal diffusion, and (2) limited resources for high resolution land datasets, are most important issues.

Fine-resolution grids in NWP models are not well designed for areas with complex terrain (Holden et al., 2011) where the PBL scheme plays an important role in predicting the air temperature (Raby et al., 2012). WRF has shown a better performance in predicting meteorological parameters compared to Mesoscale Model V5 (MM5—a well-accepted model by the scientific community) in complex terrains using the fine-resolution approach (Horvath et al., 2012). However, WRF has still some stability issues for fine-resolution grids and it produces some roll-type temperature patterns (known as Smagorinsky waves). Three solutions have been proposed to maintain the stability of WRF in a domain with sub-km grids: (1) to decrease the time steps (Bornstein et al., 2012), (2) to use a constant horizontal diffusion of 300 m²/s (Salamanca et al., 2012), and (3) using a 6-order horizontal diffusion scheme (Xue, 2000).

The time increment of the ARW solver to maintain stability is 6 times more than the horizontal grid spacing (6dx) of the domain. However, for very small grid size, the factor should be decreased to $\frac{1}{9}dx$ to control the stability of the model. To decrease the computation time, we used the time increment of $\frac{1}{2}dx$, and the Smagorinsky waves (Bornstein et al., 2012) are observed for a few hours of the day. We applied a simple averaging filter to remove the effect of virtual heatwaves.

WRF has the capability of considering three urban classes to improve calculations in SL-UCM and ML-UCM (Salamanca et al., 2011). A detailed map of a region of interest is needed to categorize urban classes (ARW user guide, 2012). Such a detailed map of U.S. cities is available to the public through the NUDAPT dataset (Ching et al., 2009). In Canada, some reports (Leroyer et al., 2011, 2014) used detailed maps but those datasets are not accessible to us. Hence, we use the classical USGS 24-class dataset that considers only one urban category.

4.3.3.3. Selecting the weather stations

For evaluation of UCMs, extensive weather data in different regions of a city is needed and there are specific protocols for that purpose (WMO, 2008; Stewart, 2011); here, without having extensive data inside urban areas, we use measured data from all weather stations around the

cities. We are aware of the issue that experimental evaluation of UHI intensity requires a detailed specification of instruments in data reporting, but the current gathered data are limited to weather stations from the Environment Canada database (<http://climate.weather.gc.ca/>) which is the only publicly available data. There are some resources available for Montreal and Vancouver (www.epicc.ca) but they are not publicly available.

4.4. Conclusion on the choice of UCM and the effect of an increase in roof albedo

I compared three UCMs in the weather research and forecasting model (WRF) for urban climate simulation of Montreal and Toronto (Canada) in a summer episode (12-July-2005 LST) using the fine-resolution grid size (333×333 m). All three models (i.e., multi-layer, single-layer, and slab model) have the same performance in predicting the 2-m air temperature and 10-m wind speed of the selected cities. The accuracy of the UCMs differs in two cities and shows a strong dependence on the sky condition (clear vs. cloudy). The averaged air temperature of the model and observed air temperature in all weather stations are well correlated ($R^2 \sim 0.95$). The mean absolute error of 2-m air temperature in Montreal and Toronto was about 1 °C and 1.6 °C, respectively. Similarly, the mean absolute error of wind speed in Montreal and Toronto was in the range of 3.7–3.9 m/s and 3.6–4.9 m/s, respectively. In the clear sky, multi-layer UCM improved the air temperature calculations, while, in the cloudy sky, single-layer UCM predicted the air temperature more accurately. The urban heat island (UHI) in Toronto is well characterized by multi-layer UCM. On the other hand, in Montreal, all UCMs overestimate the UHI during the day and underestimate the nocturnal UHI, which is mainly because in current simulations variation of anthropogenic heat emission (e.g., heat emission from buildings) with air temperature is only considered in single-layer UCM. The intensity of the UHI in Montreal was stronger than Toronto (cloudy sky, located near the lake).. My analysis indicated that the slab model is reliable for the purpose of climate simulation; but for evaluation of UHI intensity and mitigation strategies, more sophisticated models, which account for the anthropogenic heat emission, turbulence, and multi reflection in the urban canopy, should be used.

The effect of increasing the albedo of roofs by 0.6 is also investigated. Air temperature (24-hour averaged) is decreased by the values of 0.4 °C and 0.5 °C in Montreal and Toronto, respectively. In Montreal and Toronto the maximum decrease of the air temperature is about 1 °C at 0800 LST

and 1100 LST, respectively. Results of multi-layer UCM are considered the most compatible ones with observational data, and the outcome of using single-layer and slab models are compared to them. According to the results of multi-layer UCM, slab and single-layer UCMs overestimate the difference in air and skin temperature of urban areas. Diurnal prediction of the change in air temperature using the slab model is acceptable. Skin temperature difference can be well calculated using single-layer UCM.

Chapter Five: Sensitivity Analysis of Physical Parameterizations in WRF

Microphysics, radiation, land-surface, and planetary boundary layer physical processes interact with the atmosphere; some of them can be chosen based on the requirements of urban climate modeling (inclusion of ML-UCM and BEM) and the fine-resolution approach. The rest of the physical processes are chosen based on the sensitivity analysis. These models should be customized based on the available options in the WRF solver. Additionally, some options are restricted by capability of coupling with UCMs (e.g., the choice of LSM). The main limitation of proposing an accurate approach is the number of implemented physical parameterizations within models. While there are many papers discussing the validation of WRF (e.g., Zhang et al., 2009 and Millstein and Menon, 2011), none of them discussed urban areas in cold climates. I use a variety of WRF options to find the sensitivity of air temperature and wind speed for the choice of the model ensemble.

A microphysics model determines the presence of water in different phases, in addition to water vapor, cloud, and precipitation processes. Options with a mixed phase process should be used to prevent resolving updrafts in small grid size domains. Moreover, options consisting of more than three variables are able to provide more details of physical processes. Convective or shallow cumulus affects vertical moisture and heat transfer in a grid, where, introduced microphysics models are not able to capture them. Sub-grid scale precipitation and cloud tendencies are also necessary for urban climate simulation, and it needs shallow cumulus parameterization (ARW user guide, 2012). A Land-Surface Model (LSM) provides information on heat and moisture fluxes on land points and sea ice by using atmospheric feedback of other schemes in a simulation (it can be considered as a boundary condition for the model; Skamarock et al., 2008). All LSM options in the ARW solver are multi-level models that provide the lower boundary for the Planetary Boundary Layer (PBL). LSM updates surface variables (e.g., the ground temperature, soil temperature profile, soil moisture profile, snow cover, and canopy properties) in each iteration step, as independent variables. Using UCM is essential for the urban climate simulation and, consequently, Unified Noah LSM should be used as the main LSM in WRF. Three types of UCMs are implemented in the solver and they should be selected using real case simulation. The rest of the physical processes are going to be selected by sensitivity analysis of the air temperature to their variation.

A selected model ensemble would account for the climate variability (both internally and externally induced). The radiation model calculate the variation in the incoming and outgoing radiations (shortwave and longwave). Other physical parameterizations estimate the internal interactions between climate components. Also, performing simulations for short episodes ensures the validity of the boundary conditions and initial condition. Consequently, the mpdel ensemble can be used to simulate the effect of a surface treatment (i.e. albedo modification in this case) without unrealistic contribution of natural variability.

5.1. Methodology of sensitivity analysis of model ensembles within WRF

I have selected 20 different model ensembles (S01-S20) to evaluate the performance of WRF in predicting 2-m air temperature (hereafter, air temperature) and 10-m wind speed (hereafter, wind speed) in Montreal (Table 5-1). Air temperature and wind speed in 10 weather stations (MCTAVISH, PIERRE ELLIOTT TRUDEAU INTL, ST-HUBERT, STE-ANNE-DE-BELLEVUE, VARENNES, L'ACADIE, MIRABEL, L'ASSOMPTION, and STE-CLOTHIDE; like weather stations in Figure 4-3) through the domain is compared with the output of simulations. Based on USGS land categorization MCTAVISH is located in the urban area. The selected simulation period is from 09-Aug-2009 through 11-Aug-2009, starting with a clear sky condition and ending with a heavy rain period. The summer days are selected because I am ultimately using the platform for evaluating the effect of increasing albedo, which is more effective in mitigating the urban heat island during summertime and clear sky conditions. The heavy rain period also evaluates the weakest part of the numerical weather prediction model to simulate clouds and different hydraulic processes.

The simulation platform is similar to the one presented in Section 4.1.1 and the same version of WRF is used. I used the same method as discussed in Section 4.1.3 for evaluation of the model ensembles. Unified Noah LSM coupled with ML-UCM is used to parameterize fluxes from the land-surface. The only difference is the size of domains and activation of two-way nesting to reduce the computation time. The coarse domain (Domain 1) is about 700 km × 700 km with the grid size of 10 km × 10 km. The first nest (Domain 2) is about 150 km × 150 km, with the grid size of about 3 km × 3 km, that has the urban domain (Domain 3) with grid size of about 600 m × 600 m. All options for all domains are the same, except the cumulus model that is not activated for Domain 3 and the ML-UCM that is only activated for Domain 3 (similar to Figure 7-1).

Mean Bias Error (MBE) is the indication of underestimation (negative value) or overestimation (positive value) of the predicted meteorological variable compared to the measured data. Mean Absolute Error (MAE) represents the absolute error in simulation, and it is known as a natural metric to evaluate the performance of a model (Walcott, 2005). Root Mean Square Error (RMSE) is a more rigorous indicator for model assessment which is used in all similar studies.

Table 5-1. Simulation set-ups with different options on parameterizations of microphysics, cumulus, PBL, and radiation

	Microphysics	Cumulus	PBL	Radiation
S01	WDM (16) ¹	Simplified Arakawa-Schubert (4) ²	MYJ (2) ³	RRTMG (4)
S02	WDM (16)	Betts-Miller-Janjic (2) ⁵	MYJ (2)	RRTMG (4)
S03	WDM (16)	Grell 3D (5) ⁶	BouLac PBL (8) ⁷	RRTMG (4)
S04	WDM (16)	Grell 3D (5)	MYJ (2)	Dudhia (1) ⁸
S05	Eta (5) ⁹	Grell 3D (5)	MYJ (2)	RRTMG (4)
S06	WDM (16)	Grell 3D (5)	MYJ (2)	RRTMG (4)
S07	WDM (16)	Grell-Freitas (3) ¹⁰	MYJ (2)	RRTMG (4)
S08	Goddard (7) ¹¹	Grell 3D (5)	MYJ (2)	RRTMG (4)
S09	WDM (16)	Kain-Fritsch (1) ¹²	MYJ (2)	RRTMG (4)
S10	Lin (2) ¹³	Grell 3D (5)	MYJ (2)	RRTMG (4)
S11	Milbrandt-Yau (2) ¹⁴	Grell 3D (5)	MYJ (2)	RRTMG (4)
S12	Morrison (10) ¹⁵	Grell 3D (5)	MYJ (2)	RRTMG (4)
S13	NSSL (17) ¹⁶	Grell 3D (5)	MYJ (2)	RRTMG (4)
S14	NSSL with CCN (18)	Grell 3D (5)	MYJ (2)	RRTMG (4)
S15	WDM (16)	New Simplified Arakawa-Schubert (14) ¹⁷	MYJ (2)	RRTMG (4)
S16	SBU-YLin (13) ¹⁸	Grell 3D (5)	MYJ (2)	RRTMG (4)
S17	Thompson (8) ¹⁹	Grell 3D (5)	MYJ (2)	RRTMG (4)
S18	WDM (16)	Tiedtke (6) ²⁰	MYJ (2)	RRTMG (4)
S19	WSM (16) ²¹	Grell 3D (5)	MYJ (2)	RRTMG (4)
S20	WDM (16)	Zhang-McFarlane (7) ²²	MYJ (2)	RRTMG (4)

¹ Lim and Hong, (2010), ² Pan and Wu., (1995), ³ Janjic (1994), ⁴ Iacono et al. (2008), ⁵ Janjic (1994), ⁶ Grell (1993), and Grell and Devenyi (2002), ⁷ Bougeault and Lacarrere, (1989), ⁸ Dudhia (1989), and Mlawer et al. (1997), ⁹ NOAA, (2001), ¹⁰ Grell and Freitas (2014), ¹¹ Tao et al. (1989), ¹² Kain (2004), ¹³ Lin (1983), ¹⁴ Milbrandt and Yau, (2005), and Milbrandt and Yau, (2005), ¹⁵ Morrison et al. (2009), ¹⁶ Mansellet al. (2010), ¹⁷ Han and Pan (2011), ¹⁸ Lin and Colle (2011), ¹⁹ Thompson et al. (2008), ²⁰ Tiedtke (1989), and Zhang et al. (2011), ²¹ Hong and Lim, (2006), ²² Zhang and McFarlane, (1995),

5.2. Results and discussions on air temperature, wind speed, relative humidity, and precipitation in Montreal

Comparing the output of a numerical model with observations is an accepted method to evaluate a model. However, there are some limitations for extensive analysis of data, including the measurement instruments, reported data accuracy, missing data, and comparison of the point data (from weather stations) to area-averaged data (from simulations). Accepting the limitations, data from Environment Canada (2013) is used for current evaluation of 2-m air temperature, 10-m wind speed, 2-m relative humidity, and surface precipitation.

5.2.1. Air temperature

Almost all model ensembles underestimate the 2-m air temperature (Table 5-2) both in urban and rural areas. The average of the calculated MBEs shows half of the model ensembles (S01, S02, S03, S04, S08, S09, S15, S18, S19, and S20) underestimate the 2-m air temperature by the MBE of less than -1°C . MBE of the predicted air temperature for the urban station is similar (9 model ensembles underestimated the 2-m air temperature by the MBE of less than -1°C). The main reason for the underestimation of the air temperature is the exclusion of anthropogenic heat emission in urban areas. The anthropogenic heat emission can significantly contribute to an increase in the air temperature of urban areas (by up to 2°C ; Salamanca et al., 2014).

Milbrandt-Yau (S11) and NSSL (S13) produced the least MAE (1.5°C) followed by S14 (1.6°C), S16 (1.6°C), S06 (1.7°C), S10 (1.7°C), and S17 (1.7°C) through Domain 3 (Table 5-3). In the urban weather station, the MAE is minimized (1.4°C), using S03 and S06 ensembles. The choices of PBL (MYJ and BouLac; coupled to ML-UCM) shows a good agreement in predicting the 2-m air temperature in the urban area. In rural areas, the MAE of the model ensemble using the MYJ scheme was 0.3°C less than the MAE of S03 using the BouLac scheme. Skin temperature is sensitive to shortwave radiation; consequently, the 2-m air temperature is sensitive to the selected options for radiation parameterization. The RRTMG parameterization is more accurate than the combination of the Dudhia scheme for shortwave and RRTM scheme for longwave radiation (MAE difference of 1.8°C). The Goddard and WSM microphysics schemes, and Tiedtke and Kain-Fritsch cumulus parameterizations, estimate an unrealistic air temperature in both rural and urban areas. The main reason for large errors is the implementation of models

that are designed for very coarse grid cells, to resolve sub-grid processes, in a domain with a grid size of 3 km × 3 km (Domain 2).

Table 5-4 shows the RMSE of the simulations and accuracy of models based on this metric are similar to their MAE results (S14 and S16 have the least RSME of 2 °C through Domain 3; S03 and S06 have the RMSE of 1.7 °C in the urban area).

Table 5-2. MBE in predicted 2-m air temperature (°C) with different WRF settings

MBE	MCTAVISH	PIERRE ELLIOTT TRUDEAU INTL	ST-HUBERT	STE-ANNE- DE- BELLEVUE	VARENNES	L'ACADIE	MIRABEL	L'ASSOMPT ION	STE- CLOTHIDE	Average
S01	-1.5	-3.2	-1.2	-3.9	-1.8	-1.2	-2.8	-1.9	-0.7	-2.0
S02	-1.5	-3.4	-1.2	-3.5	-1.7	-0.5	-2.9	-1.9	-0.5	-1.9
S03	-0.6	-2.2	-0.2	-3.1	-0.7	-0.4	-2.2	-0.9	0.7	-1.1
S04	-1.1	-1.7	-0.7	-1.6	-0.7	-0.8	-1.6	-1.0	0.0	-1.0
S05	-0.5	-0.9	-0.6	-0.5	-0.4	-0.4	-0.1	-0.3	1.0	-0.3
S06	-0.9	-1.4	-0.6	-1.4	-0.8	-0.6	-1.3	-0.9	0.7	-0.8
S07	-0.5	-1.7	-0.4	-2.1	-0.9	-0.4	-1.7	-1.1	1.1	-0.8
S08	-1.9	-4.3	-1.8	-4.1	-2.4	-1.7	-3.2	-2.3	-1.4	-2.6
S09	-1.5	-3.4	-1.0	-3.5	-1.7	-0.6	-3.0	-1.9	-0.7	-1.9
S10	-0.6	-0.9	-0.5	-0.6	-0.5	-0.2	-0.5	-0.5	1.2	-0.3
S11	-0.2	-0.5	-0.1	-0.4	-0.2	-0.1	-0.1	-0.3	1.4	-0.1
S12	-0.4	-0.8	-0.2	-0.6	-0.3	-0.1	-0.2	-0.2	1.0	-0.2
S13	0.1	-0.3	0.1	-0.1	0.0	0.0	0.0	-0.2	1.5	0.1
S14	-0.2	-0.5	-0.1	-0.2	-0.2	-0.1	-0.2	-0.2	1.5	0.0
S15	-2.0	-4.2	-3.2	-4.1	-2.9	-1.7	-3.7	-3.1	-1.6	-2.9
S16	0.0	-0.5	0.1	-0.1	-0.1	0.0	-0.1	-0.1	1.6	0.1
S17	-0.3	-0.6	-0.2	-0.5	-0.2	-0.1	-0.1	-0.2	1.2	-0.1
S18	-1.3	-2.7	-1.3	-3.5	-1.4	-1.1	-3.1	-2.0	-0.5	-1.9
S19	-1.5	-3.4	-1.0	-3.5	-1.7	-0.6	-2.9	-1.9	-0.6	-1.9
S20	-1.0	-2.7	-0.9	-3.3	-1.3	-0.4	-2.4	-1.6	0.1	-1.5
Avg	-0.9	-2.0	-0.8	-2.0	-1.0	-0.5	-1.6	-1.1	0.4	-1.1

Table 5-3. MAE in predicted 2-m air temperature (°C) with different WRF settings

MAE	MCTAVISH	PIERRE ELLIOTT TRUDEAU INTL	ST-HUBERT	STE-ANNE- DE- BELLEVUE	VARENNES	L'ACADIE	MIRABEL	L'ASSOMPT ION	STE- CLOTTHIDE	Average
S01	2.2	3.7	2.0	4.4	2.7	1.8	3.6	2.9	2.8	2.9
S02	2.4	3.9	2.1	4.1	2.6	1.2	3.8	2.8	3.0	2.9
S03	1.4	2.5	1.3	3.5	1.6	1.2	2.7	1.8	2.3	2.0
S04	3.0	3.4	3.3	3.9	3.6	3.2	3.7	3.4	4.2	3.5
S05	1.9	2.0	2.0	2.1	1.7	1.5	1.7	1.8	2.3	1.9
S06	1.4	1.7	1.4	2.0	1.7	1.5	2.0	1.8	1.8	1.7
S07	1.6	2.3	1.5	3.2	1.9	1.4	2.7	2.2	2.0	2.1
S08	2.8	4.9	2.5	4.8	3.2	2.4	3.9	3.2	3.3	3.5
S09	2.4	3.9	1.9	4.2	2.5	1.3	3.8	2.7	3.1	2.9
S10	1.6	1.7	1.5	2.0	1.7	1.2	1.9	1.8	2.0	1.7
S11	1.4	1.3	1.3	1.8	1.4	1.0	1.4	1.6	1.8	1.5
S12	1.8	1.7	1.6	2.1	1.8	1.3	1.6	1.8	2.1	1.8
S13	1.5	1.4	1.3	1.9	1.4	1.0	1.5	1.7	1.9	1.5
S14	1.6	1.4	1.4	1.8	1.7	1.1	1.5	1.8	2.0	1.6
S15	2.9	4.5	3.7	4.5	3.6	2.5	4.2	3.8	3.2	3.7
S16	1.6	1.4	1.4	1.9	1.6	1.1	1.6	1.8	2.0	1.6
S17	1.6	1.6	1.5	2.0	1.7	1.1	1.6	1.8	2.0	1.7
S18	3.4	4.1	4.0	4.5	4.1	3.8	4.4	4.3	3.3	4.0
S19	2.4	3.9	1.9	4.2	2.5	1.2	3.8	2.7	3.1	2.9
S20	1.8	3.1	1.5	4.1	2.1	1.1	3.1	2.4	2.3	2.4
Avg	2.0	2.7	2.0	3.2	2.3	1.6	2.7	2.4	2.5	2.4

Table 5-4. RMSE in predicted 2-m air temperature (°C) with different WRF settings

RMSE	MCTAVISH	PIERRE ELLIOTT TRUDEAU INTL	ST-HUBERT	STE-ANNE- DE- BELLEVUE	VARENNES	L'ACADIE	MIRABEL	L'ASSOMPT ION	STE- CLOTHIDE	Average
S01	2.7	4.4	2.5	5.4	3.4	2.6	4.3	3.5	3.8	3.6
S02	2.9	4.9	2.8	5.1	3.3	1.6	4.6	3.6	4.0	3.6
S03	1.7	2.9	1.6	4.3	2.0	1.5	3.3	2.2	2.8	2.5
S04	3.8	4.2	4.0	4.7	4.3	3.9	4.5	4.1	4.9	4.3
S05	2.3	2.4	2.6	2.6	2.1	2.1	2.4	2.3	2.8	2.4
S06	1.7	2.2	1.9	2.5	2.1	1.9	2.4	2.2	2.2	2.1
S07	1.9	3.1	1.9	3.8	2.3	1.8	3.3	2.8	2.4	2.6
S08	3.4	5.6	3.1	5.6	3.9	3.2	4.7	4.0	4.4	4.2
S09	2.8	4.8	2.4	5.1	3.1	1.6	4.7	3.4	4.1	3.5
S10	1.9	2.1	1.9	2.4	2.1	1.5	2.3	2.1	2.5	2.1
S11	1.8	1.7	1.8	2.3	1.7	1.3	1.9	2.1	2.4	1.9
S12	2.2	2.1	2.1	2.5	2.1	1.6	2.1	2.3	2.7	2.2
S13	2.0	1.9	1.7	2.3	1.8	1.3	2.0	2.1	2.5	1.9
S14	2.0	1.8	1.8	2.2	2.0	1.4	2.0	2.3	2.6	2.0
S15	3.5	5.5	4.5	5.6	4.6	3.4	5.1	4.8	4.5	4.6
S16	2.0	1.9	1.9	2.2	2.0	1.4	2.0	2.2	2.6	2.0
S17	2.0	2.1	2.0	2.5	2.0	1.4	2.1	2.3	2.6	2.1
S18	3.8	4.7	4.7	5.4	4.8	4.7	5.2	5.2	4.3	4.8
S19	2.8	4.8	2.3	5.1	3.0	1.6	4.7	3.4	4.1	3.5
S20	2.1	3.7	2.0	4.9	2.5	1.4	3.9	3.1	3.0	3.0
Avg	2.5	3.3	2.5	3.8	2.8	2.1	3.4	3.0	3.3	3.0

5.2.2. Wind speed

Wind speed plays an important role in calculation of air temperature from skin temperature calculated in LSM. The transient effect of wind speed on air temperature is complicated; an increase in wind speed increases the convection heat transfer that reduces the skin temperature, which simultaneously causes a decrease in convection heat transfer. The wind speed is typically measured at a 10-m height from the ground; so, I analyze the 10-m wind speed for current analysis. All model ensembles underestimate the wind speed through rural and urban areas (except MIRABEL). Assuming an underestimation of 2-m wind speed as a result of underestimated 10-m wind speed, the main justification for underestimation of 2-m air

temperature is inaccuracy of predicting wind speed by PBL options. PBL options with the coupling capability to UCMs are not well designed for very fine-resolution grids.

The wind speed is highly variable with the measurement location. There are large MBE and MAE in predicted wind speed related to many of the weather stations (Table 5-5 and Table 5-6). On the other hand, the predicted wind speed in the urban weather station (MCTAVISH) has the least MAE (2.1 m/s); since the MBE of 1.7 m/s. Microphysics and cumulus parameterizations that introduce higher inaccuracy in predicting 2-m air temperature have high MBE (< -3.5 m/s), which shows the high dependency of the calculated air temperature on wind speed.

Table 5-5. MBE in predicted wind speed (m/s) with different WRF settings

MBE	MCTAVISH	PIERRE ELLIOTT TRUDEAU INTL	ST-HUBERT	STE-ANNE- DE- BELLEVUE	VARENNES	L'ACADIE	MIRABEL	L'ASSOMPTI ON	STE- CLOTIDE	Average
S01	-2.0	-6.1	-6.9	-2.9	-4.1	-5.7	0.8	-3.5	-1.3	-3.5
S02	-1.8	-6.4	-6.8	-3.4	-4.1	-4.6	0.2	-3.6	-1.0	-3.5
S03	-1.7	-5.8	-6.3	-3.3	-3.8	-4.9	0.6	-3.0	-0.8	-3.2
S04	-1.8	-5.3	-5.7	-1.7	-2.0	-3.4	1.2	-1.6	0.9	-2.2
S05	-1.5	-5.3	-6.0	-2.5	-3.0	-4.6	1.3	-2.8	-0.1	-2.7
S06	-1.7	-5.5	-6.2	-3.1	-3.3	-5.0	0.5	-2.9	-0.8	-3.1
S07	-1.7	-5.9	-6.3	-3.0	-3.8	-4.6	0.5	-3.3	-0.6	-3.2
S08	-1.9	-6.5	-6.7	-3.5	-4.2	-5.3	0.2	-3.6	-0.8	-3.6
S09	-1.8	-6.3	-6.7	-3.3	-4.2	-4.9	0.2	-3.5	-0.9	-3.5
S10	-1.7	-5.5	-6.2	-2.6	-3.2	-4.4	1.1	-2.9	-0.3	-2.9
S11	-1.6	-5.5	-6.2	-2.8	-3.3	-4.2	1.2	-2.9	-0.2	-2.8
S12	-1.5	-5.3	-6.2	-2.5	-3.4	-4.2	1.2	-2.9	-0.4	-2.8
S13	-1.6	-5.3	-6.1	-2.5	-3.4	-4.3	1.3	-3.0	-0.3	-2.8
S14	-1.5	-5.3	-6.1	-2.4	-3.3	-4.3	1.3	-2.8	-0.1	-2.7
S15	-2.1	-6.6	-7.6	-3.6	-4.6	-5.3	0.0	-4.0	-1.2	-3.9
S16	-1.5	-5.5	-6.2	-2.5	-3.4	-4.3	1.1	-2.8	-0.3	-2.8
S17	-1.6	-5.3	-6.1	-2.5	-3.2	-4.3	1.3	-3.0	-0.5	-2.8
S18	-1.9	-6.2	-7.0	-3.3	-3.7	-5.4	0.6	-3.2	-1.2	-3.5
S19	-1.9	-6.7	-6.8	-3.8	-4.4	-5.0	-0.1	-3.7	-1.1	-3.7
S20	-1.3	-5.5	-6.4	-2.6	-4.1	-5.3	1.4	-3.1	-0.9	-3.1
Avg	-1.7	-5.8	-6.4	-2.9	-3.6	-4.7	0.8	-3.1	-0.6	-3.1

The predicted wind speed in the urban area has an MAE of about 2 m/s, like that of the air temperature; adding the anthropogenic heat emission can decrease the MBE and potentially increase the accuracy of the model (smaller MAE). The average performance of model ensembles through the simulation domain based on MAE is almost the same (about 4 m/s).

Table 5-6. MAE in predicted wind speed (m/s) with different WRF settings

MAE	MCTAVISH	PIERRE ELLIOTT TRUDEAU INTL	ST-HUBERT	STE-ANNE-DE-BELLEVUE	VARENNES	L'ACADIE	MIRABEL	L'ASSOMPTION	STE-CLOTHIDE	Average
S01	2.4	6.5	7.5	3.9	5.0	6.3	3.5	4.6	3.7	4.8
S02	2.2	6.6	7.2	3.9	4.9	5.5	3.3	4.5	3.6	4.6
S03	2.2	6.0	6.7	3.8	4.7	5.7	3.2	4.1	3.7	4.5
S04	2.1	5.6	6.2	3.3	3.8	5.3	4.0	3.6	4.3	4.2
S05	2.0	5.7	6.5	3.5	3.9	5.4	3.3	3.6	3.4	4.1
S06	2.1	5.8	6.6	3.7	4.2	5.6	3.2	3.7	3.8	4.3
S07	2.1	6.1	6.7	3.6	4.6	5.5	3.4	4.2	3.8	4.4
S08	2.1	6.7	7.1	4.0	4.9	5.9	3.4	4.4	3.9	4.7
S09	2.2	6.6	7.1	3.8	4.9	5.6	3.3	4.4	3.6	4.6
S10	2.0	5.8	6.6	3.4	4.1	5.3	3.1	3.9	3.6	4.2
S11	1.9	5.8	6.6	3.5	4.1	5.2	3.0	3.7	3.4	4.1
S12	1.9	5.7	6.6	3.3	4.1	5.3	3.2	3.6	3.8	4.2
S13	1.8	5.6	6.5	3.3	4.0	5.3	3.1	3.6	3.7	4.1
S14	1.9	5.6	6.5	3.1	4.2	5.3	3.1	3.6	3.6	4.1
S15	2.4	6.8	7.9	4.1	5.3	6.0	3.4	4.7	3.7	4.9
S16	1.9	5.8	6.6	3.3	4.1	5.4	3.2	3.6	3.7	4.2
S17	1.9	5.6	6.6	3.3	4.0	5.4	3.2	3.7	3.9	4.2
S18	2.3	6.6	7.4	4.2	4.7	6.3	3.6	4.6	3.9	4.8
S19	2.4	6.8	7.2	4.2	5.0	5.7	3.3	4.3	3.5	4.7
S20	1.7	5.9	6.9	3.6	4.7	6.5	3.6	3.9	3.7	4.5
Avg	2.1	6.1	6.9	3.6	4.5	5.6	3.3	4.0	3.7	4.4

Table 5-7 provides the resulting RMSE for the weather stations and the selected model ensembles. The results are in accordance with analysis for the MAE. The main purpose of providing Table 5-7 is to have sufficient data for future comparison of models in other studies (proving all output data would occupy 300 pages).

Table 5-7. RMSE in predicted wind speed (m/s) with different WRF settings

RMSE	MCTAVISH	PIERRE ELLIOTT TRUDEAU INTL	ST-HUBERT	STE-ANNE-DE-BELLEVUE	VARENNES	L'ACADIE	MIRABEL	L'ASSOMPTION	STE-CLOTHIDE	Average
S01	2.8	8.3	9.3	5.1	6.6	8.5	4.1	6.4	4.5	6.2
S02	2.5	8.5	9.1	5.0	6.5	7.7	3.8	6.2	4.4	6.0
S03	2.7	7.7	8.7	4.9	6.2	7.9	3.9	5.5	4.5	5.8
S04	2.6	7.3	8.4	4.2	4.7	7.1	4.9	4.8	5.0	5.4
S05	2.3	7.4	8.5	4.4	5.0	7.4	4.2	4.8	4.1	5.3
S06	2.5	7.4	8.6	5.0	5.3	7.9	3.9	4.9	4.6	5.6
S07	2.4	8.0	8.6	4.8	6.0	7.6	3.9	5.8	4.6	5.8
S08	2.5	8.5	9.1	5.1	6.6	8.2	3.9	6.3	4.6	6.1
S09	2.6	8.3	8.9	4.9	6.6	7.7	3.8	6.1	4.4	5.9
S10	2.4	7.4	8.6	4.4	5.3	7.4	3.9	5.1	4.4	5.4
S11	2.2	7.3	8.6	4.5	5.2	7.3	3.8	5.0	4.1	5.3
S12	2.2	7.4	8.5	4.4	5.3	7.3	3.9	4.7	4.5	5.4
S13	2.2	7.2	8.4	4.4	5.3	7.4	3.9	4.9	4.4	5.3
S14	2.3	7.2	8.5	4.2	5.3	7.3	3.8	4.9	4.3	5.3
S15	2.8	8.5	10.1	5.2	6.9	8.2	3.9	6.4	4.5	6.3
S16	2.2	7.4	8.6	4.4	5.3	7.5	3.9	4.8	4.3	5.4
S17	2.3	7.2	8.6	4.3	5.2	7.3	4.0	4.9	4.5	5.4
S18	2.7	8.3	9.6	5.6	6.6	8.9	4.3	6.1	4.9	6.3
S19	2.9	8.7	9.5	5.6	6.6	8.1	3.9	6.1	4.4	6.2
S20	2.2	7.8	9.2	4.9	6.6	9.1	4.4	5.7	4.7	6.1
Avg	2.5	7.8	8.9	4.8	5.9	7.8	4.0	5.5	4.5	5.7

5.2.3. Relative humidity

Relative humidity is a function of moisture content, air temperature, and surface pressure. Therefore, it carries part of the error from the inaccuracy in predicting the air temperature. Since data provided by Environment Canada (2013) are limited (in some weather stations like STE-ANNE-DE-BELLEVUE, the pressure data is missing), I have calculated the relative humidity (relative humidity is not a standard output of WRF) at the 2-m height.

The relative humidity at 2-m height is overestimated through Domain 3 by all model ensembles (MBE ranges from -2% to 24%) [Table 5-8]. The least MBE is observed in the urban area (MBE ranges from -2% to 11%). Half of the model ensembles provided an MAE of less than 10% in

the urban area; while the S11 model ensemble using the Milbrandt-Yau microphysics scheme performed well in both urban area (MAE = 7%) and through the domain (MAE = 9%). Model ensembles have the same performance by means of their RMSE (Table 5-9) with the least average RMSE of 13% in urban areas. The predicted relative humidity in the urban areas is more accurate compared to rural areas because of the lack of moisture in urban regions (both moisture content of the air and moisture flux from the ground are low). Models with large MAE in predicting the 2-m air temperature have large MAE in predicting the relative humidity as well.

Table 5-8. MBE in predicted relative humidity (%) at 2-m height with different WRF settings

MBE	MCTAVISH	PIERRE ELLIOTT TRUDEAU INTL	ST-HUBERT	STE-ANNE- DE- BELLEVUE	VARENNES	L'ACADIE	MIRABEL	L'ASSOMPTI ON	STE- CLOTTHIDE	Average
S01	9	18	9	20	12	10	18	10	11	13
S02	8	17	9	19	12	9	18	10	8	12
S03	5	13	5	18	9	8	16	7	5	10
S04	4	24	19	23	20	19	25	19	16	19
S05	3	7	7	9	7	9	7	5	1	6
S06	7	11	8	13	9	10	13	7	4	9
S07	3	10	5	14	8	8	14	7	1	8
S08	10	20	12	20	15	14	19	12	11	15
S09	9	17	8	18	12	10	17	9	9	12
S10	4	8	7	10	8	7	10	6	0	7
S11	1	6	5	8	6	7	7	5	-1	5
S12	3	8	5	9	7	8	9	5	1	6
S13	1	7	4	8	6	6	7	4	-1	5
S14	4	9	6	9	7	8	9	6	0	6
S15	11	20	14	20	16	13	20	14	12	16
S16	2	8	4	9	6	7	9	5	0	6
S17	3	8	6	9	7	7	9	5	1	6
S18	-2	11	2	14	4	5	12	4	1	6
S19	8	17	8	16	12	10	16	9	7	12
S20	6	15	7	18	10	7	17	8	5	10
Avg	5	13	8	14	10	9	14	8	5	9

Table 5-9. MAE in predicted relative humidity (%) at 2-m height with different WRF settings

MAE	MCTAVISH	PIERRE ELLIOTT TRUDEAU INTL	ST-HUBERT	STE-ANNE- DE- BELLEVUE	VARENNES	L'ACADIE	MIRABEL	L'ASSOMPTIO N	STE- CLOTHIDE	Average
S01	12	19	11	20	15	12	19	14	16	15
S02	13	19	13	20	15	11	19	14	15	16
S03	9	14	9	19	12	10	17	12	14	13
S04	13	24	20	23	20	19	25	20	18	20
S05	8	10	10	12	10	11	11	10	11	10
S06	9	12	10	15	11	12	14	11	12	12
S07	9	13	9	18	11	10	16	12	12	12
S08	13	22	14	21	16	14	19	15	16	17
S09	13	19	11	19	15	12	18	14	16	15
S10	8	11	9	13	10	10	12	10	11	10
S11	7	8	9	12	9	9	10	10	10	9
S12	8	10	10	13	10	10	12	10	12	10
S13	8	9	9	13	9	9	10	10	10	10
S14	9	10	9	12	10	9	11	10	11	10
S15	15	21	15	20	18	14	21	18	16	18
S16	8	10	8	12	9	9	11	10	10	10
S17	8	10	10	13	10	10	11	10	11	10
S18	20	17	18	16	16	16	16	16	15	17
S19	14	23	13	22	16	14	22	18	15	17
S20	11	17	10	20	13	10	17	13	15	14
Avg	11	15	11	17	13	12	16	13	13	13

Table 5-10. RMSE in predicted relative humidity (%) at 2-m height with different WRF settings

RMSE	MCTAVISH	PIERRE ELLIOTT TRUDEAU INTL	ST-HUBERT	STE-ANNE-DE-BELLEVUE	VARENNES	L'ACADIE	MIRABEL	L'ASSOMPTION	STE-CLOTHIDE	Average
S01	14	22	14	25	18	15	24	17	22	19
S02	15	23	15	25	18	15	24	17	22	19
S03	12	17	11	23	15	13	21	14	18	16
S04	18	30	26	30	26	25	31	25	26	27
S05	11	12	13	14	12	14	14	12	15	13
S06	11	14	12	17	14	15	17	14	15	14
S07	11	15	12	21	14	13	20	15	15	15
S08	15	25	17	25	20	19	24	19	23	21
S09	15	22	14	24	18	15	23	17	22	19
S10	10	12	12	15	12	12	15	11	13	13
S11	9	10	11	14	11	11	12	12	13	11
S12	10	12	12	15	12	13	14	12	15	13
S13	10	11	10	15	11	11	13	12	13	12
S14	11	12	11	14	12	11	14	13	14	12
S15	18	25	19	25	22	19	25	22	23	22
S16	10	11	10	14	11	11	13	12	13	12
S17	10	11	12	15	12	12	14	12	14	12
S18	25	21	23	21	20	21	21	21	20	21
S19	17	29	16	26	20	17	26	23	20	22
S20	13	20	13	25	16	12	22	16	21	18
Avg	13	18	14	20	16	15	19	16	18	17

5.2.4. Precipitation

I am aware of the weakness of numerical weather prediction models in simulating clouds and water processes. This comparison provides a qualitative assessment of the prediction of precipitation by these model ensembles. Using the ETA microphysics scheme performed (S05) well in determining the surface rain underestimation of about -8 mm and -4 mm in the urban area and in Domain 3, respectively (Table 5-11). The MAE of S05 in the urban area is 9 mm and the average through the domain is 7 mm, which is by far the most appropriate model ensemble for prediction of precipitation using fine-resolution grid size (Table 5-12). However, simulation time for S05 was approximately four times longer than for the other ensembles. In the urban area,

MAE of the predicted precipitation by other model ensembles (not S05) was almost the same (ranging from 12 mm to 15 mm). The S10 ensemble using the Lin microphysics scheme has the least MAE (6 mm) in the rural areas. The MAE of all models through Domain 3 is less than 10 mm, except for S13 and S18 using the NSSL microphysics scheme and Tiedtke cumulus parameterization. As mentioned, the issue of fine-resolution grid cells affects the cloud convection process. Table 5-13 provides the calculated RMSE of the model ensemble in predicting the rainfall episode during the simulation period.

Table 5-11. MBE in predicted precipitation (mm) with different WRF settings

MBE	MCTAVISH	PIERRE ELLIOTT TRUDEAU INTL	ST-HUBERT	STE-ANNE- DE- BELLEVUE	L'ACADIE	L'ASSOMPTI ON	STE- CLOTHIDE	Average
S01	-15	-12	-14	-14	4	7	-5	-8
S02	-15	-14	-16	-15	-4	-6	5	-9
S03	-15	-11	-12	-11	8	-7	8	-6
S04	-14	-12	-14	-12	5	-8	7	-7
S05	-8	-8	-9	-11	4	1	3	-4
S06	-12	-12	-15	-12	6	-6	8	-6
S07	-15	-13	-16	-14	-3	-4	2	-9
S08	-13	-11	-11	-11	1	-6	3	-7
S09	-15	-13	-12	-14	-4	-5	5	-8
S10	-12	-9	-10	-13	-1	-1	1	-6
S11	-12	-10	-10	-12	-6	-7	1	-8
S12	-13	-12	-13	-11	-4	-9	3	-8
S13	-12	-9	-13	-13	4	-4	18	-4
S14	-11	-3	-12	-9	-1	-6	10	-5
S15	-16	-13	-14	-14	1	-9	5	-9
S16	-13	-12	-14	-14	-8	-5	2	-9
S17	-13	-13	-14	-12	-4	-7	1	-9
S18	-15	-13	-16	-11	-11	-9	1	-11
S19	-15	-14	-12	-14	-4	-7	4	-9
S20	-14	-14	-15	-15	-1	-9	2	-9
Avg	-14	-11	-13	-13	-1	-6	5	-4

Table 5-12. MAE in predicted precipitation (mm) with different WRF settings

MAE	MCTAVISH	PIERRE ELLIOTT TRUDEAU INTL	ST-HUBERT	STE-ANNE- DE- BELLEVUE	L'ACADIE	L'ASSOMPTI ON	STE- CLOTHIDE	Average
S01	15	12	14	14	4	7	5	10
S02	15	14	16	15	4	6	5	10
S03	15	11	12	11	8	7	8	10
S04	14	12	14	12	5	8	7	10
S05	9	8	9	11	4	1	3	7
S06	12	12	15	12	6	6	8	10
S07	15	13	16	14	3	4	2	10
S08	13	11	11	12	1	6	3	8
S09	15	13	12	14	4	5	5	10
S10	12	9	11	13	1	1	1	7
S11	12	10	10	12	6	8	1	8
S12	14	12	13	11	4	9	3	9
S13	14	9	13	13	4	4	18	11
S14	13	3	13	10	1	7	10	8
S15	16	13	14	14	1	9	5	10
S16	13	14	14	14	8	5	2	10
S17	15	13	14	13	5	8	3	10
S18	16	14	16	18	14	10	8	14
S19	15	14	12	14	4	7	4	10
S20	14	14	15	15	1	9	2	10
Avg	14	12	13	13	5	6	5	10

Table 5-13. RMSE in predicted precipitation (mm) with different WRF settings

RMSE	MCTAVISH	PIERRE ELLIOTT TRUDEAU INTL	ST-HUBERT	STE-ANNE- DE- BELLEVUE	L'ACADIE	L'ASSOMPTIO N	STE- CLOTHIDE	Average
S01	26	20	24	25	7	12	9	18
S02	27	23	27	25	7	10	8	18
S03	25	18	21	19	13	12	14	18
S04	24	21	24	22	8	15	12	18
S05	15	14	16	19	7	2	5	11
S06	21	19	25	20	11	11	14	17
S07	26	22	27	25	5	7	3	17
S08	22	19	20	20	1	10	5	14
S09	26	22	20	24	7	8	9	17
S10	20	14	18	22	2	2	2	12
S11	21	17	18	21	10	13	1	14
S12	23	20	22	19	7	15	5	16
S13	23	15	22	23	6	7	30	18
S14	21	5	21	17	2	11	16	13
S15	27	22	25	24	1	15	9	18
S16	23	22	24	24	14	9	3	17
S17	24	22	24	22	8	13	3	17
S18	27	23	28	26	22	16	10	22
S19	26	23	20	25	7	12	6	17
S20	24	23	25	25	2	15	3	17
Avg	24	19	23	23	8	11	8	16

5.3. Conclusion on the appropriate model ensemble

Several options of WRF are combined (for a total of 20 model ensembles) to evaluate their performance for reproducing the measured data (2-m air temperature, 10-m wind speed, 2-m relative humidity, and precipitation). A period of three days in August (09-Aug-2009 to 11-Aug-2009) is selected, mainly for the clear sky in the first two days and a heavy rain period on the third day. Two domains (3 km × 3 km; 600 m × 600 m) are telescopically nested into a coarse domain to cover the Greater Montreal area. Model ensembles generally underestimate the air temperature, wind speed and precipitation, whereas relative humidity is overestimated by almost all model ensembles. The combination of WDM6 (Lim and Hong, 2010), Grell 3D (Grell, 1993;

Grell and Devenyi, 2002), MYJ (Janjic, 1994), and RRTMG (Iacono et al., 2008) as microphysics, cumulus, planetary boundary layer, and radiation schemes, respectively, is the most accurate model ensemble. The mean average error (MAE) of the 2-m air temperature in the urban area is 1.4 °C compared to the measured data, and through the domain the value increases to 1.7 °C. The selected ensemble predicted the wind speed, relative humidity, and precipitation with MAE of 2.1 m/s, 9%, and 12 mm, respectively, in the urban area. In addition, the MAE of the predicted wind speed, relative humidity, and precipitation by the ensemble through the smallest domain is 4.3 m/s, 12%, and 10 mm, respectively.

Chapter Six: Characterization of Urban Morphology of Montreal

Collecting and analyzing data needs a detailed analysis of an urban area selected as the case study. I chose the Greater Montreal Area as my case study in this research. UCM coupled with a mesoscale model needs fine-resolution surface data. Surface data comprise the estimation of urban area and the urban category (i.e., low intensity, medium intensity, and high intensity), fraction of roofs and pavements, building height distribution in different urban categories, and emissivity of urban surfaces. The Montreal Municipality provided a detailed map of the city (City of Montreal, 2009). Simulation of energy consumption in the buildings needs data related to the building properties and their HVAC system. Building properties include the size of the buildings, the conductivity of building surfaces, glazing properties, and convective heat transfer coefficients of building surfaces. In this research, I will use the standard provided by ASHRAE (2007a).

The urban canopy model is responsible for a smaller region compared to the mesoscale model. Feedbacks of UCM on mesoscale (upscaling) are not significant, so many simplifications may apply to the UCMs. However, effects of atmospheric parameters on the variables of UCM (downscaling) are huge. In order to have an accurate UCM, two phenomena should be quantified precisely: radiation trapping and circulation in the canopy. For the first part, a radiation model will be developed to consider the multiple reflections between urban surfaces. Both sunlight (shortwave) and longwave (emitted from the surfaces and the sky) trapping will be considered. Isotropic and fully diffused reflection from all surfaces is an important assumption in the calculations. The second part of completing UCM is to estimate the sensitivity of air temperature to momentum and heat exchange coefficients. Different exchange coefficients have been proposed for different purposes but only a few researches have investigated exchange coefficients' effect on urban climate. Therefore, different models will be analyzed to best characterize the boundary layer in the canopy.

6.1. Methodology of simulations

For this part, first, I analyze the urban data of four different neighborhoods in Montreal (Canada). Then, I simulate the urban heat island (UHI) in Montreal using the typical urban

characteristics (Chen et al., 2011). I evaluate four methods to represent urban morphology and compare street SVF values for the case studies in Martilli (2009) and for Montreal. Like Martilli (2009), I am not addressing the effect of urban morphology on wind pattern inside the canopy. Three sets of simulations are performed to investigate the effect of (1) modified urban geometry, (2) modified SVF (using statistical modeling for parameterization), and (3) modified urban geometry and modified SVF on urban heat island intensity (UHII). The objectives are twofold: (1) to quantify the difference in UHII of Montreal between typical and accurate urban morphologies on a summer day, (2) to modify the SVF of roads and to test the modified SVF by calculating UHII. To achieve the objectives, the following steps are taken:

Step 1. Aerial images of selected neighborhoods are collected and building heights are extracted from the database of Montreal Municipality (City of Montreal, 2009). From the data, mean building height and deviation of building heights are calculated. Line drawings of the neighborhoods are provided to identify actual plan area density and frontal area density. The plan area density is the fraction of number of pixels with buildings to total number of pixels from the top view. The frontal area density is the mean of fractions of pixels with buildings from four side views (north, east, west, and south) to total number of pixels from the top view. The average of calculated parameters is considered as the characteristic of the city.

Step 2. The building energy model (BEM) calculates energy consumption and heat emission of buildings. The BEM (Salamanca and Martilli, 2010a) calculates the energy demand of the building that keeps the indoor air temperature and the indoor moisture content in the comfort range. The accuracy of BEM is restricted by the dynamics of HVAC systems and by characteristics of building envelopes. HVAC systems of buildings are diverse and their efficiency/performance is highly dependent on required load (part-load ratio). Building envelopes are also different in terms of materials properties such as reflectance, insulation, and emittance. In an idealized urban structure all buildings and their HVAC systems have the same characteristics. A simple method is used to find the average efficiency of heating systems and COP of cooling systems. The share of each energy system in total energy consumption for cooling or heating in Quebec is calculated from the data provided by the Energy Use Data Handbook (Behidj et al., 2012; Office of Energy Efficiency, 2011, and references therein). Then,

the weighted average of performance of the energy systems is calculated to represent efficiency of heating systems and COP of cooling systems.

Step 3. The air temperature of Montreal is simulated using version 3.5 of the weather research and forecasting model (WRF). The platform for mesoscale modeling is explained in Section 4.1.1. The fine-resolution grids (500m × 500m) provide more detailed information on different neighborhoods in Montreal, at the cost of poor accuracy because of the deficiency of microphysics parameterizations. For modified morphological parameters only URBPARAM.TBL is updated, and for the modified sky view factor the source code for UCM is altered.

Step 4. A SVF parameterization is proposed by statistical analysis of hypothetical urban configurations. A set of urban geometry with randomly distributed building heights is developed to find the relation between the actual SVF and the estimated SVF using different techniques. A simple UCM code is developed with MATLAB 2012R to numerically calculate view factors of different surfaces and the total absorbed energy by the canopy using numerical methods.

The sky view factor (SVF) of streets in idealized urban structures (London, Toulouse, Berlin, Salt Lake City, Los Angeles, and neighborhoods in Montreal) is determined and a new parameterization for SVF is calculated. The actual SVF (F_{rw}) is compared with calculated SVFs (F_i) to investigate the accuracy of different methods. Actual SVFs of five cities are collected from the previous study (Martilli, 2009). ENVI-met software (Bruse and Fleer, 1998) is used to calculate SVF of the neighborhoods in Montreal, and the average is used for the city. Nine receptors are placed in each neighborhood, in the middle of streets, to calculate the SVF. The ENVI-met model is capable of separating the SVF calculation accounting for the effect of buildings and vegetation. The F_{rs} is calculated by averaging the SVFs observed in 9 receptors.

Step 5. The urban heat island intensity in simulations is calculated by subtracting the spatially averaged 2-m air temperature of rural areas from the spatially averaged 2-m air temperature of the urban area, on an hourly basis. In the simulation domain (~50 km × 30 km), the total number of grids is 3 times more than the number of grids considered as urban. The actual UHII is identified by subtracting the measured temperature in a weather station located in the rural area (Mirabel Airport weather station) from the measured temperature inside the urban area (McTavish weather station).

6.1.1. Selected parameterizations

The Weather Research and Forecasting (WRF) model version 3.5 (ARW user guide, 2012; Skamarock et al., 2008) is coupled to a multi-layer urban canopy model (UCM) and a building energy model (BEM) for urban climate simulations. The UCM (Martilli et al., 2002) incorporates the urban grids into mesoscale grids and calculates the heat and moisture fluxes from urban areas to the vertical layers of the mesoscale model. The BEM (Salamanca et al., 2010a, 2010b) determines the heat emission from the buildings to the canopy. WRF has two solvers, and the ARW solver is appropriate for urban climate research (Yu et al., 2012). The ARW solver comprises several parameterizations for microphysics, cloud convection, shortwave and longwave radiations, land-surface, surface layer, and planetary boundary layer. The mesoscale model has been evaluated in different studies (Zhang et al., 2009; Millstein and Menon, 2011).

The double-moment WRF microphysics parameterization (Hong et al., 2004) is used to determine the water content of the air and the type of hydrometeors. The convection of the clouds is not considered for Domain 3, whereas for other domains the Grell 3D ensemble scheme (Grell and Devenyi, 2002) is used. The CAM shortwave and longwave schemes (Collins et al., 2004) determine the shortwave and longwave radiation effects and their interactions with the atmosphere in all domains. The land-surface model (LSM) calculates the ground temperature, soil temperature profile, soil moisture profile, snow cover, and other surface variables. The Noah LSM (NCEP, Oregon State University, Air Force, NWS Office of Hydro) proposed by Chen et al. (2001) is used to calculate ground variables as a part of inputs to the UCM. The surface-layer model determines the interactions between the LSM and planetary boundary layer (PBL). The ETA model (Janjic, 2002) is used to incorporate the Noah-LSM variables into the Mellor-Yamada-Janjic PBL model (Janjic, 1990,1994). The initial and boundary conditions of the simulations are determined using different datasets. The NARR dataset (Mesinger et al., 2006) and the USGS (U.S. Census Bureau, Geography Division, 2011) are used for the weather data and the terrestrial data, respectively.

6.2. Urban characteristics

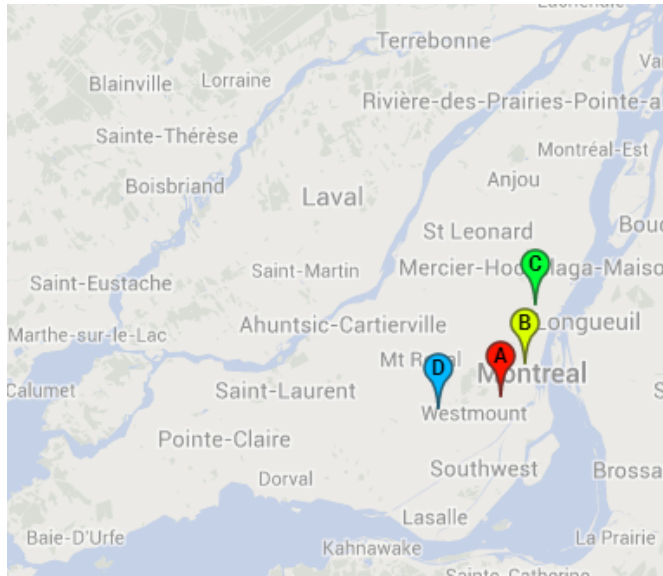
A detailed analysis of urban characteristics including the morphology and HVAC systems of buildings is essential for urban climate simulations. However, determining those parameters is not feasible because of urban expansion and dynamics of HVAC systems in the urban scale.

Therefore, a statistical method is developed to estimate dimension of buildings and the average efficiency/performance of HVAC systems.

6.2.1. Urban morphology

Four neighborhoods in Montreal are selected as a sample population of buildings (Figure 6-1): Concordia, with dense high-rise buildings; UQAM, with dense medium-rise buildings; Joliette, with row-house buildings; and a fourth neighborhood with detached-house buildings. Street orientation and urban fraction are calculated using the full aerial image of the city (www.maps.google.com). Street orientation of Montreal is calculated by averaging the orientation of main streets. There are two main angles (approximately 30 and 50 degrees from north) to represent the street orientation. Additionally, about 20% of the urban area is considered to be vegetated. Building heights are extracted from the data provided by Montreal Municipality (City of Montreal, 2009).

Figure 6-2 shows the number of buildings sorted by their height, rounded to 5-meter increments, in the selected neighborhoods. The probability distribution of building heights is required as the input to the multi-layer UCM in WRF to calculate heat emission from buildings to the canopy and energy consumption of HVAC systems. Since the building distribution is random (with a known probability distribution), in each simulation a unique heat flux from the ground to the atmosphere is calculated; however, the differences are negligible. Buildings with the height of 5 m and 10 m are most probable building heights in Montreal with 45% and 42% chance, respectively. The percentage of high-rise buildings is about 8%, which is greater than the actual value, since the linear average of building heights in different neighborhoods is being used. For a better estimation of morphological parameters, a weighted average of the values would better represent the city; nonetheless, doing so requires a huge amount of resources and effort. Moreover, WRF has the option to have up to three urban categories when the detailed map of the area of interest is available.



Concordia Neighborhood (A)



UQAM Neighborhood (B)



Joliette Neighborhood (C)



Snowdon Neighborhood (D)

Figure 6-1. Map of Montreal and selected neighborhoods (www.maps.google.com)

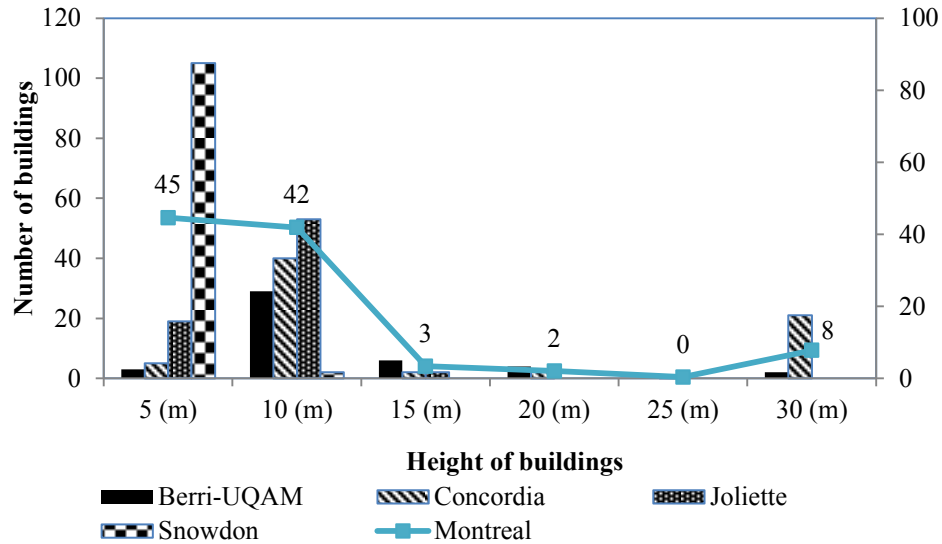


Figure 6-2. Number of buildings sorted by the height on the left axis and the probability distribution of building heights on the right axis

Average building heights, standard deviation of the height, plan area density, frontal area density, width of buildings, and width of the street for four neighborhoods in Montreal are analyzed (Table 6-1). Data of five cities are also collected (Ratti et al., 2002; Martilli, 2009) and the average of those parameters is considered for the city. Additionally, width of buildings, width of the road in 2D model, width of the road in 3D model, sky view factor of street, and size of the grid are estimated.

Table 6-1. The characteristics (average height of buildings, standard deviation of the height, plan area density, frontal area density, width of buildings, width of the road in 2D model, width of the road in 3D model, sky view factor of street, size of the grid) of selected urban areas and the regions in Montreal

	h_m (m)	σ_h (m)	λ_p	λ_f	b (m)	w_{2D} (m)	w_{3D} (m)	F_{rs}	dx
London	13.6	5	0.55	0.32	23.4	19.1	8.1	0.53	250
Toulouse	15.3	6.1	0.4	0.32	19.1	28.7	11.1	0.65	250
Berlin	18.6	4.3	0.35	0.23	28.3	52.6	19.5	0.72	250
Salt Lake City	16.3	14.1	0.22	0.11	32.6	115.6	36.9	0.87	400
Los Angeles	51.3	51.5	0.28	0.45	31.9	82.1	28.4	0.60	400
Montreal	11.3	7.30	0.39	0.24	19.1	30.4	11.0	0.72	300
UQAM	11.8	5.0	0.44	0.21	24.5	31.4	12.5	0.69	300
Concordia	22.9	20.9	0.55	0.53	23.5	19.6	8.3	0.47	300
Joliette	7.3	2.4	0.26	0.15	12.1	35.3	12.2	0.84	300
Snowdon	3.1	0.8	0.32	0.12	8.2	17.8	12.7	0.87	300

6.2.2. Efficiency/performance of energy systems in buildings

The collected data (Behidj et al., 2012; Office of Energy Efficiency, 2011, and references therein) considers two cooling systems, room and central, which have the same performance. For heating, various types of systems are considered with their respective efficiency or performance (e.g., for heat pumps). I used the energy consumption data of Quebec to find the average efficiency/performance of energy systems in Montreal, since the data for Montreal is not publicly available. More than half of the population of Quebec Province lives in the Greater Montreal area (Statistics Canada, 2007). Hence, the provided data are likely to well represent the energy consumption pattern in Montreal, where, the main energy supply is electricity. Wood and oil systems for heating are rarely used and electric baseboard heaters are the predominant heating source.

The COP is calculated from EER and SEER using eqs. 6-1 and 6-2. Then, the weighted average of efficiency and COP is calculated (Table 6-2). In my simulations, I considered the heating efficiency to be 1 and the COP of cooling equal to 2.5. The calculation of efficiency and COP is performed by the Residential End-Use Model (Office of Energy Efficiency, 2009) using a fairly complicated technique. The model compares the end use energy with the usage profile of households and the type of equipment for heating and cooling to estimate the performance of HVAC systems.

$$EER = SEER \times 0.697 + 2.0394 \quad (6-1)$$

$$COP = EER \times 0.293 \quad (6-2)$$

Table 6-2. Energy use for space cooling and heating in Quebec by equipment type and their stock efficiency in 2005
(Behidj et al., 2012, Office of Energy Efficiency 2011, and references therein)

	System type	Energy use (PJ)	Share (%)	Efficiency/performance	Weighted average efficiency/performance
Cooling	Room	2.0	40.4	2.6	2.6
	Central	3.0	59.6	2.6	
Heating	Heating Oil – Normal Efficiency	0.0	0.0	0.6	0.9
	Heating Oil – Medium Efficiency	28.7	13.0	0.7	
	Heating Oil – High Efficiency	0.0	0.0	0.8	
	Natural Gas – Normal Efficiency	10.1	4.6	0.6	
	Natural Gas – Medium Efficiency	2.9	1.3	0.8	
	Natural Gas – High Efficiency	5.0	2.3	0.9	
	Electric	92.5	41.9	1.0	
	Heat Pump	5.8	2.7	1.9 ¹²	
	Other	1.0	0.5	0.5	
	Wood	8.7	3.9	0.5	
	Wood/Electric	42.5	19.3	0.7	
	Wood/Heating Oil	10.4	4.7	0.6	
	Natural Gas/Electric	1.5	0.7	0.9	
Heating Oil/Electric	11.4	5.2	0.8		

6.3. Urban heat island and urban cool island in summer

The urban heat island is a sophisticated phenomenon depending on synoptic weather condition and anthropogenic heat emission, simultaneously. During the day solar energy provides the major contribution to heat island; however, sometimes cool island might be experienced because of the dense cloud cover. I used the simulation platform of my former study (Touchaei and Akbari, 2014) to simulate the urban climate of Montreal. As shown in Figure 6-3, the UHI is observed at midnight as a result of absorbed heat during the day and heat emission from buildings during the evening. After midnight UHI is attenuated and the 2-m air temperature starts to increase during the sunrise. The UHI is evident at 9 a.m. and it is more pronounced in the east (Centre-ville, Le Plateau-Mont-Royal, Montreal-Nord neighborhoods and Longueuil). At noon, the temperature of the whole region is increased to 23 ± 1 °C and the difference between urban

¹² The COP of the heat pump is normally higher than the value reported. The reason for the low COP might be because of the very low temperature in Quebec during the winter. In very low temperatures heat pumps are not working properly and the electric heater replaces the heating cycle. Hence the annual performance decreases by the low performance of electric heater.

and rural areas is negligible. In early afternoon, the dense cloud cover reduces the solar radiation striking the ground in the urban area and cool island is noticeable because of two main reasons: (1) an increase in the latent heat flux from water bodies around the city, and (2) a decrease in the solar radiation striking the urban area due to denser clouds. The nocturnal UHI again starts to appear during the evening and continues during the night. In simulations, urban grids have the same characteristics and there is no difference between neighborhoods. The downtown area of Montreal and part of Longueuil (on the east bank of the river) experienced the highest temperature during the 24-hour period.

Historically, in many hours of a day urban areas experience higher temperatures than their surroundings, which is loosely defined as urban heat island. On the other hand, cold climates might experience the “cool island” phenomenon more frequently. For a city like Montreal embedded in rivers, the latent heat flux is higher than the sensible heat flux compared to its surroundings. Therefore, a chance of UHI might decrease but the near surface temperature is still high. Here, I used UHII as the general term to represent the difference between the air temperature in an urban area and its surroundings.

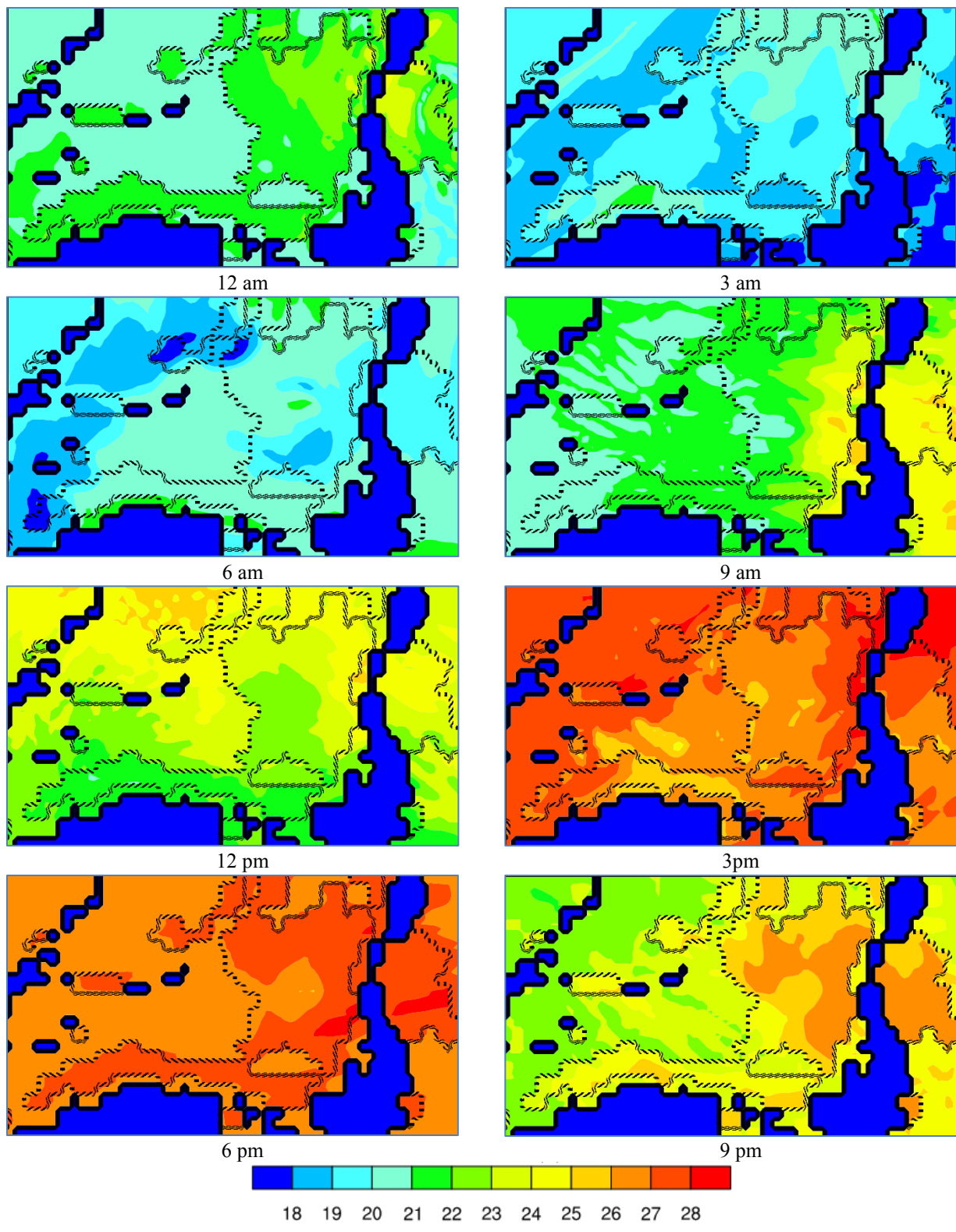


Figure 6-3. 2-m air temperature (°C) in different hours of July 14th, 2005 (the dashed line is the urban border and dark blue color represents rivers)

6.4. Methods of calculating sky view factor for a canopy

Sky view factor (SVF) of urban surfaces plays an important role in calculating the energy balance of the canopy. The SVF is highly dependent on the structure of the urban canopy. I consider four types of idealized urban canopy structure: (1) 2D model randomly distributed height of building rows, (2) 2D model with constant height of buildings, (3) 3D model, and (4) 2D model with randomly distributed height of buildings (Figure 6-4).

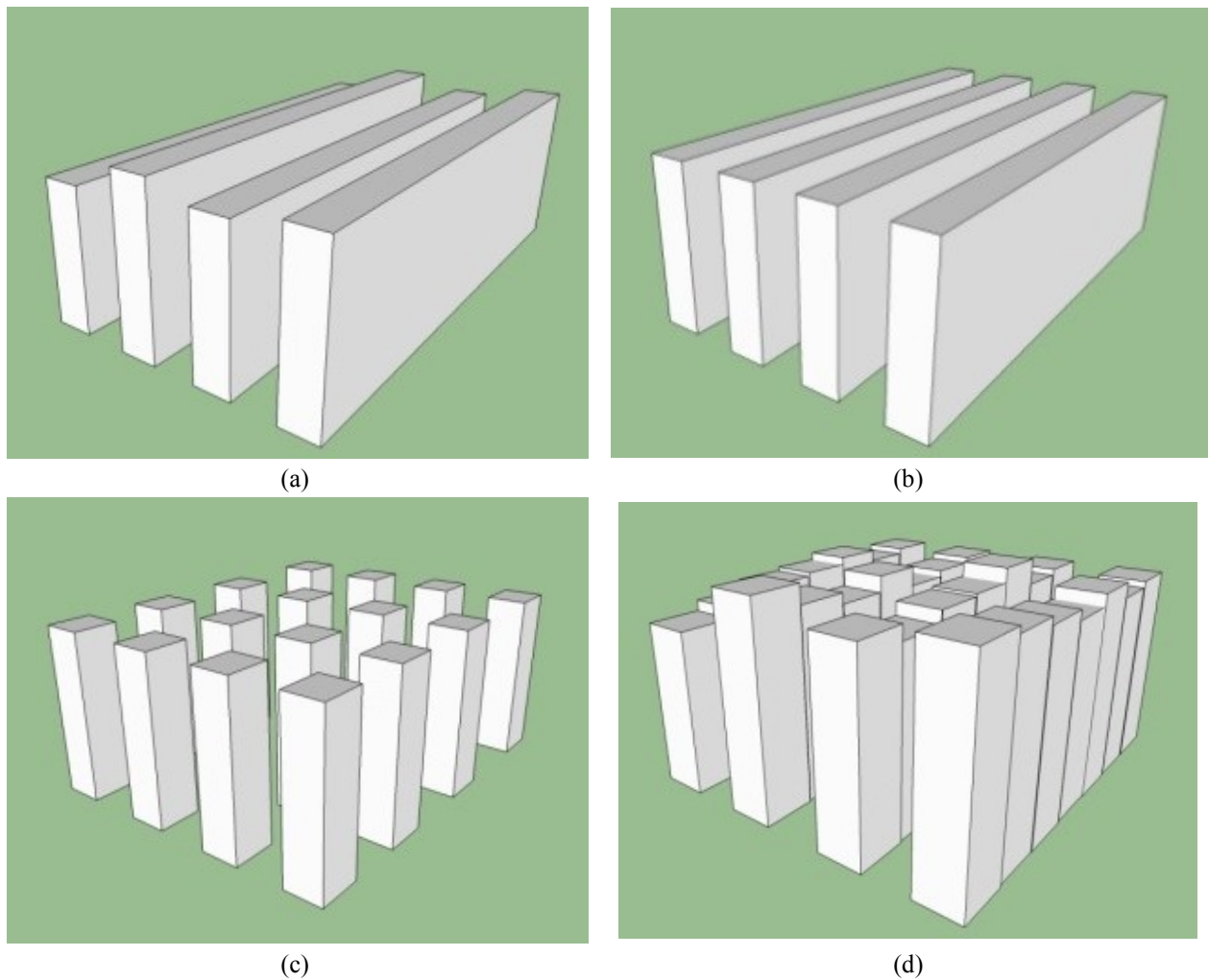


Figure 6-4. Schematic of the arrays of buildings considered as the urban morphology, (a) 2D model randomly distributed height of building rows, (b) 2D model with constant height of buildings, (c) 3D model, and (d) 2D model with randomly distributed height of buildings

The SVF of the street in the canopy with randomly distributed height of building rows (F_1) is the sum of street-to-wall view factors (F_{rw}) subtracted from unity (Siegel and Howell, 2001).

$$F_1 = 1 - F_{rw,1} - F_{rw,2} \quad (6-3a)$$

$$F_{rw} = \frac{1}{2} (1 + X - \sqrt{1 + X^2}) \quad (6-3b)$$

$$X = \frac{\tilde{h}}{w_{road}} \quad (6-3c)$$

where, \tilde{h} is the wall height and w is the street width.

For constant height of building rows, the street SVF (F_2) (Byrd, 1993) is calculated from Eq. (6-4).

$$F_2 = \left(\frac{2}{\pi XY} \right) \left[\frac{1}{2} \ln \frac{(1 + X^2) \cdot (1 + Y^2)}{1 + X^2 + Y^2} + Y \sqrt{1 + X^2} \cdot \tan^{-1} \left(\frac{Y}{\sqrt{1 + X^2}} \right) + X \sqrt{1 + Y^2} \cdot \tan^{-1} \left(\frac{X}{\sqrt{1 + Y^2}} \right) - X \tan^{-1}(X) - Y \tan^{-1}(Y) \right] \quad (6-4a)$$

$$X = \frac{dy}{h_m} \quad (6-4b)$$

$$Y = \frac{w_{road}}{h_m} \quad (6-4c)$$

where, dy and h_m represents grid size and height of buildings, respectively.

Kanda (2005) proposed eq. 6-5 to estimate the street SVF of 3D canopy.

$$F_3 = V_{loc} V_{mod} \quad (6-5a)$$

$$V_{loc} = \cos \left[\tan^{-1} \left(\frac{2h_m}{w_{road}} \right) \right] \left[2 - \frac{4}{\pi} \tan^{-1} \left(\cos \left[\tan^{-1} \left(\frac{2h_m}{w_{road}} \right) \right] \right) \right] \quad (6-5b)$$

$$V_{mod} = 0.112V_{loc}\lambda_p - 0.481\lambda_p + 0.0246V_{loc} + 0.957 \quad (6-5c)$$

In 2D UCM with randomly distributed building height, the street SVF is calculated similar to eq. 6-4, except the F_{rw} is the summation of the street-to-wall view factors of all buildings in the canopy.

$$F_4 = 1 - F_{rw} \quad (6-6a)$$

$$F_{rw} = \sum_i F_{rw,i} \quad (6-6b)$$

Finally, I propose the following parameterization for the street SVF based on statistical analysis of different urban configuration.

$$F_5 = F_1 + 2\lambda_f - \lambda_p \quad (6-7)$$

The street SVF of selected areas are calculated with the developed tool and results are shown in Table 3. The proposed parameterization shows a better estimation of the actual SVF compared to other methods.

Table 6-3. View factors of the selected cities and region in Montreal using different urban morphology

	F_{rs}	F_1	F_2	F_3	F_4	F_5
London	0.53	0.55	0.35	0.52	0.51	0.53
Toulouse	0.65	0.62	0.43	0.61	0.60	0.63
Berlin	0.72	0.70	0.56	0.71	0.70	0.72
Salt Lake City	0.87	0.84	0.79	0.87	0.87	0.87
Los Angeles	0.60	0.53	0.38	0.58	0.55	0.63
Montreal	0.72	0.73	0.53	0.69	0.68	0.69
UQAM	0.69	0.72	0.54	0.70	0.69	0.69
Concordia	0.47	0.56	0.23	0.42	0.37	0.43
Joliette	0.84	0.80	0.71	0.82	0.82	0.82
Snowdon	0.87	0.83	0.84	0.74	0.83	0.83

6.5. UHI simulation with modified data

Four sets of simulations have been performed: (1) CTRL—using the default characteristics of urban areas within WRF; (2) Morph—the morphological characteristics and building properties are updated with the provided data in this research; (3) VF—implementing the proposed SVF parameterization in CTRL; (4) VF_mod—implementing the proposed SVF parameterization in Morph. The 2-m air temperature of the urban area for simulation cases is compared with the observational data gathered at McTavish weather station (Environment Canada, 2014). All cases reproduced the nocturnal urban temperature well compared to diurnal temperature, which is underestimated (Figure 6-5). The underestimation mainly resulted from the deficiency of the microphysics parameterization to predict the cloud cover, which has been overestimated. Shortwave solar radiation is inversely proportional to the cloud cover. The underestimation of the nocturnal air temperature reported in previous research (Touchaei and Akbari, 2013) is corrected by using BEM. VF_mod increases the accuracy of predicting the 2-m air temperature almost all day. The view factor of urban surfaces is an important factor even during the nighttime, since the longwave radiation becomes dominant. The mean average error of the CTRL is about 2.6 °C, which has been reduced by 0.7 °C using the modified urban morphology and SVF parameterization (VF_mod).

Using the multi-layer UCM well replicated the diurnal cool island but it underestimates the nocturnal UHI even by coupling it to BEM (Figure 6-6). The difference of about 0.7 °C in UHI is estimated from modifying the urban morphology and building characteristics. The observed temperature difference between the urban and rural areas in simulations is the difference between spatially averaged temperatures, but the measured data are point data of two weather stations (McTavish in urban area and Mirabel in rural area).

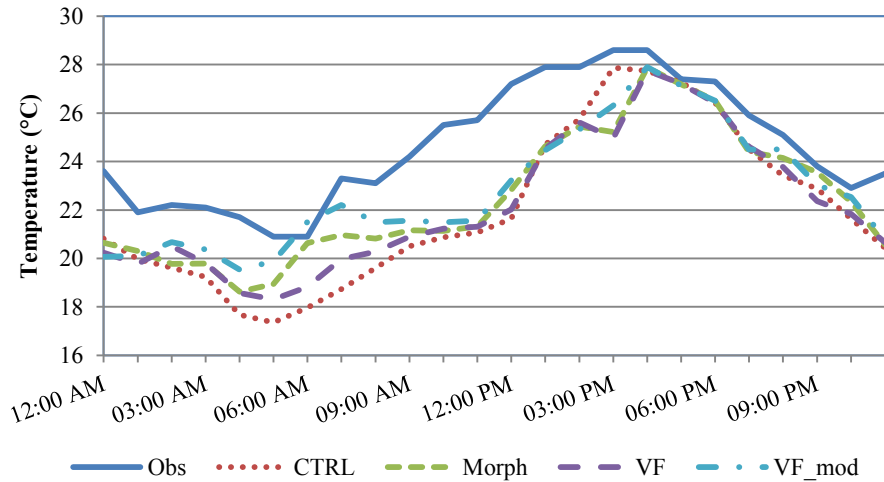


Figure 6-5. 2-m temperature observed at McTavish weather station and reproduced by considering different cases

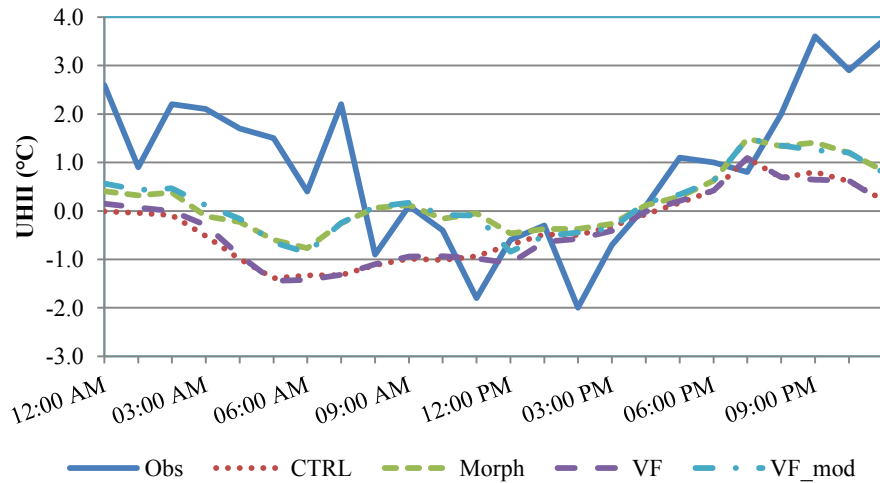


Figure 6-6. Urban heat island intensity from observed data (the difference between air temperature measured at urban area [McTavish], and rural area [Mirabel Airport]) and simulated cases

Another major interest of urban climate simulation in the neighborhood scale is to predict the effect of applying a UHI mitigation strategy on energy consumption of buildings. I calculated the

energy consumption of HVAC systems in Montreal following the framework of an earlier study (Touchaei and Akbari, 2014). The total spatially averaged energy consumption in CTRL is about 3.2 kWh/100m² of roof area, which is 1% lower than the value predicted by VF. Additionally, updating the urban morphology and building characteristics significantly increased the estimated energy consumption to 9.5 kWh/100m². Current modifications decreased the generated error but further improvement to the code should be made to give a more reliable prediction of air temperature. Estimating air temperature and energy consumption of HVAC systems requires extra data and computational time.

6.6. Conclusion on the importance of urban morphology in characterizing UHI

The urban heat island on a summer day of Montreal is simulated using the urbanized weather research and forecasting model. Basic simulation suggested an elevated nocturnal air temperature in the urban area and lower urban air temperature during the day because of the clouds. The urban morphology and HVAC system performance of buildings is modified by statistically analyzing aerial pictures and collected data for energy systems in the city. Additionally, the current methods for calculating the sky view factor of the street are tested against a new parameterization. Comparing the empirical values collected from other studies, and from a set of randomly generated urban configuration, with values from different methods suggests that the new parameterization can improve the energy calculation for urban surfaces. Three simulations have been performed to investigate the effect of updating the urban and buildings characteristic. Modifying the urban morphology improved the mean average error in estimating the 2-m air temperature by 0.4 °C, and the estimated energy consumption increased by the average of 6.3 kWh/100m². The view factor modification has a negligible effect on estimating the energy consumption but it increased the accuracy of the model in calculating the 2-m air temperature and urban heat island intensity. The best performance of the model resulted from modification of both urban morphology and view factor. For the latter, the mean average error of the 2-m air temperature decreased by 0.7 °C, and that of the nocturnal urban heat island intensity by about 0.6°C. Results suggest that the urban morphology plays an important role in simulating regional climate, and updated methods and data should be used to improve the accuracy.

Chapter Seven: Effect of Increasing Albedo on Urban Climate and Energy Consumption of Buildings in Montreal

Increasing the albedo of urban surfaces is a promising heat island mitigation strategy in tropical and moderate climates. Increasing the albedo reduces the heat absorption by roof and walls; hence, it reduces the cooling energy demand in summer and may increase the heating energy demand in winter. In this paper, effect of increasing the albedo of urban surfaces in Montreal (Canada), a cold climate region, is investigated. An algorithm is developed to select a monthly typical meteorological day to represent each month of a year. Episodic simulations are performed for the typical meteorological day of each month in 2005. The weather research and forecasting (WRF) model is coupled with a multi-layer urban canopy model and a building energy model to accurately simulate the urban climate and energy consumption of air conditioning systems. The albedo of roofs, walls, and roads is increased from 0.2 to 0.65, 0.6, and 0.45, respectively.

7.1. Methodology of evaluating seasonal performance of an increase in urban albedo

The Weather Research and Forecasting (WRF) model version 3.5 (ARW user guide, 2012; Skamarock et al., 2008) is coupled to a multi-layer urban canopy model (UCM) and a building energy model (BEM) with the parameterizations used in simulations of Chapter 9.

7.1.1. Monthly Typical Meteorological Days

The monthly typical meteorological day (MTMD) is generated to represent each month of a selected year with a single day. The method for selecting MTMDs is similar to the procedure developed by Sandia National Laboratories (Hall et al., 1978). In this empirical method all days of a month are examined and “the most typical day” is selected as the MTMD of that month. The most typical day can be selected using different parameters, depending on the objective of the analysis. For example, in order to use the MTMDs in modeling energy systems and buildings, solar irradiance, air temperature, dew temperature, and wind speed are main indices to consider. Likewise, the concentrations of air pollutants are influential parameters for air-quality modeling. The following steps describe the selection procedure:

Step 1. The data for the selected parameters are gathered from a weather station (or an air quality monitoring-station). In many cities, measured parameters in the weather station located at city

airports are reliable and have been used in TMY datasets. Similarly, in this study, I use data from the weather station of Pierre Elliot Trudeau International Airport in Montreal.

Step 2. The data are analyzed to identify controlling parameters. As an example, maxima and minima of the air temperature are important as well as the mean air temperature. The parameters selected for TMY3 (Wilcox and Marion, 2008) are used here. Those parameters are maximum dry bulb temperature, minimum dry bulb temperature, mean dry bulb temperature, maximum dew point temperature, minimum dew point temperature, mean dew point temperature, maximum wind velocity, mean wind velocity, and global solar radiation. Other parameters such as UHI intensity and pollution concentrations can be added.

Step 3. The absolute difference between the daily values and the monthly averaged values are calculated:

$$\delta_i = |x_i - \overline{x_m}| \quad (7-1)$$

Step 4. Absolute differences are multiplied by weighting factors and summed. Weighting factors shall be selected based on the purpose of a research; as an example, the solar radiation might have a greater value than other meteorological parameters when evaluating energy systems is the main objective. Here, I used the same weighting factors proposed for TMY3 (Wilcox and Marion, 2008): 1/24 (maximum dry bulb temperature), 1/24 (minimum dry bulb temperature), 2/24 (mean dry bulb temperature), 1/24 (maximum dew point temperature), 1/24 (minimum dew point temperature), 2/24 (mean dew point temperature), 2/24 (maximum wind velocity), 2/24 (mean wind velocity), and 12/24 (global solar radiation).

$$\sigma_j = \sum_{i=1}^n w_i \delta_i \quad (7-2)$$

n is the number of parameters.

Step 5. The day with the smallest difference is selected as the MTMD of a month

$$MTMD_k = \min \{ \sigma_j \}_{j=1..m} \quad (7-3)$$

k represents a month and m is the number of days in that month.

Based on this method, the following days are selected for urban climate simulation: 16 January, 14 February, 15 March, 17 April, 16 May, 6 June, 14 July, 16 August, 16 September, 16 October, 17 November, and 22 December. All MTMDs are about at mid-month because of the high weighting factor for the solar radiation, except for June and December that the solar radiation changes smoothly during those months.

7.1.2. Episodes and domains of simulations

The episodic simulations are performed for two days of each month in a sample year (i.e., 2005). The start time of the simulations is 1200 UTC on a day before the selected MTMD of each month and the simulations terminate at 0600 UTC on a day after the MTMD. The first 17 hours are considered as the spin-up time, and only the output on MTMDs is analyzed. As shown in Figure 7-1, fine-resolution grids (~400 × 400 m), for the domain that contains the urban area (Domain 3), are nested into the larger grids (Domain 1: 10 × 10 km and Domain 2: 2 × 2 km). The two-way nesting option enables the data transfer between the high-resolution domain of interest and parent domains. According to the stability condition criteria for the numerical solution, the time step of 0.75 second is selected for Domain 3. For all three domains the terrain following coordinate¹³ has 51 vertical layers with the upper pressure of 10 kPa. Domain 3 contains 115 grids from west to east and 65 grids from south to north centered at 45.54° N and 73.68° W.



Figure 7-1. Three domains of simulations (Domain 1: grid size of 10×10 km, Domain 2: grid size of 2×2 km, and Domain 3: grid size of 0.4×0.4 km) Orange lines represents the border of urban areas based on USGS (U.S. Census Bureau, Geography Division, 2011) and the light blue areas with black lines represents rivers in the domain

¹³ In this coordinate system the vertical axis is the hydrostatic pressure at each level normalized by the hydrostatic pressure at the surface and at the top of the domain ($\eta = \frac{P_h - P_{h,top}}{P_{h,surface} - P_{h,top}}$).

7.1.3. Urban parameters

The urban area is considered to be high-density residential category.¹⁴ The input data used here is considered typical for specification of urban areas (Chen et al., 2011), with a slight modification for urban morphology and efficiency of air conditioning system. The urban fraction is considered to be the 80% that does not have natural vegetation. The roughness length of the ground is assumed to be 10 cm. The UCM considers the height of the buildings to vary randomly and the roof level ranges between 5 m and 20 m. The width of buildings and roads is assumed to be 19 m and 30 m, respectively. The conductivity of the roof and walls of a building is considered to be 0.067 (W/mK). The air conditioning system with the gas heating system that has the thermal efficiency of 0.8 (which for the sake of simplicity I considered to be 1, and COP of 2 for cooling) maintains the temperature of about 21 ± 3 °C (cooling above 24 °C and heating below 18 °C). The indoor moisture content of 5 ± 3 g/kg is targeted for buildings. For calculating the sensible and latent heat required by the buildings, BEM accounts for the AC system energy demand to keep the indoor moisture and temperature at an acceptable range, which in turn depends on the number of occupants, the thickness of layers of a building envelope, and other variables.

7.1.4. Scenarios

Two scenarios are defined to study the effect of increasing the albedo of urban surfaces (i.e., roof, wall, or road). In the control scenario (CTRL), the albedo of all surfaces is considered to be 0.2 representing the current situation. In the albedo scenario (ALBEDO), the albedo of roofs, walls and roads is increased to 0.65, 0.6, and 0.45, respectively.

7.1.5. Analysis

The difference of 2-m air temperature and the difference of energy consumption between the two scenarios are calculated. The decrease in 2-m air temperature represents the mitigation of UHI. The change in energy consumption of buildings is the indication of energy savings or penalty of increasing the albedo. The energy consumption is calculated per unit area of roofs. The synoptic weather condition of the selected days has a significant effect on the variation of the air temperature and the energy consumption of buildings.

¹⁴ Urbanized-WRF has the capability of considering three urban categories: (1) commercial, (2) high density residential, and (3) low-density residential, where the detailed map of the region is available.

7.2. Simulation results

First, the effect of increasing the albedo of urban surfaces on the 12 days (representing each month of 2005) in the whole domain is analyzed. The daily spatially averaged differences of 2-m air temperature, energy consumption for air conditioning, sensible heat flux from the ground, downward shortwave radiation on the ground, and PBL height in the urban area are calculated. Then, the spatial distribution of 2-m air temperature at 0900, 1500, and 2100 LST and the daily energy consumption of buildings is discussed.

The albedo enhancement affects the air temperature of the urban area as well as its surroundings because of a change in the wind distribution and moisture content in the atmosphere. To determine the effects of increasing the albedo in the urban area, the daily spatially averaged values of variables in the 12 days of simulations are calculated (Table 1). The 2-m air temperature is decreased by up to 0.1 °C in rural areas and by up to 0.4 °C in urban areas. The 2-m air temperature of the urban area is decreased year-round. It should be noticed that the multi-layer UCM cannot consider the effect of snow in urban areas; hence, the urban heat island intensity in winter is overestimated.

The daily averaged energy penalty during the winter is negligible and the daily averaged energy savings is between 6 and 8% during the summer. The increase of the albedo has a relatively large impact on the sensible heat flux from the ground, as the measure of UHI, which is decreased by an average of 33 Wh/m² from the 60 Wh/m² average heat flux in the urban area. In contrast, the incoming solar shortwave radiation striking the ground is increased year-round. The downward solar radiation striking the surface is inversely proportional to the cloud cover, and since the cloud cover is decreased, amplification of the solar radiation is observed. When the albedo is increased, the daily averaged PBL height is 495 m (-48 m change to CTRL, maximum decrease) in August and it is 276 m (7 m change to CTRL, maximum increase) in September. In August, the effect of surface temperature decrease is more pronounced compared to the change in wind speed and the PBL height is decreased. However, in September, the change in wind speed is dominant and the PBL height is increased.

Table 7-1. Daily-spatially-averaged 2-m air temperature ($^{\circ}\text{C}$), energy consumption for air conditioning (Wh/m^2), sensible heat flux from the ground (W/m^2), downward shortwave radiation on the ground (W/m^2), and PBL height (m) in CTRL and (CTRL –ALBEDO) for Montreal (Canada) on the MTMD of each month in 2005.

		Jan	Feb	Mar	Apr	May	Jun	Jul	Aug	Sep	Oct	Nov	Dec
CTRL	Temperature	-8.4	-5.6	-1.6	12.7	10.5	19.7	22.4	21.7	16.7	10.5	2.5	-10.2
	Heat flux	20	53	92	110	117	52	86	131	15	14	18	14
	Shortwave	103	150	221	303	353	357	349	309	228	162	107	85
	PBL height	368	616	677	573	472	470	373	543	269	1199	691	426
	Energy consumption	4.46	3.93	2.93	0.74	0.26	0.59	1.59	1.30	0.15	0.60	1.79	4.57
ALBEDO - CTRL	Temperature	-0.1	-0.2	-0.2	-0.4	-0.3	-0.2	-0.1	-0.3	0.0	0.0	-0.1	-0.2
	Heat flux	-15	-32	-47	-73	-49	-14	-29	-74	-5	-10	-28	-17
	Shortwave	2	2	4	5	5	6	6	5	4	2	2	1
	PBL height	-67	-7	-19	-45	-40	-20	-9	-48	7	0	-6	-22
	Energy consumption	0.02	0.03	0.02	-0.02	-0.00	-0.05	-0.12	-0.08	-0.03	0.02	0.02	0.02

7.2.1. Urban heat island mitigation

The UHI intensity is calculated by the difference of the air temperature in the urban area and the rest of Domain 3. The spatially averaged 24-hour, diurnal, nocturnal, and peak urban intensity is presented in Table 2. The nocturnal UHI is higher than diurnal UHI and the 24-hour average UHI intensity in winter ($\sim 0.9^{\circ}\text{C}$) is higher than in summer ($\sim 0.2^{\circ}\text{C}$). In my simulations, the daily averaged albedo of an urban grid is increased by 0.46, where, the multi reflection-absorption effect in the canopy decreases the total increase of the albedo in urban areas. As a result, the temperature is reduced year-round. Additionally, the UHI intensity can be decreased annually by the estimated average of 0.1°C when increasing the albedo by 0.37.

The differences between the 2-m air temperature in CTRL and ALBEDO in the morning (9 a.m.), afternoon (3 p.m.), and evening (9 p.m.) are shown in Figure 7-2, 7-3, and 7-4, respectively. The largest decrease in the UHI intensity is observed in the populated regions of Montreal (Centre-ville, Le Plateau-Mont-Royal, Montreal-Nord neighborhoods) as well as Longueuil on east bank of the Saint-Laurent River. The hourly effect of increasing the albedo in January, October, and November is negligible.

In the morning, the 2-m air temperature decrease of $0^{\circ}\text{C} - 3^{\circ}\text{C}$ is observed. However, in May, July, and September, part of the urban area experiences an increase in the air temperature because the surrounding area receives more incoming solar shortwave radiation as a consequence of a decrease in the cloud cover of the domain. This event is attenuated in the rest of the day.

Although albedo enhancement has shown a tendency to reduce the air temperature of the east part of greater Montreal, distribution of the air temperature is highly sensitive to the incoming solar radiation on the ground and the wind pattern. The incoming solar radiation on the surface increases the skin temperature that transfers heat to the air above through convection. The convection heat transfer coefficient is a function of the wind speed and has a significant effect on the performance of albedo enhancement in decreasing the air temperature by up to 80% [1 °C to 0.2 °C] (Krayenhoff and Voogt, 2010).

In the afternoon, city-wide decrease in the 2-m air temperature is only observed in July when the air temperature is decreased by 0 °C – 2 °C. Considering all climatic variations, the effect of albedo enhancement on the air temperature is more pronounced in the morning and in the afternoon. At 9 p.m., in May, the Montreal-South neighborhood experiences a small increase in the air temperature. During the evening in June, July, and August, city-wide reduction in air temperature is more noticeable compared to the other months of the year. The wind pattern and the change in the incoming solar radiation play an important role in the non-uniform temperature variation in the urban area. Although the daily averaged 2-m air temperature is decreased in the urban areas, it is increased in some of the surrounding areas.

Table 7-2. 24-hour, diurnal, nocturnal, and peak UHI intensity and the performance of albedo enhancement to mitigate the UHI in the MTMD of each months

		Jan	Feb	Mar	Apr	May	Jun	Jul	Aug	Sep	Oct	Nov	Dec
UHI intensity	24-hour	0.6	0.8	0.9	1.7	0.2	-0.1	-0.3	0.9	-0.3	0.3	0.4	1.2
	Diurnal	0.4	0.6	0.8	1.4	0.1	-0.2	-0.6	0.6	-0.5	0.3	0.2	0.8
	Nocturnal	0.7	0.9	1.0	2.0	0.3	0.1	0.1	1.4	-0.1	0.3	0.5	1.5
	Peak	1.1	1.6	1.6	3.0	1.1	0.6	1.1	2.6	0.7	0.5	1.3	2.3
UHI reduction	24-hour	-0.1	-0.1	-0.1	-0.3	-0.2	-0.1	-0.1	-0.2	-0.1	0.0	-0.1	-0.1
	Diurnal	-0.2	-0.2	-0.3	-0.5	-0.3	-0.2	-0.2	-0.4	-0.1	-0.1	-0.2	-0.2
	Nocturnal	0.0	0.0	0.0	-0.1	-0.1	0.0	-0.1	0.0	-0.1	0.0	0.0	0.0
	Peak	-0.3	-0.4	-0.3	-0.7	-0.5	-0.5	-0.5	-0.8	-0.2	-0.1	-0.3	-0.4

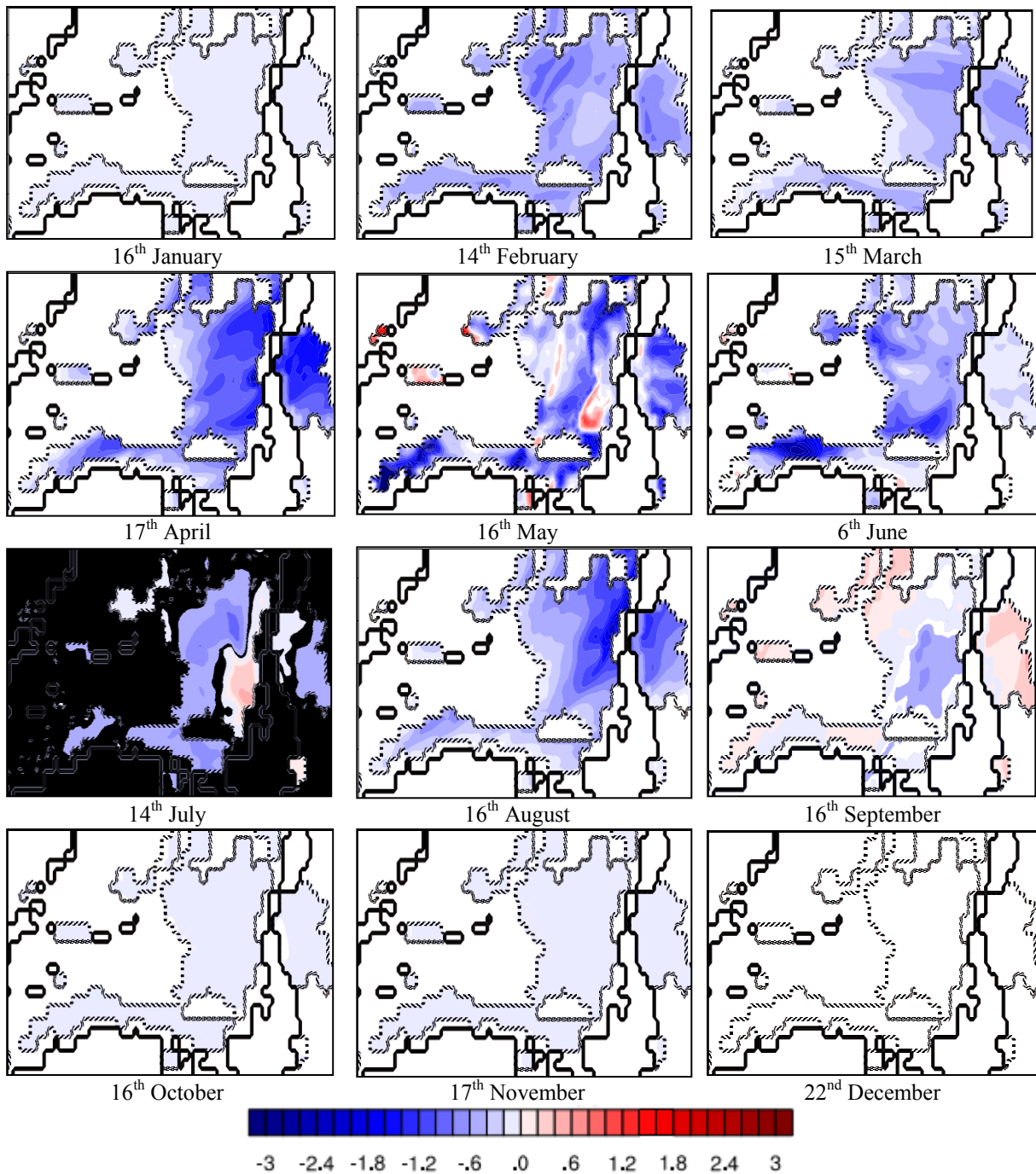


Figure 7-2. The 2-m air temperature difference ($^{\circ}\text{C}$) in ALBEDO and CTRL on MTMD of all months of a year at 9 a.m. (simulation from 0000-2300 UTC for each day). Dashed lines represents the border of urban areas based on USGS (U.S. Census Bureau, Geography Division, 2011) and bold lines represents rivers in the domain (as shown in Figure 7-1.c). A small increase in the air temperature in some part of the city is observed because of the change in the wind pattern and an increase in the incoming solar radiation when the urban albedo is increased.

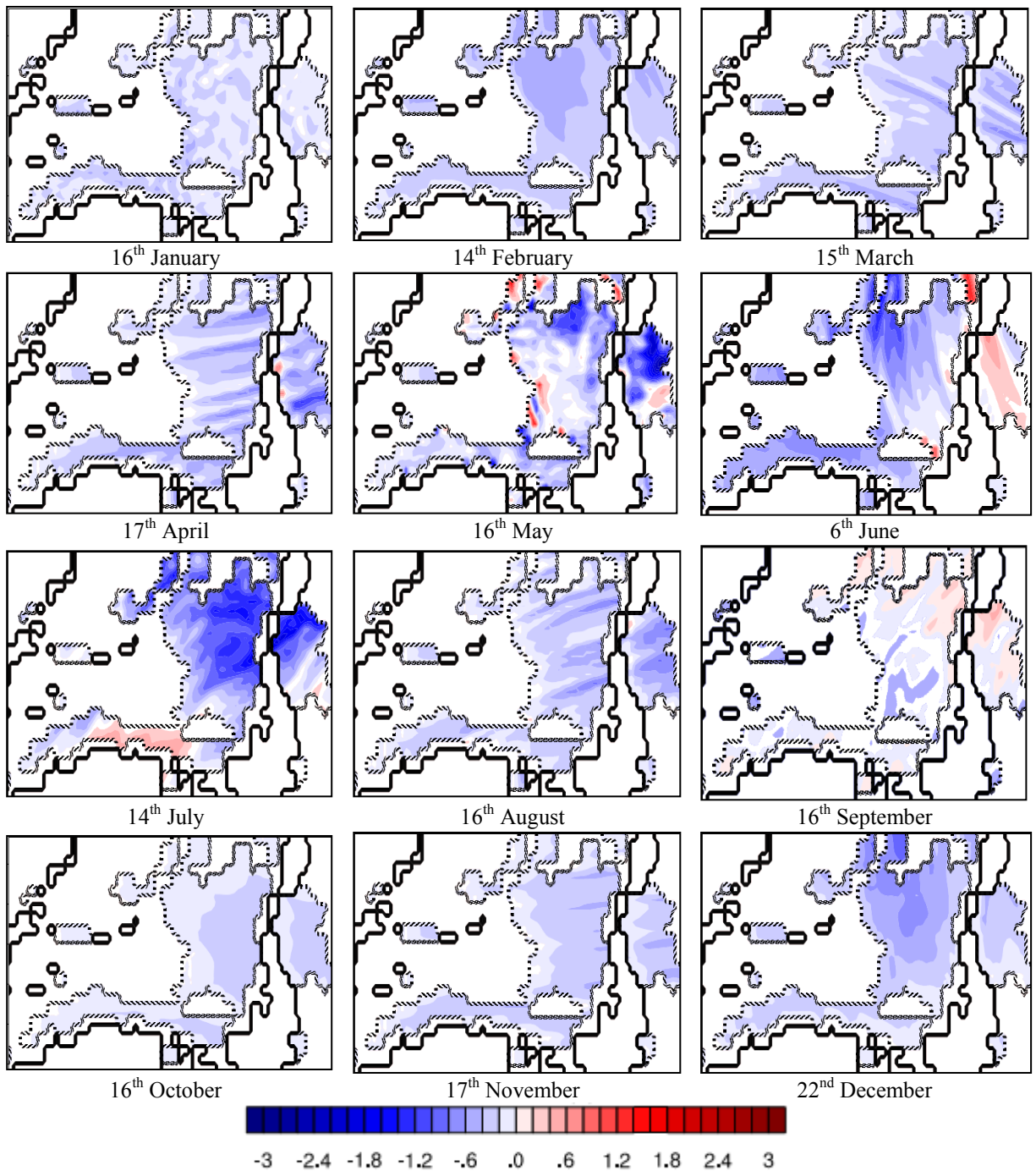


Figure 7-3. The 2-m air temperature difference (°C) in ALBEDO and CTRL on MTMD of all months of a year at 3 p.m. (simulation from 0000-2300 UTC for each day). Dashed lines represents the border of urban areas based on USGS (U.S. Census Bureau, Geography Division, 2011) and bold lines represents rivers in the domain (as shown in Figure 7-1.c). A small increase in the air temperature in some part of the city is observed because of the change in the wind pattern and an increase in the incoming solar radiation when the urban albedo is increased.

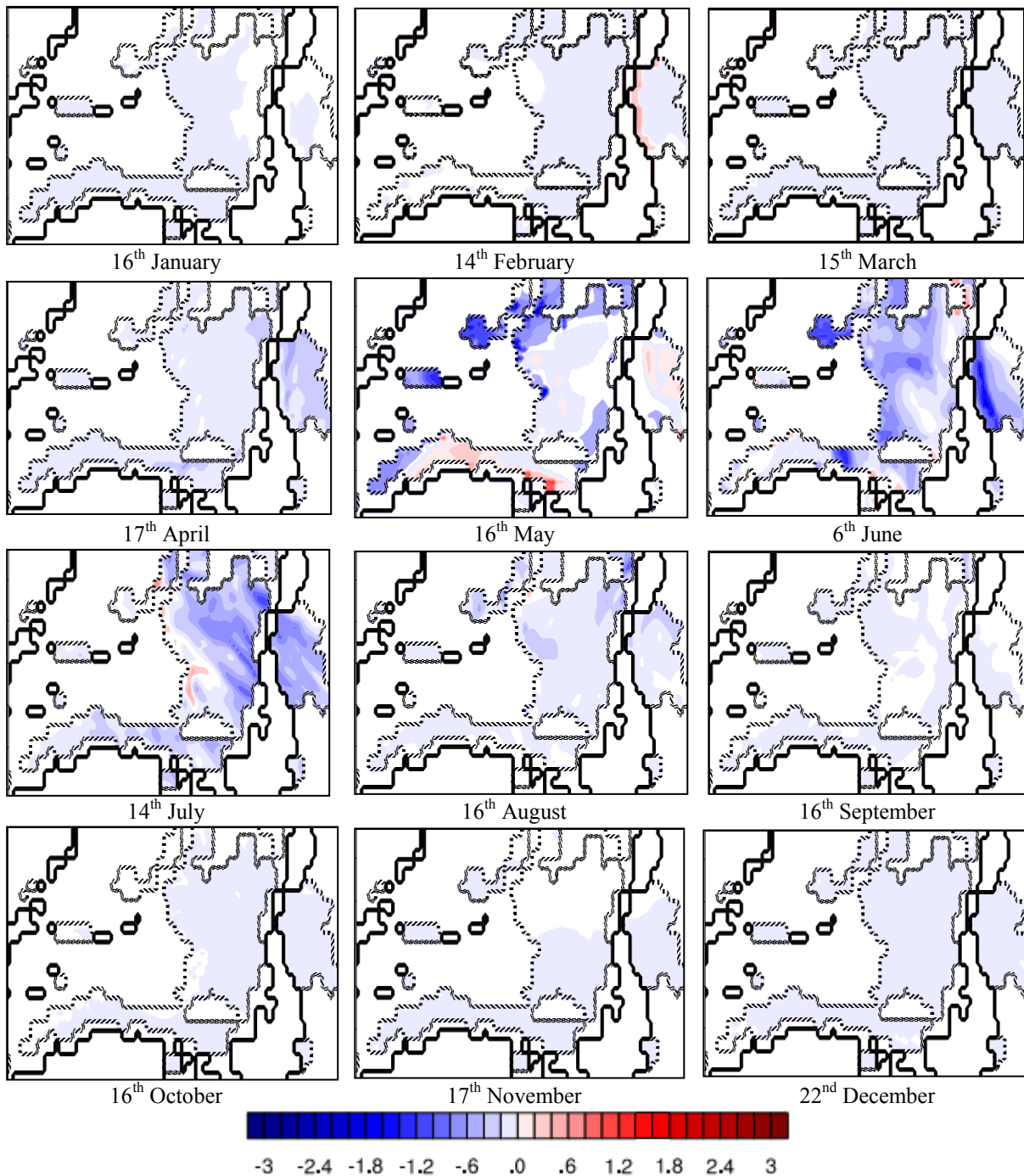


Figure 7-4. The 2-m air temperature difference (°C) in ALBEDO and CTRL on MTMD of all months of a year at 9 p.m. (simulation from 0000-2300 UTC for each day). Dashed lines represents the border of urban areas based on USGS (U.S. Census Bureau, Geography Division, 2011) and bold lines represents rivers in the domain (as shown in Figure 7-1.c). A small increase in the air temperature in some part of the city is observed because of the change in the wind pattern and an increase in the incoming solar radiation when the urban albedo is increased.

7.2.2. Energy consumption of buildings

Figure 7-5 shows the daily energy consumption difference in MTMD of summer months of the year by implementing reflective surfaces. The seasonal effect of increasing the albedo on the energy consumption of AC systems is small.

The maximum daily energy savings is about 0.29 Wh/m^2 of the roof area in July. The maximum heating penalty is as high as 0.15 Wh/m^2 in February. The energy penalty during the winter and swing season is negligible and the energy savings during the summer are evident. The net annual energy consumption difference in the urban area is about -100 Wh/m^2 ($\sim 10 \text{ kWh/100m}^2$ savings) without considering the snow on the roof.

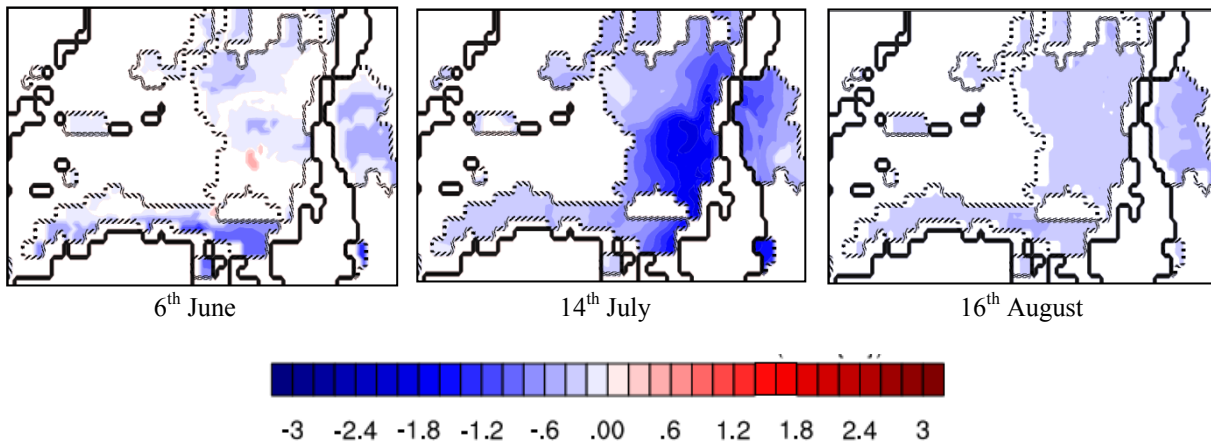


Figure 7-5. The daily-total energy consumption difference ($\text{W/m}^2\text{-h}$) in ALBEDO and CTRL on MTMD of summer months of 2005 (simulation from 0000-2300 UTC for each day). Dashed lines represents the border of urban areas based on USGS (U.S. Census Bureau, Geography Division, 2011) and bold lines represents rivers in the domain (as shown in Figure 7-1.c).

As shown in Table 3, the predicted expenditure for electricity and natural gas for heating contributes to the total air conditioning cost by approximately 53%, which is in conformance with the 52% figure reported by Zmeureanu (1995). Similarly, the heating contribution to the total energy consumption ($\sim 79\%$) is in agreement with Zmeureanu (1995), but the amount of cooling and heating are underestimated by the factor of 4. The underestimation of energy consumption using the current BEM compared to a well-evaluated model, namely “EnergyPlus,” was addressed by Bueno et al. (2011). The annual savings of $1 \text{ \$/100m}^2$ is predicted and the value would be increased by up to $4 \text{ \$/100m}^2$ considering the underestimation of the BEM. Based on the calculated energy consumption, as long as the electricity price ($\text{\$/kWh}$) is at least

three times more expensive than the natural gas price (\$/kWh) the increase in albedo is beneficial. In this calculation, the effect of snow on the roof is not considered, which potentially decreases the heating penalty during the winter (Hosseini and Akbari, 2014).

The maximum hourly cooling energy decrease is about 3 kWh/100m², while the maximum increase in hourly heating energy is about 0.6 kWh/100m². Determining the RMS of the energy consumption difference shows that the maximum increase and decrease occurs in the region at the east of the urban area (the regions where the air temperature has the maximum decrease).

Table 7-3. Annual, winter, and summer energy consumption and expenditure of buildings in CTRL, energy savings/penalty and money savings/penalty in ALBEDO. The gas price is 4.4 \$/GJ (Gaz Metro 2014) and the electricity price is 0.056 \$/kWh (Hydro Quebec 2014)

	Heating			Cooling		
	Year	Winter	Summer	Year	Winter	Summer
Energy consumption (kWh/100 m ²)	1327	800	0	341	0	258
Energy savings (-) or penalty (+) (kWh/100 m ²)	12	4	0	-22	0	-18
Expenditure (\$/100 m ²)	21	13	0	19	0	14
Money savings (-) or penalty (+) (\$/100 m ²)	0	0	0	-1	0	-1

Using BEM without a weather model, one cannot consider the climatic effect of changing the albedo of roofs. I coupled the BEM and the weather model (i.e., WRF) to investigate the direct (decreasing the energy absorption by urban surfaces) and indirect (decreasing the air temperature of the urban canopy) effect on the energy consumption of buildings. Hosseini et al. (2014) estimated the expenditure penalty of using cool roofs to be about 2 \$/100m² (only calculating the direct effect by using comprehensive BEM); while my results show the expenditure saving of about 1 \$/100m² (the indirect effect is considered without using comprehensive BEM).

7.3. Discussion on the predicted air temperature and energy consumption of HVAC systems

Urban climate simulation using fine-resolution methods is a computationally expensive process. Hence, episodic simulation is selected as a technique to capture the urban heat island and determine the effect of mitigation strategies. This method treats the rest of a month the same as the one selected day, without considering climate variability. As a result, some of the crucial

information might be missed; for example, in a month I might have cooling in some days and heating in some other days, but in this method all days are considered to be the same as a selected day. Also, investigating the accurate effect of mitigation strategies in cold climates is even more challenging because there is some heating days in summer. I used the same model ensemble for simulating the urban climate on the 21st of each month to compare the effect of selecting appropriate episodes on the calculated energy consumption of buildings.

Increasing the albedo of urban areas has an effect on their air temperature as well as that of their surroundings. To determine the effect of increasing the albedo in Domain 3, the average, maximum, and minimum of the variables in the 12 days of simulations is calculated (Table 2). The daily averaged 2-m air temperature is decreased by 0.1 °C in the whole domain and by 0.7 °C in some grid cells, while in some grid cells it is increased up to 0.5 °C. The daily average energy consumption is increased by 0.01 W/m². The maximum and minimum change of the daily average energy consumption is about 0.6 W/m². The sensible heat flux from the ground, as the measure of urban heat island, is decreased by an average of 9.2 W/m². On the average the cloud fraction, the downward shortwave radiation (directly related to cloud fraction), and the PBL height are not changed significantly. However, in some grid points the cloud fraction, the downward shortwave radiation, and the PBL height vary by as much as 30%, 115.2 W/m², and 440 m, respectively.

Table 7-4. Average, maximum, and minimum of the difference of daily averaged 2-m air temperature (°C), Energy consumption for air conditioning (W/m²), Sensible heat flux from the ground (W/m²), Downward shortwave radiation on the ground (W/m²), Cloud fraction (%), and PBL height (m) in ALBEDO case and CTRL case for Montreal (Canada) on 21st of each month in 2005.

Parameter	Average	Max	Min
2-m air temperature (°C)	-0.1	0.5	-0.7
Energy consumption for air conditioning (W/m ²)	0.01	0.64	-0.60
Sensible heat flux from the ground (W/m ²)	-9.2	51.6	-105.7
Downward shortwave radiation on the ground (W/m ²)	1.2	115.2	101.9
Cloud fraction (%)	0	30	-32
PBL height (m)	-3.6	440.9	-318.7

7.3.1. Air temperature

The daily averaged 2-m air temperature has the tendency to be decreased in the urban areas, while it is increased in some of the surrounding areas. The effect of increasing the albedo was more significant during the summer (June, July, and August); its effect in winter (January,

February, and December) is negligible. As illustrated in Figure 7-6, only in May is the increase of the temperature in rural areas noticeable.

In the morning (at 9 a.m. LST), the maximum air temperature decrease occurs in July up to 3 °C. In all months the morning air temperature is decreased almost in the whole domain, except in May where the air temperature of the rural areas is increased. In the months of the swing season the air temperature variation is not consistent.

In the afternoon (at 3 p.m. LST), the 2-m air temperature difference is negligible in winter. In summer in most parts of the urban area the air temperature is decreased by 1 °C. In May, the 2-m air temperature of some grid cells is decreased by 2 °C, while in some others it is increased by the same magnitude. In the evening (at 9 p.m. LST), the 2-m air temperature difference in March, April, and May is noticeable (changing by ± 2 °C).

7.3.2. Energy consumption of buildings

The effect of increasing the albedo in summer and winter is small except for the month of June, where the heating energy is needed to maintain the desired temperature (Figure 7-7). In July the energy consumption is changed by as much as 0.3 W/m². However, in swing season the energy consumption is changed more significantly. The maximum and minimum value for the energy consumption by the AC system is 0.6 W/m², in May. The maximum increase of the total energy consumption in the whole domain (not in the number of grid cells) appears to occur in March. On the other hand, in April, the decrease of the total energy consumption is maximal (about 2.5 W/m²). In general, increasing the albedo results in a penalty in terms of energy consumption (considering the price of heating and cooling is important for cost-benefit analysis, which is not discussed in this paper). The energy consumption of HVAC systems of buildings is calculated using different meteorological parameters such as air temperature, solar radiation, and wind speed. Therefore, the air temperature does not necessarily correlated with energy consumption of HVAC systems. For example, more energy consumption is observed on 21th of April than other months of the year despite a smaller decrease in the air temperature.

The net annual energy consumption difference in the urban area is about +90 Wh/m² (9 kWh/100m²) without snow on the roof. The maximum hourly cooling energy decrease is about 4 Wh/m², while the maximum increase in hourly heating energy is about 2 Wh/m². The peak

energy reduction in that area is estimated to be 1.4 Wh/m². Hosseini et al. (2014) used a comprehensive BEM (i.e., DOE-2) to calculate the energy consumption of buildings (with dark and cool roofs) by considering snow on the roof. In that study, the annual energy penalty of using cool roofs was estimated to be 200 kWh/100m² (18 \$/100m² conditioning expenditure in a year where the electricity price was 0.089 \$/kWh) when the snow on the roof is not considered. The annual energy savings of about 190 kWh/100m² (17 \$/100m² conditioning expenditure in a year) was calculated by considering the snow on the roof. Here, the energy calculation of the buildings in the urban area for the 21st of each month is performed without considering the snow on the roof; the annual energy penalty of using cool roofs is estimated to be 9 kWh/100m² (8 \$/100m² conditioning expenditure in a year).

7.3.3. Limitations

The BEM coupled with WRF is a simplified model, compared to other complex models, in terms of dynamic operation of HVAC systems. The BEM has shown a very good performance in predicting the heat emission from buildings to the canopy in different studies (Salamanca et al., 2010a; Bueno et al., 2011) in spite of rough estimation of energy consumption of buildings. On the other hand, analyzing the average performance of HVAC systems of buildings in an urban area has not been evaluated in any of the previous research, owing to the large detailed data needs.

Lastly, the flat rates for utilities are considered without including the peak price of the electricity, which is much higher than the regular rate. Moreover, tax and other charges that might be added by the government of Quebec are also neglected. Since both energy and expenditure savings result from albedo enhancement, taking peak demand price, tax, and other charges into account may increase the total savings.

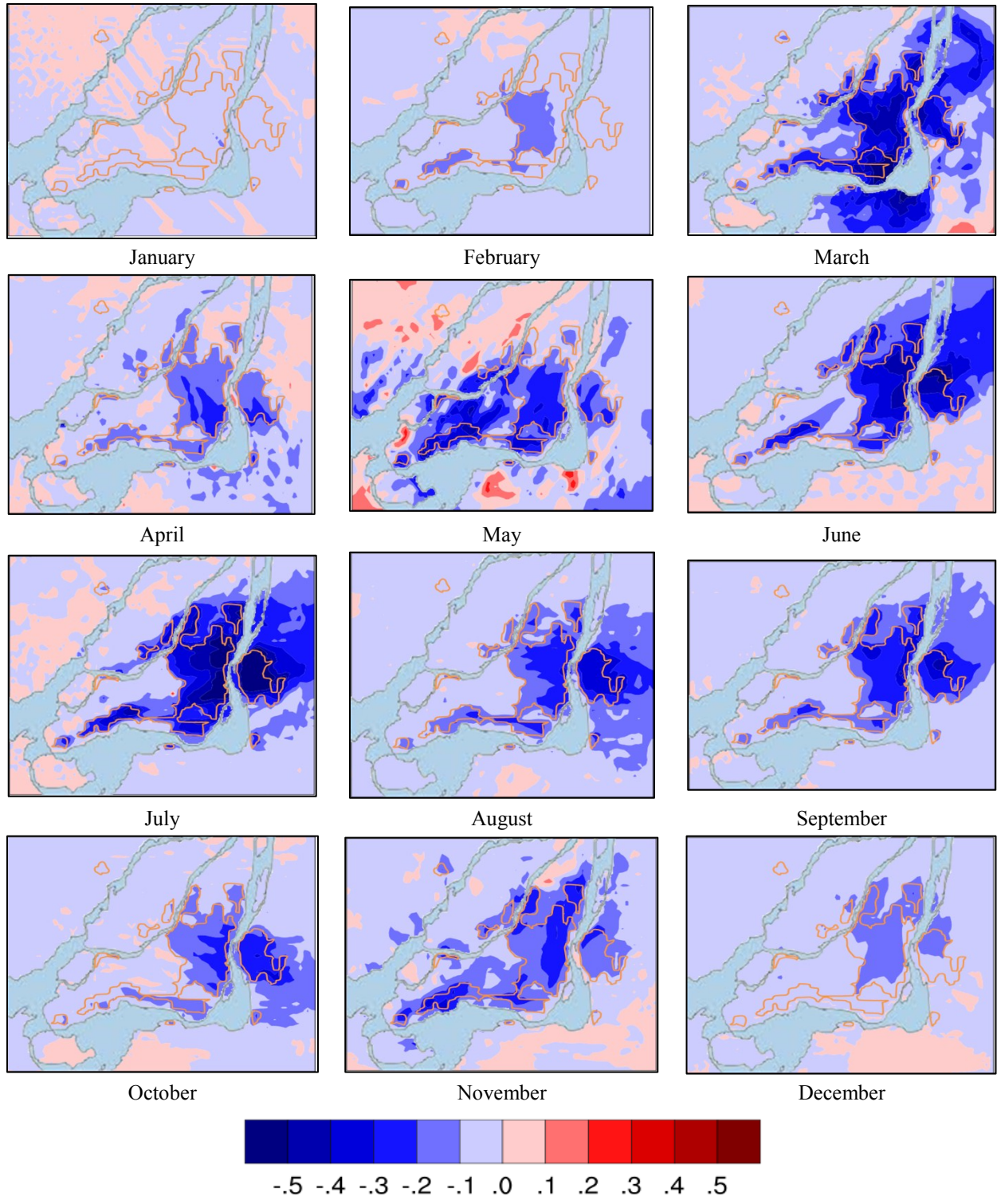


Figure 7-6. Difference of the daily averaged 2-m air temperature ($^{\circ}\text{C}$) in ALBEDO and CTRL cases on 21st day of all months of a year (simulation from 0000-2300 UTC for each day). Orange lines represents the border of urban areas based on USGS (U.S. Census Bureau, Geography Division, 2011) and the light blue areas with black lines represents rivers in the domain (as shown in Figure 7-1.c).

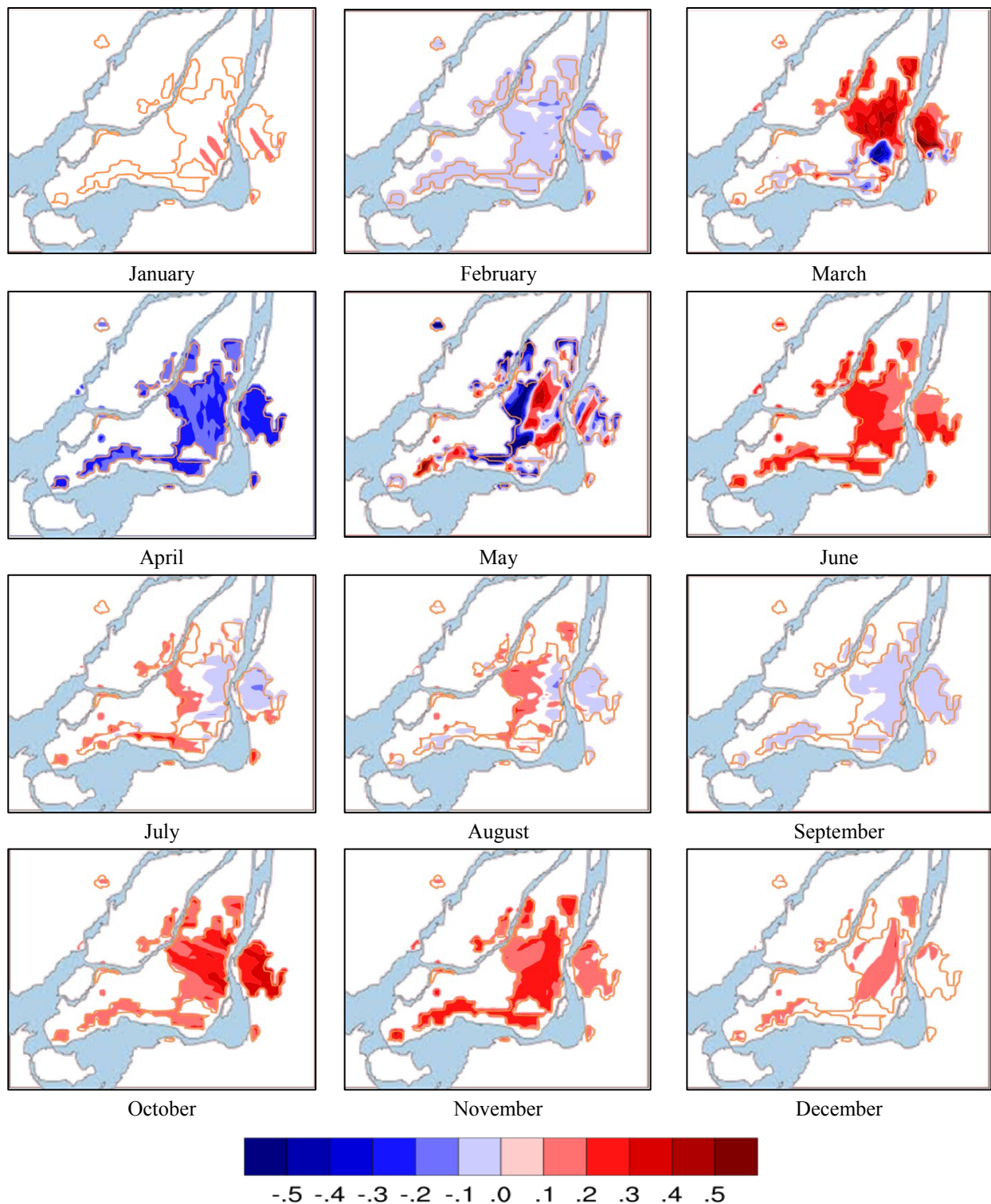


Figure 7-7. Difference of the daily average energy consumption of buildings for air conditioning (W/m^2) in ALBEDO and CTRL cases on 21st day of all months of a year (simulation from 0000-2300 UTC for each day). Orange lines represents the border of urban areas based on USGS (U.S. Census Bureau, Geography Division, 2011) and the light blue areas with black lines represents rivers in the domain (as shown in Figure 7-1.c).

7.4. Conclusion of the seasonal evaluation of an increase in the urban albedo

Increasing the albedo of urban surfaces in Montreal is modeled by coupling mesoscale, urban canopy, and building energy models. Simulations are performed for all months of 2005, with a typical meteorological day of each month representing the whole month. The albedo of roof, walls, and road is increased from 0.2 to 0.65, 0.6, and 0.45, respectively. The daily averaged urban heat island intensity of the urban area is decreased by about 0.1 °C. The annual energy consumption of the AC systems is decreased by 10 kWh/100m² of the roof area, and annual energy expenditure savings of 1 \$/100m² is estimated. The maximum reduction of the urban heat island intensity and energy consumption is about 3 °C (in the morning during the summer) and 3 Wh/m², respectively. The maximum daily averaged air temperature reduction is about 0.3 °C in April. The air temperature reduction has a significant effect on mitigating the heat island and improving air quality, comfort, and health. Using the reflective surfaces as a mitigation strategy for urban heat island control in cold climate is an effective way of decreasing the temperature. In terms of energy expenditure, increasing the albedo yields a small savings.

Chapter Eight: Energy Saving Potentials of Commercial Buildings by Urban Heat Island Reduction Strategies in Montreal

Considering limitations in the simple BEM that I used in Chapter Seven, there is a need to quantify energy savings or penalties of using reflective roofs and walls in buildings as well as reflective pavement, throughout a year. Although the BEM coupled to WRF is simple in terms of calculating the energy consumption of buildings, it determines the heat emission from buildings to the canopy well (Salamanca et al., 2010b; Hamdi and Schayes, 2007). The output of meteorological simulations in Chapter Seven is used to modify the weather file of the detailed BEM.

8.1. Methodology of the detailed energy calculation in buildings

In this section the structure and calculation algorithm of the detailed BEM (DOE-2) is explained. Then, the prototype buildings (small office, medium office, large office, and retail store) are described. Afterwards, snow properties are discussed and the measured snow depths during 2005 are presented. Lastly, an algorithm to modify the weather file is discussed.

8.1.1. Simulation tool and its structure

I used DOE-2.1.E (LBNL, 1982) to simulate four prototype buildings (small office, medium office, large office, and retail store). DOE-2 is well known for its capability of considering complicated dynamics of HVAC systems, and it is widely used by building professionals and the scientific community in order to analyze energy efficiency of given designs or efficiency of new technologies. DOE-2 consists of one translation subprogram (BDL processor) to interpret text input of the user into a language known to the program interface and four simulation subprograms—namely, LOADS, SYSTEMS, PLANT, and ECONOMICS.

The LOADS simulator calculates peak zone loads of a building. In LOADS, a set point for inside temperature is assigned and the heat transfer between zones and between each zone and ambient are calculated. The SYSTEMS simulator manages the operation of all HVAC components (including fans, coils, economizers, humidifiers, etc.). The PLANT simulator determines the operation of chillers, boilers, electrical equipment generators, and so on. The ECONOMICS simulator calculates energy and life-cycle costs. These subprograms are performed sequentially

so that the output of LOADS becomes the input for HVAC (including SYSTEMS and PLANT) and its output is then used as the input for ECONOMICS to estimate the air conditioning expenditure.

For more accurate calculation, DOE-2 applies response factors, numbers that are used to determine the transient (dynamic) heat flow through roofs and exterior walls as they react to randomly fluctuating climatic conditions. Sullivan and Winkelmann (1998) evaluated the consistency of DOE-2 calculations with real case measurements in seven prototypical buildings. Their results showed a difference from 1% to 12%, varying by the building type.

8.1.2. Roof modeling in DOE-2

A roof can be modeled as either a delayed or a quick structure. In delayed modeling the roof is modeled by defining the roof structure layer, simply using DOE-2 library materials or thermal properties of each layer. In this method all the thermal properties of layer, including their heat capacitance, are taken into account in the heat transfer equation. The less accurate way of roof modeling is to just define the overall U-value of the roof; however, thermal capacity of the roof layers will be neglected. The latter is applied to modeling the building roof with DOE-2 because of the lack of sufficient information on heat capacity of snow regarding the snow type and thickness. The heat equation through the “Quick Roof” can be written in the following form (eq. 8-1). For more details on modeling the snow on the roof see Hosseini and Akbari (2015).

$$H = U_{film} \times A_{roof} \times (T_s - T_{zone}) \quad (8-1)$$

where, H is the sensible heat, U_{film} is the combined conductance of the roof, inside film (and snow when there is snow on the roof), A_{roof} is the roof surface area, T_s is the outside roof surface temperature (snow surface temperature when there is snow on the roof), and T_{zone} is the zone space temperature.

8.1.3. Description of the buildings

Four commercial buildings were studied as prototype buildings with flat roofs. Each of the office building prototypes consists of six zones for each floor (four perimeters, one central, and a plenum zone) except for the old small office in which the plenum zone is eliminated. The retail building has five zones (core, front, back space, point of sale, and entry) and no plenum. Each prototype is simulated once with gas heating and electric cooling (using variable air volume,

VAV, for large offices and packaged single zone for others) and once with all-electric HVAC systems (using packaged terminal air conditioner with heat pump for heating). Three vintages were considered for each building: old construction with old HVAC systems (pre-1980), old construction with new HVAC systems, and new construction with new HVAC systems. The vintages are different in the case of thermal insulation, operation schedule, windows thermal conductance and shading coefficient, infiltration rate (leakage) through the building envelope, type and efficiency of HVAC system, and lighting intensity. The details of the building envelope characteristics and HVAC-systems specifications can be found in Hosseini (2015), and are summarized in Table 8-1 and Table 8-2. In building energy simulations, buildings are isolated from other surrounding buildings.

8.1.3.1. Small office building

The small single story has an area of 511 m² with eight evenly distributed windows on left and right walls (four windows on each side), and twelve windows on back and front walls (six windows on each side), and a glass door on the front wall. Each window has a dimension of 1.5 m × 1.8 m (height × width). The window fraction is 24.4% for south and 19.8% for the other three orientations. No plenum is assumed for the old construction and the floor-to-roof height is considered 3 meters; whereas, for the new construction, the floor-to-plenum height is assumed to be 2.7 m with 0.3 m height for plenum. In addition, the exterior wall system is steel frame for the old construction while wood frame is considered for new construction.

8.1.3.2. Medium office building

The medium office is a three-story building with 4985 m² overall floor area. Windows are evenly distributed all the way among all the four sides. Window sill height is 1 m and window-to-wall ratio is 33%. Moreover, floor-to-ceiling height is 2.75 m plus a 1.2 m height of plenum. In both old and new constructions, exterior walls are steel frame. For the medium office building with old construction, fifteen systems serve the fifteen zones; whereas, in the new construction, there are only three systems serving the zones (the core zones as the main control zones and the perimeters as subzones). Core zones are heated by gas furnace and perimeters are heated by electric reheat coils.

8.1.3.3. Large office building

The large office is a three-story building with 14515 m² overall floor area. Window dimensions, fractions, and locations are the same as for the medium office. The exterior wall system, however, is wood frame in both the old and the new construction. As a gas heating system, a central VAV system with boiler and air-cooled reciprocating chiller serve all the fifteen zones.

8.1.3.4. Retail store building

The single-story medium retail store has 2299 m² floor area. Windows are just in the street-facing façade (southern side wall) and the window fraction is 7.1% (25% window-to-southern wall ratio) with glazing sill height of 1.5 m. There is no ceiling for either construction, and the floor-to-roof height is 6.1 m. The exterior wall system for the old construction is steel frame while it is concrete block for the new construction. For the retail building with a gas heating system, the entry zone is heated by an electric unit heater in the old construction and a furnace unit heater in the new construction.

Table 8-1. General characteristics of prototype buildings and HVAC systems

Characteristic	Old Vintage	Old Vintage New HVAC	New Vintage
Construction			
Floor Materials	0.20 m (8") Heavy Concrete Slab-On-Grade		
Roof U-Value (W/m ² K)	0.35		0.18
Wall U-Value (W/m ² K)	0.845		0.244
Window Characteristics			
Number of Panes	2	2	2
Shading Coefficient	0.47		0.44
Glass U-Value (W/m ² K)	2.96		1.969
Interior Loads			
Occupancy (m ² /Person)	18.5		16.5
Interior Lights (W/m ²)	19.3		9.6
Miscellaneous (W/m ²)	8		6.7
HVAC System 1			
Schedule	Variable Air Volume (VAV) 7 am – 10 pm Weekdays Jan1 – Dec 31		
Ventilation	Supply		
Capacity	Zonal/Local		
Efficiency	0.58	0.61	
Economizer	Temperature		
Economizer Limit Temperature(°C)	28		
Outside Air(m ³ /h/person)	36		
Natural Ventilation	No		
Cooling Type	Air-Cooled Hermetic Reciprocating Chiller		
Capacity	Zonal/Local		
COP	5.12	6.09	
Setpoint (°C)	24		
Setup (°C)	26.7		
Heating Type	Natural Gas Hot Water boiler		
Capacity	Zonal/Local		
Efficiency (%)	76	80	
Setpoint (°C)	21		
Setup (°C)	15.6		
HVAC System 2			
Cooling Type	Packaged Single Zone (PSZ) Direct-Expansion		
Capacity	Zonal/Local		
COP	See Deru et al (2011)	ASHRAE 90.1	
Heating Type	Gas Furnace		
Capacity	Zonal/Local		
Efficiency (%)	78	80	
HVAC System 3			
Cooling Type	Packaged Terminal Air Conditioner (PTAC) Direct-Expansion		
Capacity	Zonal/Local		
COP	See Deru et al (2011)	ASHRAE 90.1	
Heating Type	Heat Pump		
Capacity	Zonal/Local		
COP	See Deru et al (2011)	ASHRAE 90.1	

Note: Most building and systems characteristics for Old Vintage (with Old and New HVAC) are the same, only changes are shown.

Table 8-2. Specific characteristics for office building and retail building prototypes

Characteristic	Old Vintage	Old Vintage New HVAC	New Vintage
Large Office Wall U-value (W/m ² K)	0.822	---	---
Retail Store Construction			
Wall U-value (W/m ² K)	0.817		0.244
Interior Loads			
Occupancy (m ² /Person)			
Interior Lights (W/m ²)	6.1, Back Space 27.8 36.1, Back Space 12.4		6.1 18.2, Back Space 15
Miscellaneous (W/m ²)	Core and Front 3.2 Point of Sale 21.5 Back Space 8		

Note: Most building and systems characteristics for Old Vintage (with Old and New HVAC) are the same, only changes are shown.

8.1.4. Snow properties

Snow on the roof, which is not considered in UCM options of WRF, can decrease the thermal conductance of the roof and naturally increase the roof albedo. Using the methodology developed by Hosseini and Akbari (2014), I considered snow on the roof for energy calculation of buildings (Figure 8-1). Snow on the ground (the same depth is used for the snow on the roof), is cataloged in four types based on Gray (1970) and Sturm et al. (1997): (1) very loose, (2) newly fallen, (3) wind-packed, and (4) late-winter packed. The first two types are considered for the first couple of weeks (20-Nov-2005 to 04-Dec-2005), followed by a long period of wind-packed snow (04-Dec-2005 to 14-Jan-2005), and ended by late-winter-packed snow on 3 April. At the beginning of the snow season, the depth of the snow is below 5 cm and eventually increases up to 34 cm in mid-December. Maximum average snow depth occurs during December and March with 15 cm and 22 cm, respectively. To calculate daily snow solar reflectivity I followed a model by Flanner et al. (2007, 2009) using Snow, Ice, and Aerosol Radiation (SNICAR). SNICAR is an online snow solar calculator mostly affected by snowpack density and thickness, albedo of the underlying ground (roof) and snow grain effective grain radius.



Figure 8-1: snow depth (cm) on the ground (Environment Canada, 2014) in Montreal, 2005, categorized in four snow types; very-loose, newly-fallen, wind-packed, and late-winter-packed

8.1.5. Weather file for DOE-2

For CTRL the weather data required by DOE-2 are extracted from the Canadian Weather Energy and Engineering Datasets (CWEEDS; Environment Canada, 2008) for Pierre Elliott Trudeau International Airport. Table 8-1 provides the statistics of the weather condition in CTRL including average dry-bulb temperature ($^{\circ}\text{C}$), average wet-bulb temperature ($^{\circ}\text{C}$), average daily max. temperature ($^{\circ}\text{C}$), average daily min. temperature ($^{\circ}\text{C}$), heating degree days (base 18.3°C), cooling degree days (base 18.3°C), maximum temperature ($^{\circ}\text{C}$), average wind speed (m/s), average sky cover (tenth), average relative humidity at 4pm (%), average daily total horizontal solar (Wh/m^2), and average max. hourly total horizontal solar (Wh/m^2). For ALB, the same file is modified according to the results of simulations described in Chapter Seven for MTMD. The air temperature, relative humidity, and wind speed in the weather file in a month is changed by adding or subtracting the difference between CTRL and ALBEDO in MTMD simulations. Sky cover is changed according to the change in cloud cover of MTMD simulations having values from 1 to 10 (cloud cover of 10 is left unchanged, even if an increase in cloud cover is predicted). Solar radiation on the ground is assumed to vary with the same ratio as of calculated solar radiation in ALBEDO to solar radiation in CTRL of MTMD simulations. All changes are calculated on an hourly basis. Table 8-2 illustrates the difference between the variables in CTRL and ALBEDO, through the year. The air temperature is decreased in all months between 0.1°C to 0.4°C . The average solar radiation on the horizontal surface is increased between $6 \text{ Wh}/\text{m}^2$ (in November and December) to $26 \text{ Wh}/\text{m}^2$ (in June and July).

Table 8-3. Summary of the weather statistics in CTRL

	Jan	Feb	Mar	Apr	May	Jun	Jul	Aug	Sep	Oct	Nov	Dec	Year
Average Dry-bulb Temperature (°C)	-11.1	-6.4	-2.9	7.5	11.7	21.5	22.5	21.7	17.5	9.9	2.6	-5.4	7.5
Average Wet-bulb Temperature (°C)	-12.4	-8.1	-5.6	3.4	7.6	16.9	17.9	17.6	14.2	7.7	0.6	-6.9	4.5
Average Daily Max Temperature (°C)	-7.1	-2.4	0.8	12.6	15.8	26.1	26.7	26.1	21.8	13.1	6.6	-2.6	11.5
Average Daily Min Temperature (°C)	-15.1	-11.0	-7.5	2.2	7.2	16.3	17.2	17.0	12.6	6.5	-1.3	-8.9	3.0
Heating Degree Days (base 18.3 °C)	1640.5	1261.5	1210.5	591	380.5	39	8	16	115	486	846	1344.5	7938.5
Cooling Degree Days (base 18.3 °C)	0	0	0	0	0	196	208	195.5	53.5	11.5	0	0	664.5
Maximum Temperature (°C)	8.9	5.6	15.0	22.8	26.1	32.2	32.2	31.7	28.9	26.1	18.3	3.9	32.2
Average Wind Speed (m/s)	4.0	3.3	4.4	4.4	4.3	3.6	3.3	3.3	3.9	4.2	5.1	4.3	4.0
Average Sky Cover (tenth)	6	6	5.7	6.2	6.7	6.4	5.4	5.8	5.2	7.2	7.9	7.3	6.3
Average Relative Humidity at 4pm (%)	52.7	51.8	43.6	45.9	50.1	54.7	54.3	55.7	59.4	67.1	63.8	60.7	55
Average Daily Total Horizontal Solar (Wh/m ²)	77	115	185	187	212	253	254	213	166	90	58	50	155
Average Max. Hourly Total Horizontal solar (Wh/m ²)	362	477	662	616	671	735	784	698	566	345	279	245	537

The maximum temperature is decreased by 0.6 °C in April, June, July, August, and December. The average annual increase in the solar radiant on a horizontal surface is about 16 Wh/m², with about 1% increase in all months. The decrease in surface temperature caused a negligible increase in the relative humidity near the surface at 4 p.m. (maximum of 3.3% in February). The wind speed is also slightly decreased throughout the year. As discussed in Chapter Seven, increasing the urban albedo may decrease the cloud cover, which is inversely proportional to the incoming solar radiation. The cloud cover is decreased in all months except March, and the

annual decrease is 0.7. As expected, the number of cooling days with the base of 18.3 °C is decreased, whereas the number of heating days with the same base is increased.

Table 8-4. Summary of the weather statistics difference between CTRL and ALB

	Jan	Feb	Mar	Apr	May	Jun	Jul	Aug	Sep	Oct	Nov	Dec	Year
Average Dry-bulb Temperature (°C)	-0.1	-0.2	-0.2	-0.4	-0.3	-0.2	-0.1	-0.4	-0.2	-0.1	-0.1	-0.2	-0.2
Average Wet-bulb Temperature (°C)	-0.1	-0.1	-0.1	-0.2	-0.1	-0.1	0.0	-0.1	-0.1	-0.1	-0.1	-0.2	-0.1
Average Daily Max Temperature (°C)	-0.1	-0.2	-0.2	-0.5	-0.2	-0.1	-0.3	-0.4	-0.3	-0.1	-0.2	-0.2	-0.2
Average Daily Min Temperature (°C)	-0.1	-0.1	-0.1	-0.2	-0.1	-0.1	0.2	-0.2	-0.2	0.0	0.0	-0.1	-0.1
Heating Degree Days (base 18.3 °C)	5.5	4.5	7.5	17.5	10.0	1.0	0.5	2.0	8.5	4.0	6.0	9.5	76.5
Cooling Degree Days (base 18.3 °C)	0.0	0.0	0.0	0.0	0.0	-4.5	-3.5	-17.0	-3.5	-0.5	0.0	0.0	-29.0
Maximum Temperature (°C)	0.0	0.0	0.0	-0.6	0.0	-0.6	-0.6	-0.6	0.0	0.0	0.0	-0.6	-0.6
Average Wind Speed (m/s)	-0.1	-0.1	-0.1	-0.3	-0.2	-0.1	-0.1	-0.2	-0.1	0.0	-0.1	-0.1	-0.1
Average Sky Cover (tenth)	-0.2	-0.3	0.5	-0.3	-1.6	-1.7	-0.7	-1.6	-0.8	-1.2	-0.7	-0.2	-0.7
Average Relative Humidity at 4pm (%)	0.7	3.3	1.8	0.1	0.3	0.0	1.9	1.5	1.2	0.8	2.1	1.8	1.3
Average Daily Total Horizontal Solar (Wh/m ²)	9	13	20	20	22	26	26	22	18	10	6	6	16
Average Max. Hourly Total Horizontal solar (Wh/m ²)	54	69	102	91	96	104	114	103	81	46	40	34	78

8.1.6. Scenarios

There are three sets of simulations designed for each commercial building (small office, medium office, large office, and retail store) with three different construction-HVAC characteristics (old construction with old system, old construction with new system, and new construction with new system) and different heating systems (gas heating and heat pump). The first set evaluates the energy consumption of a dark roof and walls (reflectivity of 0.2) with the weather file of CTRL.

The second set determines the direct effect of implementing reflective roof and walls (0.65 as the roof reflectance and 0.6 as the wall reflectance) on the energy consumption of buildings using the weather file of CTRL. The third set estimates the direct and indirect effect of increasing urban albedo on the energy consumption of buildings using the weather file of ALBEDO. Energy consumption for heating, cooling, and ventilation is calculated and the total air conditioning expenditure is estimated based on the flat rates of 9.38 cents/kWh and 38.95 cents/therm for electricity and natural gas, respectively.

8.2. Simulations results and discussions

Here, I present the energy consumption and energy expenditure of HVAC systems for the selected building prototypes. A total of 72 simulations are performed (4 building prototypes \times 3 constructions \times 2 heating systems \times 4 roof reflectivity and weather files).

8.2.1. Small office building

Table 8-3 shows the energy consumption of the small office. In the old construction with an old system using gas heating, the cooling savings of increasing the surface albedo is more than the penalties for heating and ventilation that result in with 14 \$/100m² money savings for the direct effect and an additional 13 \$/100m² due to the indirect effect. Moreover, considering the change in the weather condition results in more annual energy savings (by 112 kWh/100m²) and less annual energy penalties (by 27 kWh/100m²). On the other hand, using heat pump for space heating increases the heating penalty (by 218 kWh/100m²) because the heating system is mostly working on a part-load basis. The old construction with a new system using heat pump also has a higher heating penalty in ALBEDO (by 15 kWh/100m²) for the same reason, but it has higher cooling savings (by 48 kWh/100m²). For this case, the total expenditure penalty is reduced from 15 \$/100m² to 12 \$/100m². In the new construction with new system, expenditure savings is increased by 6 \$/100m² when gas heating is used and the expenditure penalty (-2 \$/100m²) is turned into expenditure savings (5 \$/100m²) when the heat pump is used, due to the indirect effect. In general, the increase in solar radiation reduces the heating penalty.

Table 8-5. Summary of the energy consumption and energy expenditure of a small office with different HVAC systems and building characteristics using dark roof, white roof with weather data in CTRL, and white roof with weather data in ALBEDO in Montreal, 2005. Values are normalized with 100 m² of roof area

Case	Gas heating (heating in GJ/100 m ² , cooling in kWh/100 m ²)					Heat pump (heating and cooling in kWh/100 m ²)				
	Dark CTRL	White CTRL	White ALB	Saving CTRL	Saving ALB	Dark CTRL	White CTRL	White ALB	Saving CTRL	Saving ALB
Old construction with old system										
Heating energy	63	65	65	-2	-2	12343	12567	12785	-224	-442
Cooling energy	2010	1734	1622	276	388	1832	1605	1484	227	348
Ventilation energy	4607	4641	4614	-34	-7	212	213	214	0	-2
Expenditure (\$/100 m ²)	852	838	825	14	27	1349	1349	1359	0	-9
Old construction with new system										
Heating energy	61	64	64	-2	-2	12214	12629	12643	-414	-429
Cooling energy	1723	1486	1390	237	333	1615	1356	1308	259	307
Ventilation energy	4607	4641	4614	-34	-7	201	203	203	-2	-2
Expenditure (\$/100 m ²)	821	810	798	11	22	1316	1331	1328	-15	-12
New construction with new system										
Heating energy	27	28	27	-1	0	4103	4233	4181	-130	-78
Cooling energy	1150	1043	1003	107	147	1092	988	958	105	134
Ventilation energy	1451	1453	1445	-3	5	74	71	73	3	1
Expenditure (\$/100 m ²)	344	337	331	7	13	494	496	489	-2	5

8.2.2. Medium office building

Table 8-4 provides the output of BEM for the medium office building prototype. For all cases, considering the weather in ALBEDO increases the ventilation energy penalty and the cooling savings, whereas it decreases (or does not change) the heating penalty. When the heat pump is used in all buildings the expenditure savings is dramatically increased. The reason for high savings is that the sizing procedure is performed for the dark roof and wall with the CTRL weather condition, then the size is fixed for the rest of simulations. In this way, a valid comparison of the effect of a change in building properties on the energy consumption of buildings is ensured. That means, even though HVAC systems are well designed for the dark roof and walls, still savings are gained by increasing the reflectivity of exterior surfaces. Moreover, consider that the actual weather condition (in this case ALBEDO) would result in a

better performance of HVAC systems with respect to their design efficiency. There is no change in the heating energy consumption of the medium office by modifying the weather file. This means that for a building with the characteristics of the medium office with gas heating system (its performance is less sensitive to the energy load), the increase in solar heat gain compensates for the heat transfer due to the decrease in the air temperature. The expenditure savings in the old construction building, considering the indirect effect, is increased by 26 \$/100m² and 21 \$/100m² for the old system and new system, respectively. On the other hand, in the new construction with gas heating, the expenditure savings is decreased by 1 \$/100m² because of the penalty in ventilation energy consumption.

Table 8-6. Summary of the energy consumption and energy expenditure of a medium office with different HVAC systems and building characteristics using dark roof, white roof with weather data in CTRL, and white roof with weather data in ALBEDO in Montreal, 2005. Values are normalized with 100 m² of roof area

Case	Gas heating (heating in GJ/100 m ² , cooling in kWh/100 m ²)					Heat pump (heating and cooling in kWh/100 m ²)				
	Dark CTRL	White CTRL	White ALB	Saving CTRL	Saving ALB	Dark CTRL	White CTRL	White ALB	Saving CTRL	Saving ALB
Old construction with old system										
Heating energy	81	83	83	-2	-2	16473	16861	16806	-387	-333
Cooling energy	5358	5062	4618	296	739	6068	5706	5156	362	912
Ventilation energy	10430	10399	10586	31	-156	343	336	357	7	-14
Expenditure (\$/100 m ²)	1781	1758	1732	23	49	2147	2148	2094	-2	53
Old construction with new system										
Heating energy	80	82	82	-2	-2	16400	16778	16733	-379	-334
Cooling energy	4540	4291	3913	249	627	5303	4986	4508	317	795
Ventilation energy	10167	10136	10321	30	-154	325	319	338	6	-13
Expenditure (\$/100 m ²)	1675	1657	1637	18	39	2066	2071	2024	-5	42
New construction with new system										
Heating energy	45	46	45	0	0	10247	10369	10321	-123	-74
Cooling energy	354	321	308	33	45	4347	4199	3753	149	594
Ventilation energy	1714	1702	1727	12	-13	221	217	237	4	-16
Expenditure (\$/100 m ²)	319	317	317	3	2	1390	1387	1342	3	47

8.2.3. Large office building

Table 8-5 presents the results of the simulations performed for the large office prototype. Similar to the medium office with heat pump, when the ALBEDO weather condition is used, the energy savings for ventilation is decreased (by about 15 kWh/100m²) and cooling savings is significantly increased. In all cases the annual expenditure savings is increased or remains unchanged. In all building prototypes with new construction and new system using gas heating, the use of modified weather data results in a minimum increase in the money savings, for two main reasons. First, the building insulation is enhanced and the sensitivity of the energy load to the weather condition is reduced; and second, the efficiency of the gas heating system is not as sensitive to the energy load as the heat pump. On the other hand, all buildings using a heat pump as their heating system show a great sensitivity to weather conditions that affect the performance of the HVAC system.

Table 8-7. Summary of the energy consumption and energy expenditure of a large office with different HVAC systems and building characteristics using dark roof, white roof with weather data in CTRL, and white roof with weather data in ALBEDO in Montreal, 2005. Values are normalized with 100 m² of roof area

Case	Gas heating (heating in GJ/100 m ² , cooling in kWh/100 m ²)					Heat pump (heating and cooling in kWh/100 m ²)				
	Dark CTRL	White CTRL	White ALB	Saving CTRL	Saving ALB	Dark CTRL	White CTRL	White ALB	Saving CTRL	Saving ALB
Old construction with old system										
Heating energy	74	75	75	-1	0	11183	11428	11420	-245	-237
Cooling energy	4221	4107	3617	114	604	5905	5587	4931	318	974
Ventilation energy	1694	1664	1680	30	14	268	262	283	5	-15
Expenditure (\$/100 m ²)	829	818	772	11	57	1628	1621	1560	7	68
Old construction with new system										
Heating energy	27	28	28	-1	-1	11161	11400	11396	-239	-235
Cooling energy	1560	1474	1344	85	216	5584	5283	4652	301	932
Ventilation energy	3493	3482	3546	10	-53	253	248	267	5	-14
Expenditure (\$/100 m ²)	575	569	562	6	13	1594	1588	1530	6	64
New construction with new system										
Heating energy	12	12	12	0	0	7807	7885	7885	-77	-78
Cooling energy	121	110	106	11	16	4644	4496	3867	149	777
Ventilation energy	589	585	593	4	-4	178	175	194	3	-16
Expenditure (\$/100 m ²)	110	109	109	1	1	1185	1178	1121	7	64

8.2.4. Retail store building

Energy and expenditure calculations for the retail store prototype are shown in Table 8-6. For the retail store, the cooling savings is dominant compared to the energy consumption of other systems under the influence of ALBEDO weather condition. Under those circumstances, the ventilation energy savings is also reduced for all cases. The maximum increase in the expenditure savings by updating the weather condition occurs in the old construction with old system using gas heating, by 49 \$/100m². Simulation with CTRL weather condition for the retail store using heat pump results in no savings or a penalty; however, after updating the weather condition considerable energy savings are reported. Similar to other prototypes, energy savings is highly dependent on the building vintage, and old-construction buildings have more savings when reflective surfaces are implemented.

Table 8-8. Summary of the energy consumption and energy expenditure of a retail store with different HVAC systems and building characteristics using dark roof, white roof with weather data in CTRL, and white roof with weather data in ALBEDO in Montreal, 2005. Values are normalized with 100 m² of roof area

Case	Gas heating (heating in GJ/100 m ² , cooling in kWh/100 m ²)					Heat pump (heating and cooling in kWh/100 m ²)				
	Dark CTRL	White CTRL	White ALB	Saving CTRL	Saving ALB	Dark CTRL	White CTRL	White ALB	Saving CTRL	Saving ALB
Old construction with old system										
Heating energy	96	102	102	-5	-6	20400	20841	20891	-441	-491
Cooling energy	3006	2727	2165	279	840	3600	3191	2736	409	864
Ventilation energy	6312	5384	5410	929	902	249	241	245	7	4
Expenditure (\$/100 m ²)	1243	1151	1102	92	141	2275	2277	2239	-2	35
Old construction with new system										
Heating energy	95	100	100	-5	-5	20273	20698	20768	-425	-495
Cooling energy	2696	2447	1941	249	755	3453	3059	2620	394	834
Ventilation energy	6176	5270	5296	906	881	235	228	231	7	4
Expenditure (\$/100 m ²)	1196	1106	1063	90	133	2248	2250	2215	-2	32
New construction with new system										
Heating energy	32	33	33	-1	-1	6848	7009	7050	-161	-202
Cooling energy	2100	1915	1744	185	356	2083	1935	1786	147	297
Ventilation energy	3402	3110	3222	293	180	133	120	124	13	9
Expenditure (\$/100 m ²)	633	593	587	40	46	850	850	840	0	10

8.3. Conclusion on the energy consumption of commercial buildings

Increasing the albedo of urban surfaces has two types of effects: (1) direct, reducing the solar heat gain by the buildings, and (2) indirect, changing the meteorological variable or the weather condition. Four commercial building prototypes (small office, medium office, large office, and retail store) are selected to investigate the effect of increasing the roof and walls albedo on their energy consumption. The albedo of roof and walls are increased from 0.2 to 0.65 and 0.6, respectively. The meteorological variables are hourly updated with respect to the results of mesoscale modeling (analyzed and discussed in Chapter Seven). In mesoscale modeling the albedo of pavements is also increased from 0.2 to 0.45. Statistical analysis of the meteorological variable shows 0.1 °C to 0.4 °C decrease in the air temperature as well as about 1% increase in the incoming solar radiation in all months. In general, the cooling energy savings is increased and heating penalty is decreased by updating the weather data. Buildings using heat pump as the heating system show more sensitivity to the weather condition. Furthermore, buildings with old construction and weak insulation are getting more advantage from the implementation of reflective roof and walls. Other than heating and cooling systems, the energy consumption of the fan in the ventilation system may play an important role in expenditure analysis. In new constructed buildings using a gas heating system where both the efficiency of the HVAC system and the building construction characteristics are not sensitive to weather conditions, the result is a minimum change in energy estimations. The maximum money savings from albedo enhancement of buildings is about 11%, from the combined direct (7%) and indirect (4%) effects.

Chapter Nine: Effect of Increasing the Urban Albedo on Air Quality of Montreal

This chapter is dedicated to the air quality modeling to evaluate the effect of an increase in urban albedo in Montreal on air temperature and concentration of pollutants. I have coupled WRF with its multi-layer urban canopy model (ML-UCM), building energy model (BEM), and chemical transport. WRF-CHEM is evaluated based on measured data, showing a good performance in predicting the concentration of ozone and particulate matters (Tessum et al., 2014; Liao et al., 2014). Additionally, accuracy of the predicted pollutant concentrations is increased by increasing the horizontal resolution of grids (Fountoukis et al., 2013).

9.1. Methodology of meteorological and air quality modeling

The methodology section is divided in four sub-sections: (1) domain and episode of simulations, (2) meteorological setup, (3) chemistry setup, and (4) input data.

9.1.1. Simulation domain and the summer episode

The Greater Montreal area is located in Zone 6 (cold climate) based on the ASHRAE (2007a) climate categorization. WRF-CHEM is configured with three domains (one coarse and two nested) with grid sizes of 9 km × 9 km, 3 km × 3 km, and 1 km × 1 km (similar to Figure 7-1). The coarse domain (Domain 1) has 51×51 grids and the second domain (Domain 2) has 52×52 grids. For the nested domain in Domain 2, which covers the city, 91 grids are distributed from west to east and 67 grids are assigned for south to north (Domain 3). Two-way nesting ensures the transmission of information between nests. The vertical coordinate is terrain following¹⁵ with 30 levels (1.0, 0.9995, 0.999, 0.9985, 0.9978, 0.9966, 0.9949, 0.9924, 0.9886, 0.9829, 0.9761, 0.9665, 0.9531, 0.9344, 0.9147, 0.8891, 0.8558, 0.8125, 0.7563, 0.6832, 0.6082, 0.5332, 0.4582, 0.3832, 0.3082, 0.2332, 0.1582, 0.0832, 0.0082, 0.0) where the lowest atmospheric level is at 5 m height. The time step for Domain 1 is 60 sec and the time step ratio of Domain 2 and Domain 1 are 1/3 and 1/15, respectively. Three consecutive days in July (10th to 12th LST) with highest

¹⁵ In this coordinate system the vertical axis is the hydrostatic pressure at each level normalized by the hydrostatic pressure at the surface and at the top of the domain ($\eta = \frac{P_h - P_{h,top}}{P_{h,surface} - P_{h,top}}$).

hourly maximum temperature in 2005 are selected as the simulation period. Running the model started at 7 p.m. on 07-July-2005 LST and ended at 11 p.m. on 12-July-2005 LST. The result of the first 53 hours are neglected to abate the effect of initial conditions for both meteorology and chemistry parts. Simulations are performed for two cases: (1) CTRL—albedo of all urban surfaces is equal to 0.2; and (2) ALBEDO—albedo of roofs, walls, and roads are increased to 0.65, 0.6, and 0.45, respectively.

9.1.2. Meteorological setup

Some restrictions are imposed for running WRF-CHEM coupled with ML-UCM and BEM. Similar to the previous meteorological simulations, Noah LSM is the only land-surface scheme to be coupled to ML-UCM with BEM. The LSM works with MYJ (Janjic, 1994) and BouLac (Bougeault and Lacarrere, 1989) PBL options; and through the sensitivity analysis in Chapter Five, I found that the performance of MYJ in predicting the air temperature was better than BouLac. Another limitation is to use National Emission Inventory 2005 (NEI-05; EPA, 2005) with a tool provided by the WRF package. Using NEI-05 is only feasible with limited options for microphysics and radiation parameterizations. I use RRTMG (Iacono et al., 2008) and Lin (Lin, 1983) as radiation and microphysics schemes, respectively. It should be mentioned that the Lin scheme acts as a double-moment parameterization when the aerosol model is activated. The Grell 3D (Grell, 1993; Grell and Devenyi, 2002) cumulus model is selected based on recommendations from Chapter Five. The cumulus model is not used for Domain 3.

The third order Runge-Kutta method is used for forward time marching. To ensure the stability of the model, a damping option for the vertical velocity is turned on. Horizontal Smagorinsky first-order closure is used for calculation of eddy coefficient, turbulence, and mixing.

9.1.3. Chemistry setup

To simulate the effect of an albedo increase on urban climate and concentration of pollutants, version 3.6.1 of WRF-CHEM is used. The model ensemble has different options for gaseous chemical mechanisms, aerosol models, and photolysis calculations (WRF-CHEM User's Guide, 2014). In addition, various choices of anthropogenic and biogenic emissions are available within the model (WRF-CHEM Emission Guide, 2014).

There are thousands of reactions happening in the atmosphere (Atkinson et al., 2004, 2006, 2007, 2008, 2010, 2013), and many chemical mechanisms with different levels of complexity to consider as part of the reactions and related chemical species for air quality modeling. Some of

the chemical mechanisms consist of many species and reactions, which is not computationally efficient for urban air quality simulations. As an example, the Master Chemical Mechanism (MCM) lists about 2500 chemical species and more than 7000 reactions for important organic compounds. Meanwhile, the chemical mechanism cannot be too simple or it would not be accurate (Appendix B). The second-generation Regional Acid Deposition Model Mechanism (RADM2: Stockwell et al., 1990), selected for this study, comprises 21 inorganic species and 42 organic species as well as 9 inorganic photolysis reactions, 12 organic photolysis reactions, 29 inorganic reactions, and 108 organic reactions. The model also calculates the absorption cross sections and quantum yields for the photolysis reactions. RADM2 is validated and compared against other chemical mechanisms (Poppe et al., 1996; Kuhn et al., 1998). A comparison of RADM2 with other chemical mechanisms indicated that the ozone concentration was underestimated (Gross et al., 2003). Choice of the anthropogenic emission data limited us in using the combination of RADM2 and MADE/SORGAM aerosol model.

The MADE/SORGAM modal aerosol model is the combination of the Modal Aerosol Dynamics Model for Europe (MADE; Ackermann et al., 1998) and the Secondary Organic Aerosol Model (SORGAM; Schell et al., 2001). The model is governed by conservation equation on the k^{th} moment of aerosols in Aitken mode (aerosol size of 0.01-0.1 μm) and accumulation mode (aerosol size of 0.1-1 μm) with source and sink term on nucleation, condensation, and coagulation. Nucleation occurs in the sulfuric acid-water system (Kulmala et al., 1998). Binkowski and Shankar (1995) calculate the rate of condensation in two steps: 1) production of condensable materials in chemical reactions, and 2) condensation of ambient volatile species on aerosols. Coagulation is assumed as the result of Brownian motion (Whitby et al., 1991; Binkowski and Shankar, 1995) and collision of particles within the Aitken mode is assigned to the accumulation mode. The total number of aerosol particles in each mode, all primary and secondary species, and coarse mode aerosols (anthropogenic, marine, and soil) are transported in WRF-CHEM. The size distribution of aerosol particles is calculated from eq. 9-1 (Ackermann et al., 1998) for three median diameters (Figure 9-1).

$$\frac{dN}{d(\ln d_p)} = \frac{N}{\sqrt{2\pi} \ln \sigma_p} e^{-\frac{(\ln d_p - \ln d_{pg})^2}{2 \ln^2 \sigma_p}} \quad (9-1)$$

d_p is the particle diameter, N is the number concentration, σ_p is the standard deviation, and d_{pg} is the median diameter.

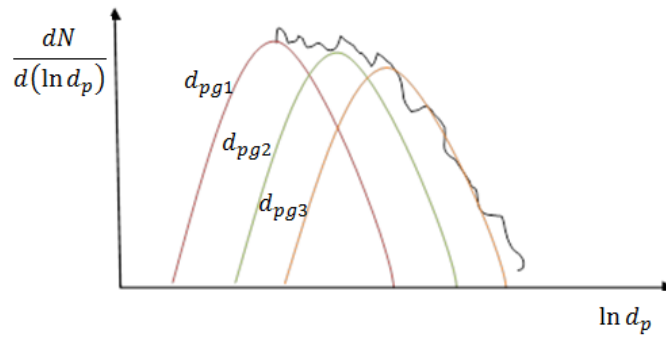


Figure 9-1. Schematic of the size distribution of aerosols considered the MADE/SORGAM

The k^{th} moment can be defined by eq. 9-2.

$$M_k = N d_{pg}^k e^{\frac{-k^2 \ln^2 \sigma_p}{2}} \quad (9-2)$$

Obviously, M_0 is the number of aerosol particles. In addition, M_2 and M_3 are indications of total particulate surface area and total particulate volume within the mode suspended in a unit volume of air, respectively.

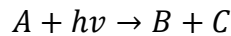
Dry deposition velocity of aerosols is calculated based on surface resistance, settling velocity, and Brownian diffusivity (Slinn and Slinn, 1980; Pleim et al., 1984).

$$v_d = \frac{1}{r_a + r_d + r_a r_d v_G} + v_G \quad (9-3)$$

v_G is the settling velocity, r_a is surface resistance, and r_d is the Brownian diffusivity.

The organic chemistry is based on SORGAM (Schell et al., 2001); however, the biogenic precursors and their resulting particle concentrations are not considered because of the incompatibility with the selected chemical mechanism (RADM2).

The last important part of the reactions is the photolysis reactions. Photolysis reaction in the atmosphere in the simplest form is like:



Rate of change in the number of molecules is the lysis reaction rate

$$-\frac{d[A]}{dt} = \frac{d[B]}{dt} = \frac{d[C]}{dt} = k[A]$$

where, $[A]$ is the number density of molecules and k ($\frac{1}{s}$) is the photolysis rate. The photolysis reaction rate is a probability function as follows:

$$k = q_x \sigma_x f_I$$

q_x ($\frac{\text{molecules}}{\text{photon}}$) is quantum yield, σ_x ($\frac{\text{cm}^2}{\text{molecule}}$) is absorption cross section, and f_I ($\frac{\text{photons}}{\text{cm}^2 \cdot s}$) is the actinic flux distribution function

$$k = \int_{\lambda} q_{x(\lambda)} \sigma_{x(\lambda)} f_{I(\lambda)} d\lambda$$

Calculating the photolysis rate in the troposphere for chemical transport models is challenging because the effect of clouds and aerosols should be considered. The Fast-J photolysis model is an accurate and fast algorithm for considering the effect of cloud, aerosols, and ozone on photolysis rate (Wild et al., 2000). The model solves the multi-reflection in the atmosphere using exact scattering phase function and optical depths to predict the photolytic intensities ($f_{I(\lambda)}$).

All other WRF-CHEM options (e.g., wet scavenging, cloud chemistry, sub-grid aqueous chemistry, aerosols radiation feedback, etc.) are turned on to consider the full sophistication of the problem.

9.1.4. Input data

9.1.4.1. Meteorological input

Initial and boundary conditions are determined using hourly, high-resolution 32 km, North America Regional Reanalysis (NARR) data (Mesinger et al., 2006). Standard 24-category USGS 24-category land use land cover (U.S. Census Bureau, Geography Division, 2011) dataset within WRF is used for calculations in LSM. USGS only provides a single class of urban type (only the high-density residential type) where the street orientation in Montreal is 45° and 135° from the north. Urban areas are divided into 80% urban fraction and 20% natural vegetation. The building height distribution is 45%, 42%, 3%, 2%, and 8% for 5 m, 10 m, 15 m, 20 m, and 30 m, respectively (see Section 6.2.1). Widths of the buildings and roads are assumed to be 20 m and 30 m, respectively. The thermal conductance of the roof and walls are 0.067 (W/mK). The HVAC systems use gas heating where the heating efficiency is 1 and the cooling COP is 2.5. The indoor comfort range is maintained by the temperature of about 21 ± 3 °C (cooling above 24 °C and heating below 18 °C) and moisture content of 5 ± 3 g/kg.

9.1.4.2. *Anthropogenic emissions*

Anthropogenic emissions are constructed with the help of a tool developed by the WRF-CHEM community that is called “emiss_v03.” The tool has anthropogenic emission for the contiguous 48 states of the United States, southern Canada and northern Mexico with 4-km spatial resolution for summer. The input data is divided into three parts (weekdays, Saturday, and Sunday) with temporal increment of an hour. The emiss_v03 reads the input emission data and the header of the WRF input file (wrfinput) and calculates the spatial and temporal variation in the domain of interest. Since the spatial resolution of the emission data is 4 km, I have generated the anthropogenic emission data for the coarsest domain (9 km × 9 km), and then downscaled them for other nested domains (3 km × 3 km and 1 km × 1 km). The tool is designed to generate input emission data for the RADM2 chemical mechanism and MADE/SORGAM modal aerosol models. The input emission data has 19 vertical levels. The data is used as the input to the model and it is not temperature sensitive.

The National Emission Inventory of 2005 (NEI-05) of the US-EPA provides the following species for my simulations with WRF-CHEM: Carbon monoxide, Nitrogen Oxides (NO or NO₂), Sulfur dioxide, Ammonia, Ethane, different Alkanes, Ethylene, Isoprene, Aromatics, Formaldehyde, Acetaldehyde, Higher aldehydes, Benzaldehyde, Acetone, Methylene ketone, different ketones, Methanol, Glyoxal, Methylglyoxal, Biacetyl, Phenols, Cresols, Methacrolein, Methacrolein, Methylvinyl ketone, Methylvinyl ketone, Propylene, Acetylene, Benzene, Butanes, Pentanes, Toluene, Xylenes, Propane, Dienes, Styrenes, Organic Acids, Unspecified primary PM2.5 – nuclei mode, Unspecified primary PM2.5 – accumulation mode, Sulfate PM2.5 – nuclei mode, Sulfate PM2.5 – accumulation mode, Nitrate PM2.5 – nuclei mode, Nitrate PM2.5 – accumulation mode, Organic PM2.5 – nuclei mode, Organic PM2.5 – accumulation mode, Elemental Carbon PM2.5 – nuclei mode, Elemental Carbon PM2.5 – accumulation mode, and Unspecified Primary PM10 (total of 55 species).

Typically, WRF-CHEM reads NEI-05 in two sets of 12 hours as input for one day. However, my simulation period is 4 days, including weekdays, Saturday, and Sunday, which made us merge the separate input files into a single input emission file (WRF-CHEM has the option to either read input emission data hourly or by 12-hour increments).

Ozone is the secondary pollutant from the reaction of NO_x with oxygen. Figure 9-2 illustrates the spatial distribution of anthropogenic NO_x emission in Domain 3 during a weekday at 12 a.m., 6 a.m., 12 p.m., and 6 p.m.. Emission of NO_x mainly occurs in the mid-north part of the city. Moreover, all around the city emission of NO_x is dominant during the evening. The same emission pattern for NO_x is also observed during the weekend (Sunday). Similar to NO_x, the spatial distribution of total anthropogenic emission of PM_{2.5} is shown in Figure 9-3. Again, the mid-north region is more exposed to PM_{2.5} emissions than the other parts of the city. Unlike the NO_x emission, PM_{2.5} is emitted in a smaller area. The temporal variation of PM_{2.5} and NO_x during the simulation period is also demonstrated in Figure 9-4. During the weekdays the average emission of both NO_x and PM_{2.5} is higher than the weekend. Since NEI-05 considers the same pattern for all pollutants during the weekdays, on 11 July and 12 July the rates of emission for NO_x and PM_{2.5} are identical. The maximum NO_x emission of about 190 (mole/km² per hour) occurs during weekdays at 6 p.m.. The increase in the emission starts at 7 a.m. (2 hours after sunrise) and a few hours before sunset the emission rate declines. PM_{2.5} emission varies between 0.18 and 0.51 (μg/m²/s). the rate of change in the PM_{2.5} emission rise in the morning is the same as the rate of increase in the NO_x emission. However, PM_{2.5} decay is slower. Finally, anthropogenic emission of SO₂ during a weekday as an important contributor to nucleation of aerosols is shown in Figure 9-5. The SO₂ emission is limited to the urban region and the maximum emission occurs in the southwest part of the city.

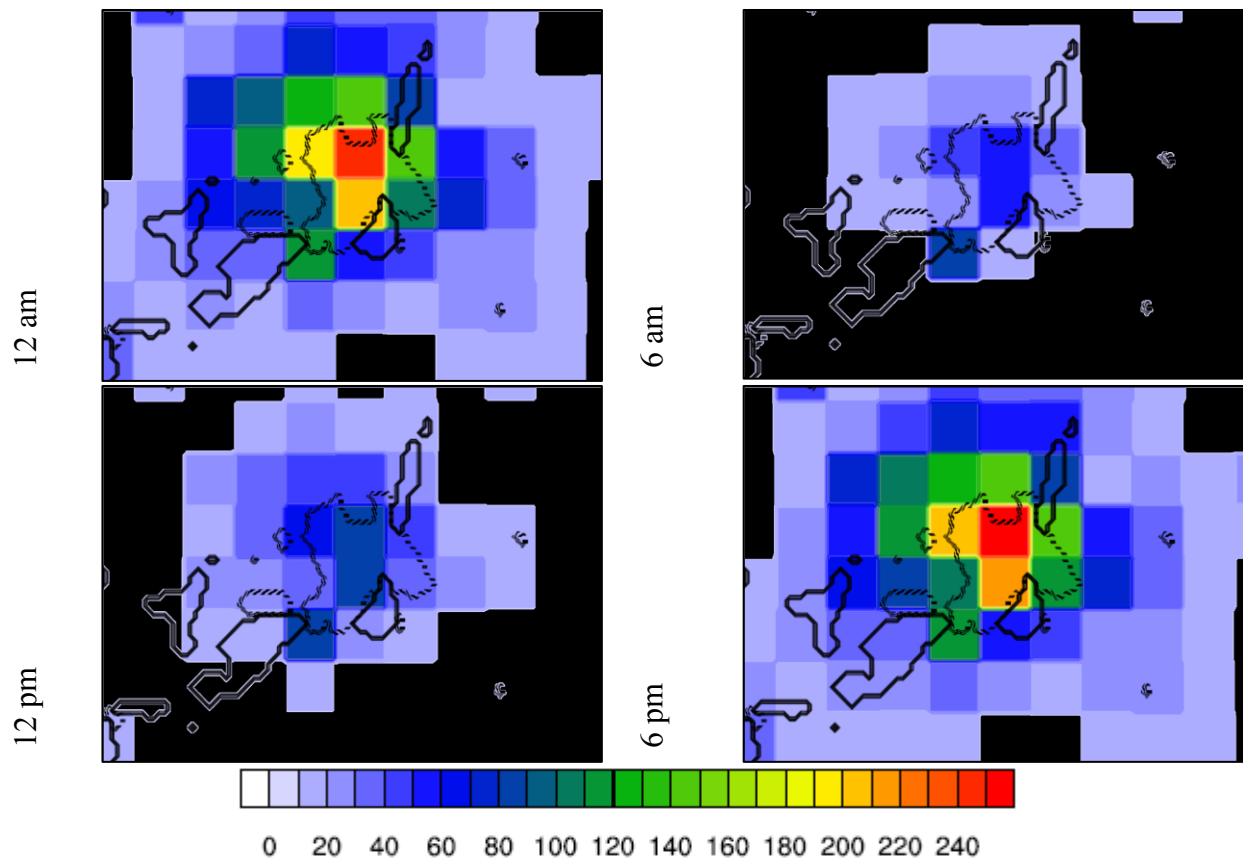


Figure 9-2. NOx emission (mole/km²/hr) in different hours of a weekday in Domain 3 (the dashed line is the urban border and dark blue color represents rivers)

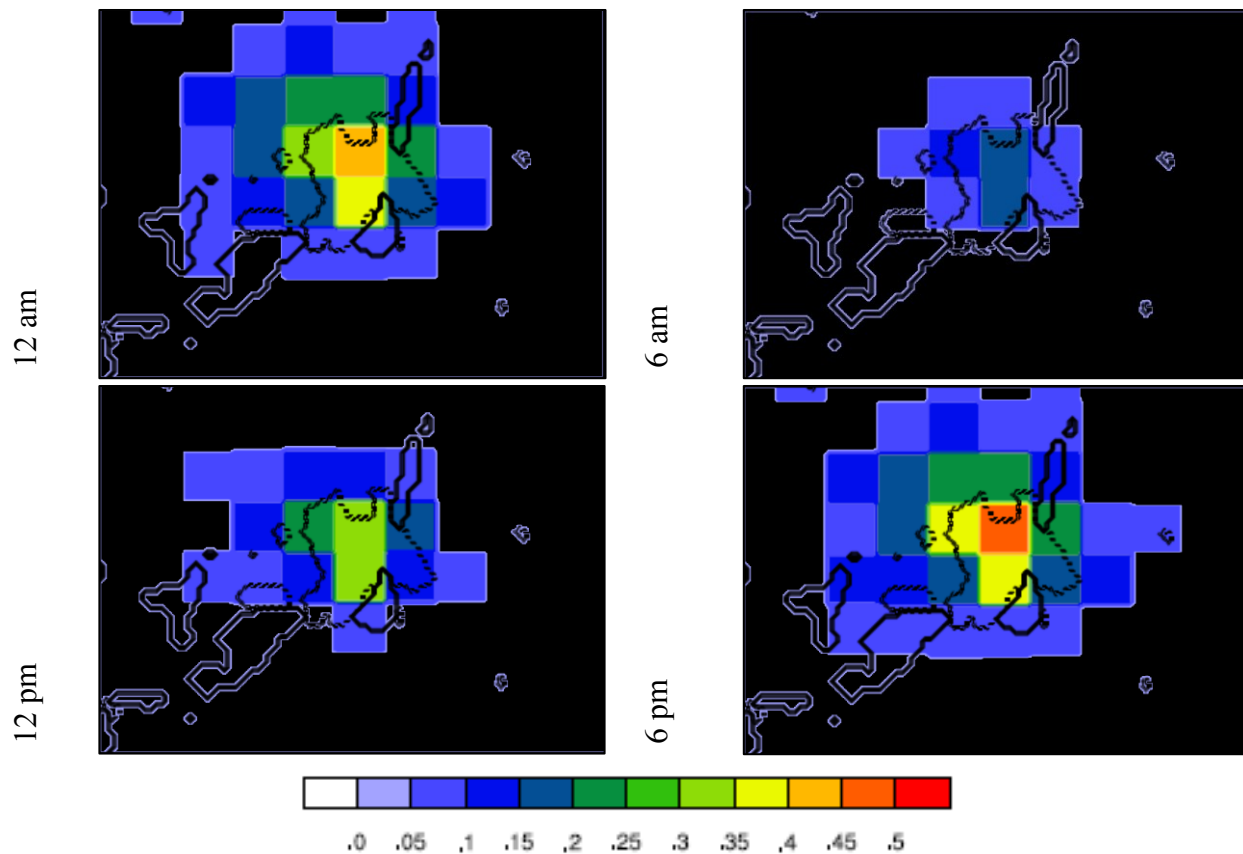


Figure 9-3. PM2.5 emission ($\mu\text{g}/\text{m}^2/\text{s}$) in different hours of a weekday in Domain 3 (the dashed line is the urban border and dark blue color represents rivers)

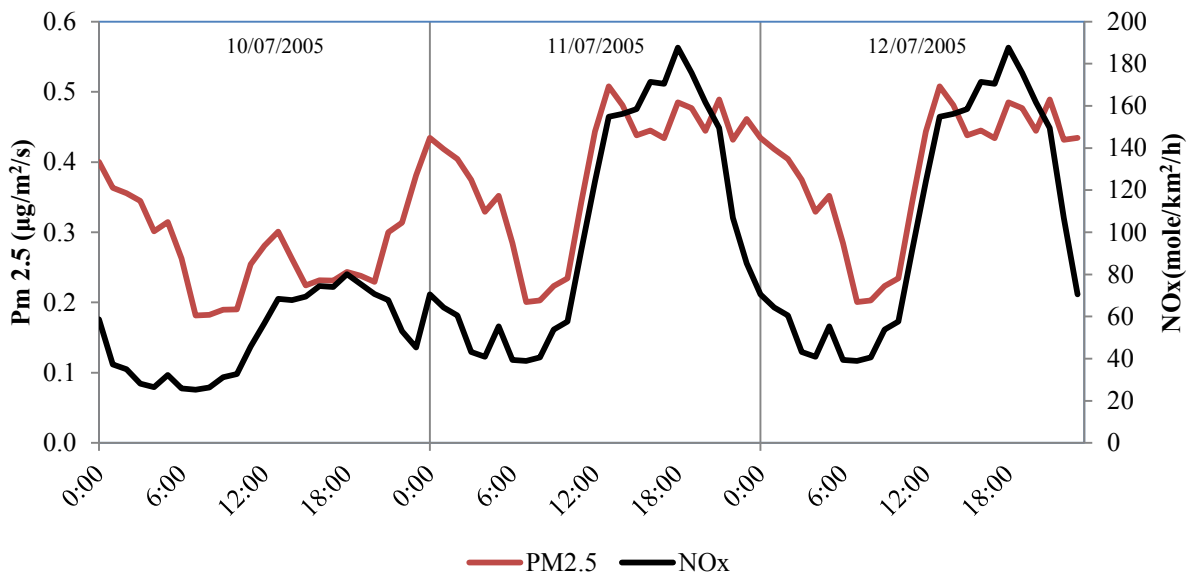


Figure 9-4. Temporal variation of the spatially averaged PM 2.5 and NOx emission during the three-day heatwave period in the urban area

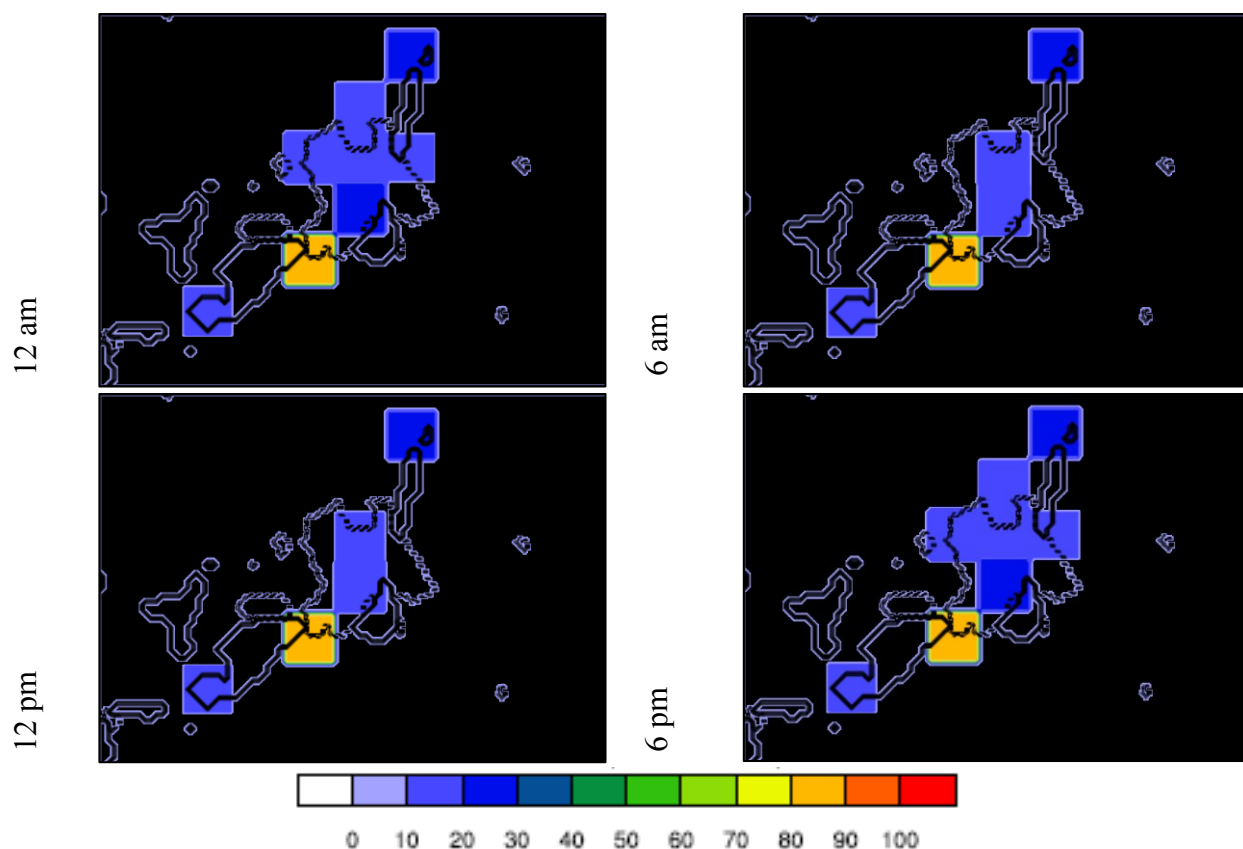


Figure 9-5. SO₂ emission (mole/km²/hr) in different hours of a weekday in Domain 3 (the dashed line is the urban border and dark blue color represents rivers)

9.1.4.3. Biogenic emissions

Running the MEGAN biogenic emission preprocessor is simple; the “bio-emiss” tool was developed by the National Center for Atmospheric Research (NCAR) to provide the biogenic emission processor input. The resolution of the data is (1 km × 1 km), which fits well with my simulations. The average isoprene emission (mole/km²/hr) in Domain 3 for biogenic calculations in MEGAN is shown in Figure 9-6. The model considers the dependence of the biogenic emission to the air temperature in the solver.

9.1.4.4. Other data

Although WRF-CHEM has options for biomass burning, volcanic, aircraft, sea-salt, and dimethyl sulfide from sea emissions, these have been neglected for urban-scale simulations to reduce the computation cost. Since my focus is the small domain (D3) nested through coarser domains, I assumed a negligible effect of boundary and initial conditions on concentration of pollutants in Domain 3. Therefore, the default WRF-CHEM profile of gas tracers is used for initialization and for the boundary condition.

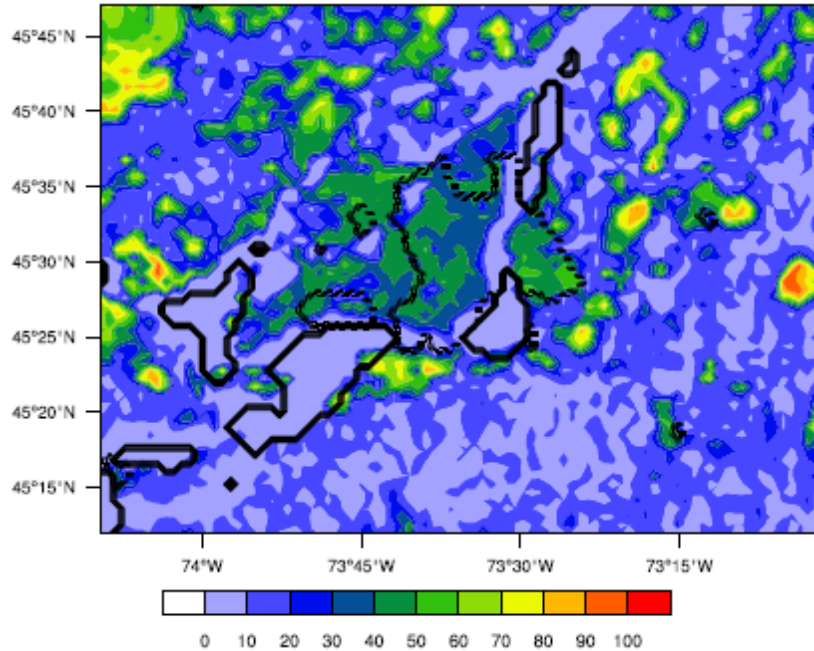


Figure 9-6. Average isoprene emission (mole/km²/hr) in Domain 3 for biogenic calculations in MEGAN (the dashed line is the urban border and dark blue color represents rivers)

9.2. Results of the simulations with WRF-CHEM, and discussion

Here the 2-m air temperature (T_a), surface temperature (T_s), shortwave radiation on the ground (SW), sensible heat flux from the surface (HF), planetary boundary layer height ($PBLH$), 2-m mixing ratio (Q), moisture flux from the surface (QF), 10-m wind speed (W), ozone concentration (O_3), PM_{2.5} concentration ($PM_{2.5}$), and energy consumption (E) are analyzed. In general, spatially averaged values through the urban area are addressed, except for T_a , O_3 , and $PM_{2.5}$, of which the spatial distribution in some specific hours is discussed.

9.2.1. Air temperature

As shown in Figure 9-7, T_a is decreased by the maximum of 1°C in the heatwave period because of the albedo increase in the heatwave period. Average 24-hour decrease in T_a is about 0.5 °C while the maximum decrease is about 1.1 °C. As expected, the air temperature reduction mainly occurs during daytime and the average decrease is about 0.7 °C. The air temperature in rural areas is slightly decreased (by a maximum of 0.1 °C) because of the advection by wind. The albedo enhancement tends to be more effective in the morning. On the other hand in the evening where the stored heat within urban structures is released, the decrease in T_a is not significant. The peak temperature in the three consecutive days is decreased by 0.8 °C, 0.6 °C, and 0.7 °C.

During the nighttime, the effect of increasing albedo is negligible but a small decrease is still observed (~ 0.1 °C), since less energy is absorbed during the day.

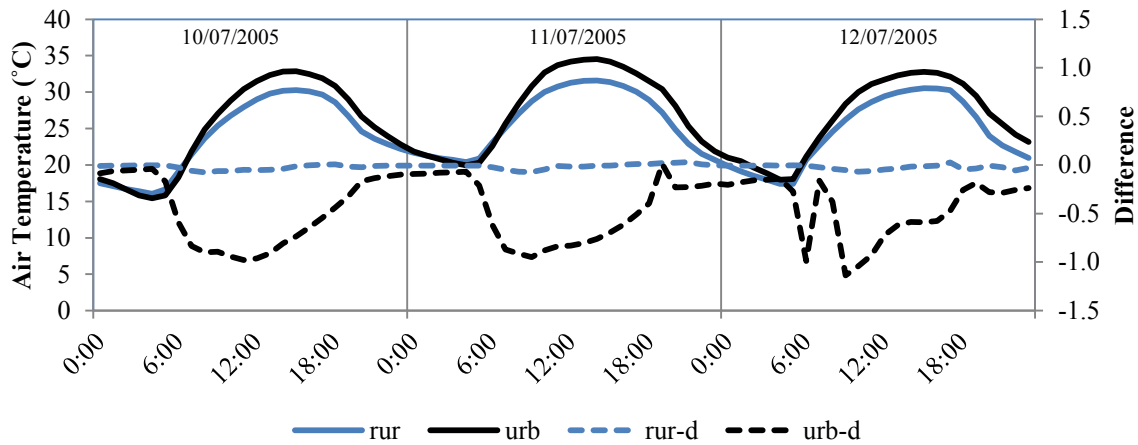


Figure 9-7. 2-m air temperature of urban and rural areas in the three-day heatwave period and the difference between CTRL and ALBEDO. rur, urb, rur-d, and urb-d denote rural area in CTRL, urban area in CTRL, difference between ALBEDO and CTRL in rural area, and difference between ALBEDO and CTRL in urban area, respectively.

Figure 9-8 and Figure 9-9 illustrate the spatial distribution of the change in air temperature by albedo enhancement at 12 a.m., 6 a.m., 12 p.m., and 6 p.m. on 11 July 11th and 12th. The western part of Montreal takes the most advantage from the urban-scale increase in albedo. In some grid cells, T_a is decreased by up to 3 °C, while in some others a small increase is observed. On 12 July at 12 p.m., some parts of the city experienced an increase in temperature. The reason for that was an increase in incoming solar radiation striking those regions. The solar radiation is inversely proportional to the cloud cover in a grid. Based on the physics of the model, a decrease in surface temperature and consequently air temperature increases the chance of condensation. Hence, the cloud cover above a grid may be underestimated. Adding the complication of the wind pattern, causing a change in the air temperature and moisture availability, results in the increase of air temperature in some grid cells. The nighttime effect (12 a.m.) of the change in urban albedo is negligible throughout the city. Skin temperature is highly sensitive to the land category; consequently, the 2-m air temperature is related to the land category. The spatial distribution of T_a in rural areas is eliminated to avoid unrelated discussion, since the focus of my research is on the urban climate.

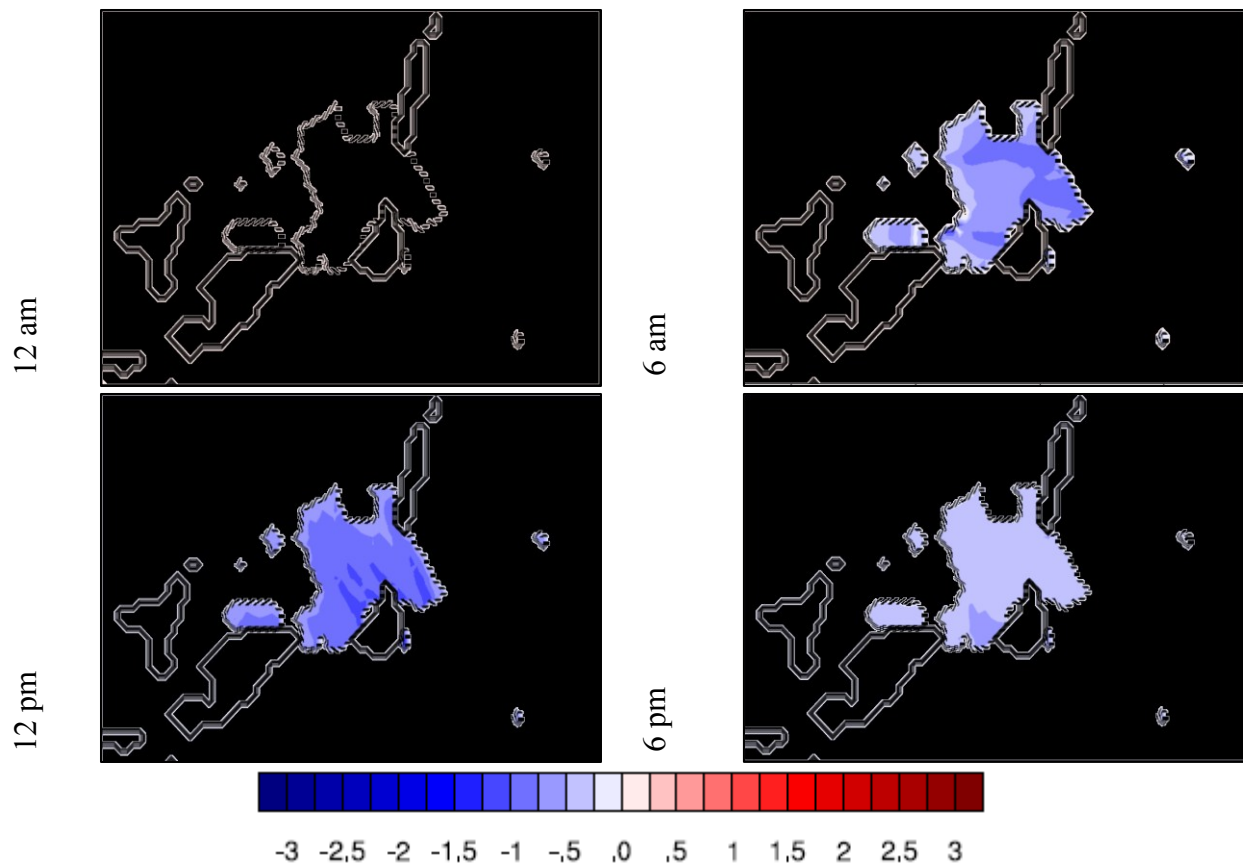


Figure 9-8. 2-m air temperature difference (°C) between CTRL and ALBEDO on July 11th, 2005 (the dashed line is the urban border and dark blue color represents rivers).

9.2.2. Skin temperature

The surface temperature is highly correlated to the urban fabric and the incident solar radiation. Since the absorptivity of the urban areas is higher than that of rural areas, the urban surface temperature is always higher than T_s in rural areas by up to 10 °C around noon (Figure 9-10). The rate of change in T_s is higher in the morning than its rate in the evening because of the thermal storage in urban structures (the reason albedo enhancement is more effective in the morning). Maximum decrease of T_s from albedo enhancement occurs almost at its peak with about 4 °C. On 12 July, the skin temperature is decreased during the nighttime because the wind speed in urban areas is modest (< 1 m/s). Other factors influencing the change in T_s during the nighttime (average of about 0.4 °C) are a reduction in the amount of longwave radiation between surfaces (surface temperatures are reduced in ALBEDO compared to CTRL) and a decrease in the heat emission from buildings. The average 24-hour decrease in T_s is about 1.7 °C.

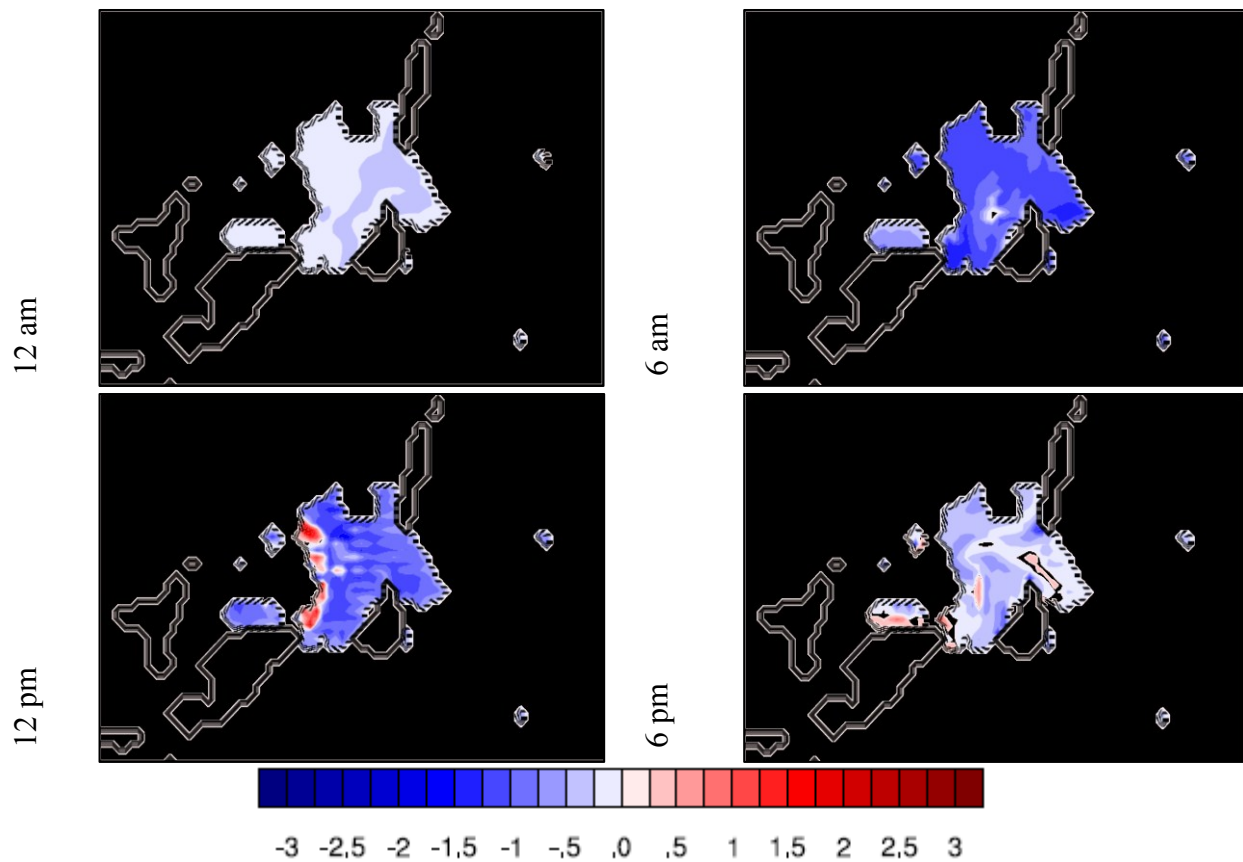


Figure 9-9. 2-m air temperature difference (°C) between CTRL and ALBEDO on July 12th, 2005 (the dashed line is the urban border and dark blue color represents rivers).

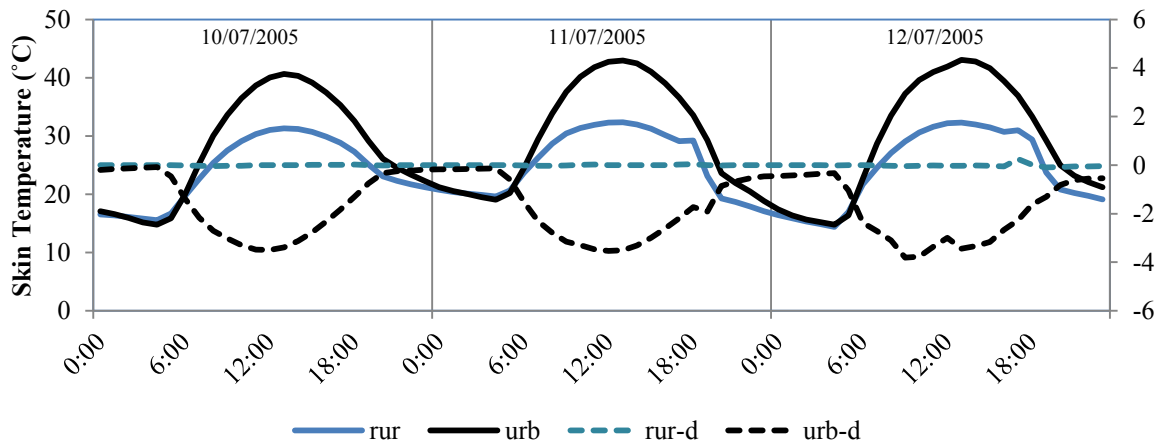


Figure 9-10. Surface temperature of urban and rural areas in the three-day heatwave period and the difference between CTRL and ALBEDO. rur, urb, rur-d, and urb-d denote rural area in CTRL, urban area in CTRL, difference between ALBEDO and CTRL in rural area, and difference between ALBEDO and CTRL in urban area, respectively.

9.2.3. Shortwave radiation

The shortwave radiation on the ground is directly related to the cloud cover and multi-reflection between urban surfaces. Figure 9-11 shows that SW increases by about 1%–2% almost in all hours. The shortwave radiation in urban and rural areas is almost the same ($< 0.2\%$). On 12 July the decrease in cloud cover causes the shortwave radiation to be $7 \text{ W/m}^2/\text{h}$ higher than previous days.

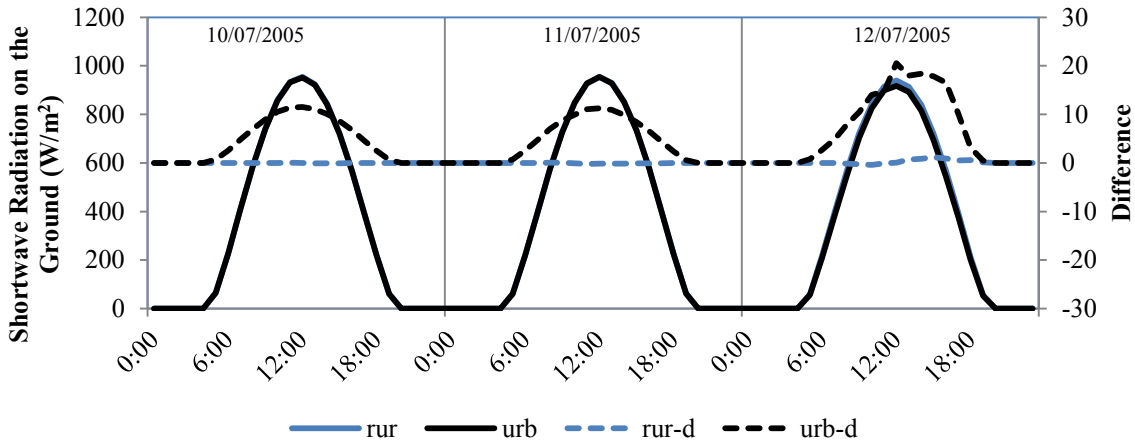


Figure 9-11. Shortwave radiation on the ground in urban and rural areas in the three-day heatwave period and the difference between CTRL and ALBEDO. rur, urb, rur-d, and urb-d denote rural area in CTRL, urban area in CTRL, difference between ALBEDO and CTRL in rural area, and difference between ALBEDO and CTRL in urban area, respectively.

9.2.4. Sensible heat flux

Sensible heat flux is a good indication for evaluation of mitigation strategies. The 2-m air temperature is calculated based on T_s and HF (eq. A-15 in Appendix A). Therefore, decreasing HF can be interpreted as a decrease in the air temperature. The sensible heat flux is decreased by a factor of 3 at peak (from 447 W/m^2 to 292 W/m^2) of all days (Figure 9-12). In the urban area, the average 24-hour HF in CTRL is about 140 W/m^2 , which drops to 85 W/m^2 by albedo enhancement.

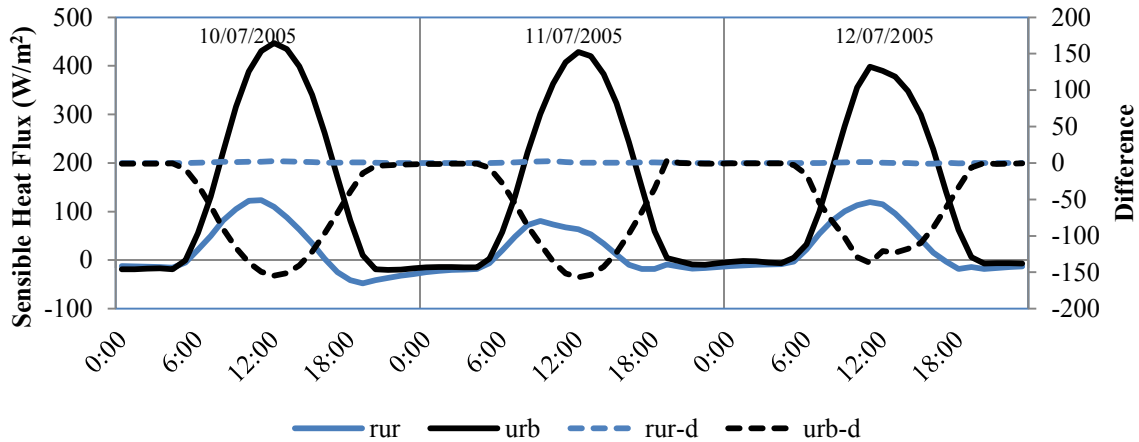


Figure 9-12. Sensible heat flux of urban and rural areas in the three-day heatwave period and the difference between CTRL and ALBEDO. rur, urb, rur-d, and urb-d denote rural area in CTRL, urban area in CTRL, difference between ALBEDO and CTRL in rural area, and difference between ALBEDO and CTRL in urban area, respectively.

9.2.5. PBL height

The surface roughness of the urban areas is higher than the surface roughness of rural areas, which results in higher PBLH in urban areas. Planetary boundary layer height is an influential factor in predicting the dispersion of pollutants in urban areas. *PBLH* is proportional to T_s , so a decrease in T_s reduces the *PBLH* (Figure 9-13). A very low wind speed introduced an error in predicting *PBLH* (~ 0 m) between 8 p.m. (July 11th) and 6 a.m. (July 12th).

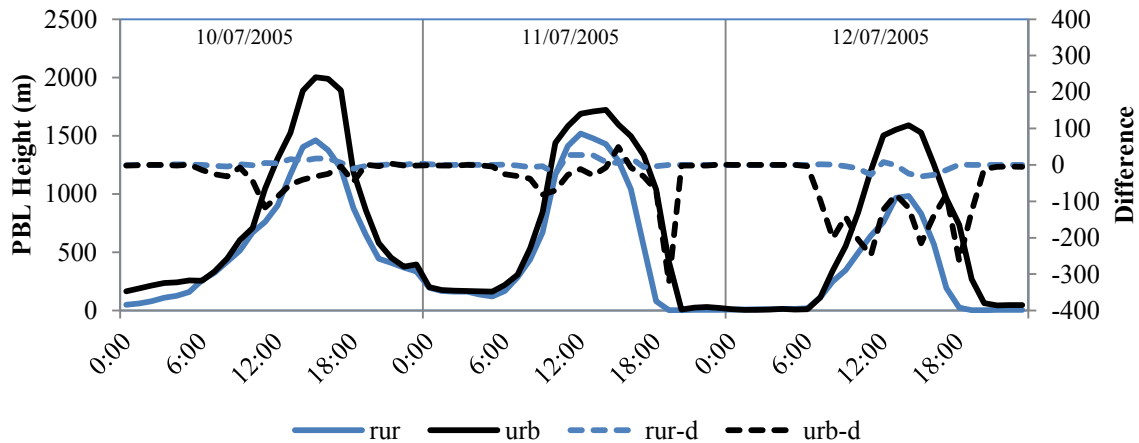


Figure 9-13. PBL height above urban and rural areas in the three-day heatwave period and the difference between CTRL and ALBEDO. rur, urb, rur-d, and urb-d denote rural area in CTRL, urban area in CTRL, difference between ALBEDO and CTRL in rural area, and difference between ALBEDO and CTRL in urban area, respectively.

9.2.6. Mixing ratio

Figure 9-14 shows the mixing ratio in CTRL indicating the dependency of mixing ratio to the wind speed. In rural areas, Q is higher than the mixing ratio in urban areas. The change in the air temperature of the urban area affects the 2-m moisture content of the city and the rural areas because of the advection. Generally, albedo enhancement increases the near surface mixing ratio (i.e., moisture content of air) on all days, except during some hours.

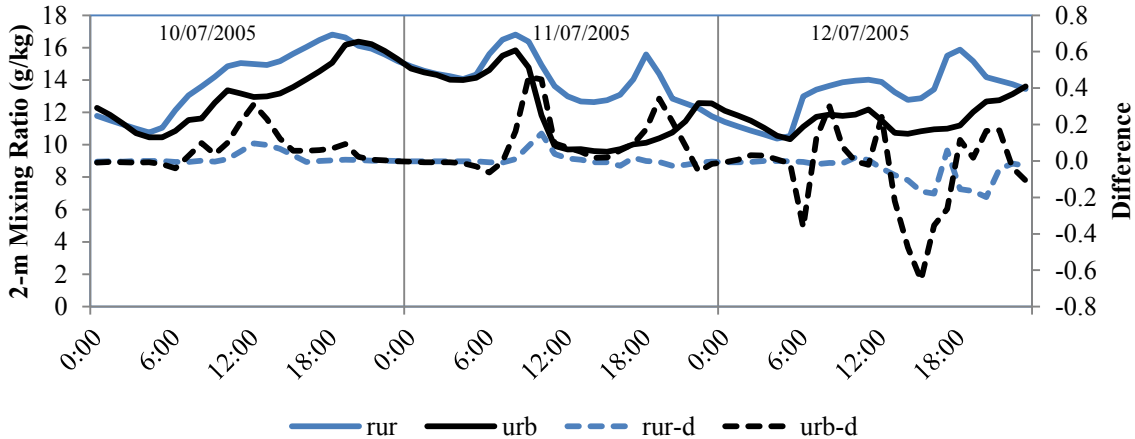


Figure 9-14. 2-m mixing ratio of urban and rural areas in the three-day heatwave period and the difference between CTRL and ALBEDO. rur, urb, rur-d, and urb-d denote rural area in CTRL, urban area in CTRL, difference between ALBEDO and CTRL in rural area, and difference between ALBEDO and CTRL in urban area, respectively.

9.2.7. Moisture flux

The QF in rural areas is much higher than QF in urban areas; they both have their maximum about noon (Figure 9-15) because of the high surface temperature. Hourly QF decrease is evident during the heatwave period. Decreasing T_s changes the surface pressure and mixing ratio, two influential parameters to determine moisture flux from the surface to PBL. The decrease in skin temperature causes up to about 0.005 g/m^2 of moisture flux to the atmosphere. During the night, there is no moisture flux into the atmosphere.

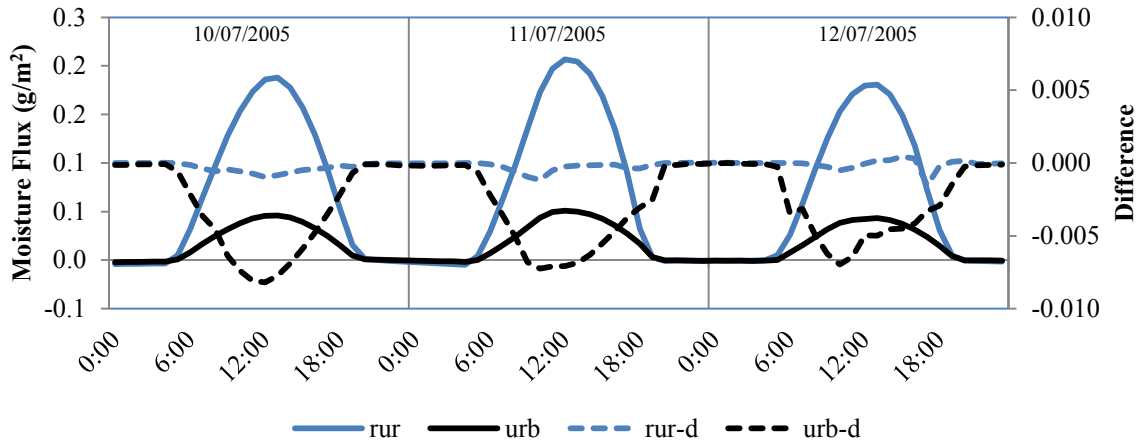


Figure 9-15. Moisture flux of urban and rural areas in the three-day heatwave period and the difference between CTRL and ALBEDO. rur, urb, rur-d, and urb-d denote rural area in CTRL, urban area in CTRL, difference between ALBEDO and CTRL in rural area, and difference between ALBEDO and CTRL in urban area, respectively.

9.2.8. Wind speed

Stable conditions (low wind speed) on the third day caused the air temperature to reach its maximum value. The wind speed is decreased and the daytime effect of the albedo enhancement is evident in Figure 9-16—except for 12 July when for a few hours the wind speed is increased.

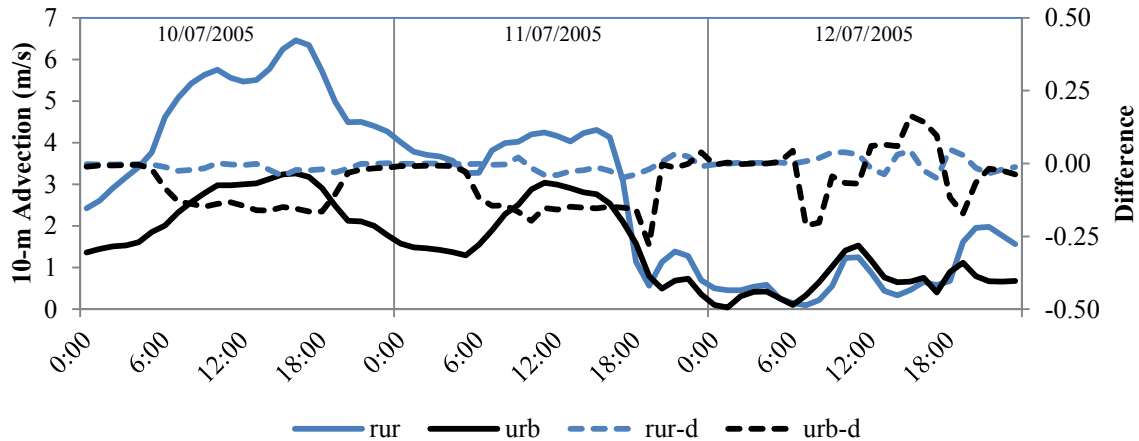


Figure 9-16. 10-m wind speed (advection) in urban and rural areas in the three-day heatwave period and the difference between CTRL and ALBEDO. rur, urb, rur-d, and urb-d denote rural area in CTRL, urban area in CTRL, difference between ALBEDO and CTRL in rural area, and difference between ALBEDO and CTRL in urban area, respectively

9.2.9. Ozone concentration

Ozone concentration (Figure 9-17) is not high enough to be considered as a threat; 65 ppbv is the threshold set in Canadian cities for 8-hour averaged O_3 (Barton, 2008). Higher O_3 on the third

day shows the high dependency of ozone generation to the air temperature. Hourly averaged O_3 reduction was negligible (< 0.1 ppbv). On the third day the variation of O_3 has inconsistency because of the combined effect of air temperature, wind speed, and PBL height.

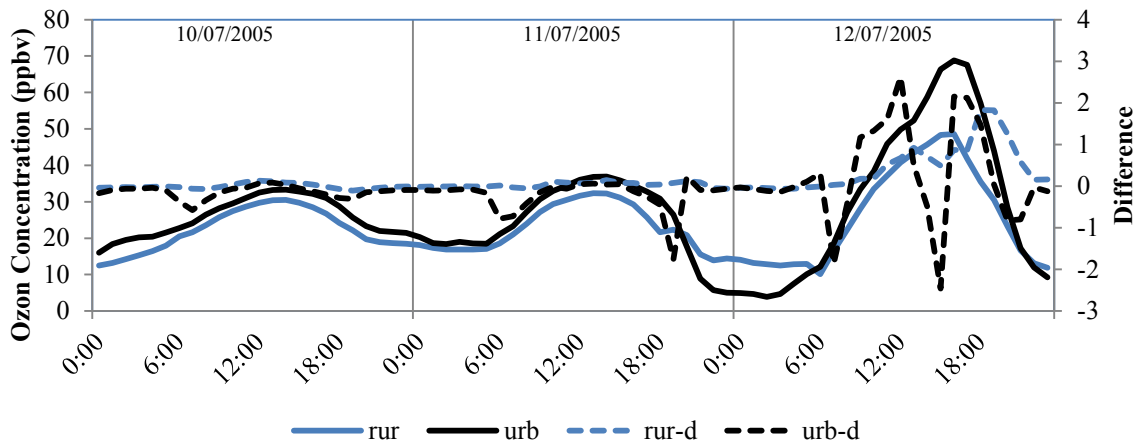


Figure 9-17. Ozone concentration at 5m from the ground in urban and rural areas in the three-day heatwave period and the difference between CTRL and ALBEDO. rur, urb, rur-d, and urb-d denote rural area in CTRL, urban area in CTRL, difference between ALBEDO and CTRL in rural area, and difference between ALBEDO and CTRL in urban area, respectively.

On 11 July, the slight decrease in the O_3 occurs in the evening and the morning, when the ozone reduction is observed through the urban area (Figure 9-18).

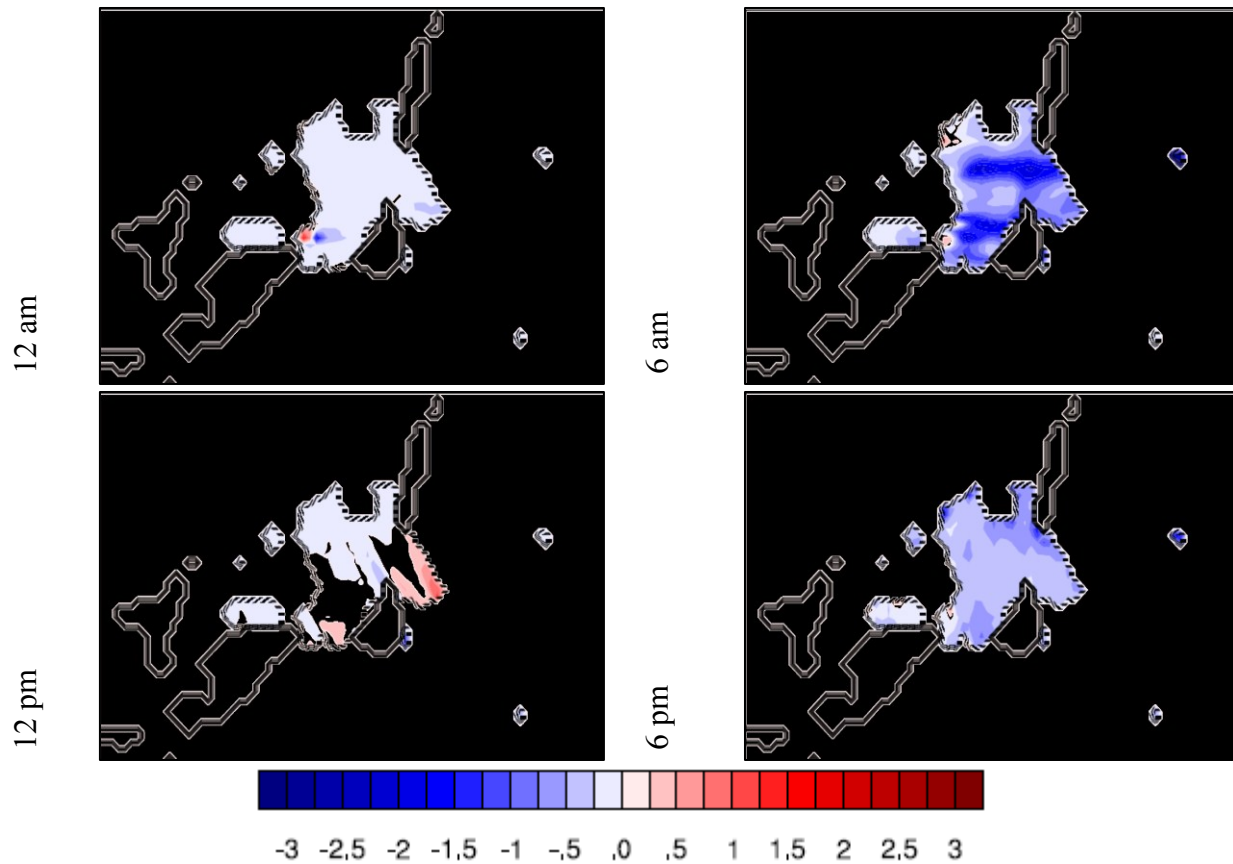


Figure 9-18. Ozone concentration difference (ppbv) between CTRL and ALBEDO on July 11th, 2005 (the dashed line is the urban border and dark blue color represents rivers).

On 12 July, for some hours and in some grids O_3 is decreased and in some other grids and hours O_3 is increased (Figure 9-19). Spatial distribution of the ozone concentration shows the complication of the process which is affected by wind pattern and air temperature, simultaneously. The albedo enhancement did not have significant effect on ozone concentration, and the difference is less than 4% of the ozone concentration in CTRL.

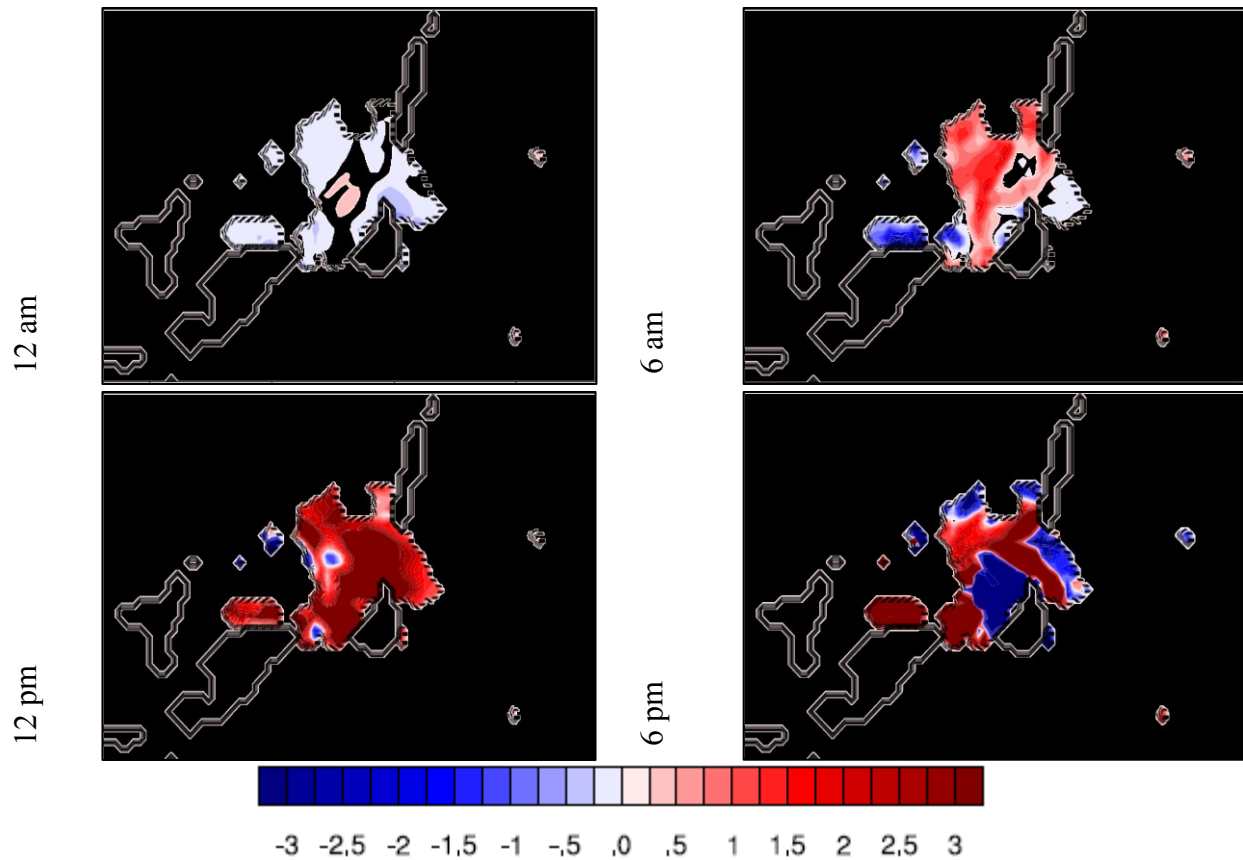


Figure 9-19. Ozone concentration difference (ppbv) between CTRL and ALBEDO on July 12th, 2005 (the dashed line is the urban border and dark blue color represents rivers).

9.2.10. PM 2.5 concentration

The concentration of $PM_{2.5}$ on the third day is above the threshold set point, below $30 \mu\text{g}/\text{m}^3$ averaged over 24 hours (Barton, 2008). The albedo enhancement decreases the peak $PM_{2.5}$ (from $140 \mu\text{g}/\text{m}^3$ to $125 \mu\text{g}/\text{m}^3$) and decreases the 24-hour average by $2 \mu\text{g}/\text{m}^3$, which is still above the threshold set (Figure 9-20).

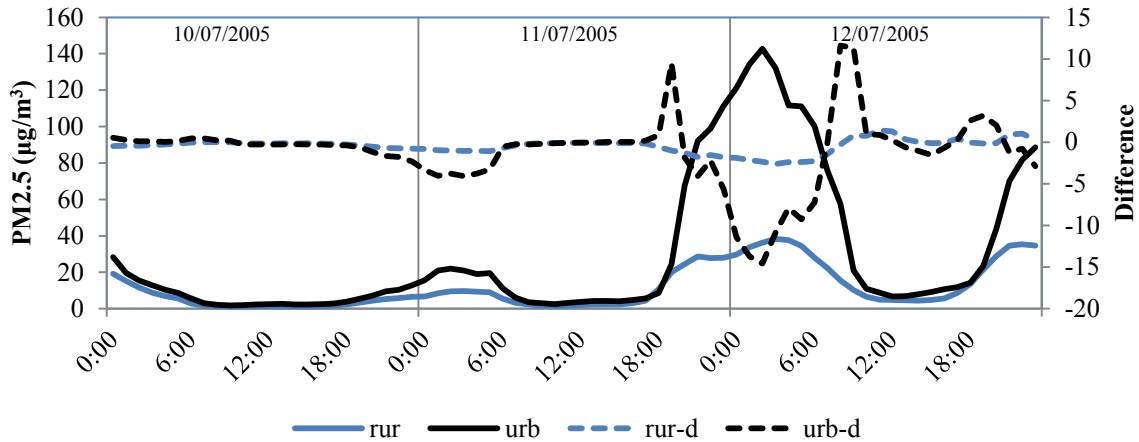


Figure 9-20. PM_{2.5} concentration at 5m from the ground in urban and rural areas in the three-day heatwave period and the difference between CTRL and ALBEDO. rur, urb, rur-d, and urb-d denote rural area in CTRL, urban area in CTRL, difference between ALBEDO and CTRL in rural area, and difference between ALBEDO and CTRL in urban area, respectively.

Figure 9-21 shows the spatial distribution of the difference between PM_{2.5} in ALBEDO and CTRL. Comparing the $PM_{2.5}$ with anthropogenic emission of SO₂ shows the effect of temperature in nucleation of SO₂ causing a reduction of PM_{2.5} in southern Montreal.

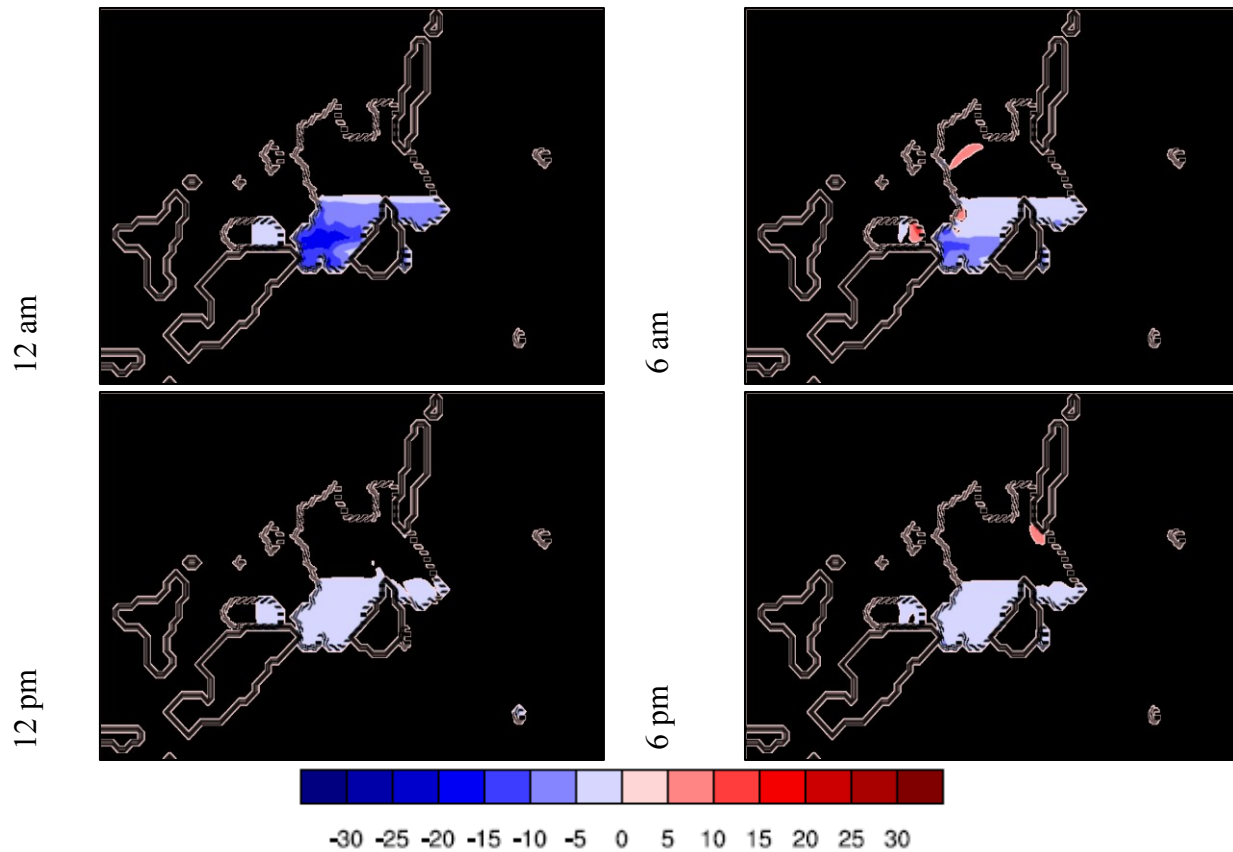


Figure 9-21. PM_{2.5} concentration difference ($\mu\text{g}/\text{m}^3$) between CTRL and ALBEDO on July 11th, 2005 (the dashed line is the urban border and dark blue color represents rivers)

On 12 July, similar to the previous day, the maximum decrease occurs in the south part of the city (Figure 9-22). However, in some other parts an increase in the concentration of particulate matter is observed mainly due to the decrease in PBL height. High correlation between the height of PBL and the concentration on PM_{2.5} is resulted from the simulations.

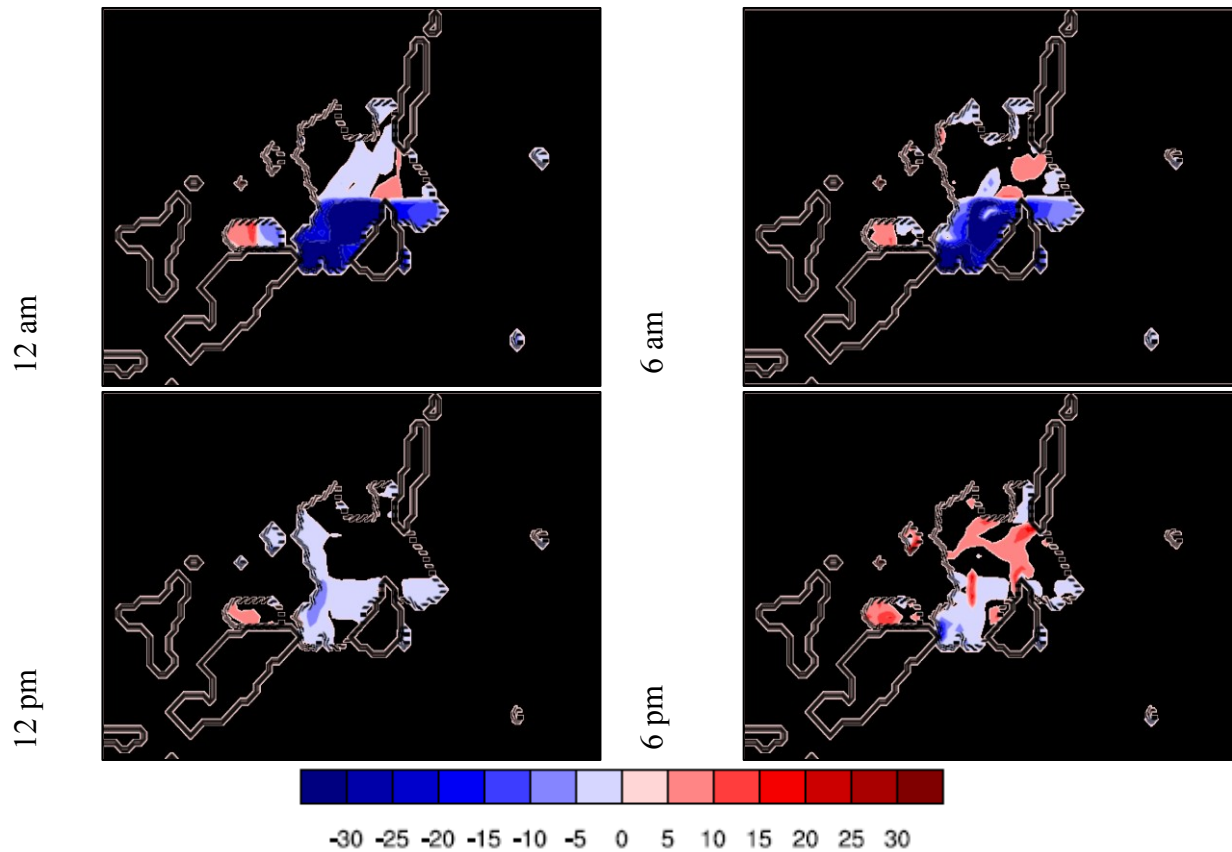


Figure 9-22. PM2.5 concentration difference ($\mu\text{g}/\text{m}^3$) between CTRL and ALBEDO on July 12th, 2005 (the dashed line is the urban border and dark blue color represents rivers)

9.2.11. Energy consumption

The peak energy consumption of HVAC systems occurs in the evening of all days (Figure 9-23). The maximum E is about $4 \text{ W}/\text{m}^2$ on the hottest day and the minimum E is negligible during nighttime. Increasing the albedo can reduce the energy consumption of buildings by reducing the solar gain from roof and walls, and the reduced ambient temperature. The average decrease in E is about $0.1 \text{ W}/\text{m}^2$ and the maximum E is $0.4 \text{ W}/\text{m}^2$. The average energy savings is roughly about 5% of the energy consumption.

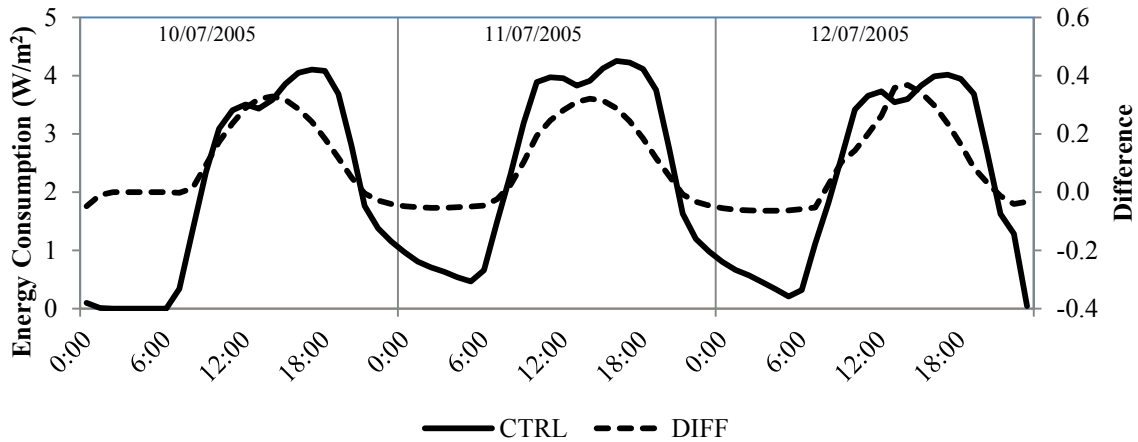


Figure 9-23. Energy consumption of HVAC systems of buildings in the three-day heatwave period and the difference between CTRL and ALBEDO (DIFF).

9.3. Conclusion on the characterization of the effect of an increase in the urban albedo on the air quality of Montreal

In this chapter the chemistry part of the WRF is added to the platform that I developed for urban climate modeling to investigate the effect of increasing the urban albedo on concentration of pollutants. Additionally, different meteorological parameters are analyzed for better understanding of their interactions with aerosols. In my simulations, all sophistications of climate modeling coupled to chemistry are considered. The albedo of roofs, walls, and roads in Montreal are increased by 0.45, 0.4, and 0.25, respectively. The air temperature is decreased during the selected heatwave period, with the maximum hourly decrease of about 1°C. The 1-hour ozone concentration is changed with less than 4% of the base case, which is considered to be negligible. That is to say, the decrease in the height of the planetary boundary layer counteracts the effect of a decrease in temperature on reaction rate of ozone generation. The concentration of PM2.5 decreases mostly in the southern part of Montreal, with a 24-hour average of about 2 µg/m³. The PM2.5 concentration is found to be highly dependent on the height of the planetary boundary layer. The energy consumption of HVAC systems is reduced by 0.4 W/m² at the peak.

Chapter Ten: Summary and Conclusion

The rapid expansion of dense urban areas around the world puts more people at risk of climate variability. Typical higher temperature of cities is a well-documented side effect of the urbanization; it causes premature deaths and inflates energy costs. Meanwhile, the rate of smog formation is higher in summertime, showing a strong dependency on the air temperature. Air pollution is also considered as a threat to public health, in terms of rising cancer incidents involving respiratory organs. Hence, mitigation strategies are proposed to fight the high temperature of urban areas, loosely called “urban heat island (UHI).”

Among scientifically justified mitigation strategies, albedo enhancement (i.e., increasing reflectivity) of urban areas is a low-cost and applicable strategy. Increasing the urban albedo is linked to an increase in reflectance of individual elements of the urban fabric (e.g., roofs, walls, and roads). The albedo enhancement backscatters the incoming solar radiation striking urban surfaces, causing less solar heat gain. Therefore, lower heat transfer to the air decreases the near surface air temperature in the city. In addition, the cooling energy consumption of buildings is reduced as a result of lower heat gain by building surfaces (direct effect) and lower temperature around the buildings community-wide (indirect effect). On the other hand, there are penalties related to lower solar heat gain, such as potential increase in heating during winter. However, the energy input to the system (here, the solar radiation) is much lower during the winter, which decreases the magnitude of the response. In other words, the higher zenith angle and cloud cover attenuates the energy passing through the atmosphere and reduces the winter energy penalties compared to the summer energy savings.

In cold climates, increasing the albedo is more compelling because the solar elevation causes a higher difference between the incoming radiation in summer and in winter. Moreover, in winter, a cold urban area is covered with snow which conceals underlying dark and light color differences. Having the basics, I investigated the effect of increasing albedo in two Canadian cities in detail.

10.1. Summary

Two main objectives are pursued: (1) developing a platform for urban climate simulation in cold regions, and (2) informing policymakers on the magnitude of the effect of implementing a high albedo strategy on urban heat island, energy consumption of buildings, and air pollution. The Weather Research and Forecasting (WRF) ensemble with various options for microphysics, cloud convection, planetary boundary layer, radiation, and land surface models was selected to perform simulations. WRF is the only mesoscale meteorological model with different options for urban canopy modeling, building energy modeling, and online coupling to chemical transport modeling. In addition the solver of WRF (ARW) is capable of simulating a domain with sub-kilometer grid size.

The first task is to build a systematic approach in selecting an appropriate parameterization for cold climates and sub-kilometer grid sizes. The 2-m air temperature, 10-m wind speed, and 2-m relative humidity are the typical measured data in weather stations selected to determine the accuracy of the model. Urban canopy models (UCMs) are compared using the selected meteorological variables and their measured data from weather stations around the Greater Montreal and the Greater Toronto areas. A multi-layer UCM is selected as the best option to assess mitigation strategies considering the effect of vertical flux of heat and momentum. Thereafter, the maximum decrease in air temperature by increasing roof albedo from 0.2 to 0.8 in a summer period is about 1 °C in both cities.

WRF can be set up with different parameterizations for microphysics, cloud convection, planetary boundary layer, radiation, and land surface. I performed an analysis on the sensitivity of air temperature, wind speed, relative humidity, and precipitation to the choice of model ensemble for a summer period. Almost all different options compatible with ML-UCM were tested. Similar to the comparison for UCMs, output of each set of models is compared to observed data. The model ensemble using WDM6 (Lim and Hong, 2010), Grell 3D (Grell, 1993; Grell and Devenyi, 2002), MYJ (Janjic, 1994), and RRTMG (Iacono et al., 2008) as microphysics, cumulus, planetary boundary layer, and radiation schemes, respectively, has an acceptable mean average error in both urban and rural areas compared to other model ensembles, while functioning in a timely, efficient manner.

The importance of the urban morphology on predicting the air temperature of Montreal was determined. High heterogeneity of urban areas along with dynamic performance of HVAC systems need an extensive data gathering and analysis to prepare appropriate inputs for ML-UCM. However, much of the information from large urban dataset would be lost through assuming an idealize canopy. Therefore, I developed an algorithm to estimate urban and building properties based on limited data. In addition, some modification of sky view factor is tested and the air temperature is compared with a base case considering default settings of WRF. Urban heat island intensity (i.e., the difference between the air temperature in the urban area and its surroundings) and energy consumption of HVAC systems are compared for different cases. Considering the modified urban characteristics results in a 0.7 °C decrease in the predicted UHI intensity, and a change in the predicted energy consumption by a factor of 3.

Another contribution of this dissertation is to apply a practical method for annual assessment of albedo enhancement in Montreal. Since the climate simulation with fine-resolution horizontal grid size is not computationally feasible for a long period, I have developed an algorithm based on Typical Meteorological Year (Hall et al., 1978) to select monthly typical meteorological days (MTMDs) in a year. Then, 24 simulations for the 12 MTMDs of a year and for two scenarios (CTRL—albedo of 0.2 for all urban surfaces, and ALBEDO—albedo of 0.65, 0.6, and 0.45 for roofs, walls, and roads, respectively). The annual energy consumption of the AC systems decreases by 10 kWh/100m² of the roof area, and annual energy expenditure savings of 1 \$/100m² is estimated. The daily averaged air temperature in summer is decreased between 0.1 °C and 0.3 °C.

To consider the sophistication of the dynamics of the HVAC system and the effect of snow on the energy consumption of buildings, four prototype commercial buildings are selected for further analysis. Hourly data of climate simulation in MTMDs is used to modify the weather data of the DOE-2 building energy model. Then, the simulations are performed considering snow on the roof for three cases; (1) dark roof with actual weather data, (2) white roof with actual weather data, and (3) white roof with modified weather data. In all cases, increasing the reflectivity of roof and walls results in money savings (or the penalty is negligible). The maximum money savings from albedo enhancement of buildings is about 11% with combined direct (7%) and indirect (4%) effects.

Finally, the meteorological model is coupled to the chemistry part to quantify the effect of albedo enhancement on the air temperature by considering the interactions between the aerosols and incoming radiation. Furthermore, the feedback of the change in meteorological variables (air temperature, wind speed, planetary boundary layer height, etc.) on concentration of ozone and fine particulate matter (PM_{2.5}) is estimated. The air temperature is decreased during the selected heatwave period, with a maximum hourly decrease of about 1°C. The 1-hour ozone concentration is changed with less than 4% of the base case, which is considered to be negligible. The concentration of PM_{2.5} is decreased mostly in southern part of Montreal, with a 24-hour average of about 2 µg/m³. The energy consumption of HVAC systems is reduced by 0.4 W/m² at the peak.

10.2. Conclusion

This research has focused on improving the current state of the knowledge for better understanding the physics of land–atmosphere interactions. A platform is proposed for urban climate simulation based on the comparison with observations in Canadian cities. Additionally, the bulk effect of an increase in urban albedo is characterized. There is a need to modify the platform and to further quantify the effect of albedo enhancement in future because of the current shortcomings in microphysics, cloud convection, and planetary boundary layer models. In particular, using fine-resolution horizontal grids is challenging for an adequate understanding of sub-kilometer non-resolvable phenomena.

10.2.1. Urban climate and air quality modeling

The basis for urban climate modeling is the mesoscale meteorological modeling that deals with large-scale processes that are not yet quantified. As an example, the controversial results on the change in the downwelling solar radiation on the ground are simply assumed as the error in the model. By accepting the model ensemble, one realizes that the errors also propagate in the final solutions. Therefore, further investigation in atmospheric science is required to better predict the water-related processes for urban-scale simulations. The sensitivity analysis is accepted as the best choice to select the set of options with the least mean average error.

The input data are very limited (specifically anthropogenic emissions) and they might be a source of errors. Averaging the pollution in a larger grid and then downscaling it to a smaller grid might change the location of the point source emission.

10.2.2. The albedo enhancement strategy

Increasing the albedo of urban surfaces is found to be an effective strategy to decrease the air temperature and energy consumption of buildings in urban areas without any significant effect on the concentration of pollutants. The positive effect of the strategy on reducing the air temperature and energy consumption is persistent throughout the selected year, but the concentrations of pollutants are estimated only in the summer period. Hence, a thorough analysis of seasonal effect of the albedo enhancement of air quality is needed.

Besides the scientific part of applying a mitigation strategy, implementation is complicated in term of logistics. There should be critical thinking and policy development on incentives for owners, prioritizing the building types for modification, passing laws and regulations, and education. Recent developments in the roofing industry initiated the promotion of highly reflective materials, but more effort is needed for such options to become a regular choice of customers.

10.3. Contributions

This research advances the study of implementing highly reflective materials in urban areas through the following innovative contributions:

1. *A systematic approach for characterizing the effect of surface modification on urban air temperature, air quality, and energy consumption of buildings.* The approach that is used through the thesis provides a guideline for researchers to consider different aspects of urban climate and air quality modeling along with detailed energy calculations for buildings. The step-by-step approach is applicable for any mitigation strategy and for any climate region by considering all influential factors.
2. *A set of recommendations to select the most appropriate model ensemble for urban climate simulation in cold climates using high-resolution grid spacing.* The recommendations indicate the high sensitivity of air temperature and wind speed to the

choice of model ensemble that results in a significant difference in calculations. Applying the recommendations increases the accuracy of the mesoscale modeling in cold climates.

3. *An algorithm to efficiently use limited data for identifying urban morphology of a city.* The proposed algorithm enables the researchers to characterize morphological parameters to identify the geometry of the “ideal urban canopy” in a multi-layer urban canopy model. This user-friendly method would be applied to cities with a lower level of heterogeneity.
4. *An algorithm to select a day of a month for urban climate simulation in a timely manner.* The algorithm functions with the minimum loss of information within the framework of urban climate simulation.
5. *A novel approach for quantifying the effect of increasing urban albedo by considering the contribution of synoptic weather, urban geometry, heat emission from buildings, and chemical reactions.* The integration of mesoscale model with urban canopy and building energy model as well as chemical reactions in the urban areas provides the broader view of selecting a mitigation strategy.

The systematic approach, recommendations, and algorithms are applied to a case study and the effects of increasing the urban albedo on air temperature, air quality, and building energy consumption are presented. Results of this research can be immediately used by urban planners, politicians, and city engineers, if they are concerned about mitigating urban heat island. The introduced methodology is encouraged to be used for all Canadian cities.

10.4. Future works

As is summarized in this chapter, an increase in the urban albedo is a promising strategy to reduce the air temperature of urban areas in cold regions. In addition, a significant savings in the energy consumption of HVAC systems of buildings (~5%) can be achieved without a notable effect on the concentration of pollutants. Future studies are limited by the computational resources from carrying out more intense annual evaluation of the albedo enhancement and the available parameterizations for fine-resolution grids. On the other hand, more detailed data for urban morphology, building characteristics, anthropogenic emission, and biogenic emission will likely become available to be used with the developed platform. More accurate input data will increase the accuracy of the model. In addition, some activities in urban areas (e.g.,

transportation) are not considered in this model but can be added in future. The developed platform for urban climate modeling can be tested for warmer climates to investigate mitigation strategies.

10.5. Policy recommendations

Current study shows that increasing urban albedo decreases the air temperature, improves the air quality, and reduced the energy consumption of the building (and saves energy expenditure). Therefore, I would recommend setting standards and regulations in Montreal to implement this mitigation strategy for fighting urban heat island. the implementation of such strategy would be achieved without any incremental cost. Roofs are normally renovated in a period of 15-20 years and during the installation of new roof, reflective materials can be used. Moreover, in Montreal, streets and roads are frequently repaved and in the new pavement asphalt can be replaced by reflective cement. Walls are painted in a period of 5-10 years; reflective paints can reduce the heat absorption by walls. Akbari et al. (2001) and Rosenfeld et al. (1996) are among a few studies addressing the policy issues of implementing reflective surface materials. They have suggested monetary incentives for promoting reflective materials. However, this approach might not be effective for Montreal with low energy price. In future, with possible increase in energy price, monetary incentive can be used as a self-motivating strategy.

References

- Ackermann, I.J., Hass, H., Memmesheimer, M., Ebel, A., Binkowski, F. S., Shankar, U., (1998). “Modal aerosol dynamics model for Europe: development and first applications.” *Atmospheric Environment*, 32 (17), pp. 2981–2999.
- Air Resources Board, (2009). “2008 Estimated Annual Average Emissions.” (Air Resources Board of California Environmental Protection Agency) [online: http://www.arb.ca.gov/app/emsinv/emssumcat_query.php?F_DIV=-4&F_DD=Y&F_YR=2008&F_SEASON=A&SP=2009&F_AREA=CO&F_CO=19].
- Akbari, H. and Konopacki, S., (2005). “Calculating energy-saving potentials of heat-island reduction strategies.” *Energy Policy*, 33, pp. 721–756.
- Akbari, H., Pomerantz, M. and Taha, H., (2001). “Cool surfaces and shade trees to reduce energy use and improve air quality in urban areas.” *Solar Energy*, 70(3), pp. 295–310.
- Akbari, H. and Konopacki, S., (2004). “Energy effects of heat-island reduction strategies in Toronto, Canada.” *Energy*, 29, pp. 191–210.
- Akbari, H., Menon, S. and Rosenfeld, A., (2009). “Global cooling: increasing world-wide urban albedos to offset CO₂.” *Climatic Change*, 94, pp. 275–286.
- Akbari, H. and Matthews, H. D., (2012). “Global cooling updates: reflective roofs and pavements.” *Energy and Buildings*, 55, pp. 2–6.
- Akbari, H., Matthews, H. D. and Seto, D., (2012). “The long-term effect of increasing the albedo of urban areas.” *Environmental Research Letters*, 7, 024004.
- Arnfield, J. and Grimmond, C., (1998). “An urban canopy energy budget model and its application to urban storage heat flux modeling.” *Energy and Building*, 27, pp. 61-68.
- Arnfield, A.J. (2003) “Two decades of urban climate research: a review of turbulence, exchanges of energy and water, and the urban heat island.” *International Journal of Climatology*, 23, 1-26.
- ARW user guide, (2012). “ARW version 3 modeling system user’s guide.” National Center for Atmospheric Research, Boulder (CO), US.
- Ashie, Y., Ca, V. T. and Asaeda, T., (1999). “Building canopy model for the analysis of urban climate.” *Journal of Wind Engineering and Industrial Aerodynamics*, 81, pp. 237-248.
- ASHRAE. (2007a). “ASHRAE Standard 90.1.” ASHRAE handbook. Atlanta, GA (US).

- ASHRAE. (2007b). "ASHRAE HVAC applications." ASHRAE handbook. Atlanta, GA (US).
- Atkinson, B. W., (2003). "Numerical modelling of urban heat-island intensity." *Boundary Layer Meteorology*, 109, pp. 285–310.
- Atkinson, R., et al., (2004). "Evaluated kinetic and photochemical data for atmospheric chemistry: Volume I - gas phase reactions of Ox, HOx, NOx and SOx species." *Atmospheric Chemistry and Physics*, 4, pp. 1461-1738.
- Atkinson, R., et al., (2006). "Evaluated kinetic and photochemical data for atmospheric chemistry: Volume II – gas phase reactions of organic species." *Atmospheric Chemistry and Physics*, 6, pp. 3625-4055.
- Atkinson, R., et al., (2007). "Evaluated kinetic and photochemical data for atmospheric chemistry: Volume III – gas phase reactions of inorganic halogens." *Atmospheric Chemistry and Physics*, 7, pp. 981-1191.
- Atkinson, R., et al., (2008). "Evaluated kinetic and photochemical data for atmospheric chemistry: Volume IV – gas phase reactions of organic halogen species." *Atmospheric Chemistry and Physics*, 8, pp. 4141-4496.
- Atkinson, R., et al., (2010). "Evaluated kinetic and photochemical data for atmospheric chemistry: Volume V – heterogeneous reactions on solid substrates." *Atmospheric Chemistry and Physics*, 10, pp. 9059-9223.
- Atkinson, R., et al., (2013). "Evaluated kinetic and photochemical data for atmospheric chemistry: Volume VI – heterogeneous reactions with liquid substrates." *Atmospheric Chemistry and Physics*, 13, pp. 8045-8228.
- Austin, J., (1999). "Day-of-week patterns in diurnal profiles of NO₂/NO ratios Los Angeles Area, 1989 through 1998." Planning and Technical Support Division California Air Resources Board. [Online: www.arb.ca.gov/research/weekendeffect/NONO2ratio092299.doc].
- Baldwin, A. C., Barker, J. R., Golden, D. M., and Hendry, D. G. (1977). "Photochemical smog: rate parameter estimates and computer simulations." *The Journal of Physical Chemistry*, 81 (25), pp. 2483-2492.
- Barton, J. (2008). "Canada-Wide Standards and Innovative Transboundary Air Quality Initiatives." *Journal of Toxicology and Environmental Health, Part A*, 71, pp. 74-80.

- Behidj, N., et al., (2012). "Energy Use Data Handbook, 1990-2009." Natural Resource Canada, Ottawa (ON), Canada.
- Beranová, R. and Huth, R., (2005). "Long-term changes in the heat island of Prague under different synoptic conditions." *Theoretical and Applied Climatology*, 82 (1-2), pp. 113-118.
- Berdahl, P., and Bretz, S. E. (1997). "Preliminary survey of the solar reflectance of cool roofing materials. *Energy and Buildings*." 25, pp. 149- 158.
- Berdahl, P., Akbari, H., Levinson, R., and Miller, W. A. (2008). "Weathering of roofing materials – An overview. *Construction and Building Materials*." 22(4), pp. 423-433.
- Best, M. J., (2005). "Representing urban areas within operational numerical weather prediction models." *Boundary Layer Meteorology*, 114 (1), pp. 91-109.
- Binkowski, F.S. and Shankar, U., (1995). "The regional particulate matter model, 1. mode description and preliminary results." *Journal of Geophysical research*, 100, pp. 26191-26209
- Bornstein, R. and Lin, Q., (2000). "Urban heat islands and summertime convective thunderstorms in Atlanta: Three case studies." *Atmospheric Environment*, 34, pp. 507-516.
- Bornstein, R. D., Gutierrez, E., Gonzalez, J., Martilli, A., Chen, F., and Ching, J. K., (2012). "Effect of sub-kilometer grid-spacing and time step magnitude on the formation of horizontal-vorticies in urbanized-WRF simulations of NYC. AMS, 17th Conference on Air Pollution Meteorology with the A&WMA. New Orleans (LA), US.
- Bougeault, P., Lacarrere, P., (1989). "Parameterization of orography–induced turbulence in a mesobeta—scale model." *Monthly Weather Review*, 117, pp. 1872–1890.
- Brooks, H. E., Doswell, C. A., and Maddox, R. A. (1991). "On the use of mesoscale and cloud-scale models in operational forecasting." *Weather and Forecasting*, 7, pp. 120-132.
- Brown, M. J., Grimmond, S., Ratti, C., (2001). "Comparison of methodologies for computing sky view factor in urban environments," *International Society of Environmental Hydraulics Conf. Tempe, AZ*.
- Bruse, M. and Fleer, H., (1998). "Simulating surface–plant–air interactions inside urban environments with a three dimensional numerical model". *Environmental Modelling and Software*, 13, pp. 373–384.
- Bueno, B., Norford, L., Pigeon, G. and Britter, R., (2011). "Combining a detailed building energy model with a physically-based urban canopy model." *Boundary Layer Meteorology*, 140(3), pp. 471-489.

- Byrd, L.W., (1993). "View factor algebra for two arbitrary sized nonopposing parallel rectangles," *Journal of Heat Transfer*, 115 (2), pp. 517-518.
- Carter, W. P., Wine, A. M., Darnall, K. R., and N. Pitts, J. (1979). "Smog chamber studies of temperature effects in photochemical smog." *Environmental Science and Technology*, 13 (9), pp. 1094–1100.
- Cintineo, R., Otkin, J. A., Xue, M., and Kong, F. (2014). "Evaluating the performance of planetary boundary layer and cloud microphysical parameterization schemes in convection-permitting ensemble forecasts using synthetic GOES-13 satellite observations." *Monthly Weather Review*, 142, pp. 163-182.
- City of Montreal, (2009) "Montreal Cartographic Plans." Montreal (QC), Canada.
- Civerolo, K. et al., (2007). "Estimating the effects of increased urbanization on surface meteorology and ozone concentrations in the New York City metropolitan region." *Atmospheric Environment*, 41 , pp. 1803–1818.
- Chen, F. and Dudhia, J., (2001). "Coupling an advanced land surface–hydrology model with the Penn State–NCAR MM5 modeling system. Part I: model implementation and sensitivity." *Monthly Weather Review*, 129, pp. 569-585.
- Chen, S.H., and Sun, W.Y., (2002), "A one-dimensional time dependent cloud model." *Journal of Meteorological Society of Japan*, 80, pp. 99–118.
- Chen, F. et al., (2009). "Development of the integrated WRF/Urban modeling system and its application to urban environmental problems." *The Seventh International Conference on Urban Climate*, 29 June - 3 July, Yokohama, Japan.
- Chen, F., et al. (2011). "The integrated WRF/urban modelling system: development, evaluation, and applications to urban environmental problems. *International Journal of Climatology*, 31, pp. 273–288.
- Ching, J., et al., (2009). "National urban database and access portal tool." *Bulletin of American Meteorological Society*, 90, pp. 1157–1168.
- Ching, J., (2013). "A perspective on urban canopy layer modeling for weather, climate and air quality applications." *Urban Climate*, 3, pp. 13–39.
- Chou, M. D., and Suarez, M. J. (1994). "An efficient thermal infrared radiation parameterization for use in general circulation models." *NASA Tech. Memo. 104606*, 3, 85pp.

- Clough, S., Shephard, M., Mlawer, E., Delamere, J., Iacono, M., Cady-Pereira, K. et al. (2005). "Atmospheric radiative transfer modeling: a summary of the AER codes." *Journal of Quantitative Spectroscopy and Radiative Transfer*, 91, pp. 233–244.
- Collins, W. J., Stevenson, D., Johnson, C., and Derwent, R., (1997). "Tropospheric ozone in a global-scale three-dimensional Lagrangian model and its response to NO_x emission controls." *Journal of Atmospheric Chemistry*, 26, pp. 223–274.
- Collins, W.D., et al., (2004). "Description of the NCAR Community Atmosphere Model (CAM3.0)," NCAR Technical Note. NCAR, Boulder (CO), US.
- Csiszar, I., and Gutman, G. (1999). "Mapping global land surface albedo from NOAA AVHRR." *Journal of Geophysical Research*, 104, pp. 6215–28.
- Cullather, R. I., Harshvardhan, and Campana, K. A. (1997). "Climatology of cloud and radiation fields in a numerical weather prediction model." *Theoretical and Applied Climatology*, 57, pp. 11-33.
- Dickerson, R. R., Kondragunta, S., Stenchikov, G., Civerolo, K. L., Doddridge, B. G., and Holben, B. N. (1997). "The impact of aerosols on solar ultraviolet radiation and photochemical smog." *Science*, 278, pp. 827-830.
- LBNL, (1982). "DOE-2 Engineers Manual, version 2.1A," Lawrence Berkeley Laboratory, 1982, LBL 11353, Berkeley (CA), US.
- Dudhia, J., (1989). "Numerical study of convection observed during the winter monsoon experiment using a mesoscale two-dimensional model." *Journal of Atmospheric Sciences*, 46, pp. 3077–3107
- Duffie, J.A., and Beckman, W.A., (1991). "Solar Engineering of Thermal Processes.", Wiley and Sons, Inc., Hoboken (NJ), US.
- Dupont, S., Otte, T. L. and Ching, J. K. S., (2004). "Simulation of meteorological fields within and above urban and rural canopies with a mesoscale model (MM5)." *Boundary Layer Meteorology*, 113, pp. 111–158.
- Environment Canada, (2013). [Online: <http://climate.weather.gc.ca/>].
- Environment Canada, (2008). [Online: http://climate.weather.gc.ca/prods_servs/engineering_e.html].
- EPA, (2005). [Online: <http://www.epa.gov/ttnchie1/net/2005inventory.html>].

- Eyring, V., and et al. (2006). "Assessment of temperature, trace species, and ozone in chemistry-climate model simulations of the recent past." *Journal of Geophysical Research*, 111, D22308.
- Flanner, M. G., Zender, C. S., Randerson, J. T., and Rasch, P. J. (2007), "Present day climate forcing and response from black carbon in snow," *Journal of Geophysical Research*, 112, D11202,
- Flanner, M. G., Zender, C. S., Hess, P. G., Mahowald, N. M., Painter, T. H., Ramanathan, V., and Rasch, P. J., (2009), "Springtime warming and reduced snow cover from carbonaceous particles." *Atmospheric Chemistry and Physics*, 9, pp. 2481-2497.
- Ford, A., (2009). "Modeling the environment." Island Press, 2 ed., Washington (DC, US)
- Fountoukis, C., Koraj, D., Denier van der Gon, H. A. C., Charalampidis, P. E., Pilinis, C., and Pandis, S. N., (2013). "Impact of grid resolution on the predicted fine PM by a regional 3-D chemical transport model." *Atmospheric Environment*, 68, pp. 24–32.
- Gantt, B., Meskhidze, N., Zhang, Y., and Xu, J., (2010). "The effect of marine isoprene emissions on secondary organic aerosol and ozone formation in the coastal United States." *Atmospheric Environment*, 44, pp. 115–121.
- Gago, E., Roldan, J., Pacheco-Torres, R. and Ordóñez, J., (2013). "The city and urban heat islands: A review of strategies to mitigate adverse effects." *Renewable and Sustainable Energy Reviews*, 25, pp. 749–758.
- Gao, H. O., (2007). "Day of week effects on diurnal ozone/NO_x cycles and transportation emissions in Southern California." *Transportation Research*, 12, pp. 292–305.
- Gaz Metro, (2014). [Online: <http://www.grandesentreprises.gazmetro.com/prix-du-gaz/evolution-prix-du-gaz.aspx?culture=en-ca>].
- Geduld, J., (2008). "No breathing room, national illness costs of air pollution (summary report)." Canadian Medical Association, Ottawa (ON), Canada.
- Georgescu, M. A. and Moustauoi, M., (2012). "Seasonal hydro-climate impacts of sun corridor expansion." *Environmental Research Letter*, 7, 034026.
- Gray, DM., (1970). "Handbook on the principles of hydrology." Canadian National Committee for the International Hydrological Decade. Ottawa (ON), Canada.
- Grell, G. A., (1993), "Prognostic evaluation of assumptions used by cumulus parameterizations." *Monthly Weather Review*, 121, pp. 764–787.

- Grell, G. A, Devenyi, D., (2002), "A generalized approach to parameterizing convection combining ensemble and data assimilation techniques." *Geophysical Research Letters*, pp. 29, 1693.
- Grell, G. A. and Freitas, S. R., (2014). "A scale and aerosol aware stochastic convective parameterization for weather and air quality modeling," *Atmospheric Chemistry and Physics*, 14, pp. 5233-5250.
- Gross, A., and Stockwell, W.R., (2003), "Comparison of the EMEP, RADM2 and RACM mechanisms." *Journal of Atmospheric Chemistry*, 44, pp. 151–170
- Hall, I., Prairie, R., Anderson, H., and Boes. E.. (1978). "Generation of Typical Meteorological Years for 26 SOLMET stations. SAND78-1601." Sandia National Laboratories, Albuquerque, (NM), US.
- Hamdi, R., Schayes G., (2007). "Validation of Martilli's urban boundary layer scheme with measurements from two mid-latitude European cities." *Atmospheric Chemistry and Physics*, European Geosciences Union (EGU), 7 (17), pp.4513-4526.
- Hämmerle, M., Gál, T., Unger, J., Matzarakis, A., (2011). "Comparison of models calculating the sky view factor used for urban climate investigations," *Theoretical and Applied Climatology*, 105 (3-4), pp. 521-527.
- Han, J. and Pan, H., (2011). "Revision of convection and vertical diffusion schemes in the NCEP Global Forecast System." *Weather Forecasting*, 26, pp. 520–533.
- Hess, G., Carnovale, F., Cope, M., and Johnson, G. M. (1992). "The evaluation of some photochemical smog reaction mechanisms-1. temperature and initial composition effects." *Atmospheric Environment*, 26 (4), pp. 625-641.
- Hippler, H., Rahn, R., and Troe, J. (1990). "Temperature and pressure dependence of ozone formation rates in the range 1–1000 bar and 90–370 K." *Journal of Chemical Physics*, 93(9), pp. 6560-6570.
- Hirsch, C., (2007). "Numerical computation of internal and external flows." John Wiley and Sons, Burlington (UK).
- Holden, Z. A., Abatzoglou, J. T., Luce, C. H., and Baggett, L. S., (2011). "Empirical downscaling of daily minimum air temperature at very fine resolutions in complex terrain." *Agricultural and Forest Meteorology*, 151, pp. 1066–1073.

- Hong, S.Y., Dudhia, J., and Chen, S.H., (2004). "A revised approach to ice microphysical processes for the bulk parameterization of clouds and precipitation," *Monthly Weather Review*, 132, pp. 103–120.
- Hong, S., and Lim, J. J., (2006). "The WRF single–moment 6–class microphysics scheme (WSM6). *Journal of Korean Meteorological Society*, 42, pp. 129–151.
- Horvath, K., Koracin, D., Vellore, R., Jiang, J., and Belu, R., (2012). "Sub-kilometer dynamical downscaling of near-surface winds in complex terrain using WRF and MM5 mesoscale models." *Journal of Geophysical Research*, 117, D11111.
- Hosseini, M., and Akbari H., (2014). "Heating energy penalties of cool roofs: The effect of snow accumulation on roofs." *Advances in Building Energy Research*, 8 (1), pp. 1-13.
- Hosseini, M., (2014). "Cool roofs savings and penalties in cold climates: The effect of snow accumulation on roof." MSc thesis, Concordia University, Montreal (QC), Canada.
- Howard, L., (1833). "The climate of London, deduced from meteorological observations, made in the metropolis, and at various places around it." 2nd ed., Harvey and Darton, London, UK.
- Hydro Quebec, (2014). [Online: <http://www.hydroquebec.com/residential/understanding-your-bill/rates/residential-rates/rate-d/>].
- Iacono, M. J., Delamere, J. S., Mlawer, E. J., Shephard, M. W., Clough, S. A., and Collins, W. D., (2008). "Radiative forcing by long–lived greenhouse gases: calculations with the AER radiative transfer models." *Journal of Geophysical Research*, 113, D13103.
- IPCC, (2014). "Summary for policymakers. In: *Climate Change 2014: Impacts, Adaptation, and Vulnerability. Part A: Global and Sectoral Aspects.*" Contribution of Working Group II to the Fifth Assessment Report of the Inter-governmental Panel on Climate Change, pp. 1-32, New York (NY), USA.
- Iqbal, M., (1983), "An introduction to solar radiation." Academic Press Inc., New York (NY), US.
- Jacobson, M. Z. (2001a). "GATOR-GCMM: A study of day- and nighttime ozone layers aloft, ozone in national parks, and weather during the SARMAP Field Campaign." *Journal of Geophysical Research*, 106, pp. 5403-5420.
- Jacobson, M. Z. (2001b). "GATOR-GCMM: A global through urban scale air pollution and weather forecast model. 1. Model design and treatment of subgrid soil, vegetation, roads, rooftops, water, sea ice, and snow." *Journal of Geophysical Research*, 106, pp. 5385-5402.

- Jacobson, M. Z. and Ten Hoeve, J. E., (2012). “Effects of urban surfaces and white roofs on global and regional climate.” *Journal of Climate*, 25 (3), pp. 1028.
- Johnson, T. G., Watson, J. D. (1984). “The determination of view-factors in urban canopies,” *Journal of Climate and Applied Meteorology*, 23, pp. 329-335.
- Janjic, Z. I., (1990). “The step-mountain coordinate: physical package,” *Monthly Weather Review*, 118, pp. 1429–1443.
- Janjic, Z. I., (1994). “The step–mountain Eta Coordinate Model: Further developments of the convection, viscous sublayer, and turbulence closure schemes.” *Monthly Weather Review*, 122, pp. 927–945.
- Janjic, Z. I., (2002). “Nonsingular implementation of the Mellor–Yamada Level 2.5 Scheme in the NCEP meso model,” NCEP Office Note, No. 437, 61 pp
- Judek, S., Jessiman, B., Stieb, D. and Vet, R., (2004). “Estimated number of excess deaths in Canada due to air pollution.” Health Canada, Ottawa (ON), Canada.
- Kain, J. S., (2004). “The Kain–Fritsch convective parameterization: An update.” *Journal of Applied Meteorology*, 43, pp. 170–181.
- Kalnay, E. and Cai, M., (2003). “Impact of urbanization and land-use change on climate.” *Nature*, 423 , pp. 528-531.
- Kanda, M., Kawai, T., and Nakagawa, K., (2005). “A Simple Theoretical Radiation Scheme for Regular Building Arrays.” *Boundary Layer Meteorology*, 114, pp. 71–90.
- Karlsson, J. and Roos, A., (2000). “Modelling the angular behavior of the total solar energy transmittance of windows.” *Solar Energy*, 69, pp. 321–329.
- Kastendeuch, P. P. (2013). “A method to estimate sky view factors from digital elevation models,” *International Journal of Climatology*, 33 (6), pp. 1574–1578,
- Kayleigh , A. et al., (2013). “Streams in the urban heat island: spatial and temporal variability in temperature.” *Freshwater Science*, 32(1), pp. 309–326.
- Kikegawa, Y., Genchi, Y., Yoshikado, H. and Kondo, H., (2003). “Development of a numerical simulation system toward comprehensive assessments of urban warming countermeasures including their impacts upon the urban buildings energy-demands.” *Applied Energy*, 76, pp. 449–466.

- Klemp, J. B., Skamarock, W. C., and Dudhia, J., (2007) "Conservative split-explicit time integration methods for the compressible non-hydrostatic equations," *Monthly Weather Review*, 135, pp. 2897-2913.
- Korolevych, V. Y. and Richardson, R. B., (2012). "Low-frequency rotation of surface winds over Canada." *Atmosphere*, 3, pp. 522-536.
- Kosatsky, T., King, N. and Henry, B., (2005). "How Toronto and Montreal (Canada) respond to heat." *Verlag Berlin Heidelberg*, pp. 167-171.
- Koster, R. D., et al., (2000). "A catchment-based approach to modeling land surface processes in a general circulation model: 1. model structure." *Journal of Geophysical Research: Atmospheres*, 105(D20), pp. 24809-24822.
- Krayenhoff, S. E., and Voogt, J. A., (2010) "Impacts of urban albedo increase on local air temperature at daily–annual time scales: Model results and synthesis of previous work." *Journal of Applied Meteorology and Climatology* 49, pp. 1634-1648.
- Kuhn, M., (1998). "Intercomparison of the gas-phase chemistry in several chemistry and transport models," *Atmospheric Environment*, 32, pp. 693–709.
- Kulmala, M., Laaksonen, A., and Pirjola, L., (1998). "Parameterizations for sulfuric acid/water nucleation rates." *Journal of Geophysical Research: Atmospheres*, 103(D7), pp. 8301–8307.
- Kusaka, H. and Kimura, F., (2004). "Coupling a single-layer urban canopy model with a simple atmospheric model: Impact on urban heat island simulation for an idealized case." *Journal of Meteorological Society of Japan*, 82, pp. 67–80.
- Kusaka, H., Kondo, H., Kikegawa, Y. and Kimura, F., (2001). "A simple single-layer urban canopy model for atmospheric models: Comparison with multi-layer and slab models." *Boundary Layer Meteorology*, 101, pp. 329–358.
- Levinson, R., Akbari, H., and Berdahl, P. (2005). "Solar spectral optical properties of pigments, part II: Survey of common colorants." *Solar Energy Materials and Solar Cells*, 89(4), pp. 351-389.
- Levinson, R. M., and Akbari, H., (2010). "Potential benefits of cool roofs on commercial buildings: conserving energy, saving money, and reducing emission of greenhouse gases and air pollutants." *Energy Efficiency*, 3 (1), pp. 53-109.

- Leroyer, S., Belair, S., Mailhot, J., and Strachan, I. B., (2011). "Microscale numerical prediction over Montreal with the Canadian External Urban Modeling System." *Journal of Applied Meteorology Climatology*, 50, pp. 2410-2428.
- Leroyer, S., Belair, S., Husain, S., and Mailhot, J., (2014). "Subkilometer numerical weather prediction in an urban coastal area: A case study over the Vancouver Metropolitan Area." *Journal of Applied Meteorology Climatology*, 53, pp. 1433–1453.
- Li, D., Bou-Zeid, E., and Oppenheimer, M., (2014a). "The effectiveness of cool and green roofs as urban heat island mitigation strategies." *Environmental Research Letter*, 9, 055002.
- Li, D., and Bou-Zeid, E., (2014b). "Quality and sensitivity of high-resolution numerical simulation of urban heat islands." *Environmental Research Letter*, 9, 055001.
- Liao, J., Wang, T., Wang, X., Xie, M., Jiang, Z., Huang, X., Zhu, J., (2014). "Impacts of different urban canopy schemes in WRF/Chem on regional climate and air quality in Yangtze River Delta, China." *Atmospheric Research*, 145–146, pp. 226–243.
- Lim, K. S., and Hong, S., (2010). "Development of an effective double-moment cloud microphysics scheme with prognostic Cloud Condensation Nuclei (CCN) for weather and climate models," *Monthly Weather Review*, 138, pp. 1587-1612
- Lin, Y., R. Farley, D., and Orville, H. D., (1983). "Bulk parameterization of the snow field in a cloud model." *Journal of Climate and Applied Meteorology*, 22, pp. 1065–1092.
- Lin, Y., and Colle, B. A., (2011). "A new bulk microphysical scheme that includes riming intensity and temperature–dependent ice characteristics." *Monthly Weather Review*, 139, pp. 1013–1035.
- Liou, K.N., (1980), "An Introduction to Atmospheric Radiation." 2nd ed., Academic Press, San Diego (CA), US.
- Liu, G., Hogrefe, C., and Rao, S. T. (2003). "Evaluating the performance of regional-scale meteorological models: effect of clouds simulation on temperature prediction." *Atmospheric Environment*, 37, pp. 1425 – 1433.
- Liu, Y., Chen, F., Warner, T. and Basara, J., (2006). "Verification of a mesoscale data-assimilation and forecasting system for the Oklahoma City area during the Joint Urban 2003 field project." *Journal of Applied Meteorology and Climatology*, 45, pp. 912-929.
- Louis, J. F., (1979). "A Parametric Model of Vertical Eddies Fluxes in the Atmosphere", *Boundary Layer Meteorology*, 17, pp. 187–202.

- Mansell, E. R., Ziegler, C. L., and Bruning, E. C., (2010). “simulated electrification of a small thunderstorm with two–moment bulk microphysics.” *Journal of Atmospheric Sciences*, 67, pp. 171–194.
- Martilli, A., Clappier, A. and Rotach, M., (2002). “An urban surface exchange parameterization for mesoscale models.” *Boundary Layer Meteorology*, 104, pp. 261–304.
- Martilli, A. (2009). “On the derivation of input parameters for urban canopy models from urban morphological datasets.” *Boundary Layer Meteorology*, 130, pp. 301–306.
- Mass, C., et al., (2006). “Mesoscale Model Development and the meteorological community,” AMS report.
- Masson, V., (2000). “A physically-based scheme for the urban energy budget in atmospheric models.” *Boundary-Layer Meteorology*, 94, pp. 357–397.
- Mesinger, F., et al., (2006). “North American Regional Reanalysis.” *Bulletin of American Meteorological Society*, 87(3), pp. 343–360.
- Menon, S., Akbari, H., Mahanama, S., Sednev, I., and Levinson, R., (2010). “Radiative forcing and temperature response to changes in urban albedos and associated CO₂ offsets.” *Environmental Research Letters*, 5, 014005.
- Met Office, 2011. Met Office Unified Model. [Online: <http://www.metoffice.gov.uk/research/modelling-systems/unified-model>].
- Milbrandt, J. A., and Yau, M. K., (2005a). “A multimoment bulk microphysics parameterization. Part I: analysis of the role of the spectral shape parameter.” *Journal of Atmospheric Sciences*, 62, pp. 3051–3064.
- Milbrandt, J. A., and Yau, M. K., (2005b). A multimoment bulk microphysics parameterization. Part II: a proposed three–moment closure and scheme description.” *Journal of Atmospheric Sciences*, 62, pp. 3065–3081.
- Millstein, D. and Menon, S., (2011). “Regional climate consequences of large-scale cool roof and photovoltaic array deployment.” *Environmental Research Letter*, 6, 034001.
- Millstein, D.E., and Fischer, M.L., (2014). “Reflective 'cool' roofs under aerosol-burdened skies: radiative benefits across selected Indian cities.” *Environmental Research Letters*, 9, 104014.
- Ming, T., de_Richter, R., Liu, W., Caillol S., (2014). “Fighting global warming by climate engineering: Is the Earth radiation management and the solar radiation management any

- option for fighting climate change?” *Renewable and Sustainable Energy Reviews*, 31, pp. 792-834.
- Mirzaei P.A. and Haghghat, F., (2010). “Approaches to study Urban Heat Island - Abilities and limitations.” *Building and Environmental*, 45, pp. 2192–2201.
- Mlawer, E. J., Taubman, S. J., Brown, P. D., Iacono, M. J., and Clough, S. A., (1997). “Radiative transfer for inhomogeneous atmospheres: RRTM, a validated correlated-k model for the longwave.” *Journal of Geophysical Research*, 102, pp. 16663–16682.
- Monin, A. and Obukhov, A., (1954). “Basic laws of turbulent mixing in the surface layer of the atmosphere.” *Tr. Akad. Nauk SSSR Geophys. Inst.*, 24(151), pp. 163-187.
- Moriyama, M. and Matsumoto, M., (1988). “Control of urban night temperature in semi-tropical regions during summer.” *Energy Buildings*, 11, pp. 213–219.
- Moriyama, M. and Takebayashi, H., (1999). “Making Method of “Klimatope” Map Based on Normalized Vegetation Index and One-Dimensional Heat Budget Model.” *Journal of Wind engineering and industrial aerodynamics*, 81(1-3), pp. 211–220.
- Morris, C. and Simmonds, I., (2000). “Associations between varying magnitudes of the urban heat island and the synoptic climatology in Melbourne, Australia.” *International Journal of Climatology* , 20, pp. 1931–1954.
- Morrison, H., Thompson, G., Tatarskii, V., (2009). “Impact of cloud microphysics on the development of trailing stratiform precipitation in a simulated squall line: Comparison of one- and two-moment schemes.” *Monthly Weather Review*, 137, pp. 991–1007.
- Navigant Consulting, (2009). “Assessment of international urban heat island research; review and critical analysis of international UHI studies.” U.S. Department of Energy, Washington D.C., US.
- NOAA, (2001). “National oceanic and atmospheric administration changes to the NCEP Meso Eta analysis and forecast system: increase in resolution, new cloud microphysics, modified precipitation assimilation, modified 3DVAR analysis.” [online <http://www.emc.ncep.noaa.gov/mmb/mmbpll/eta12tpb/>.].
- Office of Energy Efficiency, (2009). “Residential End-Use Model.” Natural Resources Canada, Ottawa (ON), Canada.
- Office of Energy Efficiency, (2011) “Comprehensive energy use database.” Natural Resources Canada, Ottawa (ON), Canada.

- Ohashi, Y. and Kida, H., (2002). "Local circulations developed in the vicinity of both coastal and inland urban areas: a numerical study with a mesoscale atmospheric model." *Journal of Applied Meteorology*, 41, pp. 30–45.
- Oke, T. R., (1987). "Boundary layer climates." New York: Routledge.
- Oleson, K. W., Bonan, G. B. and Feddema, J., (2010). "Effects of white roofs on urban temperature in a global climate model." *Geophysical Research Letters*, 37 (3), L03701.
- Otte, T. L., Lacser, A., Dupont, S. and Ching, J. K. S., (2004). "Implementation of an urban canopy parameterization in a mesoscale meteorological model." *Journal of Applied Meteorology*, 43, pp. 1648-1665.
- Oyeyinka, O. O. et al., (2011). "Cities and climate change: global report on human settlements." 1st ed. Earthscan, London, UK.
- Pan, H. L., and Wu., W. S., (1995). "Implementing a Mass flux convective parameterization package for the NMC medium range forecast model." NMC office note, 409.40, pp. 20–233.
- Parker, D. E., (2004). "Large-scale warming is not urban." *Nature*, 432, pp. 290.
- Patz, J. A., Campbell-Lendrum, D., Holloway, T. and Foley, J. A., (2005). "Impact of regional climate change on human health." *Nature*, 438, pp. 310-317.
- Peterson, T. C., (2003). "Assessment of urban versus rural in situ surface temperatures in the contiguous united states: no difference found." *Journal of Climate*, 16, pp. 2941–2959.
- Pielke, R. A. S., (2002). "Mesoscale Meteorological Modeling." 2nd ed., Academic Press, San Diego (CA), US.
- Pleim, J.E., Venkatram, A., and Yamartino, R., (1984). "ADOM/TADAP model development program, Vol. 4. the dry deposition module," Ministry of the Environment, Ottawa (ON), Canada.
- Poppe, D., et al., (1996). "Gas-phase reactions in atmospheric chemistry and transport models: A model intercomparison," EUROTRAC Special Publication, International Scientific Secretariat, Garmisch-Partenkirchen.
- Prado, R. T., and Ferreira, F. L. (2005). "Measurement of albedo and analysis of its influence the surface temperature of building roof materials." *Energy and Buildings*, 37(4), pp. 295-300.
- Raby, J., Passner, J., Vaucher, G., and Raby, Y. (2012). "Performance comparison of high resolution weather research and forecasting model output with north american mesoscale

- model initialization grid forecasts.” White Sands Missile Range, NM 88002-5501: Army Research Laboratory.
- Rajeevan, M., Kesarkar, A., Thampi, S. B., Rao, T. N., Radhakrishna, B., and Rajasekhar, M. (2010). “Sensitivity of WRF cloud microphysics to simulations of a severe thunderstorm event over Southeast India.” *Annales Geophysicae*, 28 (2), pp. 603–619.
- Ratti, C., Di Sabatino, S., Britter, R., Brown, M., Caton, F., and Burian, S., (2002). “Analysis of 3-D urban databases with respect to pollution dispersion for a number of European and American cities.” *Water, Air, and Soil Pollution*, 2, pp. 459–469.
- Ratti, C., Di Sabatino, S., Britter, R., (2005). “Urban texture analysis with image processing techniques: winds and dispersion.” *Theoretical and Applied Climatology*, 84, pp. 77-90.
- Rizwan, A. M., Dennis, L. Y.C., Liu, C., (2008). “A review on the generation, determination and mitigation of Urban Heat Island.” *Journal of Environmental Sciences*, 20, pp. 120–128.
- Roos, A., (1997). “Optical characterization of coated glazings at oblique angles of incidence: measurements versus model calculations.” *Journal of Non-Crystalline Solids*, 218, pp. 247–255.
- Rosenfeld, A., Akbari, H., Romm, J. and Pomerantz, M., (1998). “Cool communities: strategies for heat island mitigation and smog reduction.” *Energy and Buildings*, 28, pp. 51-62.
- Rosenfeld, A., Akbari, H., Romm, J. and Pomerantz, M., Taha, H., (1996). “Policies to reduce heat islands: magnitudes of benefits and incentives to achieve them.” LBNL 38679 report, Lawrence Berkeley National Laboratory, Berkeley (CA), US
- Roth, M., Oke, T. and Emery, W., (1989). “Satellite-derived urban heat islands from three coastal cities and the utilization of such data in urban climatology.” *International Journal of Remote Sensing*, 10, pp. 1699-1720.
- Sailor, D.J., and Fan, H., (2002). "Modeling the diurnal variability of effective albedo for cities." *Atmospheric Environment*, 36 (4), pp. 713-725.
- Sailor, D. J., and Lu, L., (2004). “A top–down methodology for developing diurnal and seasonal anthropogenic heating profiles for urban areas.” *Atmospheric Environment*, 38 , pp. 2737–2748.
- Sailor, D.J., (2014). “Risks of summertime extreme thermal conditions in buildings as a result of climate change and exacerbation of urban heat islands.” *Building and Environment*, 78, pp. 81-88.

- Salamanca, F., Krpo, A., Martilli, A. and Clappier, A., (2010a). “A new building energy model coupled with an urban canopy parameterization for urban climate simulations—part I. formulation, verification, and sensitivity analysis of the model.” *Theoretical and Applied Climatology*, 99, p. 331–344.
- Salamanca, F. and Martilli, A., (2010b). A new building energy model coupled with an urban canopy parameterization for urban climate simulations—part I. Validation with one dimension off-line simulations. *Theoretical and Applied Climatology*, 99, p. 345–356.
- Salamanca, F., Martilli, A., Tewari, M., and Chen, F. (2011). “A study of the urban boundary layer using different urban parameterizations and high-resolution urban canopy parameters with WRF.” *Journal of Applied Meteorology and Climatology*, 50, pp. 1107-1128.
- Salamanca, F. et al. (2012a). “Top-of-atmosphere radiative cooling with white roofs: experimental verification and model-based evaluation.” *Environmental Research Letters*, 7, 044007.
- Salamanca, F., and Martilli, A., (2012b). “A numerical study of the urban heat island over Madrid during the DESIREX (2008) Campaign with WRF and an evaluation of simple mitigation strategies.” *International Journal of Climatology*, 32(15), pp. 2372–2386.
- Santamouris, M., (2013). “Using cool pavements as a mitigation strategy to fight urban heat island—A review of the actual developments.” *Renewable and Sustainable Energy Reviews*, 26, pp. 224–240.
- Salamanca, F., Georgescu, M., Mahalov, A., Moustou, M., and Wang, M., (2014). “Anthropogenic heating of the urban environment due to air conditioning.” *Journal of Geophysical Research: Atmospheres*, 119 (10), pp. 5949–5965.
- Sarrat, C., Lemonsu, A., Masson, V. and Guedalia, D., (2006). “Impact of Urban Heat Island on Regional Atmospheric Pollution.” *Atmospheric Environment*, 40, pp. 1743–1758.
- Sasamori, T., (1968). “Radiative cooling calculation for application to general circulation experiments.” *Journal of Applied Meteorology*, 7, pp. 721–729.
- Seinfeld, J.H., (1989). “Urban air pollution: state of the science.” *Science*, 243 (4892), pp. 745-752.
- Seinfeld, J. H., and Pandis, S. N., (2006). “Atmospheric chemistry and physics.” John Wiley & Sons.

- Schayes, G. and Grossi, P., (1997). "Sensitivity analysis on boundary layer height on idealized cities (model study)." *The Determination of the Mixing Height – Current Progress and Problems*, EURASAP Workshop, 1-3 October 1997, Riso National Laboratory, Roskilde, Denmark.
- Schell, B., Ackermann, I. J., Hass, H., Binkowski, F. S., and Ebel, A., (2001), "Modeling the formation of secondary organic aerosol within a comprehensive air quality model system." *Journal of Geophysical Research: Atmospheres*, 106(D22), pp. 28275–28293.
- Scherba, A., Sailor, D.J., Rosenstiel, T.N., and Wamser, C.C., (2011). "Modeling impacts of roof reflectivity, integrated photovoltaic panels and green roof systems on sensible heat flux into the urban environment." *Building and Environment*, 46, pp. 2542-2551.
- Siegel, R. and Howell, J. R., (2001) "Thermal radiation heat transfer," 4th ed., Taylor and Francis-Hemisphere, Washington D.C., US.
- Skamarock W. C., et al., (2008). "A description of the advanced research WRF Version 3" National Center for Atmospheric Research, Boulder (CO), USA.
- Slinn, S.A. and Slinn, W.G.N., (1980). "Prediction for particle deposition on natural waters." *Atmospheric Environment*, 14, pp. 1013-1016.
- Stathopoulou, E., Mihalakakou, G., Santamouris, M., and Bagiorgas, H. S. (2008). "On the impact of temperature on tropospheric ozone concentration levels in urban environments." *Journal of Earth System Sciences*, 117(3), pp. 227–236.
- Statistics Canada, (2007) "2006 Census of Population." Ottawa (ON), Canada.
- Steyn, D.G., (1980). "The calculation of view factors from fisheye-lens photographs, *Atmosphere-Ocean*," 18 (3), pp. 254-258.
- Stewart, I.D., (2011). "A systematic review and scientific critique of methodology in modern heat island literature," *International Journal of Climatology*, 31, pp. 200-217.
- Stockwell, W. R., Middleton, P., Chang, J. S., and Tang, X., (1990), "The second generation regional acid deposition model chemical mechanism for regional air quality modeling." *Journal Geophysical Research*, 95, pp. 16343-16367
- Sturm, M., Holmgren, J., Konig, M., and Morris, K., (1997). "The thermal conductivity of seasonal snow". *Glaciology*, 43, (143), pp. 26-41.

- Synnefa, A., Santamouris, M., and Apostolakis, K. (2007). "On the development, optical properties and thermal performance of cool colored coatings for the urban environment. *Solar Energy*." 81(4), pp. 488-497.
- Szegedi, S. and Kircsi, A., (2003). "Effects of the synoptic conditions on the development of the urban heat island in Debrecen, Hungary." *Acta Climatologica et Chorologica*, 36-37, pp. 111-120.
- Taha, H., Akbari, H., Rosenfeld, A. and Huang, J., (1988). "Residential cooling loads and the urban heat island the effects of albedo." *Building and Environment*, 23(4), pp. 271-283.
- Taha, H., (1997a). "Urban climates and heat islands: albedo, evapotranspiration, and anthropogenic heat." *Energy and Buildings*, 25, pp. 99-103.
- Taha, H., Douglas, S. and Haney, J., (1997b). "Mesoscale meteorological and air quality impacts of increased urban albedo and vegetation." *Energy and Buildings*, 25, pp. 169-177.
- Taha, H., Chang, S. and Akbari, H., (2000). "meteorological and air quality impacts of heat island mitigation measures in three U.S. cities," LBNL, Berkeley (CA) USA.
- Taha, H., (2005). "Urban surface modification as a potential ozone air-quality improvement strategy in California – Phase one: initial mesoscale modeling," Altostratus Inc. for the California Energy Commission, PIER Energy-Related Environmental Research, CEC-500-2005-128, Martinez (CA), US.
- Taha, H., (2008a). "Urban surface modification as a potential ozone air-quality improvement strategy in California: A mesoscale modeling study." *Boundary Layer Meteorology*, 127, p. 219–239.
- Taha, H., (2008b). "Episodic performance and sensitivity of the urbanized mm5 (umm5) to perturbations in surface properties in Houston Texas." *Boundary Layer Meteorology*, 127, pp. 193-218.
- Taha, H., (2008c). "Meso-urban meteorological and photochemical modeling of heat island mitigation." *Atmospheric Environment*, 42, pp. 8795–8809.
- Taha, H., (2009a). "Mesoscale and meso-urban meteorological and photochemical modeling of heat island mitigation in California: results and regulatory aspects." Conference on Countermeasures to UHI, Berkeley (CA) USA,
- Taha, H., (2009b). "Urban surface modification as a potential ozone air-quality improvement strategy in California - Phase two: fine-resolution meteorological and photochemical

- modeling of urban heat islands.” Altostratus Inc. for the California Energy Commission, PIER, Martinez (CA), US.
- Takebayashi, H. and Moriyama, M., (2007). “Surface heat budget on green roof and high reflection roof for mitigation of urban heat island.” *Building and Environment*, 42, pp. 2971–2979.
- Takebayashi, H. and Moriyama, M., (2012). “Relationships between the properties of an urban street canopy and its radiant environment: introduction of appropriate urban heat island mitigation technologies.” *Solar Energy*, 86, pp. 2255–2262.
- Tao, W., Simpson, J., and McCumber, M., (1989). “An ice–water saturation adjustment.” *Monthly Weather Review*, 117, pp. 231–235.
- Tartaglione, N., Mariani, S., Accadia, C., Speranza, A., and Casaiol, M., (2005). “Comparison of rain gauge observations with modeled precipitation over Cyprus using Contiguous Rain Area analysis.” *Atmos. Chem. Phys.*, 5, pp. 2147–2154.
- Tessum, C. W., Hill, J. D., and Marshall, J. D., (2014). “Twelve-month, 12 km resolution North American WRF-Chem v3.4 air quality simulation: performance evaluation.” *Geoscientific Model Development Discussion*, 7, pp. 8433–8476.
- Tewari, M., Chen, F., Wang, W., Dudhia, J., LeMone, M. A., Mitchell, K., Ek, M., Gayno, G., Wegiel, J., and Cuenca, R. H., (2004) “Implementation and verification of the unified NOAA land surface model in the WRF model.” 20th conference on weather analysis and forecasting/16th conference on numerical weather prediction, pp. 11–15.
- Thompson, G., Field, P. R., Rasmussen, R. M., Hall, W. D., (2008). “Explicit forecasts of winter precipitation using an improved bulk microphysics scheme. Part II: implementation of a new snow parameterization.” *Monthly Weather Review*, 136, pp. 5095–5115.
- Tiedtke, M., (1989). “A comprehensive mass flux scheme for cumulus parameterization in large–scale models.” *Monthly Weather Review*, 117, pp. 1779–1800.
- Touchaei, A.G., Matthews, D., Bahri, M., and Hosseini, M. M., (2013). “Can urban ozone generation be modeled correctly based on major gaseous atmospheric reactions?” 15th Conference on Atmospheric Chemistry, AMS 93rd Annual Meeting, January, Austin (TX), US

- Unger, J., (2009). "Connection between urban heat island and sky view factor approximated by a software tool on a 3D urban database," *International Journal of Environment and Pollution*, 36, pp. 59-80
- United Nations, (2014). "World urbanization prospects." New York (NY), USA.
- Unwin, D. J., (1980). "The synoptic climatology of Birmingham's urban heat island, 1965–74." *Weather*, 35(2), p. 43–50.
- U.S. Census Bureau, Geography Division, (2011). "Geographic Terms and Concepts - Urban and Rural." [Online: http://www.census.gov/geo/www/2010census/gtc/gtc_urbanrural.html].
- Valler, J. D. A., (2012). "The physics and chemistry of ozone." (Feather River Air Quality Management District) [Online: <http://www.fraqmd.org/OzoneChemistry.htm>].
- Walcek, C. J., and Yuan, H. H. (1994). "Calculated influence of temperature-related factors on ozone formation in the lower troposphere." *Journal of Applied Meteorology*, 34, pp. 1056-1069.
- Whitby, E. R., McMurry, P. H., Shankar, U., and Binkowski, F. S., (1991). "Modal aerosol dynamics modeling." Rep. 600/3-91/020, Atmos. Res. and Exposure Assess. Lab., U.S. Environ. Prot. Agency, Research Triangle Park, (NC), US.
- WHO, (2002). "The world health report." The World Health Organization, Geneva, Switzerland.
- Wilcox, S., and Marion, W., (2008). "Users manual for TMY3 data sets." Technical Report NREL/TP-581-43156, National Renewable Energy Laboratory, Golden (CO), US.
- Wild, O., Zhu, X., Prather, M.J., (2000). "Fast-J: accurate simulation of in- and below-cloud photolysis in tropospheric chemical models." *Journal of Atmospheric Chemistry*, 37 (3), pp 245-282.
- Willmott, C. J., and Matsuura, K. (2005). "Advantages of the mean absolute error (MAE) over the root mean square error (RMSE) in assessing average model performance." *Climate Research*, 30, pp.79–82.
- WMO (2008). "Guide to meteorological instruments and methods of observation, Part II – Observing Systems, Chapter 11." WMO-No.8, 7th Edition, World Meteorological Organization, Geneva, Switzerland.
- Wong, E., (2008). "Reducing Urban Heat Islands: Compendium of Strategies." [Online: <http://www.epa.gov/hiri/resources/pdf/BasicsCompendium.pdf>].
- WRF-CHEM Emission Guide, (2014). "WRF-Chem Version 3.6 User's Guide."

- WRF-CHEM User's Guide, (2014). "WRF-Chem Emissions Guide."
- Wu, S., Mickley, L. J., Jacob, D. J., Logan, J. A., Yantosca, R. M., and Rind, D. (2007). "Why are there large differences between models in global budgets of tropospheric ozone?" *Journal of Geophysical Research*, 112 (D5), D05302.
- Wyngaard, J. C., (2004). "Toward numerical modeling in the 'Terra Incognita'." *Journal of the Atmospheric Sciences*, 61, pp. 1816-1826.
- Xie, B., Fung, J. C. H., Chan, A., and Lau, A., (2012). "Evaluation of nonlocal and local planetary boundary layer schemes in the WRF model." *Journal of Geophysical Research*, 117, D12103.
- Xue, M. (2000). "High-order monotonic numerical diffusion and smoothing." *Monthly Weather Review*, 128, pp. 2853-2864.
- Yu, S. et al. (2012). "Comparative evaluation of the impact of WRF/NMM and WRF/ARW meteorology on CMAQ simulations for PM_{2.5} and its related precursors during the 2006 TexAQS/GoMACCS study." *Atmospheric Chemistry and Physics* 12, pp. 4091–4106.
- Zmeureanu, R., (1995). "Analysis of energy performance of a sample of 115 homes in Montreal Buildings." Department of Energy (DOE); Oak Ridge National Laboratory (ORNL); American Society of Heating, Refrigerating and Air Conditioning Engineers (ASHRAE); Building Environment and Thermal Envelope Council (BETEC), pp. 421-424, Clearwater Beach (FL), U.S.
- Zeldin, M., and Meisel, W., (1978). "Use of meteorological data in air quality trend analysis." Environmental Protection Agency. Triangle Park (NC), US.
- Zhang, G. J., and McFarlane, N. A., (1995). "Sensitivity of climate simulations to the parameterization of cumulus convection in the Canadian Climate Centre General Circulation Model." *Atmosphere– Ocean*, 33, pp. 407–446.
- Zhang, Y., Dulière, V., Mote, P. W., and Salathé, E. P. (2009). "Evaluation of WRF and HadRM mesoscale climate simulations over the U.S. Pacific Northwest." *Journal of Climate*, 22, pp. 5511–5526.
- Zhang, C., Wang, Y., and Hamilton, K., (2011). "Improved representation of boundary layer clouds over the southeast pacific in ARW–WRF using a modified Tiedtke cumulus parameterization scheme." *Monthly Weather Review*, 139, pp. 3489–3513.

- Zhang, J., and Gong, W. (2013). "Sensitivity of simulated cloud properties to meteorological model configurations." 12th Annual CMAS Conference, (October 28-30). Chapel Hill (NC), US.
- Zhao, Q., Black, T. L., and Baldwin, M. E., (1997a). "Implementation of the cloud prediction scheme in the Eta model at NCEP." *Weather Forecasting*, 12, pp. 697-712.
- Zhao, Q., and Carr, F. H., (1997b). "A prognostic cloud scheme for operational NWP models." *Monthly Weather Review*, 125, pp. 1931-1953.

Appendix A: Description of WRF solver and physical models

A.1. Governing equations

Like all other physical problems, formulation of climate is based on conservation laws (mass, momentum, energy).

- Conservation of mass (air)

$$\frac{\partial \rho}{\partial t} + \nabla \cdot \rho \vec{V} = 0 \quad (\text{A-1})$$

- Conservation of mass (water)

$$\frac{\partial q_m}{\partial t} + \vec{V} \cdot \nabla q_m = S_{q_m} \quad (m = 1, 2, 3) \quad (\text{A-2})$$

- Conservation of mass (other gaseous and aerosol contaminant)

$$\frac{\partial \chi_m}{\partial t} + \vec{V} \cdot \nabla \chi_m = S_{\chi_m} \quad (m = 1, 2, \dots, M) \quad (\text{A-3})$$

- Conservation of momentum

$$\frac{D\vec{V}}{Dt} = \frac{\partial \vec{V}}{\partial t} + \vec{V} \cdot (\nabla \vec{V}) = -\frac{1}{\rho} \nabla p - g\vec{k} - 2\vec{\Omega}_e \times \vec{V} \quad (\text{A-4})$$

- Conservation of energy

$$\frac{D\theta}{Dt} = \frac{\partial \theta}{\partial t} + \vec{V} \cdot \nabla \theta = S_\theta \quad (\text{A-5})$$

The right hand side of the equations represents the source and sink of independent variables. Different physical processes and interactions within the grids should be parameterized. The parameterizations describe the averaged sub-grid fluxes as well as source and sink terms.

These equations are in Cartesian coordinate system but they have to be converted to a desired coordinate system. Terrain following vertical coordinate system is an appropriate choice for mesoscale models because the main goal is to find the variation of different parameters (e.g.

temperature, wind velocity, etc.) near the ground. Vertical variation of sigma coordinate is defined as Eq. (3-6).

$$\sigma = \frac{p_h - p_{ht}}{p_{hs} - p_{ht}} \quad (\text{A-6})$$

A.2. Input data

Ungrib, Geogrid, and Metgrid are three main components of WRF Preprocessing System (WPS) to define the simulation domain, degrib weather data, and interpolate terrestrial and weather data to the simulation domain, respectively. Geogrid defines both parent and nesting simulation domains and interpolates the Land Use Land Cover (LULC) data for them. Interpolation of data depends on different map projections (polar stereographic, Lambert-Conformal, Mercator, and latitude-longitude) implemented in WPS.

Basically, input data contains information related to land characteristics (e.g. land use, vegetation, surface roughness, terrain, albedo, etc.) and weather data (temperature, relative humidity, wind velocity, etc.) in GRIB 1/2 format. Two land datasets are provided as a part of software; USGS24 and MODIS. Weather data should be imported from external sources. GRIB is a meteorological format of weather data which is the output of data assimilating models in a specific domain. Data assimilating models use observed data from different sources (e.g. satellites, ships, buoys, etc.) and interpolate them to the entire domain. There are many different types of data available that can be used as the input of WPS. However, my case studies are in North America so I will use North American Regional Reanalysis dataset (NARR) based on a study by Mesinger et al. (2006).

A.3. Solver

This is the key component of the software in modeling system that contains several initializations and composed of numerical integration program. It uses the fully compressible non-hydrostatic equations and Arakawa C-grid staggering with Runge-Kutta 2nd and 3rd order time integration options (Figure A-1 illustrates the flowchart of information transfer in WRF).

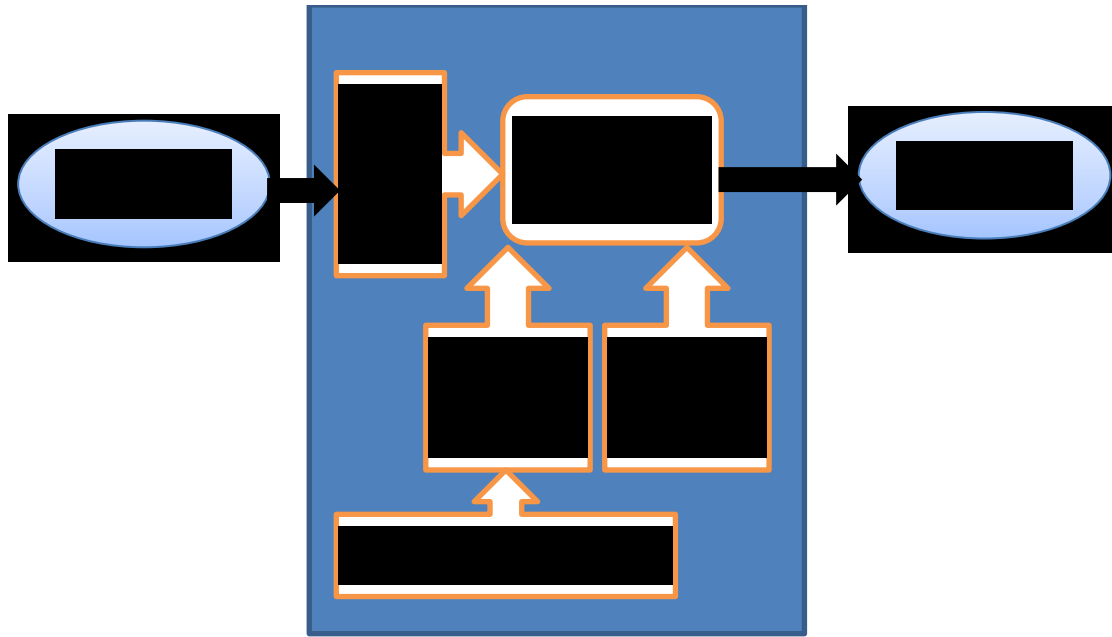


Figure A-1. Information transfer flowchart of WRF model

The ARW solver is utilized by time-split integration scheme for time discretization (Klemp, et al., 2007; Skamarock et al., 2008). There are low and high frequency modes with low and high energy, respectively, and they are treated separately to maintain the stability. For low or small frequency waves, the Runge-Kutta (RK3) time integration scheme is used. High frequency or acoustic waves and gravity waves that propagate horizontally are integrated by using predictor-corrector time integration scheme. Vertically propagating acoustic waves and buoyancy oscillations are discretized by implicit time integration scheme. The ARW solver uses the Arakawa C grid staggering method and velocities are staggered half a grid distance from mass points where all other properties are defined.

Turbulent model of meteorological models, in general, is Kinetic Turbulent Energy (TKE) sub-grid scale model using K-theory (Pielke, 2002) and the ARW solver follows the same approach (ARW user guide, 2012). Different kind of filters are applied to formulate the horizontal and vertical diffusion for numerical reasons or because the turbulent variables could not be resolved in sub-grid (studying this filters are out of the scope of this section for further detail refer to ARW solver description; Skamarock et al., 2008). Eddy viscosities change by time and space and affect the shear stress in right hand side (RHS) of the momentum equation.

A.3.1. Initial and boundary conditions

WRF supports different models but my interest is in real cases and, as described before, IC and BCs for this case is provided by WPS. Output of WPS contains 3D field of temperature, velocity components, and relative humidity, in addition to, 2D time-dependent fields surface pressure and sea-level pressure, layers of soil temperature and moisture, snow depth, skin temperature, sea surface temperature, and a sea ice flag. Terrestrial static fields (e.g. albedo, terrain elevation, Coriolis parameters, vegetation, LULC, etc.) are also included in the output. Real program interpolates these data in the full domain for ARW solver.

A.3.2. Nesting

One of the main capabilities of the ARW solver is nesting which can give a higher resolution results for part of the parent domain. Nesting is either one-way or two-way, in the former, only the coarse grid information transfers to the fine grid as its IC and BC and, in the latter, results of the integration in fine grid update coarse domain variables as well.

A.4. Parameterizations

A.4.1. Microphysics

A.4.1.1. Lin scheme

This model improved the previous models (applicable for tropical climate) by adding the effect of snow and its related processes. Number of precipitation particles is considered as exponential function of size distribution. Terminal velocity is a function of particles' diameter and density. Conservation equation for the mass of water is applied to the combination of cloud ice, cloud water, and water vapor. Conservation of mass is also applied to snow, rain, and hail mixing ratios. Snow production occurs in two regimes: (1) below 0 °C, and (2) more than 0 °C. Parameterization of microphysics models predicts source and sink terms of snow (ice crystal aggregation, accretion, sublimation, and melting), hail (snow crystal aggregation, accretion, raindrop freezing, sublimation, and melting), and rain (auto-conversion, accretion, freezing and melting, and evaporation) in the mass conservation equations. The parameterizations are based Lin et al. (1983). Ice and snow aggregation is expressed as a function of their mixing ratios and temperature. The collision-coalescence process is separately characterized for ice and snow. Accretion takes place during precipitation between hail, snow, and rain and it can be parameterized as a function of mixing ratio of hydrometeors, temperature, and density.

Deposition of snow and hail mainly depend on the super-saturation with respect to ice and snow, respectively. Melting and evaporation are complicated processes in producing and decomposing rain where conduction and convection heat transfer should be considered. Transformation of cloud ice and cloud water to snow (i.e. Bergeron process) is estimated by deposition and riming of ice crystals. Raindrop freezing makes snowflakes in low temperatures (0 to -40 °C); this process is a function of mass, temperature, and mixing ratio of raindrops. Conversion of cloud drops into raindrops by collisions is determined by the mixing ratio of cloud water, concentration of cloud drops, and density. To obtain the velocity field, conservation equation of momentum was established and combined with conservation of mass to construct the vorticity equation. Snow, hail, and rain effects are added to the energy conservation equation. Lin scheme is tested for different cases by Lin et al. (1983). Experiments proved the higher efficiency of the model compared with previous models that do not consider the effect of snow.

This model is improved for fine resolutions and implemented in WRF by Chen et al. (2002). They used the microphysics models with an advanced cumulus model that considers non-hydrostatic pressure to increase the accuracy of predictions. Results are not validated with observational data but the results were claimed to be acceptable.

A.4.1.2. SBU-YLin scheme

Lin et al. (2011) proposed a new model with more accurate prediction of riming intensity of ice and snow. They reduced the number of variables and conversion processes compare with Lin et al. (1983) to get a more computationally efficient parameterization. The model considered the effect of riming intensity and temperature on mass, terminal velocity, and precipitating ice instead of considering constant empirical values in calculations. The new model was implemented in WRF to simulate two events and results were compared with observational data. Results showed the ability of the model in prediction of surface precipitation comparable to more sophisticated models.

A.4.1.3. Eta scheme

Eta model (NOAA, 2001) is a parameterization of microphysics processes that improves previous model of NCEP (Zhao et al., 1997a; 1997b). The model considers six species of water (water vapor, cloud ice or cloud water, ice, snow, graupel, and sleet). Different forms of ice exist depending on the super-cooled rain freezing process or cloud water riming physics. Moreover,

the model can consider mixed phase of rain and snow for temperature of more than $-10\text{ }^{\circ}\text{C}$. Temperature range specifies the presence of cloud water ($> 0\text{ }^{\circ}\text{C}$), cloud ice ($< -15\text{ }^{\circ}\text{C}$), or the chance for either of them. Condensation algorithm is designed for high resolution grid-size to efficiently adjust temperature, moisture, and cloud condensate fields. Melting and freezing processes are the same as Lin scheme. Additionally, it considers the effect of melting (freezing) on rain (ice) generation and increasing (decreasing) relative humidity. Latent heat capacity of rain and ice in freezing and melting processes considerably affects the temperature. Smaller errors generated from the simulation for predicting the surface precipitation of an episodic event using the new parameterization compared to observational data.

A.4.1.4. WRF Single-Moment 6-class (WSM6) scheme

WRF Single-Moment 6-class (WSM6) scheme (Hong and Lim, 2006) is the improved version of previous parameterizations proposed by Hong et al. (2004). For processes related to graupel, approach of the Lin scheme was implemented in WRF and it increased the accuracy of results for 3D real case simulation of a heavy rainfall over Korea using high resolution grid spacing. For coarse grids, effect of increasing the number of variables was negligible. In the basic model, Lin scheme was improved by parameterization of cloud ice sedimentation. Many modifications were performed to have a realistic model: 1) more accurate dependence of snow to temperature, 2) advanced model for calculating ice nuclei number concentration, and 3) new algorithm for auto-conversion of cloud water to rain. For a heavy rainfall experiment, results of this model were a better representative of cloud ice in the domain of simulation.

A.4.1.5. WRF Double-Moment 6-class (WDM6) scheme

WDM6 (Lim and Hong, 2010) is the double-moment version of WSM6 (Hong and Lim, 2006). In the double-moment scheme both mixing ratio and number concentration are considered as independent variables. This model can calculate the number concentration of cloud, rain, and cloud condensation nuclei. Numbers of cloud and rain drops are an exponential function of their size; the interception is a function of mixing ratio and temperature. This assumption significantly changes the number of small size raindrops.

A.4.1.6. Thompson Scheme

Thompson Scheme predicts the mixing ratios of five hydrometeors (cloud water, rain, cloud ice, snow, and graupel) and the number concentration of cloud ice (Thompson et al., 2008).they

proposed a new snow parameterization based on a generalized gamma distribution shape for each hydrometeor species (use the reference to find the constants for gamma distribution). The model was more accurate in saturation adjustment, vapor deposition, sublimation, and evaporation. It also added more flexibility to improve variable gamma distribution shape parameter for cloud water droplets based on observations. In addition, a lookup table for freezing of water drops and for transferring cloud ice into the snow category can be modified for calibration.

A.4.1.7. Morrison Scheme

Morrison double-moment scheme (Morrison 2009) considers five species (cloud droplets, cloud ice, snow, rain, and graupel). The velocity components and the perturbation of potential temperature, geopotential, and surface pressure of dry air, along with water vapor mixing ratio, and the different cloud microphysics variables are used in a set of prognostic equations to predict the mixing ratio. The number concentrations are calculated from the specified size distribution and the predicted mixing ratio. Comparison of the model showed that the rain evaporation process was the modified key factor.

A.4.1.8. National Severe Storms Laboratory (NSSL) Scheme

The NSSL Scheme has the capability of considering lightning in microphysical models (Mansell et al., 2010) to understand the charging processes of hydrometeors and evolution of storms. Two independent moments, mass mixing ratio and number concentration, of cloud droplets, rain, ice crystals, snow, and graupel is predicted well by the model. The results of simulated electrification and lightning for a small continental storm were consistent with observations.

A.4.1.9. Goddard Scheme

Tao et al. (1989) proposed a saturation adjustment scheme as a function of liquid water and ice saturation values to calculate the amount of condensation and deposition of cloud water and cloud ice. The scheme is a single-moment microphysical model that can predict the mixing ratio of different hydrometeors. The adjustment is added to Lin Scheme.

A.4.1.10. Milbrandt-Yau Scheme

Milbrandt-Yau Scheme like other double-moment schemes (e.g. Thomson Scheme) uses gamma size distribution of the form $N_{(D)} = N_0 D^\alpha e^{-\gamma D}$ (Milbrandt and Yau, 2005a; 2005b). However,

they added the radar reflectivity as the third moment to the equations to predict the shape parameter (α) in prognostic equations.

A.4.2. Cumulus

A.4.2.1. Simplified Arakawa-Schubert Scheme

In this model a simple set of equations considered the mass and energy balance in clouds (Pan and Wu., 1995). High energy parcels are assumed to move upward to reach a level of free convection. The percentage of the parcels at a point below the cloud is specified to determine the entrainment rate and it was assumed that the parcel will lose the energy in the cloud. In this model surface rainfall is also parameterized in the moisture balance equation.

A.4.2.2. Betts-Miller-Janjic Scheme

Janjic (1994) modified the earlier version of a cumulus parameterization by adding convective mixing to the thermodynamically driven process and keeping the total enthalpy unchanged in the deep convection profile. Additionally, for shallow clouds, which are identified by a jump in relative humidity, a positive change in entropy change is conditionally added to the equations. To predict the shallow clouds, the humidity profile plays an important role and it was modified to consider the effect of atmospheric stability on the temperature profile. The comparison of the model showed a good estimation of cloud convection.

A.4.2.3. Grell 3D Scheme

This model divides parameterizations into dynamic control and feedback (Grell, 1993; Grell and Devenyi, 2002). The dynamic control governs the effect of convection by the environment and the feedback parameterization determines the adjustment of the environment by the convection. Grell 3D Scheme accounts for both entrainment rate and detrainment rate in the steady state plume equation. The model uses the updraft and downdraft mass flux to calculate normalized mass flux, normalized condensation and evaporation profiles, moist static energy, and liquid water content. Data assimilation technique was used to find the feedback of cloud ensemble to the larger scale model.

A.4.2.4. Grell-Freitas Scheme

The main importance of Grell-Freitas Scheme is to predict the cloud convection in high-resolution grid size simulations (Grell and Freitas, 2014). The model limited the number of ensembles in Grell 3D scheme to optimize the calculation time in numerical weather prediction

simulations. Although some simplifications are applied to effectively parameterize the cloud convection, some complication of aerosols, tracer transport, and wet scavenging is considered.

A.4.2.5. Kain-Fritsch Scheme

Kain-Fritsch Scheme is a newer version based on the Lagrangian approach mass flux parameterization uses the vertical momentum conservation equation to capture instabilities (Kain, 2004). The model calculates the decay of the convective available potential energy of cloud convection and the outputs are temperature, water vapor mixing ratio, and cloud water mixing ratio tendencies. The model also estimates the surface rainfall. The newer version that has been used in this study considers the momentum entrainment rate, variable cloud radius, shallow convection, and variable minimum cloud depth threshold for updraft convection as well as downdraft convection of clouds.

A.4.2.6. New Simplified Arakawa-Schubert Scheme

Han and Pan (2011) developed the New Simplified Arakawa-Schubert scheme using turbulent diffusion-based approach and considering the convection-induced pressure gradient forcing in momentum equation. A finite entrainment and detrainment rates for heat, moisture, and momentum was specified. To avoid excessive grid-scale precipitation by depleting more instability in deep convection, cumulus convection was modified to be stronger and deeper. A larger mass flux from and to cloud base and higher cloud tops suppressed heavy grid-scale rainfalls. In shallow convection, the heating or cooling behavior in lower-atmospheric layers above the PBL is improved by employing a parabolic eddy diffusivity profile with a maximum value for vertical mixing of the heat and moisture.

A.4.2.7. Tiedtke Scheme

Tiedtke (1989) proposed a mass flux based model that considers the eddy transport of energy in prognostic equations. In addition to updraft and downdraft of clouds, a penetrative convection closure was parameterized for deep convection. Shallow convection is governed by the same turbulent moisture flux as of penetrative convection for near surface layers (surface evaporation is dominant). Midlevel convection related to the mesoscale circulation and instability above PBL is determined when large-scale ascent of the humid air (relative humidity of about 90%) to an unstable layer.

A.4.2.8. Zhang-McFarlane Scheme

This model modified the cumulus parameterization in the Canadian Climate Center General Circulation Model by considering the exchange of unstable air exchange with adjacent layers (Zhang and McFarlane, 1995). The formulation is based on the mass flux of hydrometeors along with their energy conservation.

A.4.3. Planetary boundary layer (PBL)

A.4.3.1. Mellor-Yamada-Janjic (MYJ)

Janjic (1994) considers the viscous sublayer (vertical transport is determined by molecular diffusivity) above water bodies and a turbulent layer above the water sublayer and lands (level 2). In addition, the model calculates TKE above turbulent layer (level 2.5) to reduce the spin up time for the model. The level 2.5 closure scheme has been modified by adding an upper limit to the length scale and TKE as a function of buoyancy and shear stress of the flow (Janjic, 2002).

MYJ is less biased amongst different available PBL options in WRF compared to the satellite images of surface temperature (Li and Bou-Zeid, 2014b). MYJ is also has the minimum bias for different urban categories (about 0°C for industrial category and high-density residential category and about 1°C for low-density residential category). Thermal roughness length affect the surface temperature during the day, and the surface temperature during the night is strongly related to the choice of PBL. Urban vegetation (i.e. pervious surfaces) is not considered in UCMs of WRF, which poses a large bias in calculated surface and air temperatures.

A.4.3.2. Bougeault- Lacarrere (BouLac)

This model calculated the TKE in a prognostic equation as a function of vertical molecular dissipation, mass flux, horizontal velocity, and heat (Bougeault and Lacarrere, 1989).

$$\frac{\partial e}{\partial t} = -\frac{1}{\rho} \frac{\partial}{\partial z} \rho \overline{w'e'} - \overline{w'u'} \frac{\partial u}{\partial z} - \overline{w'v'} \frac{\partial v}{\partial z} + \frac{g}{\theta} \overline{w'\theta'} - \varepsilon \quad (\text{A-7})$$

Vertical velocity fluctuation is w' , air density is ρ , horizontal velocities are u and v , $\frac{g}{\theta}$ is the buoyancy coefficient, θ' is the fluctuation of the potential temperature and ε is the molecular dissipation. More detailed description of BouLac Scheme is presented in Multi-layer Urban Canopy Model (Section 3.2.3).

A.4.4. Land-Surface

Surface temperature in WRF is calculated from prognostic energy balance equation on the surface. Net radiation on the surface is the summation of sensible heat flux, latent heat flux, and ground heat flux, eq. 3-8.

$$Rad = HFX + LH + GFX \quad (A-8)$$

where

$$HFX = \rho c_p C_h U (\theta_s - \theta_a) \quad (A-9)$$

$$C_h \text{ or } St = \frac{Nu}{Re \cdot Pr} \quad (A-10)$$

$$Pr = \frac{\vartheta}{\alpha} \left(\vartheta = \frac{\mu}{\rho} \text{ and } \alpha = \frac{k_{cond}}{\rho c_p} \right) \quad (A-11)$$

$$Re = \frac{Ul}{\vartheta} \quad (A-12)$$

$$Nu = \frac{hl}{k_{cond}} \quad (A-13)$$

$$LH = C_l U (q_s - q_a) \quad (A-14)$$

C_l is the Dalton number or moisture flux exchange coefficient.

In WRF 2-m air temperature is calculated through the following diagnostic equation:

$$T_{2m} = T_s - \frac{HFX}{\rho C_{h2} U_{2m}} \quad (A-15)$$

$$C_{h2} = C_h |_{z=2m} \quad (A-16)$$

$$C_h = \frac{k^2}{\left[\ln \left(\frac{z}{z_0} \right) - \psi_m \left(\frac{z}{L} \right) \right] \left[\ln \left(\frac{z}{z_{0T}} \right) - \psi_h \left(\frac{z}{L} \right) \right]} \quad (A-17)$$

$k = 0.4$ is von Karman constant. z_0 is the momentum roughness length (m); z_{0T} is the thermal roughness length (m); and L is the Monin-Obukhov length scale (m) [the length scale is calculated from eq. 3-18 and it is typically given from empirical data for different types of land

categories]. Ψ_m and Ψ_h are the stability correction functions for momentum and heat, respectively.

$$L = - \frac{u_*^3}{k \frac{g}{\theta_0} \frac{Q}{\rho c_p}} \quad (\text{A-18})$$

where

$$Q = \rho c_p \overline{w'\theta'} \quad (\text{A-19})$$

The stability correction functions for momentum and heat are calculated from eqs. 3-20 and 3-21.

$$\Psi_m = \int_0^{\frac{z}{L}} \frac{1 - \phi_M}{\frac{z}{L}} d\left(\frac{z}{L}\right) \quad (\text{A-20})$$

$$\Psi_h = \int_0^{\frac{z}{L}} \frac{1 - \phi_H}{\frac{z}{L}} d\left(\frac{z}{L}\right) \quad (\text{A-21})$$

$$\phi_M = \frac{kz}{u_*} \frac{\partial V}{\partial z} \quad (\text{A-22})$$

$$\phi_H = \frac{\beta kz}{\theta_*} \frac{\partial \theta}{\partial z} \quad (\text{A-23})$$

Stability correction functions are estimated with the logarithmic change in speed and temperature, eqs. 3-24 and 3-25.

$$V_{(z)} = \frac{u_*}{k} \left[\ln\left(\frac{z}{z_0}\right) - \Psi_m\left(\frac{z}{L}\right) \right] \quad (\text{A-24})$$

$$\theta_{(z)} = \theta_{(z_0)} + \frac{\theta_*}{\beta k} \left[\ln\left(\frac{z}{z_0}\right) - \Psi_h\left(\frac{z}{L}\right) \right] \quad (\text{A-25})$$

As it has been shown, so far and in eqs. 3-26 to 3-28, the vertical flux of momentum is analogous to the vertical flux of energy. Therefore, only the detailed formulation of momentum has been presented.

$$\overline{w'u'} = -K_m \frac{\partial u}{\partial z} = -u_*^2 \cos \mu \quad (\text{A-26})$$

$$\overline{w'v'} = -K_m \frac{\partial v}{\partial z} = -u_*^2 \sin \mu \quad (\text{A-27})$$

$$\overline{w'\theta'} = -K_h \frac{\partial \theta}{\partial z} \quad (\text{A-28})$$

Vertical flux of momentum and heat in the model is a simple representation of K-theory (eqs. 3-29 to 3-31).

$$\mu = \arctan(v/u) \quad (\text{A-29})$$

$$u_* = \sqrt{\tau/\rho} \quad (\text{A-30})$$

$$K_m = kLu_* \quad (\text{A-31})$$

Richardson is an important measure of the atmospheric stability as represented by eq. A-32.

$$Ri = \frac{g}{\theta_0} \frac{\frac{\partial \theta}{\partial z}}{\left(\frac{\partial u}{\partial z} + \frac{\partial v}{\partial z}\right)} \quad (\text{A-32})$$

A.5. Physics interactions

All mentioned models are interacting with each other and using state variables from the governing equations. As a result, they have to use their inputs/outputs to update results in each time step. Table 3-1 shows the physical models interaction of the ARW solver in WRF.

Table A-1. Physical models interaction with the ARW solver, i indicates the input to the model and o represents the output of the model (Skamarock et al., 2008)

		Microphysics	Cumulus	Surface	PBL	Radiation
Atmospheric State Tendencies	Momentum		i		io	
	Potential Temperature	io	io		io	io
	Water vapor	io	io		io	i
	Cloud	io	o		io	i
	Precipitation	io	o			i
Surface fluxes	Longwave up			o		i
	Longwave down			i		o
	Shortwave up			o		i
	Shortwave down			i		o
	Surface convective rain		o	i		
	Surface resolved rain	o		i		
	Heat flux			o	i	
	Moisture flux			o	i	
	Surface stress			o	i	

A.6. Urban Canopy Models

A.6.1. Single layer UCM

Single layer UCM calculates the multi-reflection effect (radiation trapping) according to the urban geometry (eqs. 3-34 and 3-35; Kusaka et al., 2001). It also provides a more accurate estimation for sensible heat by assuming a wind distribution in the canopy (eq. 3-36). In most cases, the horizontal wind is vertically distributed as a combination of logarithmic and exponential function (eq. 3-39 and 3-40). The model considers two-dimensional approximation for streets (very long streets) with a single orientation. The surface properties could be averaged for different orientations of streets.

$$E_w = E_{w,1} + R_w \times E_{w,1} \times F_{w \rightarrow w} + R_g \times E_{g,1} \times F_{g \rightarrow w} \quad (\text{A-33})$$

$$E_g = E_{g,1} + R_w \times E_{w,1} \times F_{w \rightarrow g} \quad (\text{A-34})$$

$$H_a = \frac{2\tilde{h}H_w + \delta H_g}{\delta} \quad (\text{A-35})$$

$$\begin{cases} H_w = C_w(T_w - T_s) \\ H_g = C_g(T_g - T_s) \end{cases} \quad (\text{A-36})$$

$$C_w = C_g = \begin{cases} 7.51U_s^{0.78} & U_s > 5 \text{ m/s} \\ 6.15 + 4.18U_s & U_s \leq 5 \text{ m/s} \end{cases} \quad (\text{A-37})$$

$$U_s = U_r e^{-0.389 \frac{h}{\delta}} \quad (\text{A-38})$$

$$U_r = U_a \frac{\Psi_{mr}}{\Psi_m} \quad (\text{A-39})$$

$$\Psi_m = \int_{\frac{z_0-d}{L}}^{\frac{z-d}{L}} \frac{\varphi_m}{\frac{z-d}{L}} d\left(\frac{z-d}{L}\right) \quad (\text{A-40})$$

$$\varphi_m = \begin{cases} \left(1 - 19 \frac{z-d}{L}\right)^{-1/4} & \frac{z-d}{L} \leq 0 \\ 1 + 5.3 \frac{z-d}{L} & 0.5 > \frac{z-d}{L} > 0 \end{cases} \quad (\text{A-41})$$

where E_w is the total heat absorbed by walls, E_g is the total heat absorbed by the ground, $E_{w,1}$ is the heat absorbed by walls from sky, $E_{g,1}$ is the heat absorbed by the ground from sky, H_a is the sensible heat flux from the canopy to the atmosphere, H_w is the sensible heat flux from walls to the canopy, H_g is the sensible heat flux from the ground to the canopy, C_w is the convection heat transfer coefficient from walls to the canopy, C_g is the convection heat transfer coefficient from the ground to the canopy, U_s is the wind speed in the canopy, U_r is the wind speed at roof level, and U_a is the synoptic wind speed.

A.6.2. Multi-layer UCM

More accurate urban parameterization, than slab and SL-UCM models, is needed to better understand the effect of a complex surface like urban areas and its vertical mixing. Multi-layer UCM developed by Martilli et al. (2002) has been integrated in WRF (Chen et al., 2011) and validated for different cities (Hamdi and Schayes, 2007). ML-UCM divides the urban canopy to separate units and calculate the urban surface parameters (wall and roof temperature, heat fluxes, etc.) related to each unit. This type of model usually predicts the vertical exchange of momentum, heat, and moisture more accurately (other two models are not including the conservation equation for Turbulence Kinetic Energy, TKE). Building heights in the model are not constant and their shading is estimated by the model (for the constant building width and road width). Based on my estimation, this model increases the time of simulation up to 35% compared to the slab model.

The multi-layer UCM that I use for the simulations is based on a model proposed by Martilli (2002). In his model conservation equations are presented in tensor form for the mesoscale model that they used for validation.

$$\text{mass (air): } \frac{\partial \rho U_i}{\partial x_i} = 0 \quad (\text{A-42})$$

$$\text{momentum}^{16}: \frac{\partial \rho U_i}{\partial t} = -\frac{\partial p}{\partial x_i} + \frac{\partial \rho U_i U_j}{\partial x_j} - \frac{\partial \rho \bar{u}_i \bar{w}}{\partial z} - \rho \frac{\theta'}{\theta_0} g \delta_{i3} - 2\varepsilon_{ijk} \Omega_j (U_k - U_k^g) + D_{u_i} \quad (\text{A-43})$$

$$\text{energy: } \frac{\partial \rho \theta}{\partial t} = -\frac{\partial \rho \theta U_j}{\partial x_j} - \frac{\partial \rho \bar{\theta} \bar{w}}{\partial z} - \frac{1}{C_p} \left(\frac{p_0}{p}\right)^{R_{air}/C_p} \frac{\partial R_{lw}}{\partial z} + D_\theta \quad (\text{A-44})$$

$$\text{mass (water): } \frac{\partial \rho q}{\partial t} = -\frac{\partial \rho q U_j}{\partial x_j} - \frac{\partial \rho \bar{q} \bar{w}}{\partial z} + D_h \quad (\text{A-45})$$

U , ρ , p , u_i , w , θ , Ω , U^g , C_p , R , R_{lw} , q , h , and D are wind speed components, air density, pressure, wind speed perturbation components in horizontal surface, vertical wind speed perturbation, potential temperature, angular velocity of the earth, geostrophic wind velocity, heat capacitance of the air, universal gas constant, longwave radiation, moisture content, moisture content perturbation, and effect of buildings on the equation, respectively.

In general, vertical perturbation from turbulence is assumed to have linear relation to the variation of mean value of properties in a grid.

$$\bar{w} \bar{a} = -K_z \frac{\partial A}{\partial z} \quad (\text{A-46})$$

It results in a prognostic equation for conservation of TKE.

$$\frac{\partial \rho E}{\partial t} = -\frac{\partial \rho E U_j}{\partial x_j} - \frac{\partial \rho \bar{e} \bar{w}}{\partial z} - \rho \frac{1}{\theta_0} g \frac{\partial \theta}{\partial z} + \rho K_z \left[\left(\frac{\partial U_x}{\partial z} \right)^2 + \left(\frac{\partial U_y}{\partial z} \right)^2 \right] - \rho C_\varepsilon \frac{E^{3/2}}{l_\varepsilon} + D_E \quad (\text{A-47})$$

Consequently, turbulent coefficient can be estimated by TKE.

$$^{16} \delta_{ij} = \begin{bmatrix} 1 & 0 & 0 \\ 0 & 1 & 0 \\ 0 & 0 & 1 \end{bmatrix} \text{ and } \varepsilon_{ijk} = \begin{bmatrix} 0 & 0 & 0 \\ 0 & 0 & 1 \\ 0 & -1 & 0 \end{bmatrix} \begin{bmatrix} 0 & 0 & -1 \\ 0 & 0 & 0 \\ 1 & 0 & 0 \end{bmatrix} \begin{bmatrix} 0 & 1 & 0 \\ -1 & 0 & 0 \\ 0 & 0 & 0 \end{bmatrix}$$

$$K_z = C_k l_k E^{1/2} \quad (\text{A-48})$$

where $C_k = 0.4$ and $C_\varepsilon = 0.71$.

Length scales are calculated from following equations:

$$\int_z^{z+l_{up}} \beta(\theta(z) - \theta(z')). dz' = E(Z) \quad (\text{A-49})$$

$$\int_{z-l_{down}}^z \beta(\theta(z') - \theta(z)). dz' = E(Z) \quad (\text{A-50})$$

$$l_k = \min(l_{up}, l_{down}) \quad (\text{A-51})$$

$$l_\varepsilon = (l_{up} l_{down})^{1/2} \quad (\text{A-52})$$

In the governing equations of the mesoscale model, the last term (D; forcing) considers the effect of buildings on generating or dissipating momentum, energy, and TKE (eq. 3-44, 3-45, and 3-48). Louis (1979) formulations are applied for horizontal surfaces with a constant value for von Karman coefficient and drag coefficient of walls for 2D urban areas. However, for urban climate modeling these constants should be modified to a value that can represent three dimensional urban structures.

$$D_A = \frac{F_a^H + F_a^V}{V^A} \quad (\text{A-53})$$

where D_A is the forcing term of conservation of A (momentum, energy, and TKE) in the mesoscale model, F_a^H is the horizontal forcing of the prognostic variables, F_a^V is the vertical forcing of the prognostic variables, and V^A is the volume of the air in the grid.

A.6.2.1. Building Energy Model

The building energy model calculates the sensible heat and latent heat of a building based on eqs. 3-55 and 3-56 to find the energy consumption of air conditioning system and heat emission to the canopy from eqs. 3-57 and 3-58 proposed by Kikegawa et al. (2003). In this model, temporal variation of indoor air temperature is solved based on the difference between the indoor sensible load and the sensible heat load provided by HVAC. Indoor air humidity is also treated the same, based on the difference between the indoor latent heat load and the latent heat load provided by

the HVAC system. Indoor sensible heat load is calculated by the convective heat transfer between room surfaces, supply air ventilation rate, heat released from equipment, and anthropogenic heat of occupants. Firstly, the BEM considers no sensible heat ($H_{out} = 0$) or latent heat ($E_{out} = 0$) to calculate temperature and moisture of the room without air conditioning. Then, the difference of temperature and moisture to target temperature and moisture, respectively, are determined to estimate H_{out} and E_{out} . Outputs of BEM to the mesoscale model are temperature of urban surfaces, heat flux, and moisture flux from the urban area. Heat emission to the urban canopy is equal to the sum of heat removed and the electricity used by the system during cooling hours. And, heat emission to the canopy is equal to the energy content of natural gas used by the system during the heating hours. Surface temperature of walls, floor, and ceiling are estimated using Fourier law of 1D diffusion conduction. Windows are assumed to be non-absorbent and the temperature is constant along its thickness.

$$\rho c_p V^R \frac{\partial T}{\partial t} = H_{in} - H_{out} \quad (\text{A-54})$$

$$H_{in} = H_{win} + H_{wall} + H_{equip} + H_{occup} + H_{vent}$$

$$H_{win} = \sum A_{win} h_{win} (T_{win} - T_r)$$

$$H_{wall} = \sum A_{wall} h_{wall} (T_{wall} - T_r)$$

$$H_{equip} = A_{floor} q_{equip}$$

$$H_{occup} = A_{floor} P \phi_p q_{occup,h}$$

$$H_{vent} = (1 - \beta) \rho c_p V_{ach} (T_a - T)$$

$$\rho l_v V^R \frac{\partial q_v}{\partial t} = E_{in} - E_{out} \quad (\text{A-55})$$

$$E_{in} = E_{vent} + E_{occup}$$

$$E_{vent} = (1 - \lambda) \rho l_v V_{ach} (q_{v_a} - q_v)$$

$$E_{occup} = A_{floor} P_{occup} \phi_p q_{occup,s}$$

in which ρ , c_p , l_v , V^R , T_z , q_{vz} , H , and E are air density, specific heat capacitance of air, specific latent heat of evaporation, volume of the zone, temperature of the zone, mixing ratio of the zone,

sensible heat energy, and latent heat energy, respectively. Here, A , h , λ , V_{ach} , q_{equip} , $q_{occup,h}$, $q_{occup,s}$, P_{occup} , ϕ_p , and q_{Va} are area of the wall, or floor, or window, convection heat transfer coefficient, thermal efficiency of the total heat exchanger, volume of the exchanged air, sensible heat gain from equipment, sensible heat generation by occupants, latent heat generation by occupants, peak number of occupants, ratio of hourly occupants to P_{occup} , respectively.

Heat transfer through walls and roofs are similar. Eqs. 3-59 to 3-61 shows the formulation for walls.

$$\frac{\partial T_{wall}}{\partial t} = \frac{1}{\Delta x} (C_s^{-1} HFX - K_s \frac{\partial T_{wall}}{\partial x} \Big|_{n-1}) \quad (A-56)$$

$$HFX = (1 - R_w)R_{sw} + \epsilon R_{lw} + \epsilon \sigma T_{wall}^4 + H \quad (A-57)$$

$$H = \begin{cases} h(T_z - T_{wall}) & \text{outdoor} \\ h_{wall}(T_z - T_{wall}) & \text{indoor} \end{cases} \quad (A-58)$$

Heat transfer through windows (eq. 3-62) is more complicated because of the transmittance of energy that is determined by eq. 3-63.

$$\rho_{wind} C_{wind} \delta_{wind} \frac{dT_{wind}}{dt} = \epsilon_{wind} (R_{lw_{outdoor}} - \sigma T_{wind}^4) + H_{outdoor} + \quad (A-59)$$

$$\epsilon_{wind} (R_{lw_{indoor}} - \sigma T_{wind}^4) + H_{indoor}$$

Solar energy transmitted through windows:

$$g(z) = g_0(1 - az^\alpha - bz^\lambda - cz^\gamma) \quad (A-60)$$

$z = \theta/90$ (θ is in degree), $a + b + c = 1$ and $a = 8$, $b = 0.25/q$, $\alpha = 5.2 + 0.7q$, $\lambda = 2$, $\gamma = 5.26 + 0.06p + (0.73 + 0.04p)q$ where p is the number of panes and q represents the category (with a value between 1 to 10 and 4 for standard glasses). The model considers different layer of urban surfaces, for instance, walls can have three layers with different properties.

Appendix B: Can urban ozone generation be modeled correctly based on major gaseous atmospheric reactions?¹⁷

In this section, first, we introduced governing equations that affect meteorological parameters. Then, reaction rates and parameterization methods of different types of atmospheric reactions of the model discussed. Thereafter, important reactions that were used in the model presented.

B.1. Governing equations

Governing equations of the model are mainly based on the conservation laws of mass, momentum, and energy. Physical interpretation of the conservation laws for our model can be written as:

$$\left(\begin{array}{c} \text{generation of} \\ \text{pollutants} \end{array} \right) - \left(\begin{array}{c} \text{Dissipation of} \\ \text{pollutants} \end{array} \right) + \left(\begin{array}{c} \text{Inflow of} \\ \text{pollutants} \end{array} \right) - \left(\begin{array}{c} \text{Outflow of} \\ \text{pollutants} \end{array} \right) = \left(\begin{array}{c} \text{Accumulation of} \\ \text{pollutants} \end{array} \right)$$

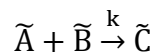
Generation of pollutants consists of anthropogenic emission and chemical reactions, whereas, dissipation mechanisms comprise deposition mechanism (dry and wet) and chemical reactions.

B.2. Atmospheric reactions and reaction rates

There are hundreds of gaseous constituents in the troposphere, where different types of reactions take place. Reactions of the model were categorized in four major groups of photochemical, oxygen, nitrogen, and carbon reactions. In this paper, main focus was in the rate of the reactions, for photochemical reactions that require solar energy and other three groups of the chemical reactions. Hence, methods of parameterization of the reactions were discussed first and then reactions were introduced.

B.2.1. Parameterization of reaction rates

For a simple reaction



the rate of generation and dissipation of each component can be calculated from:

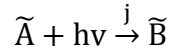
¹⁷ Materials presented in Appendix B is presented in the 93rd AMS annual meeting, Austin (TX, US), 2013.

$$\frac{d\tilde{A}}{dt} = \frac{d\tilde{B}}{dt} = \frac{d\tilde{C}}{dt} = k[\tilde{A}][\tilde{B}]$$

The reaction rate, k , can be determined by the collision theory as shown in eq. B-1 (Seinfeld and Pandis, 2006).

$$k = Ae^{-\frac{E}{RT}} \quad (\text{B-1})$$

For photolysis reaction like



The rate of dissipation of \tilde{A} (or rate of generation of \tilde{B}) is

$$\frac{d\tilde{A}}{dt} = \frac{d\tilde{B}}{dt} = j \cdot [\tilde{A}]$$

For the base case (generally temperature of 300 K), A_0 and E_0 have been obtained experimentally and are used to determine reaction rates in different temperatures. From collision theory, for gases, A is directly related to the square root of temperature (Seinfeld and Pandis, 2006). E is the required energy for reaction to be completed and is independent of the ambient temperature. Therefore:

$$A = A_0 \left(\frac{T}{T_0}\right)^{\frac{1}{2}} \quad (\text{B-2})$$

Replacing A in the reaction rate formula (B-1) yields

$$k = A_0 \left(\frac{T}{T_0}\right)^{\frac{1}{2}} \cdot e^{-\frac{E_0}{RT}} \quad (\text{B-3})$$

This parameterization will be used for the reaction rates wherever experimental data is not available. Atmospheric reactions and their corresponding rates can be found in references (Seinfeld and Pandis, 2006; Atkinson et al., 2004).

B.2.2. Parameterization of photolysis rate

Photolysis rate is normally based on quantum yield and cross section of a reaction (see Atkinson et al., 2004, and references therein). However, here, we used the parameterized rate of the

photochemical reactions. Each photolysis reaction is a function of the zenith angle (z) and can be estimated from parameterization type proposed by Collins et al. (1997).

$$j = \alpha e^{-\beta \cdot \sec(z)} \quad (\text{B-4})$$

Four main photochemical reactions were considered in this work and two constants (α, β) were estimated based on the available data for photolysis reaction rate of 15 degrees zenith angle (Collins et al., 1997) and zenith sun (Seinfeld and Pandis, 2006) at 0.5 km altitude (Table B-1).

Table B-1. rate of photolysis reaction of 15 degrees zenith angle (Collins et al, 1997) and zenith sun (Seinfeld and Pandis, 2006) at 0.5 km altitude

Reaction	Z = 0°	Z = 15°
$j_{\text{O}_3+h\nu \rightarrow \text{O}}$	6.5×10^{-4}	4.71×10^{-4}
$j_{\text{O}_3+h\nu \rightarrow \text{O}_\text{D}}$	5×10^{-5}	3.24×10^{-5}
$j_{\text{NO}_2+h\nu \rightarrow \text{O}+\text{NO}}$	1.39×10^{-2}	9×10^{-3}
$j_{\text{H}_2\text{O}_2+h\nu \rightarrow 2\text{OH}}$	2.87×10^{-5}	7.98×10^{-6}

B.2.3. Photochemical reactions

The rates of photochemical reactions depend on the solar radiation energy, which primarily relates to the zenith angle. There are different estimates for photolysis rate as a function of altitude; however we considered only the reaction rates near the Earth's surface. In addition to one intermediate reaction of hydrogen peroxide, three main photolysis reactions in the troposphere take place. Ozone dissociates into oxygen atom and oxygen molecule. The oxygen atom may become ground state oxygen (O) or excited oxygen (O_D) in the following reactions:



The respective reaction rates for these two reactions are:

$$j = 6.45e^{-9.2\sec(z)} \left(\frac{1}{\text{sec}}\right) \quad (\text{B-7})$$

$$j = 12.1e^{-12.4\sec(z)} \left(\frac{1}{\text{sec}}\right) \quad (\text{B-8})$$

Nitrogen dioxide photodissociation is analogous to photolysis of ozone.



$$j = 3439.6e^{-12.4\text{sec}(z)} \left(\frac{1}{\text{sec}}\right) \quad (\text{B-10})$$

Hydrogen peroxide is an important intermediate reactant and generates hydroxide, which is highly reactive.



$$j = 2.75 \times 10^{11} \cdot e^{-36.8\text{sec}(z)} \left(\frac{1}{\text{sec}}\right) \quad (\text{B-12})$$

B.2.4. Oxygen reactions

Oxygen atom involves in reactions in a wide range of atmospheric temperature. The first reaction is collision of ground oxygen atom and oxygen molecule by other atmospheric constituents, mainly nitrogen, to produce ozone.



$$k = 5.5 \times 10^{-34} \left(\frac{T}{300}\right)^{-2.6} [\text{N}_2] \left(\frac{\text{cm}^3}{\text{molecule}\cdot\text{sec}}\right) \quad 18 \quad (\text{B-14})$$

where M represents gases that collide with parents in a reaction and leave the reaction without any change. In atmospheric reactions, M is the mixture of oxygen and nitrogen. The second reaction is the dissipation of ozone when it reacts with the ground oxygen atom.



$$k = 8 \times 10^{-12} e^{-\frac{2060}{T}} \left(\frac{\text{cm}^3}{\text{molecule}\cdot\text{sec}}\right) \quad (\text{B-16})$$

The next reaction is the conversion of the excited oxygen atom into the ground oxygen atom by collision, with the other atmospheric constituents.



¹⁸ Based on the data provided by Hippler et al. (1990)

$$k_0 = 2.9 \times 10^{-11} [M] \left(\frac{\text{cm}^3}{\text{molecule}\cdot\text{sec}} \right) \quad 19 \quad (\text{B-18})$$

Finally, we considered the reaction of excited oxygen atom with H₂O (the only reaction that can produce OH in the atmosphere). Some other OH radicals are generated in the following process, but they are also indirect results of this reaction.



$$k_0 = A_0 = 2.2 \times 10^{-10} \left(\frac{\text{cm}^3}{\text{molecule}\cdot\text{sec}} \right) \quad (\text{B-20})$$

B.2.5. Nitrogen reactions

The only effective reaction in the atmosphere, excluding the photolysis reaction of NO₂, is the dissipation of ozone from the nitric oxide reaction.



$$E_0/R = 1500 \text{ K} \quad (\text{B-22})$$

$$A_0 = 3 \times 10^{-12} \left(\frac{\text{cm}^3}{\text{molecule}\cdot\text{sec}} \right) \quad (\text{B-23})$$

B.2.6. Carbon reactions

Carbon monoxide is an important pollutant that is mainly emitted from anthropogenic activities, or more specifically from incomplete combustion. Carbon monoxide reacts with hydroxyl radical, which was generated by the reaction between the oxygen atom and the water molecules.



$$k_0 = A_0 = 1.5 \times 10^{-13} \left(\frac{\text{cm}^3}{\text{molecule}\cdot\text{sec}} \right) \quad (\text{B-25})$$

The hydrogen radicals are highly reactive and simultaneously react with the oxygen molecules and produce Hydroperoxyl radical.

¹⁹ Here, [M] is the concentration of N₂ and O₂ mixture



$$k_0 = A_0 = 1.5 \times 10^{-13} \left(\frac{\text{cm}^3}{\text{molecule}\cdot\text{sec}} \right) \quad (\text{B-27})$$

Hydroperoxyl radical generation is followed by its reaction to nitric oxide and reproduction of nitrogen dioxide.



$$k = 3.6 \times 10^{-12} e^{\frac{270}{\text{T}}} \quad (\text{B-29})$$

Hydroperoxyl radical also reacts with itself to produce hydrogen peroxide.



$$k = 2.2 \times 10^{-13} e^{\frac{600}{\text{T}}} \quad (\text{B-31})$$

Hydrogen peroxide reacts with O $\dot{\text{H}}$ in the following manner



$$k = 2.9 \times 10^{-12} e^{-\frac{160}{\text{T}}} \quad (\text{B-33})$$

The termination reaction for this cycle is the production of nitric acid.



$$k = 3.3 \times 10^{-30} \left(\frac{\text{T}}{300} \right)^{-3} [\text{N}_2] \quad (\text{B-35})$$

B. 3. Simulation

The model is simulated using the STELLA software based on the stock and flow method (Ford, 2009). One stock is defined for each gaseous component with several inflows and outflows. The inflows and outflows represent the rate of production or generation and dissipation or dispersion of a pollutant (Figure B-1). Simulation was run for the city of Los Angeles from 12:00 PM (hour 0) of August 21 to 12:00 PM (hour 96) August 25. We used TMY3 data for wind velocity (m/s),

temperature (K) and zenith angle (degrees) for the four days (National Solar Radiation Data Base, http://rredc.nrel.gov/solar/old_data/nsrdb/1991-2005/tmy3/by_state_and_city.html#Top) . The desired time interval to record the concentration of pollutants was one second. However due to the software’s computational limitation, an 18 seconds interval was chosen. To increase the accuracy of the simulation, the fourth order Runge-Kutta discretization method was used. Other options were second order Runge-Kutta and Euler explicit that both produce larger errors (Hirsch, 2007; Pielke, 2002). Nitric oxide and nitrogen dioxide anthropogenic emissions were considered to have the ratio of 10:1 (Valler, 2012). Emission of carbon monoxide considered to be four times more than total NOx emission (Air Resources Board, 2009). Diurnal variation of anthropogenic emission assumed to be identical in each day of simulation. According to references (Gao, 2007; Sailor and Lu, 2004; Gantt et al., 2010), anthropogenic heating and pollution emissions in Los Angeles start to increase from morning and reach their peak before noon. As illustrated in Figure B-2, after the constant emission generation during the day, heating and pollution emission decrease eventually, by decreasing anthropogenic activities. This assumption is logical because in summertime and during working days anthropogenic activities and cooling load gradually reach their peak value when temperature increases. Wind velocity, temperature, zenith angle and relative humidity of Los Angeles were used as the inputs of the simulations (Figure B-3).

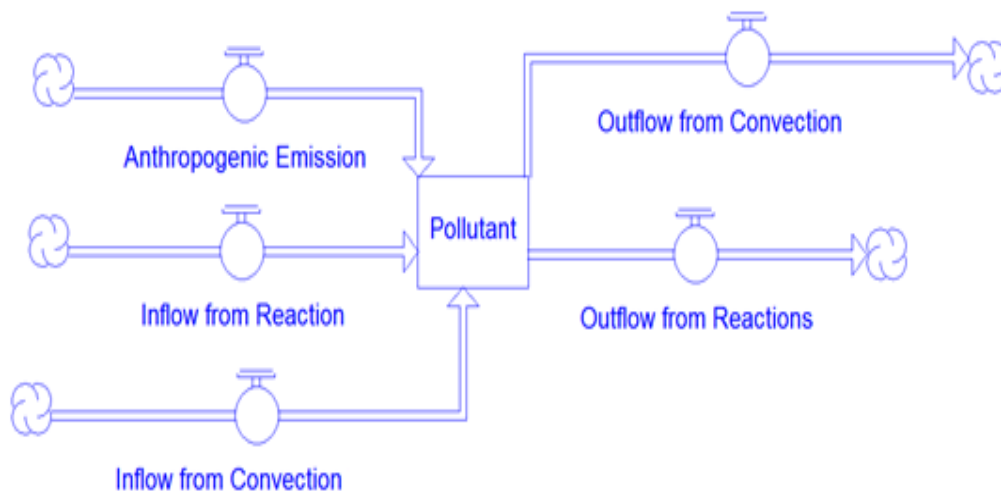


Figure B-1. Schematic of stock and flows for a pollutant in STELLA software

B.4. Results and Discussion

The first cycle (hour 0 to 24) of different calculated variables were ignored, according to the spin-up cycle of the simulation. Qualitative change in the anthropogenic emissions and the photochemical reaction rates were then observed (Figure B-4 and B-5) to verify the proposed model. As illustrated in Figure B-5, nitric oxide was consumed as soon as it was produced from the human activities or generated from the chemical reactions. The concentration of nitric oxide is much less than the other pollutants and its maximum value was less than 5 ppb. Carbon monoxide and nitrogen dioxide had similar periodic behavior and the concentration of these components was proportional to the rate of their emission. Nitrogen dioxide had a sharp increase when the zenith angle became small, and had a gradual decrease after passing its peak value. Concentration of carbon monoxide increased and decreased smoothly and periodically. Furthermore, wind is the critical parameter in this simulation which speeds up the process of pollution dispersion. The reaction rates of pollutants in nighttime were small, there is no photochemical reaction. As a result, when running the model for a case in which the wind velocity was zero, persistent accumulation of the pollutants and a negligible dissipation from the chemical reactions in nighttime captured.

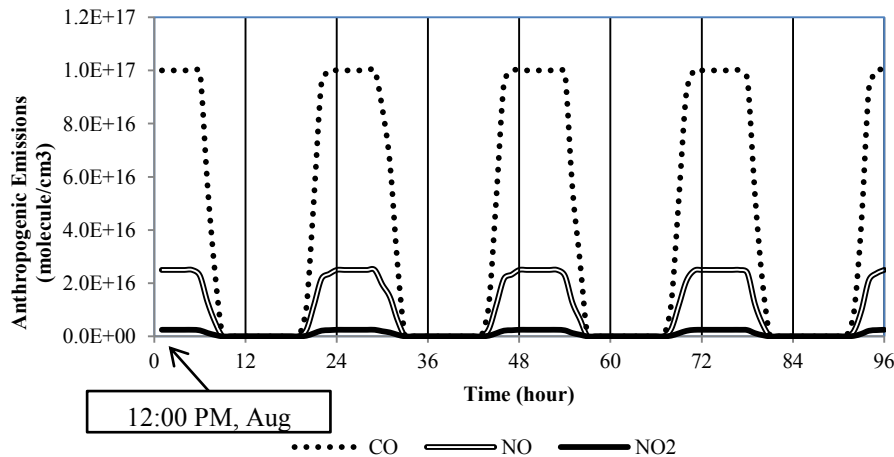


Figure B-2. Anthropogenic emissions of NO₂, NO and CO ($\frac{\text{molecule}}{\text{cm}^3}$) as a function of time (hour)

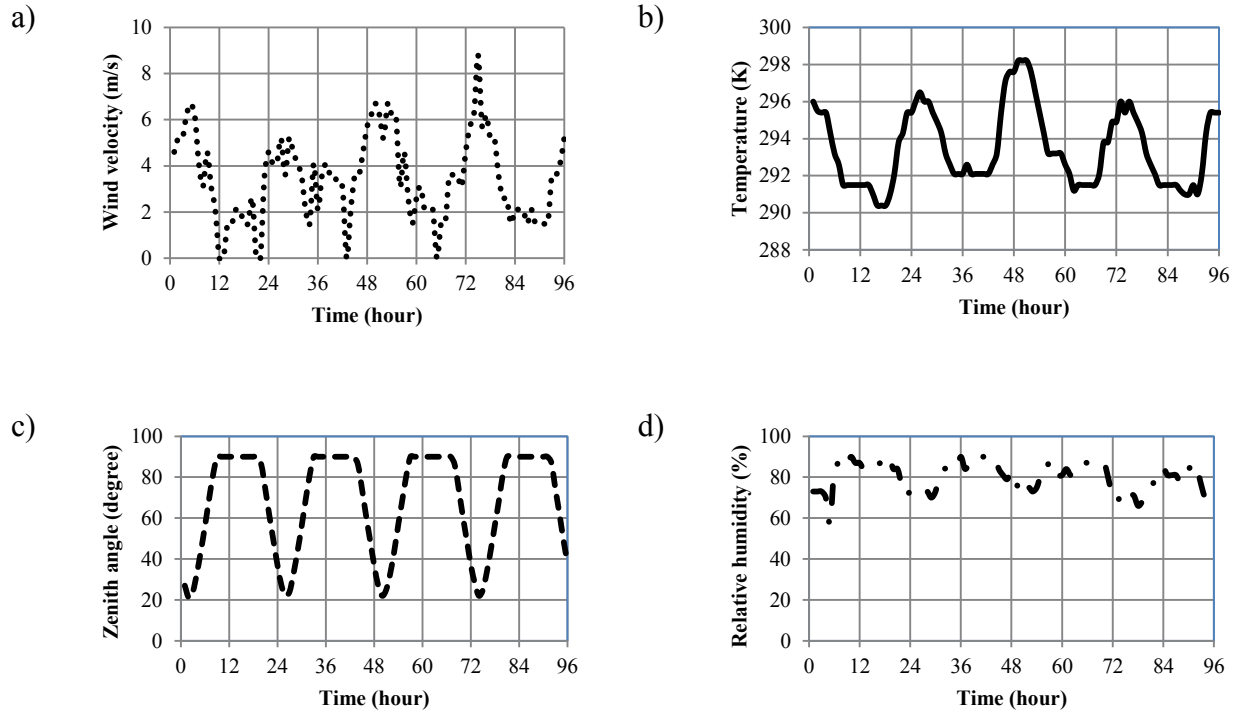


Figure B-3. a) Wind velocity (m/s), b) Temperature (K), c) Zenith angle (degree), and d) Relative humidity (%) of Los Angeles in specified period of time (National Solar Radiation Data Base, 2011)

Verification of the model was based on variation of the concentration of nitrogen dioxide and nitric oxide, and the rate of photochemical reactions. In a real case, the maximum concentration of nitric oxide occurs in the morning followed by an increase in the concentration of nitrogen dioxide (Austin, 1999). Simulation results qualitatively followed the same pattern, however, the maximum concentration of NO_2 occurred a couple of hours later than the expected time. Figure B-5 illustrates the reaction rates of the four photochemical reactions, considering as the other parameters, to evaluate the model. All the reaction rates had their maximum value at the exact time when the zenith angle was minimum. This result clearly shows that the photolysis processes in this group of the reactions were captured, accurately. The small increase in the hydroperoxyl reaction rate is due to the small reaction rate coefficient of the reactions that produced hydroperoxyl.

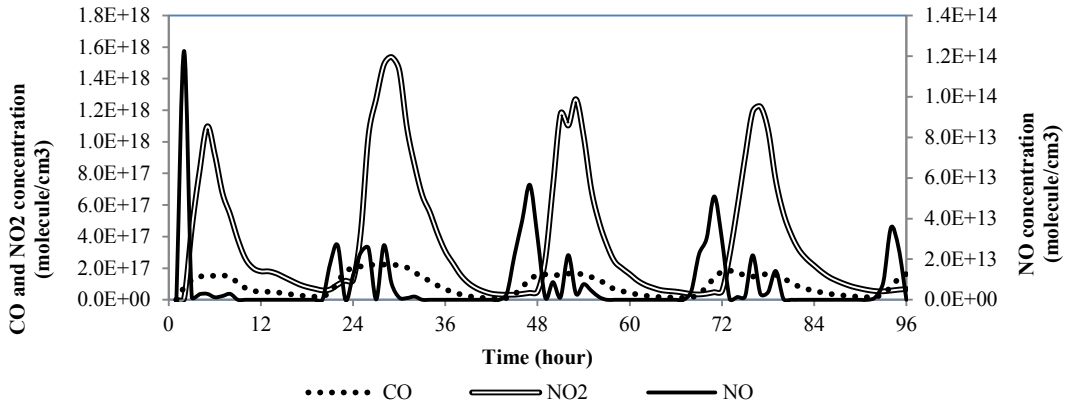


Figure B-4. Time series CO, NO₂ and NO concentration ($\frac{\text{molecule}}{\text{cm}^3}$) variation

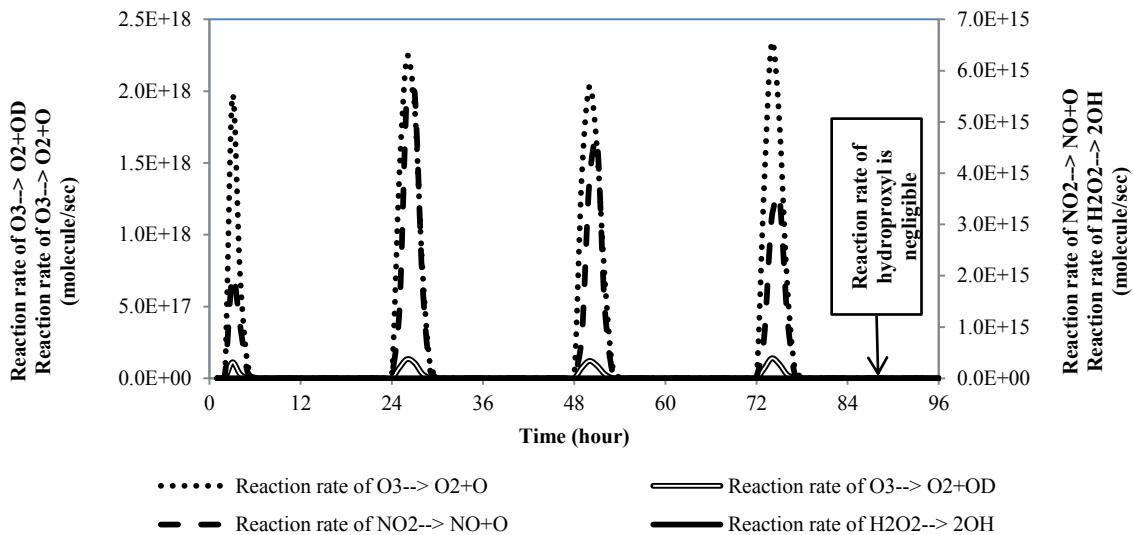


Figure B-5. Cyclic changes of photochemical reaction rates

The most important result of this modeling is variation of the ozone concentration during the simulation period (Figure B-6). The ozone concentration started to grow rapidly after a lag when temperature started to increase. Thereafter, the ozone concentration got its maximum value as temperature reached its peak. The temperature increase in simulation of the late summer episode was accompanied by the least value of solar zenith angle, which had direct effect on the photolysis rate as discussed in Section B.2.3. In the stagnant case the ozone concentration was almost constant, indicated that the net rate of ozone generation is negligible. The minimum concentration of ozone occurred right before noon and it was about $1.2 \times 10^{17} \left(\frac{\text{molecule}}{\text{cm}^3}\right)$, or

40(ppb). The maximum concentration of ozone was about $7.5 \times 10^{18} \left(\frac{\text{molecule}}{\text{cm}^3}\right)$ or 300(ppb), and after a few hours it started to decrease smoothly. Finally, we determined the sensitivity response of the ozone concentration to the temperature variation by keeping the relative humidity, wind velocity and anthropogenic emission constant. The temperature was the only parameter changed to 0.9 and 1.1 of its initial value. As a result, by increasing the temperature, the ozone concentration reduced and vice versa (Figure B-7). This result is a consequence of the rate coefficient of the reaction (B-13), the only reaction that produced ozone, which was inversely proportional to the temperature. However, all the other reaction rate coefficients were proportional to the temperature. Therefore, to improve the ozone concentration dependence on temperature, volatile organic compounds and the other related reactions should be considered. The role of VOCs in ground-level ozone generation is to form radical intermediates converting NO to NO₂. This increase in the NO₂/NO ratio results an increase in the O₃ concentration. Increase in the concentration of NO₂ produced by trees in an urban area enhances the ozone generation before noon. Additionally, increasing temperature also enhances NO₂ generation from the reaction of VOCs.

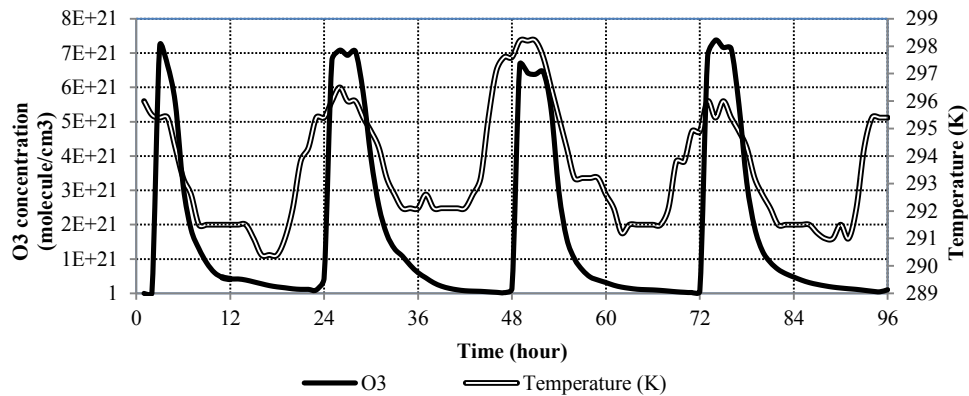


Figure B-6. Time series Ozone ($\frac{\text{molecule}}{\text{cm}^3}$) and Temperature (K) variation

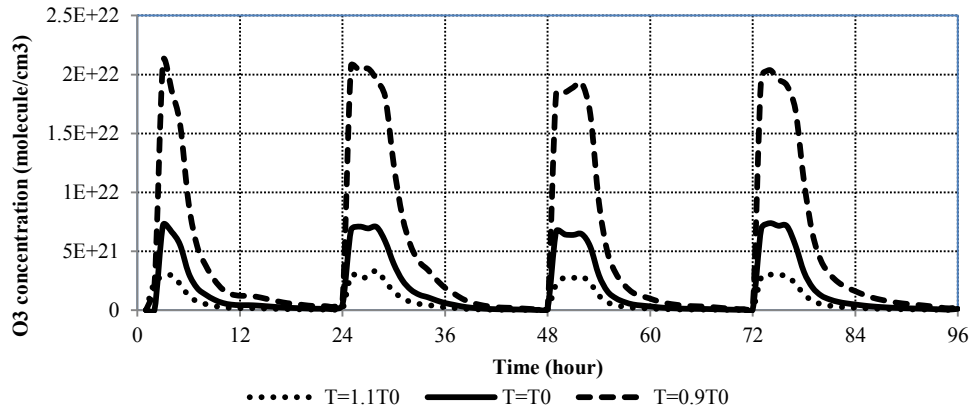


Figure B-7. Sensitivity of ozone to the temperature ($T = 0.9T_0$, $T = T_0$ and $T = 1.1T_0$)

B.5. Limitations

The reactions that we considered were based on the major inorganic gaseous components in the atmosphere, introduced in the references (Atkinson, et al., 2004; Seinfeld and Pandis, 2006) and had been used in many other researches. There may be other reactions considered by other references as the main atmospheric reactions, but they're not widely used.

The STELLA software has some restrictions to simulate the problem due to a limited number of numerical schemes. Its limited number of time intervals was a problem in the simulations. The simulations were performed by 32000 time steps instead of our desired 345000 time steps (in this case each time step would be equal to 1 second).

These results represent only in a qualitative form and numbers can not represent the exact values of the variables as the hypothetical anthropogenic emission assumption could be much different from the actual case. The actual case of the anthropogenic activities for a short episode was not available.

Fluctuations, in the peak concentration of different pollutants, were generated by the numerical iteration in some time intervals. The output data presented were digested by omitting irrelevant noises in the system.